A micromechanical investigation on the mechanism of energy dissipation in granular materials

by

Abdurrahim Essayah

2022

James Watt School of Engineering University of Glasgow

Submitted in fulfilment of the requirement for the degree of

Doctor of Philosophy

Declaration of originality

This thesis entitled “A micromechanical investigation on the mechanism of energy dissipation in granular materials” is submitted to the University of Glasgow for the degree of Doctor of Philosophy. I declare that this thesis is my work conducted under the supervision of Dr Zhiwei Gao and Dr Thomas Shire. I have acknowledged all significant sources of assistance and taken reasonable precautions to guarantee the work is unique and does not violate any copyright laws.

Declaration of copyright

The following publications are based on this thesis:

Essayah, A., Shire, T. and Gao, Z., 2022. The relationship between contact network and energy dissipation in granular materials. Granular Matter, 24(4), pp.1-11.

Essayah, A., Gao, Z., & Shire, T. 2022. Micromechanical investigation about the stored plastic work in granular materials during drained triaxial shearing. UKCAM conference. (Presented).

Essayah, A., Gao, Z., & Shire, T. 2021. Micromechanical investigation of stored plastic work. GM3, UK. (Presented)

Essayah, A., Shire, T., & Gao, Z. 2019. Micro-scale investigation of energy dissipation in granular materials. GM3, UK. (Presented)

Abstract

Energy dissipation is crucial for understanding the mechanics of granular materials. Discrete element modelling has been carried out to investigate the mechanism of energy dissipation in granular materials.

Firstly, the relationship between energy dissipation and contact networks is investigated. Using the discrete element method, a series of triaxial compression tests with different stress paths have been simulated. The energy dissipation was analysed using two existing contact force network partitioning approaches, one based on the magnitude of average contact force and the other one based on the contribution of contact forces to the global deviator stress. The results indicate that for both techniques, neither the strong nor the weak contact networks exhibit negligible energy dissipation. When the average contact force partitioning approach is used, more than 70% of the energy dissipation occurs in the weak contact network, although the dissipation per sliding contact is greater in the strong contact network because the tangential contact force is greater. When the contact network is partitioned depending on the contribution of contact forces to global deviator stress, the strong contact network dissipates around 60% of the total energy. A new normal contact force threshold is found for partitioning the contact force based on the contribution to energy dissipation. Almost 93% of energy dissipation occurs at contacts with a normal contact force that is less than two times the average normal contact force. As a result of little particle sliding, interactions with a greater normal contact force result in a negligible amount of energy loss.

Secondly, a quantitative investigation of stored plastic work and energy dissipation in granular materials has been studied using discrete element modelling. Drained triaxial compression tests on samples with different particle size distributions (PSD) have been simulated. The elastic stiffness is measured using stress probe tests and then used to calculate the elastic and plastic strain in the samples. The total work input is decomposed into two parts, including the elastic free energy and plastic work, which are dependent on the elastic and plastic strain, respectively. The plastic work is further decomposed into stored plastic work and dissipated

energy. There is little elastic free energy in the material due to the small elastic strain. The stored plastic work is much smaller than the dissipated energy for samples with all particle size distributions. This could be due to a lack of interlocking among spherical particles, which is expected to 'freeze' plastic work in the material.

Finally, DEM simulation was also carried out to analyse some of the existing energy dissipation and stored plastic work equations. These energy dissipation functions showed inaccuracy in predicting the amount of energy dissipation. A new modified dissipation function was produced. This new function was able to offer a reasonable prediction for samples with different particle size distributions. Furthermore, a new stored plastic work function is developed based on the DEM results. As the quantity of stored plastic is small, a suitable function should be depending on the pressure increment. The new function can provide a good prediction for samples with different particle size distributions.

Acknowledgements

All the praises are for the almighty, Allah who bestowed me with the ability and potential to complete this thesis. I am grateful to God for the chances, challenges, and fortitude that have enabled me to complete the thesis. I learned so much over this process, not just from an academic standpoint but also from a personal perspective.

I would like to thank my supervisors, Dr Zhiwei Gao and Dr Thomas Shire, for their direction, understanding, patience, and most significantly, their positive support and kind attitude in helping me complete my thesis. It was a wonderful honour and privilege to have them as my supervisors.

There are no words to express my gratitude to my parents who supported me with their prayers and motivation that set me on the right path.

I would like to thank my wife for her love and support, for all the late nights and early mornings, and for keeping me sane during the last several months. Thank you for being my closest companion.

I would like to express my deepest gratitude to all of my dearest friends who have stood with me through thick and thin.

Last but not least, I would like to thank the faculty at the University of Glasgow for providing the greatest atmosphere and information to improve my skills.

Table of contents

List of Figures

List of Tables

List of Notation

Symbol	Meaning
ε_i	Axial strain
K	Bulk modulus
T_{crit}	Critical timestep
q	Deviator stress
$W_f^{c,t}$	Energy dissipation
$E_{c,fd}^{\beta}$	Friction dissipation per single contact
I	Inertia number
p	Mean effective stress
N_c	Number of contacts
N_p	Number of particles
ρ	Particle density
v	Poisson ratio
$\delta\varepsilon_r$	Radial strain
G	Shear modulus
$\delta\varepsilon_d$	Shear strain
T_{sim}	Simulation timestep
$\dot{\varepsilon}$	Strain rate
σ_{ij}	Stress tensor
l_j^c	The component of the branch vector
f_i^c	The component of the contact force acting on the particle
K^n	The contact normal tangent stiffness
$\sigma'_{measured}$	The current stress within the assembly
d	The diameter of the maximum particles
Ψ^e	The elastic part of the free energy
ΔE	The error of energy balance
FOS	The factor of safety
g	The gain parameter
δW^e	The increment of elastic work

$\delta\Psi$	The increment free energy
$\delta\Phi$	The increment of energy dissipation
Δs	The increment of relative tangential displacement
δW^p	The increment of plastic work
δW	The incremental applied work
Δs	The incremental tangential displacement at the sliding contact
σ_2	The intermediate principal stress
α_n	The interparticle overlap
σ_1	The major principal stress
m_p	The mass of the particle
m	The mass of the smallest particle
$\dot{\varepsilon}_{max}$	The maximum allowable strain rate
σ_3	The minor principal stress
I_p	The moment of inertia a particle
W_{sn}	The normal component of strain energy
F_n	The normal force of the contact networks
Ψ^p	The plastic part of the free energy
r_a and r_b	The radius of two overlapping particles
W_{kr}	The rotational kinetic energy
ω_p	The rotational speed of the particle
F_s^c	The shear component of the contact force
k_t	The shear tangent stiffness
$\dot{\varepsilon}_{i,t}$	The strain rate of boundaries
δW_{st}	The tangential component of strain energy
F^t	The tangential force of contact force
$\sigma'_{required}$	The target stress
W_{kin}	The total translational kinetic energy
v_p	The translation speed for particle
β	Timestep
$\emptyset E_{tot}^{\beta}$	Total cumulative energy dissipation
δE_{tot}^{β}	Total increment energy dissipation across all contact

$\boldsymbol{n}$	Unit vector along the line joining the sphere centres
$\delta\varepsilon_v$	Volumetric strain

Chapter 1: Introduction

The mechanics of granular materials is complex due to the interaction among individual particles. Sand is a typical granular material that is widely seen in geotechnical engineering. Their mechanical response is crucial for understanding the development of natural hazards (landslides and debris flows) and the performance of many essential components of infrastructure, such as buildings, bridges, and dams. Therefore, extensive research has been done on the mechanics of granular materials.

Energy dissipation has a significant influence on the mechanical behaviour of granular materials, such as shear strength and dilatancy. The energy aspect has been included in many constitutive models to characterise the behaviour of the soil. The Cam-Clay model, upon its initial development, was constructed under the assumption that all plastic work is dissipated through friction dissipation (Roscoe et al., 1963). Furthermore, the modified Cam-Clay model also utilised the energy consideration and addressed some of the deficiencies in the original model by adding the increment of volumetric strain to the dissipation to the equation (Roscoe and Burland, 1968).

In addition, all proposed changes to the Cam-Clay model, such as those changes provided by Gens and Potts (1988) kept energy consideration as a fundamental part. Furthermore, the energy consideration was used for many other constitutive models, such as NorSand (Jefferies and Shuttle, 2002, Jefferies, 1993), Severn-Trent sand (Gajo and Muir Wood, 1999) and the state-dependent sand model by Manzari and Dafalias (1997). The energy-based approach is also considered a key in seismic analysis and geotechnical earthquake engineering. There are many energy-based approaches have been proposed to predict the possibility of sand liquefaction during the seismic loading (Trifunac, 1995, Law et al., 1990, Berrill and Davis, 1985).

The contemporary ideas of thermomechanics are applied to develop families of models that explain the elastic/plastic behaviour of soils deforming under triaxial conditions. These theories rely in some way on the dissipation and free energy functions, which after specifying both functions, the corresponding yield loci, flow rules, isotropic and kinematic hardening rules, and elasticity law are defined systematically (Collins, 1997, Collins and Houlsby, 1997, Collins and Kelly, 2002, Collins and Hilder, 2002, Houlsby, 1981). Even though energy dissipation has been previously investigated, there is still a lack of details on the microscale behaviour of energy dissipation under different stress paths, confining pressure, and initial density. In addition, providing microscale investigation regarding the free energy (free energy is the energy stored in the representative volume element) can help distinguish the difference between the internal energy that is stored or dissipated in the system.

1.1 Scope of research

This study aimed to contribute to the understanding of the mechanisms of energy dissipation at the micro-scale using discrete element modelling (DEM) simulations. All simulations conducted within the scope of this research were conducted using idealised, completely spherical particles. The simulations used in this study were carried out using a modified version of the LAMMPS code (Plimpton, 1995). Simulations were performed on high-performance computers, allowing the modelling of relatively larger samples with a substantial number of particles. DEM offers an idealised numerical environment in which loading conditions can be properly controlled and stress-strain response can be exactly quantified. Using three-dimensional loading conditions this research will provide a quantitative investigation regarding energy dissipation and free energy. Consideration is given to the impact of loading conditions on the mechanical behaviour of energy dissipation. The effect of particle size distribution on the energy dissipation mechanism will also be investigated.

1.2 Research objectives

Using numerical simulations, the following objectives will be addressed in this study:

1. Investigation of the relationship between contact networks and energy dissipation:
    a. DEM simulations of samples with uniform PSDs.
    b. Examination of the contact force partitioning methods based on the contribution of the contact network to force transmission.
    c. Investigation of the effect of the partitioning method on the relationship between contact networks and energy dissipation.
    d. Proposing an alternative partitioning method for dividing the contact network based on the contribution of the contact network to energy dissipation.
2. Investigation of stored plastic work in granular materials
    a. providing a deeper understanding of the mechanism of stored plastic work using different examples.
    b. Investigating the effect of different PSDs on the amount of stored plastic work.
    c. Proposing new energy dissipation and stored plastic work equations based on the DEM results.

1.3 Thesis chapter organisation

This thesis contains seven chapters. Chapter 1 introduces the subject, scope and objectives of the research in this thesis. In Chapter 2, a literature review of the DEM simulation is presented, with a particular emphasis on its application in investigating the macro and micro-mechanical behaviour of granular materials. Additionally, the chapter conducts a thorough review of existing literature concerning energy dissipation and stored plastic work, while also identifying areas where research gaps persist.

Chapter 3 describes the DEM simulation that will be used throughout this study. The chapter focuses on describing the methods required to perform DEM simulation, including a description of the contact model, servo-control, periodic boundaries, and the selection of

simulation parameters used throughout this study. In addition, this chapter describes the method used in this study to monitor the energy dissipation during simulations.

Chapter 4 investigates the effect of the contact networks partitioning method, sample initial density, confining pressure, and stress path on the relationship between contact networks and energy dissipation.

Chapter 5 investigates the distinction between energy dissipation and plastic work by analysing the plastic work stored in granular materials. This chapter also examines the influence of various PSDs with varying particle numbers on the results of plastic work storage.

Chapter 6 provides an evaluation of energy dissipation and stored plastic work functions in granular materials. This chapter utilises the same simulations as chapter 5 to evaluate a variety of free energy and dissipation functions and provides an alternative function based on the DEM simulation findings.

Chapter 2: Literature review

This chapter presents a literature review of the DEM simulation, with a particular emphasis on its application in investigating the macro and micro-mechanical behaviour of granular materials. Additionally, the chapter conducts a thorough review of existing literature concerning energy dissipation and stored plastic work, while also identifying areas where research gaps persist.

2.1 Discrete element method

The DEM is based on modelling granular materials as an assembly of rigid particles by considering the interparticle interaction (Cundall and Strack, 1979). A contact model is applied to calculate the contact forces developed between neighbouring particles. The existing contacts between particles can break and new contacts can be developed.

Figure *2.1* is a flowchart to show the key stages of DEM simulation and the calculation that will be carried out during every timestep (O'Sullivan, 2011). Even with a simple contact model to simulate inter-particle contact, DEM proves to be effective in capturing the essential mechanical response characteristics of granular materials. By simplifying particle shapes and employing a basic contact model, DEM simulations can effectively analyse systems comprising a large number of particles while accurately representing soil behaviour. In DEM models, virtual specimens can be subjected to loads and deformations to explore their response, making it a valuable tool for investigating physical laboratory tests (O'Sullivan, 2011). DEM simulation allows monitoring the mechanisms of granular materials at the particle scale which can simplify the complexity of the material's response. These mechanisms are involved in evaluating contact force, particle rotations, particle orientation and contact sliding, etc., all this information is difficult or might be impossible to be quantified in laboratory experiments.

Soil grains have several shape properties, such as sphericity, roundness, and roughness, which are influenced by their production, transit, and deposition histories, as well as their mineralogical composition. The degree of interlocking between soil grains varies according to the degree of form irregularity. Numerous experimental investigations have been used to

examine the influence of particle shape on soil behaviour (Cho et al., 2006, Shin and Santamarina, 2013, Yang and Wei, 2012). Cho et al. (2006) examined a large dataset derived from physical tests and demonstrated that particle shape influences packing density, small strain stiffness, volumetric response, and strength. Consideration of the non-spherical shape of soil grains in DEM simulations is challenging. Several methods that can be used to create non-sphere particles will be discussed here.

Regularly shaped particles method

The production of particles having non-spherical shapes can be achieved by using regularly-shaped particles, such as ellipses in two-dimensional space (Fu and Dafalias, 2011), ellipsoids in three-dimensional space (Ng, 2009b), polygons in two-dimensional space (Pena et al., 2008), and polyhedrons in three-dimensional space (Langston et al., 2013) (see Figure *2.2*).

Sphere or regularly shaped clusters particles method

Alternatively, several spheres or regularly-shaped particles are bonded together to produce a new form of particle shape (clusters/ clumps) (see Figure *2.3*) (Ferellec and McDowell, 2010, Kozicki et al., 2012, Yang and Wei, 2012).

Superquadrics method

Superquadrics are a class of parametric shapes that are derived from the fundamental quadric surfaces. In mathematical terms, a superquadric is defined as a spherical product of two parametric 2D curves. The superquadric's implicit formula in the body-fixed coordinate system is represented as follows:

$$f(x,y,z) = \left[\left(\frac{x}{a}\right)^{\frac{2}{\varepsilon_2}} + \left(\frac{y}{b}\right)^{\frac{2}{\varepsilon_2}}\right]^{\varepsilon_2/\varepsilon_1} + \left(\frac{z}{c}\right)^{\frac{2}{\varepsilon_1}} - 1 = 0 \quad (1)$$

where a, b and c are the half-lengths along the related principal axis; ε_1 and ε_2 are the roundness parameters which control the edge sharpness. By altering the values of the five parameters, it is possible to make modifications to a wide range of shapes. By replacing the squaring operations with arbitrary powers, a greater number of shapes can be represented. Furthermore, through the manipulation of roundness parameters, a diverse range of shapes can be achieved, encompassing prevalent particle forms such as cylinders, prolate spheroids, boxes, and cubes. Figure *2.4* shows some examples of particles when semi-axes equal to 1,1,2, respectively (Gao et al., 2022).

Level set method

In DEM simulations, the level set method is used to represent and monitor the shape and boundaries of particles. It provides a flexible framework for accurately capturing particles' complex geometries and deformations. By modifying the level set function, the method can simulate changes in particle morphology and fragmentation. In DEM simulations, the level set method can be used to generate particles and their initial positions. By defining a suitable level set function that describes the intended particle shapes, it is possible to create particles based on the contour of the function (Harmon et al., 2021, Wang and Ji, 2022). This enables simulations of granular materials with complex and irregular particle geometries by facilitating the initialization of realistic particle configurations.

Spherical harmonics method

The concept behind spherical harmonic analysis involves expanding the radial dimension of a particle's surface using a unit sphere. By doing so, the associated coefficients of the spherical harmonic series can be computed (Wei et al., 2018, Zhou and Wang, 2017, Zhou et al., 2015). These coefficients represent the particle's shape and can be described based on the various frequencies of spherical harmonics present. The amplitudes of these frequencies determine the strength of the morphological features in the frequency domain (Wei et al., 2018). For more comprehensive insight into the utilisation of the spherical harmonics method for the generation of particles with non-spherical shapes, further details can be found in the seminal

work by Capozza and Hanley (2021). Their research provides an in-depth exploration of the application of spherical harmonics for producing non-spherical particles.

Rotational resistance

Rotational resistance is another method used to investigate the influence of particle shape on the behaviour of granular materials (Huang, 2014). Several researchers have proposed an alternate method, which involves the addition of extra rotational resistance (Huang et al., 2017a, Iwashita and Oda, 1998, Jiang et al., 2015). This method is explained in the PhD thesis by Huang (2014). Although this technique has been used in several works, it is not physically realistic (Hanley et al., 2018).

Despite the recognised importance of particle shape, using spherical particles in DEM simulations offer several advantages, making them a popular choice in many applications. Some of these advantages can be related to simplicity and computational efficiency. Spherical particles have a simple and well-defined geometry, which simplifies their representation and computational analysis in DEM simulations. Calculating particle-particle interactions and contact forces for spherical particles is computationally efficient compared to more complex particle shapes. Furthermore, contact detection between spherical particles is straightforward and efficient. As a result, spherical particles have been selected for use in this research to simplify the process and reduce the computational time required to achieve all the research goals.

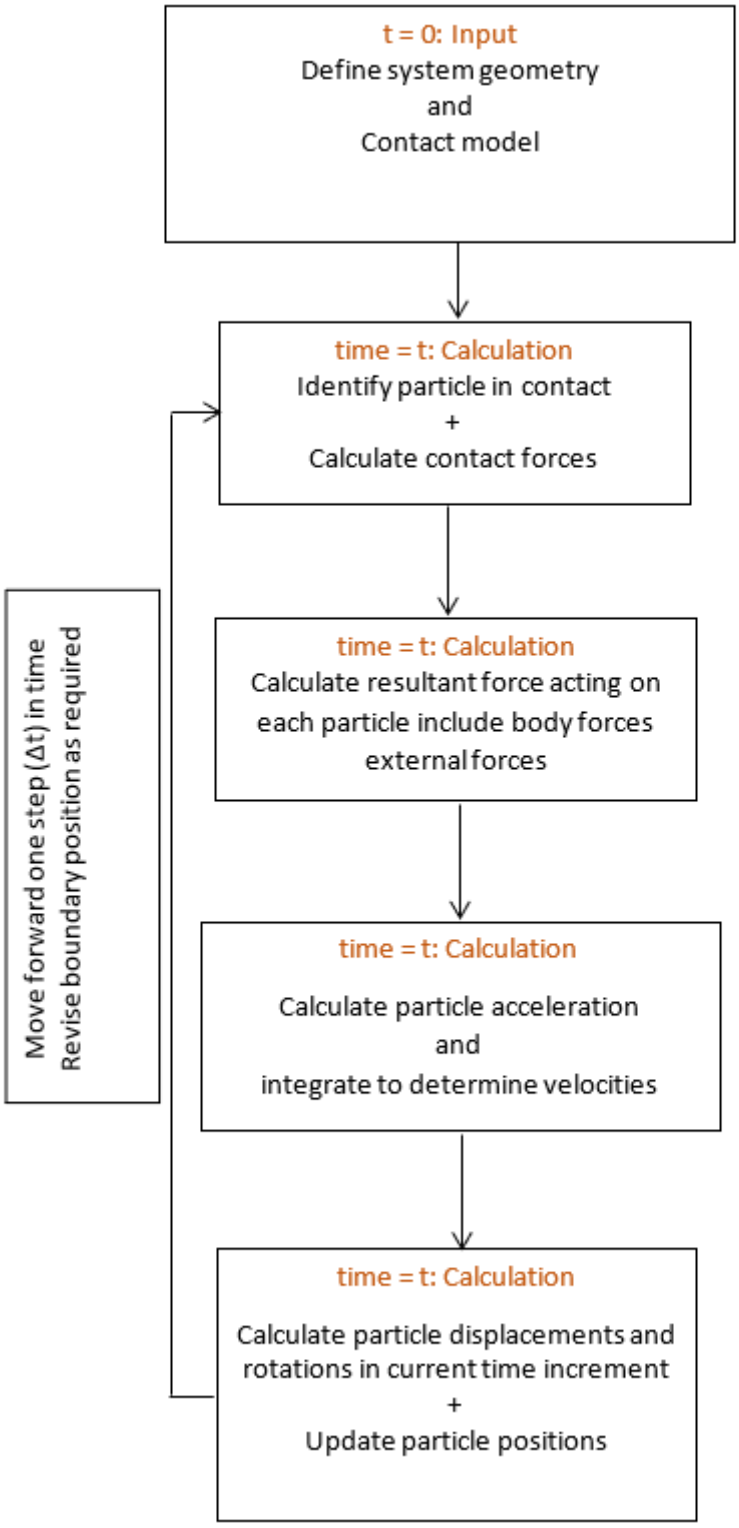

Figure 2.1 Flowchart for DEM simulation (O'Sullivan, 2011).

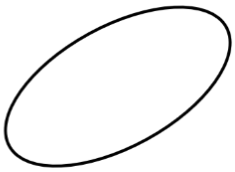

Ellipses

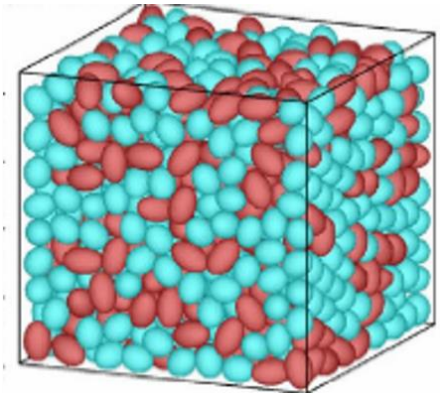

Ellipsoid

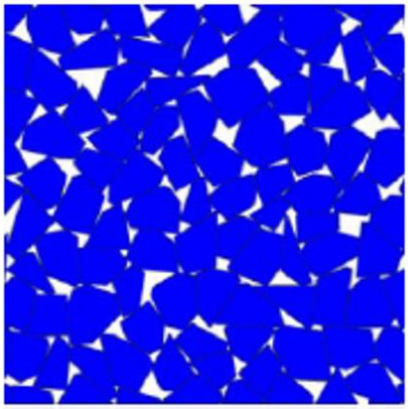

Polygons

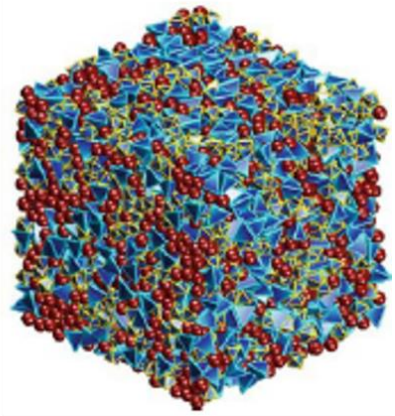

Polyhedrons

Figure 2.2 Different particle shapes used for DEM simulations (Fu and Dafalias, 2011, Ng, 2009b, Pena et al., 2008).

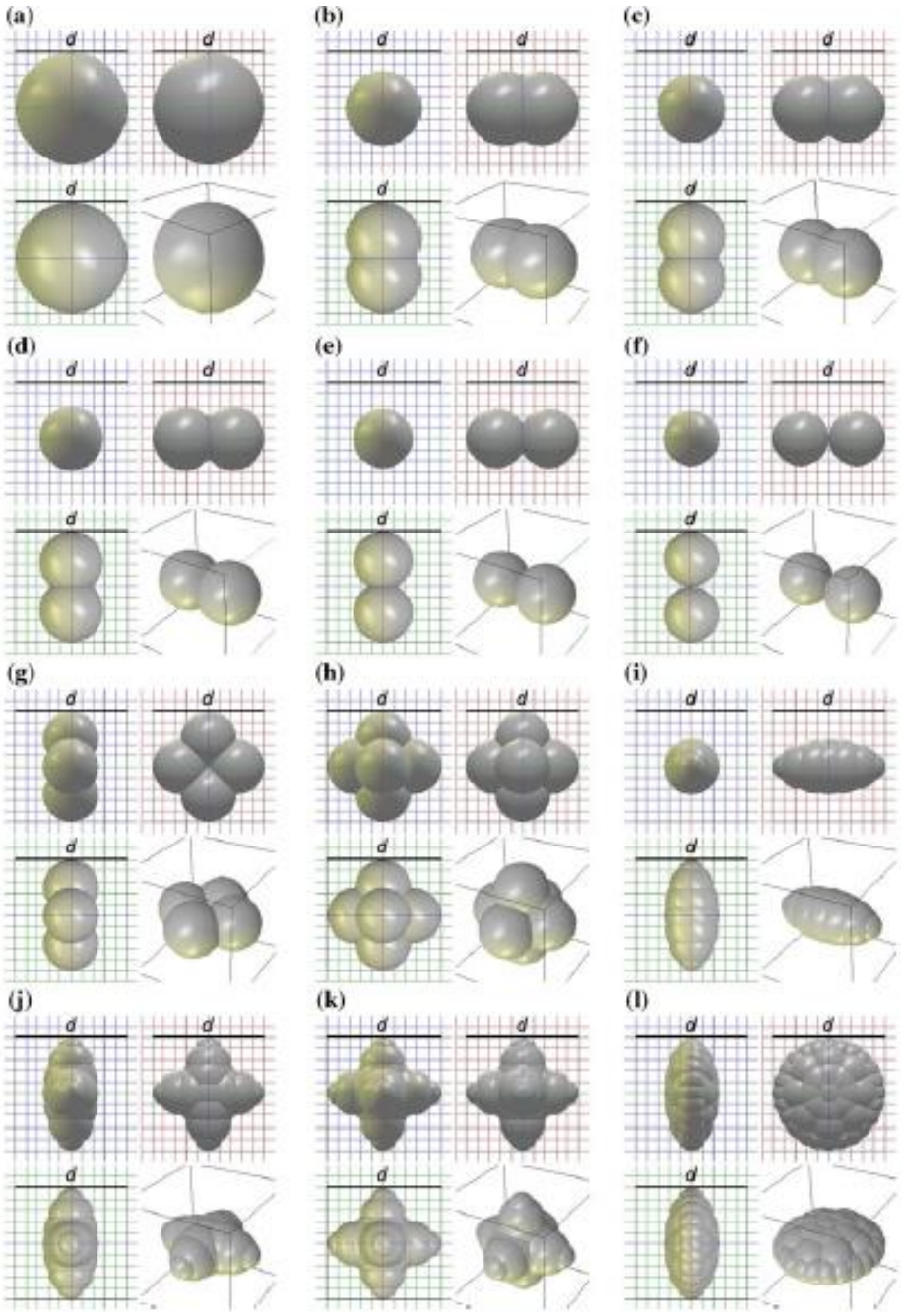

Figure 2.3 Symmetric clusters of spheres used in DEM simulations (Kozicki et al., 2012).

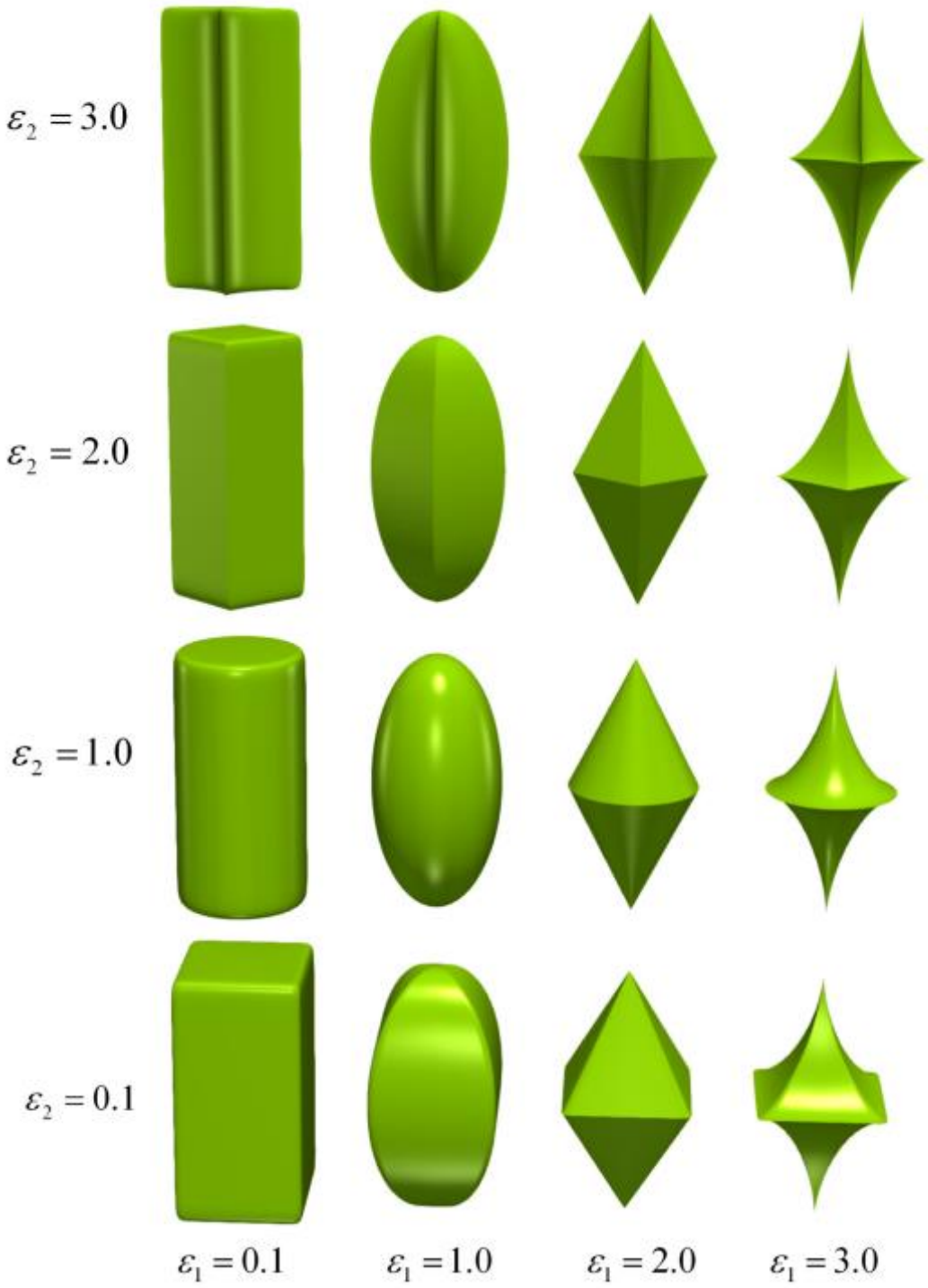

Figure 2.4 Superquadrics particles with semi-axes a = b = 1 and c =2, ε_1 and ε_2 varying between 1 3(Gao et al., 2022).

2.2 Macro- and micro-mechanical behaviour of granular materials using DEM.

2.2.1 Macroscale response of granular materials using DEM.

The macroscale behaviour of granular materials during quasi-static deformation is influenced by the spatial and size distributions of the constituent particles and the displacement behaviour at the interparticle contacts (Thornton and Antony, 1998). Experimental and theoretical studies of granular materials are restricted by the lack of quantitative information happening inside the material. Laboratory investigations on real materials depend on the estimation of macroscopic stress and strain states derived from boundary measurements, which are in turn based on material behaviour assumptions. However, it is uncommon to get information regarding the interior response of materials during these laboratory testing. Furthermore, since exact replicas of the physical system are not available, comparisons between sets of test data are uncertain (O'Sullivan, 2011). In the traditional approach, attempts to mathematically model granular media are based on intuitive speculation as to how to best modify continuum mechanics theories to model the observed experimental behaviour. As a result, new parameters are invariably introduced into the theories, whose precise meaning is not entirely clear. This makes it difficult to choose suitable experiments to properly test a hypothesis (Thornton and Antony, 1998).

Alternative strategies such as computer simulation integrate theory and experiment into a single environment, allowing material properties to be adequately described and quantifiable findings to be produced. This technique provides perfect control over experiments while also providing information on interior micromechanical processes (Huang, 2014, Lee et al., 2012, Thornton and Antony, 1998). Discrete element simulation is a well-established method used for studying the behaviour of granular materials. Several studies have utilised DEM to examine the macroscale response of particulate materials. A few of these are highlighted below.

Stress-strain relationship using DEM

Granular materials are composed of discrete particles that interact through contact forces. Understanding the stress-strain relationship in granular materials is essential for predicting their behaviour under different loading conditions. The DEM method offers a powerful computational tool to investigate the macroscopic behaviour of granular materials, enabling a detailed analysis of the stress-strain relationship and its influence on the macroscopic response. Several works have examined the stress-strain relationship during DEM simulation. In these studies, DEM simulations effectively capture the state-dependent behaviour of granular soil, such as contraction and static liquefaction in very loose soil and dilatancy and hardening in dense soil. Thornton and Antony (1998) conducted a study where they investigated the quasi-static shear deformation of granular media through DEM simulations. In their research, they used spherical particles to create samples with varying degrees of compaction, including loose and dense samples. These samples were subjected to constant mean effective stress 100 kPa and compressed within a periodic boundary. Figure *2.5* and Figure *2.6* depict the findings of the study, supporting the conclusion that the stress-strain-dilation response observed in both the dense and loose systems aligns with typical behaviour observed in laboratory experiments. The dense system displays a higher initial shear modulus, exhibiting a peak in the stress-strain curve at approximately 5% strain, followed by strain-softening behaviour. On the other hand, the loose system does not exhibit any strain softening; the deviator stress increases at a decreasing rate until it stabilizes at a relatively constant value at around 15% strain. The volumetric strain responses, determined by changes in void ratio, highlight that the dense system experiences expansion, while the loose system undergoes contraction. At larger strains, both systems deform while maintaining a constant volume, associated with a consistent deviator stress independent of the initial packing density. According to traditional soil mechanics, this constant volume deformation at large strains would correspond to a "critical void ratio" unaffected by the initial packing density.

Huang et al. (2014a) Provided DEM research that addressed the sensitivity of the critical state response to different coefficients of interparticle friction using samples with gradings that are indicative of real soil. The majority of samples in the study employed a particle size distribution (PSD) that closely resembled Toyoura sand. Additionally, a subset of simulations

is considered analogous to Dunkirk sand. The Toyoura sand grading consisted of 20,164 spherical particles, while the Dunkirk sand grading comprised 43,906 spherical particles. They used two different boundary conditions: periodic boundaries and rigid walls. They investigated three distinct loading paths: conventional drained compression (CDC), constant volume compression (CVC), and constant mean effective stress (p') compression (CPC). After the isotropic consolidation, the coefficient of friction (μ) was adjusted to values of 0.1, 0.25, 0.5, 0.75, or 1.0, corresponding to the desired shearing conditions. The sample was allowed to reach a state of equilibrium before commencing the shearing process. Their finding regarding the stress-deformation behaviours of a representative subset of periodic boundary simulations conducted on conventional drained triaxial compression tests is presented in Figure 2.7. All simulations in this subset sheard with identical initial conditions, including an initial void ratio (e_0) of 0.533 and an initial isotropic stress of 100 kPa. Throughout the shearing process, the confining pressure of σ_3= 100 kPa was maintained. During shearing, the interparticle friction coefficients utilised in the simulations varied. In Figure 2.7 (a), it can be observed that all samples initially exhibited high stiffness due to their dense initial state. As the value of μ increased, the stiffness also increased. However, for samples with μ exceeding 0.5, the deviatoric stresses reached their peak almost vertically, which indicates an unrealistically rigid response. Figure 2.7(a) also demonstrates that both the peak and critical state strengths increased with higher values of μ. When μ was increased, the samples displayed a more brittle post-peak behaviour. Figure 2.7(b) illustrates that the volumetric strain (ε_v), which indicates dilatation, increased with higher values of μ. Nevertheless, when μ surpassed 0.5, further increases in μ had negligible effects.

Liu et al. (2013) conducted 3D DEM simulations to examine the impact of particle size distribution on the stress-strain and critical state behaviour of granular materials in conventional drained triaxial tests under both compression and extension. They employed five distinct particle sizes, as illustrated in Figure *2.8*. Each sample's particle size was characterized by its coefficient of uniformity C_u, which is a shape parameter used to differentiate between well-graded and poorly-graded coarse-grained soil. The samples consisted of spherical particles, and the number of particles varied approximately from 2,277 to 8,617. Figure *2.9* depicts the stress-strain relationships of specimens with different grain

size distributions (GSDs). When all specimens were subjected to relatively large strains (greater than 25%), they attained a critical state characterised by constant stress and volume. In both *Figure 2.9*(a) and (b), the final deviatoric stress under each loading condition was the same regardless of the GSDs. In contrast, the ultimate deviatoric stress in compression tests was greater than that in extension tests.

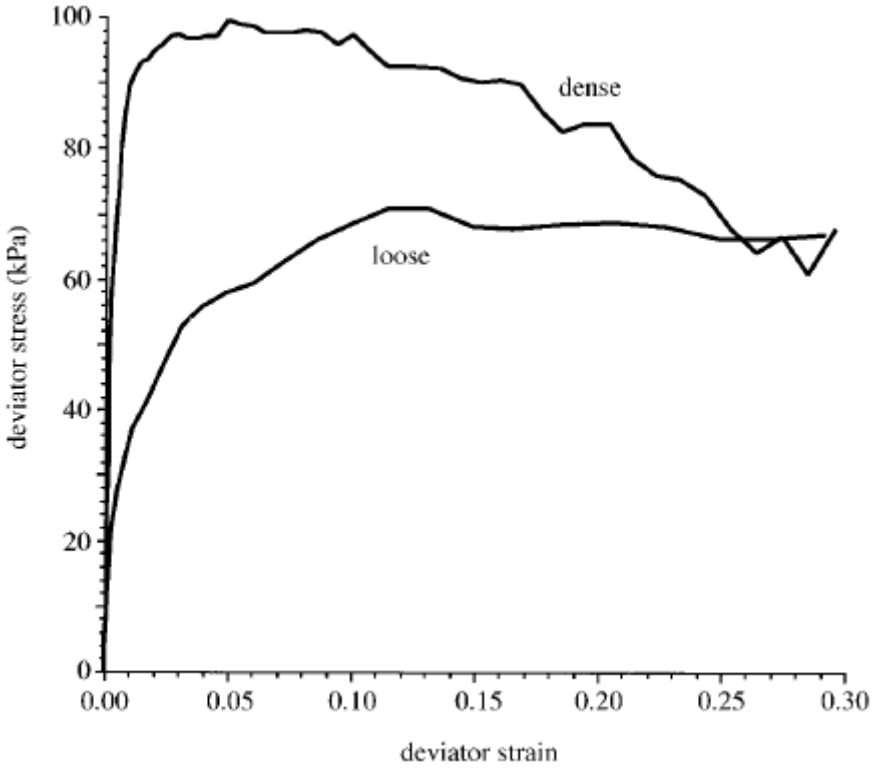

Figure 2.5 The relationship between deviator stress and deviator strain (Thornton and Antony, 1998).

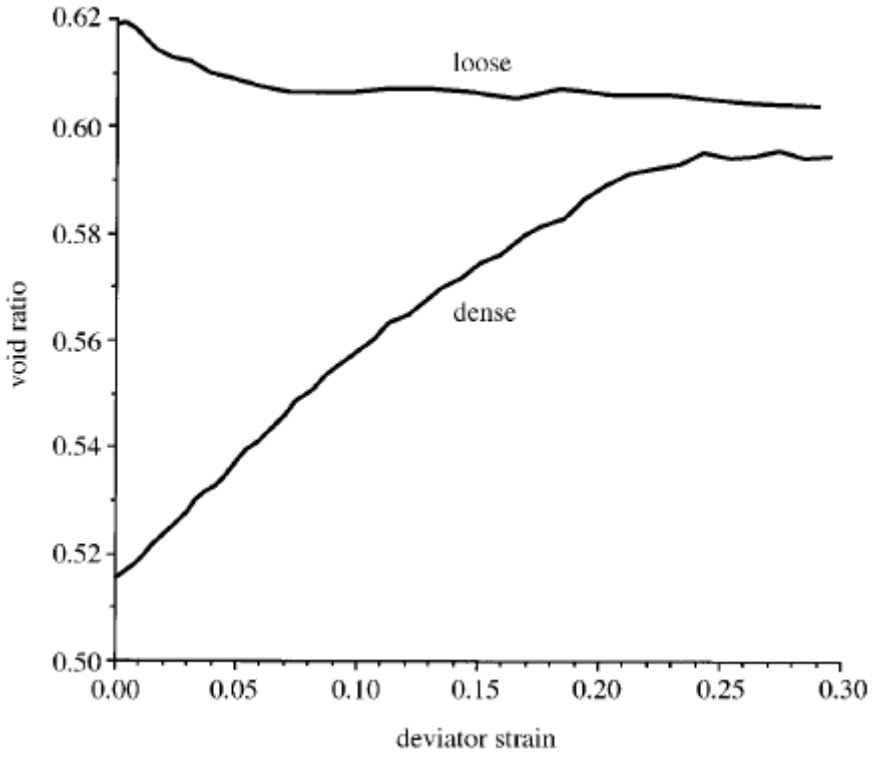

Figure 2.6 The relationship between void ratio and deviator strain (Thornton and Antony, 1998).

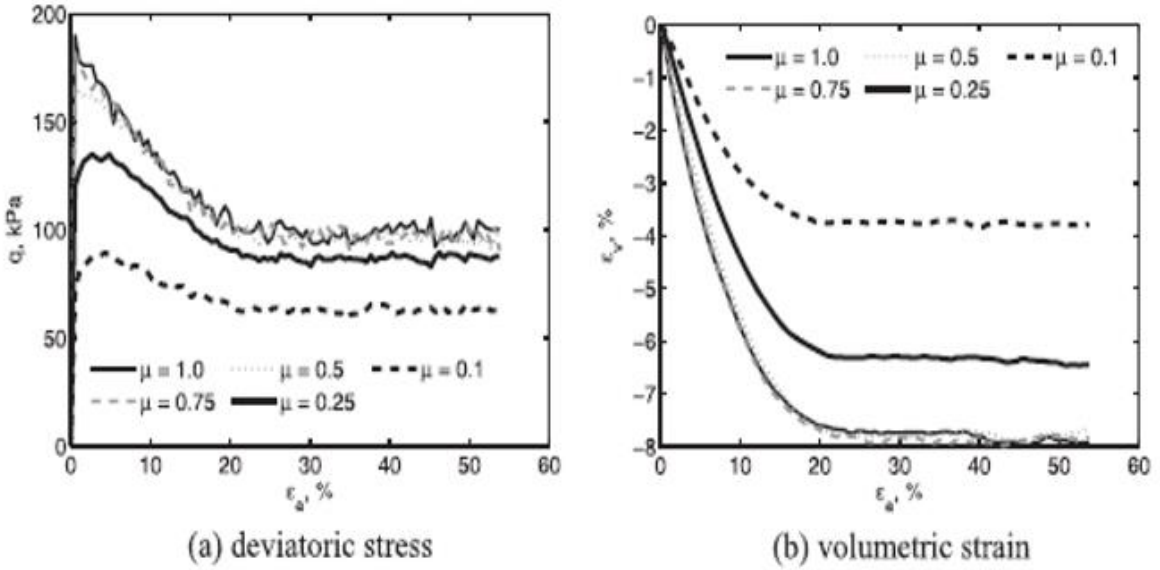

Figure 2.7 Comparison of stress-strain behaviour with different interparticle friction; a) relationship between axial strain and deviator stress; b) evolution of volumetric strain *(Huang et al., 2014a)*

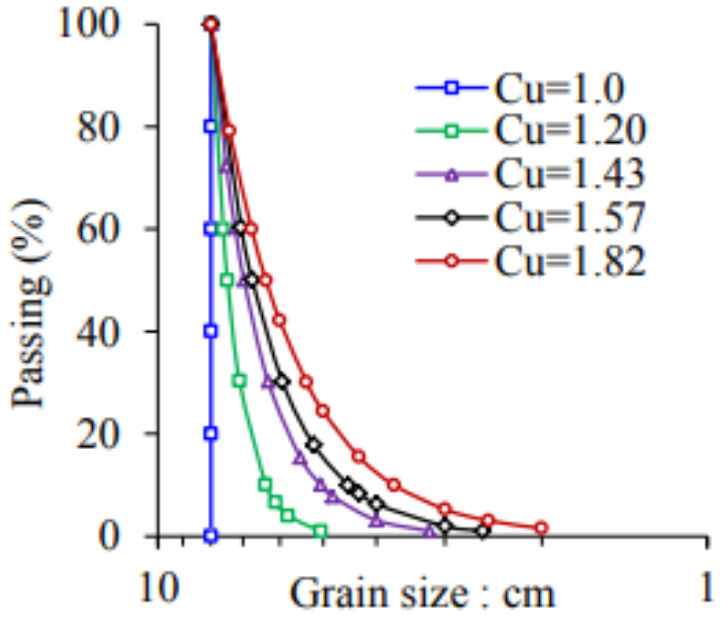

Figure 2.8 Particle size distribution used by Liu et al. (2013).

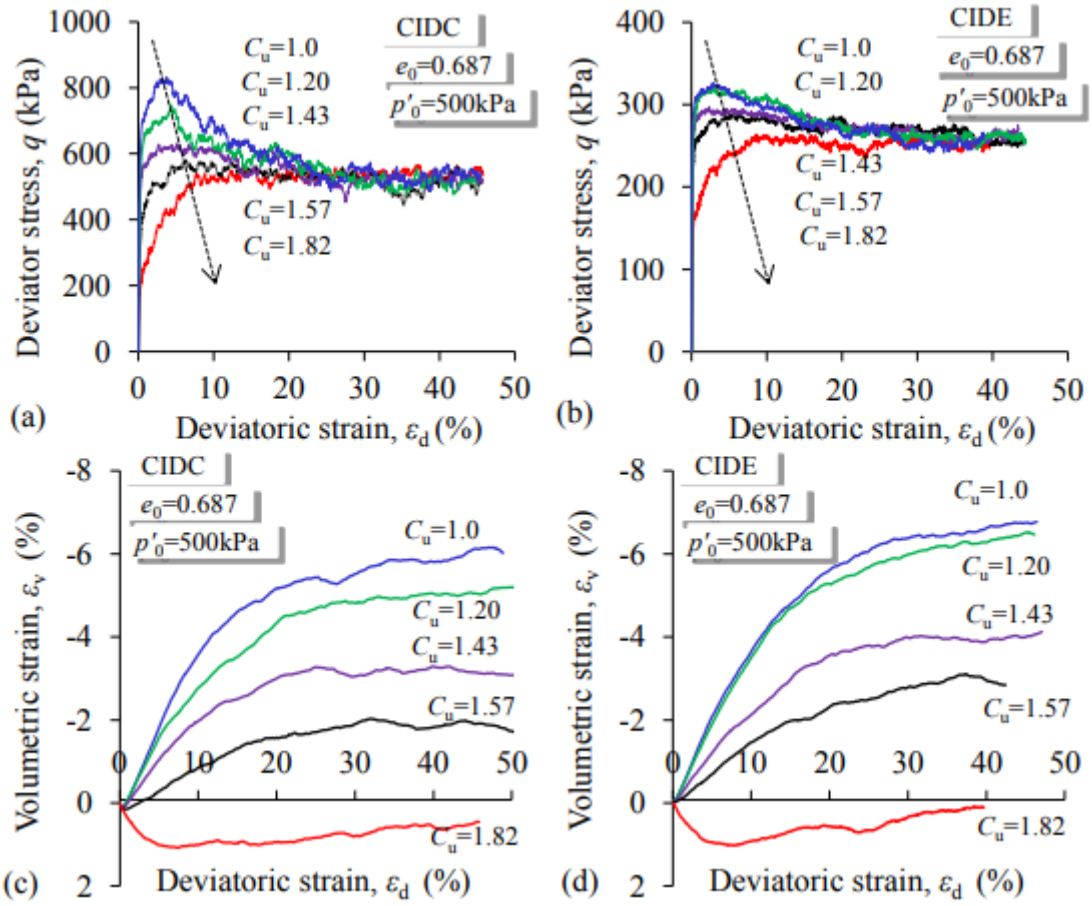

Figure 2.9 Stress-strain responses of granular soil with different GSDs: (a) Deviator stress against deviator strain of compression tests; (b) Deviator stress against deviator strain of extension tests; (c) Volumetric strain against deviator strain of compression tests; (d) Volumetric strain against deviator strain of extension tests (Liu et al., 2013).

Critical-state behaviour using DEM

The term 'critical void ratio' has been utilised first by Casagrande (1936) to characterize a specific state in sandy soils with constant volume. Taylor (1948) proposed two alternative definitions: the constant σ_3 critical void ratio and the constant-volume critical void ratio. The former definition is derived from drained triaxial tests and differs from Casagrande's definition by considering the void ratio after the consolidation as the initial void ratio. Roscoe et al. (1958) brought these two definitions together, forming the concept of a unique critical void ratio line (C.V.R line) in (p', e, q) space based on the behaviour of Weald Clay. This concept served as a fundamental element in the framework of critical

state soil mechanics (CSSM) described by Schofield and Wroth (1968b). The original CSSM framework depicted the critical state through two distinct relationships, as illustrated in Figure *2.10*.

$$q = Mp' \tag{2}$$

$$\Gamma = v + \lambda lnp' \tag{3}$$

The equations represent various parameters associated with the critical state line (CSL) in $v - lnp'$ space where M describes the inherent frictional coefficient between grain surfaces, while Γ represents the intersection point of the CSL with the p' = 1 kPa axis in $v - lnp$' space. The specific volume v, defined as $1 + e$ (where e is the void ratio), and λ indicates the slope of the CSL in $v - lnp'$ space. Soils that initially lie above the CSL, as defined by 4 in $v - lnp'$ space, are classified as being in a 'wet' or loose state and tend towards the CSL. Conversely, soils that start below the CSL are in a 'dry' or dense state and tend to expand or dilate towards the CSL.

DEM simulations have been employed to investigate the critical-state behaviour of granular materials using both 2D disk systems (Maeda et al., 2010) and 3D sphere systems (Gu et al., 2014, Guo and Zhao, 2013, Huang et al., 2014a, Ng, 2009a). As depicted in Figure *2.11*, the previous DEM studies have confirmed that, under triaxial compression loading conditions, the CSL is unique and independent of initial states and loading conditions. It is worth mentioning the work of Zhao and Evans (2011), they observed variations in the position of the CSL in $e - log(p')$ space in relation to the initial void ratio. Nevertheless, their observations were limited to strains up to 10% axial strain, and the genuine response of the critical state, which is typically attained at strains surpassing 10% axial strain, remains uncertain.

Perez et al. (2016) utilised 3D DEM simulations to investigate triaxial tests across different initial densities and confining pressures. Their objective was to evaluate the quasi-static conditions for shearing in granular media within the framework of critical state soil mechanics. The simulation involved 10,624 particles, representing Toyoura sand, and the samples were enclosed with periodic boundaries. Isotropic compression was applied to achieve various combinations of void ratio and stress state. Subsequently, the samples were subjected to shearing under constant p' conditions. The simulations were conducted using different inertial numbers, denoted as I, which quantified the inertia effects by considering the ratio of inertial forces to imposed forces. The quasi-static regime was indicated by small

values of I, while intermediate values represented a dense flow regime, and large values indicated a collisional dynamic regime. In Figure *2.12* the critical void ratio is presented for different combinations of I and p'. It is worth noting that each data point represents the average value of e and p' over the last 10-20% of axial strain to account for fluctuations in the load-deformation response. When $I \geq$ 2.5e3 the CSLs exhibit a downward movement with decreasing I. However, for $I \leq$ 2.5e3., the CSLs show no significant variation.

Gu et al. (2014) investigated the mechanical behaviour of granular soils at different initial densities and confining pressures in drained and undrained triaxial tests by using 3D DEM simulations. Figure *2.13* shows their findings regarding the CSLs for both undrained and drained tests. As seen in Figure *2.13*a, the stress ratio q/p is a constant of 0.78 at the critical state, despite the initial conditions and stress paths. The shear stress ratio is smaller than those in experiments which is probably due to the rounded particle shape and lack of rolling resistance. It can be noticed too in Figure *2.13*b that the critical void ratio varies linearly with $p^{0.78}$.

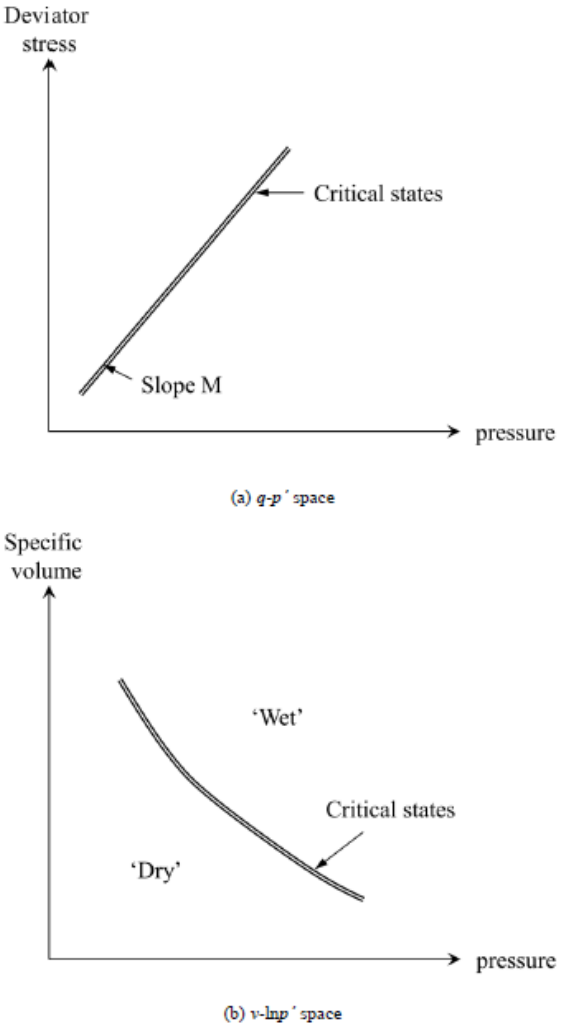

Figure 2.10 The proposed definition of CSL (Schofield and Wroth, 1968b)

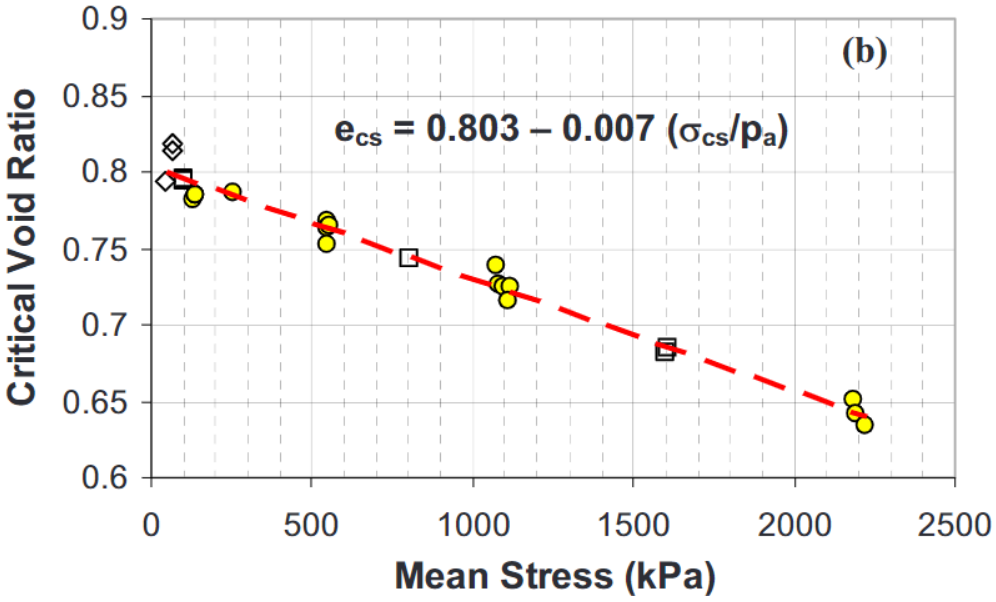

(a)

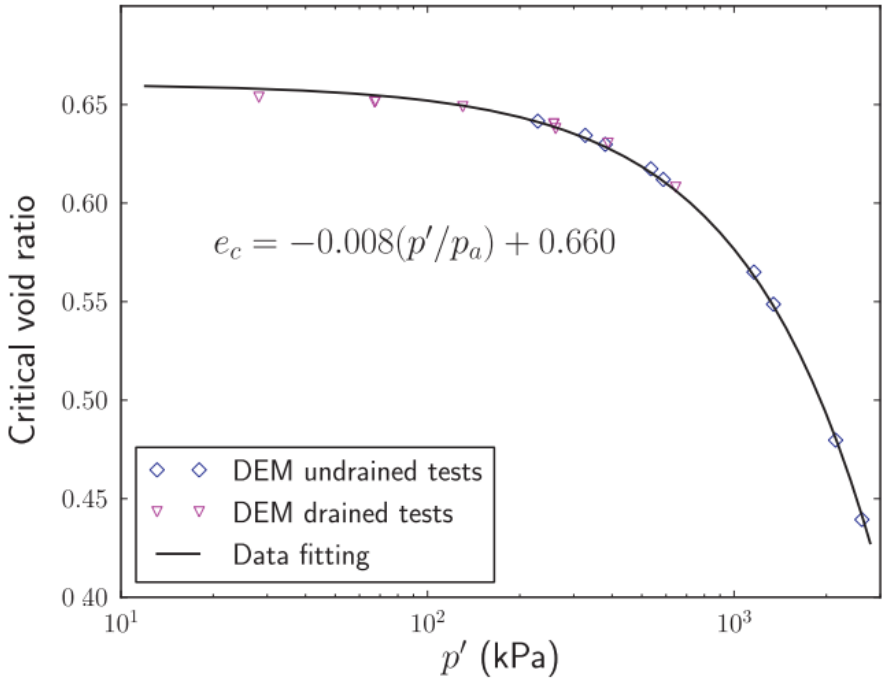

(b)

Figure 2.11 The CSL in $e - log(p')$ space based on DEM studies under conventional triaxial loading conditions for Ng (2009a) and Guo and Zhao (2013) respectively.

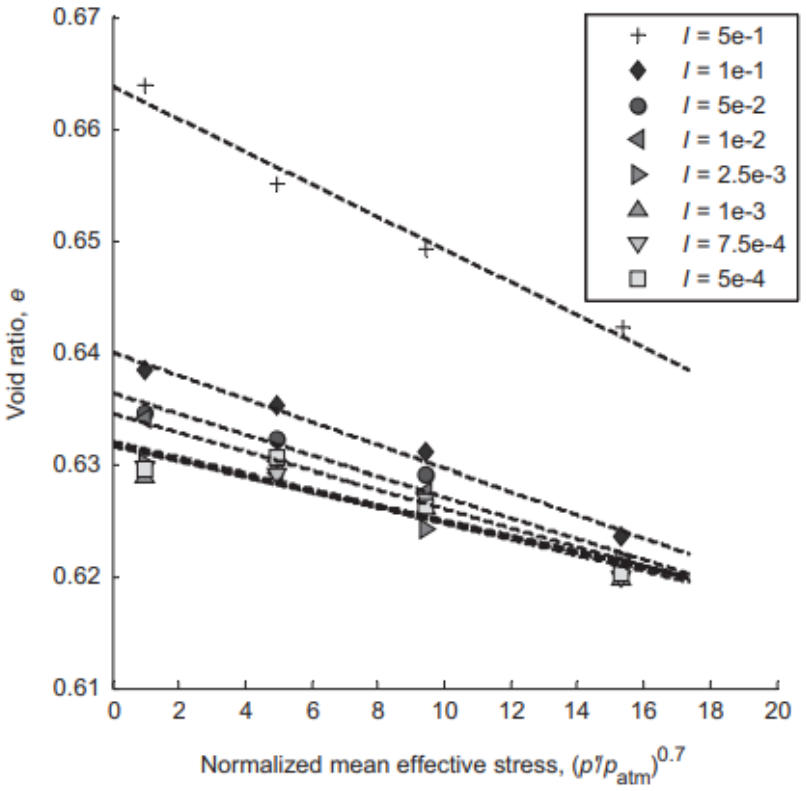

Figure 2.12 Void ratio at critical state for different values of I and p' (Perez et al., 2016).

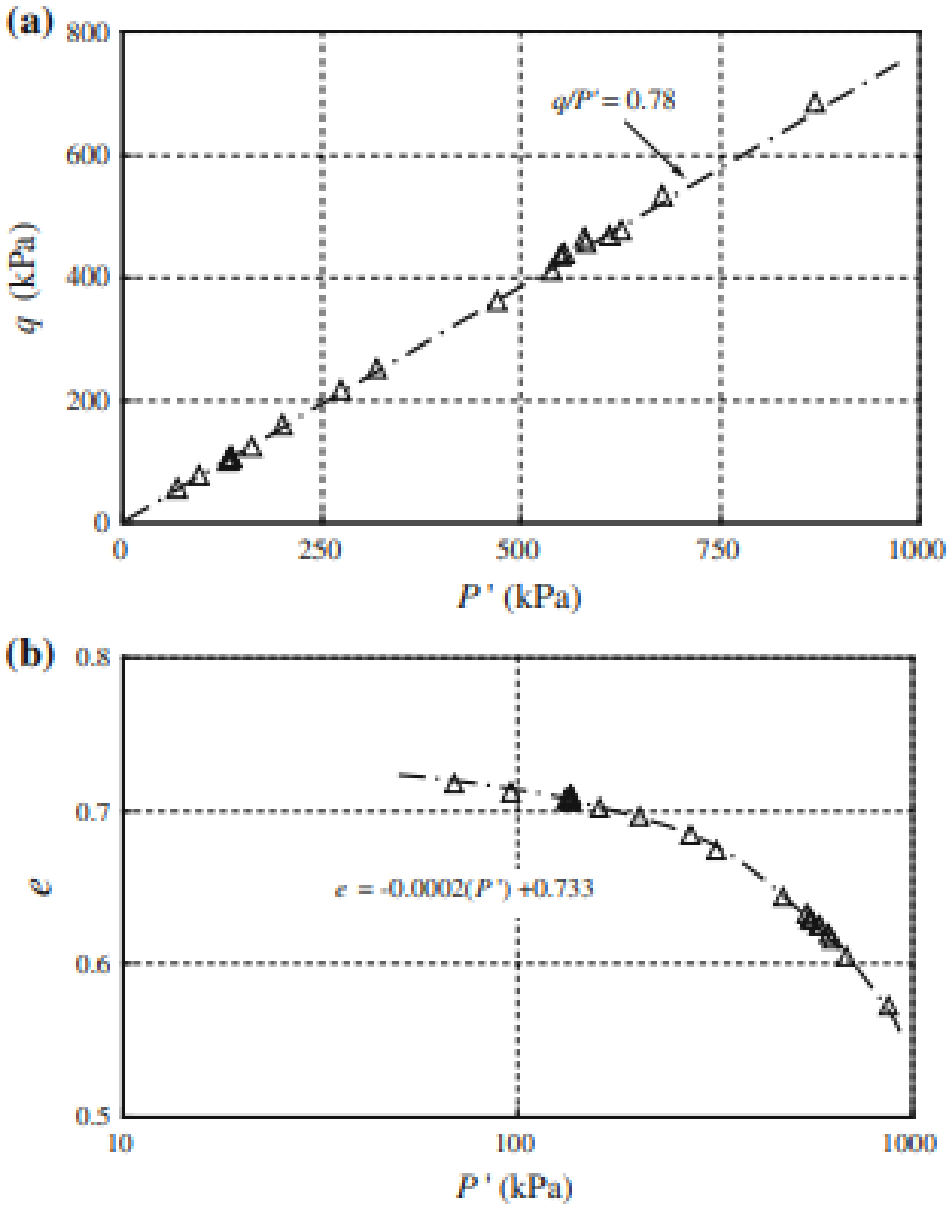

Figure 2.13 Critical state line in a) $q - p$ space and b) $e - log\ (p')$ space (Gu et al., 2014).

2.2.2 Microscale behaviour of granular materials using DEM

DEM simulation has been used in several studies to bridge the gap between the macro and micro behaviour of granular materials. It is commonly acknowledged in the mechanics of granular materials that the internal structure, such as, contact network, sliding of contact network and energy dissipation has a significant influence on the macroscopic behaviour of these materials (Kruyt and Rothenburg, 2006, Radjai et al., 1999, Shire et al., 2014, Thornton and Antony, 1998).

Force transmission and contact networks in granular materials

The applied loads are distributed evenly across typical solids and liquids. This is not true for granular materials, which consist of discrete macroparticles (Jaeger et al., 1996). In granular materials, forces are transferred between particles through their contact points. The mode of propagation shows a complex force network with quick branch shape changes during material deformation (Peters et al., 2005). Photoelastic experiments on two-dimensional arrays of discs have been utilised to directly evaluate the stress distribution in granular materials (Dantu, 1957, De Josselin de Jong, 1969). This technique works by placing granular material between crossed-polarising filters. Each facet of the granular material rotates the polarisation of light according to the level of local stress. The tests indicate that load is transferred via heavily stressed columns of particles known as strong force chains, as presented in Figure 2.14 (Radjai, 2015).

Zheng et al. (2019) used a photoelastic experimental approach to demonstrate the development of a force chain network in a photoelastic granular system with soft confining limits (*Figure 2.15*). During each step of shear, records are kept of the particle positions, orientations, and photoelastic reactions. Analysing these data allows for the determination of the coordination number of each particle, which serves as an indicator of the transition to the jammed state before any dilation occurs. In the context of two-dimensional frictional granular systems, the term "jammed" refers to a state in which particles are densely packed and exhibit limited movement. Once a granular material reaches the jammed state, the particles become locked in, requiring a significant amount of force or energy for further movement or rearrangement. The jamming state is achieved when the coordination number, denoted as Z, equals 3 (Jaeger et al., 1996). The coordination number represents the average number of force-bearing contacts per particle within the force network (Zheng et al., 2019).

The initial state of the granular sample is deliberately set to be unjammed, meaning there are no initial forces present, as depicted in the first snapshot of Figure *2.15*. They found that during the initial stage of compression, the coordination number rapidly reaches 3. At this point, the granular system is primarily undergoing compression, increasing by packing friction and densification of the sample. The coordination number continues to rise with strain even after reaching Z = 3, although at a slower rate. They concluded that this phenomenon can be attributed to the fact that the granular system has already entered the jammed state. Beyond this specific point, as the compression strain increases, the sample experiences oscillation between jamming and unjamming states along the yield boundary due to the application of additional external loading.

Later research employing DEM simulations gives a better understanding of force transmission in granular materials and its link to the content network. The inhomogeneous load transmission in the soil has also been demonstrated using DEM simulation. DEM simulations have proven that stress is transmitted across granular materials through a highly inhomogeneous network. As load is applied to the soil, it is mostly transmitted by strong contact particles forming a sparse network that carries above-average force and is aligned in the direction of major principal stress (Radjai, 2015). This strong chain is supported by weak networks that carry the below-average force that is perpendicular to the major principal stress (Radjai, 2015). Cundall and Strack (1979) used a numerical simulation of a simple shear test to investigate the force transmission in granular materials, they demonstrate a good qualitative agreement between the simulation and a corresponding photoelastic experiment by Oda and Konishi (1974). Radjai et al. (1997) suggest that the contact force network can be divided into two complementary subnetworks: a strong network that carries an above-average normal contact force and a weak network carrying a below-average normal contact force, as shown schematically in Figure 2.16. They used two-dimensional simulation and concluded that the strong networks carry the whole deviator stress while the weak network only contributes to the main effective stress.

Thornton and Antony (1998) used three-dimensional DEM simulation to investigate the quasi-static deformation of granular materials. They used a sample containing 3620 elastic sphere particles with an average diameter of 0.26mm. They evaluated the macroscopic and microscopic behaviour of loose and dense samples at the micro-scale. They partitioned the contacts as proposed by Radjai et al. (1997) to examine the contribution of the strong and weak networks to deviator stress. Figure 2.17 shows that most of the deviator stress is carried by the strong network, with a small contribution from the weak network. This finding does not support observations by Radjai et al. (1997), as it can be seen in Figure 2.17 that weak contact also contributes to deviator stress. Subsequent studies separated the contact force networks, based on the average normal force approach (Thornton and Antony, 1998, Shi et al., 2018, Kruyt, 2016, Estrada et al., 2008). However, there is evidence to suggest that separating the contact force in this way may not be appropriate. For example, Huang et al. (2017b) used DEM to examine the Radjai approach to separating contact networks using average normal force. They found that weak contacts also participate in stress transmission and contribute to structural anisotropy, whereas some of the weak contact orientation occurs in the same direction as the major principal stress. They have also shown that the characteristic normal contact force, which indicates the transition from a negative to a positive contribution to the overall deviator, changes until the critical state is reached, after which it remains constant. Finally, they observed that characteristic normal contact force for demarcating strong and weak networks based on contribution to deviator stress and the structural anisotropy varies. Thus, they concluded that using average normal force to separate the networks is not a robust method. Kruyt (2016) proposed an alternative definition of weak and strong contact with his partitioning method being based on comparing the contact force with the average force corresponding to the contact orientation. Contrary to Radjai et al. (1997) findings, the load in Kruyt definition is carried out equally by strong and weak contact.

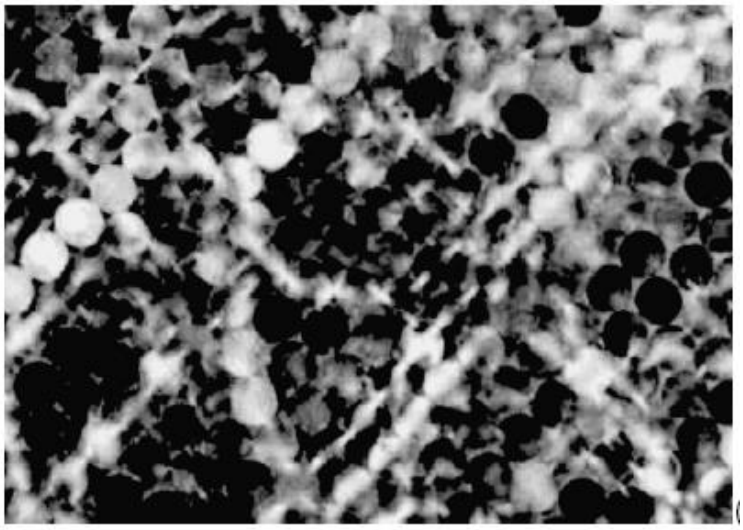

Figure 2.14 Photoelastic experiment showing that most of the load is transferred by the particles that are marked with a line that is called strong contact (Radjai, 2015).

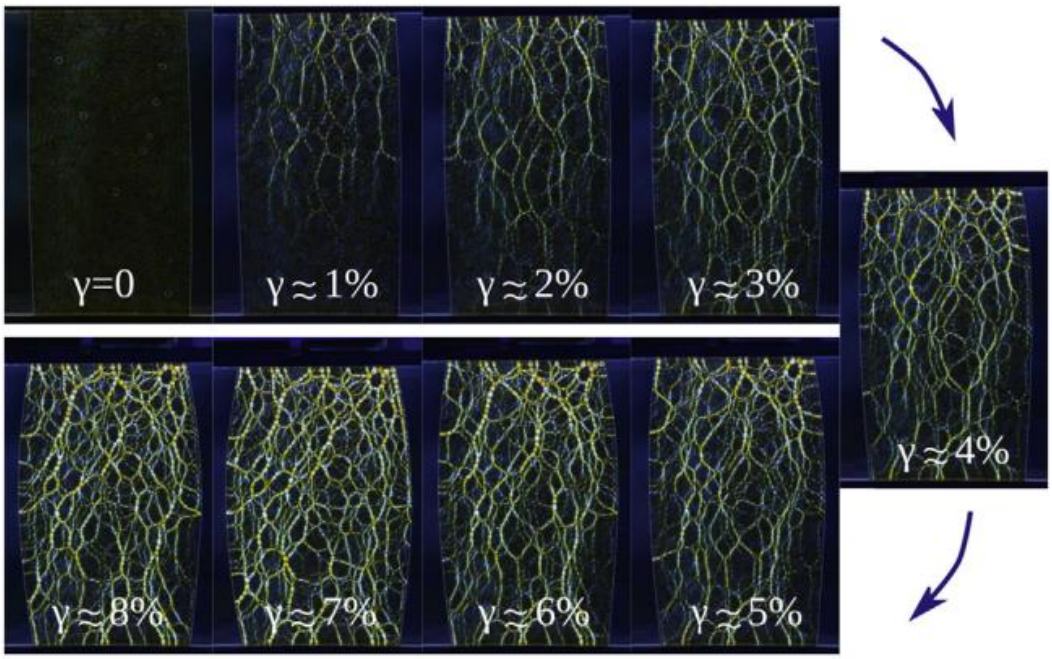

Figure 2.15 Photoelastic test: force transmission in particles system under shear at the different strain levels (Zheng et al., 2019).

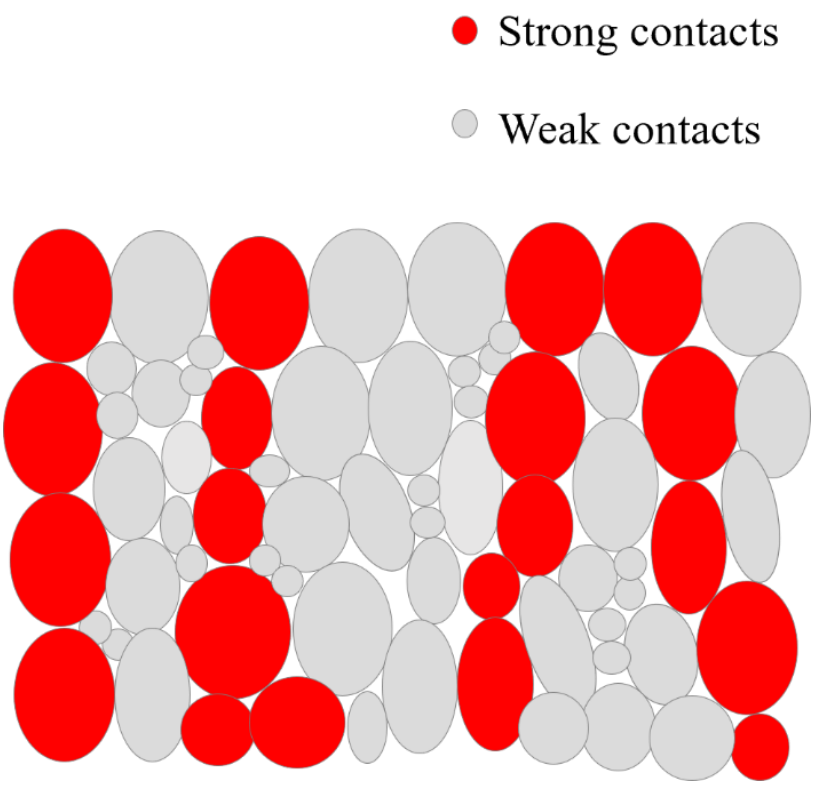

Figure 2.16 Examples of strong and weak networks

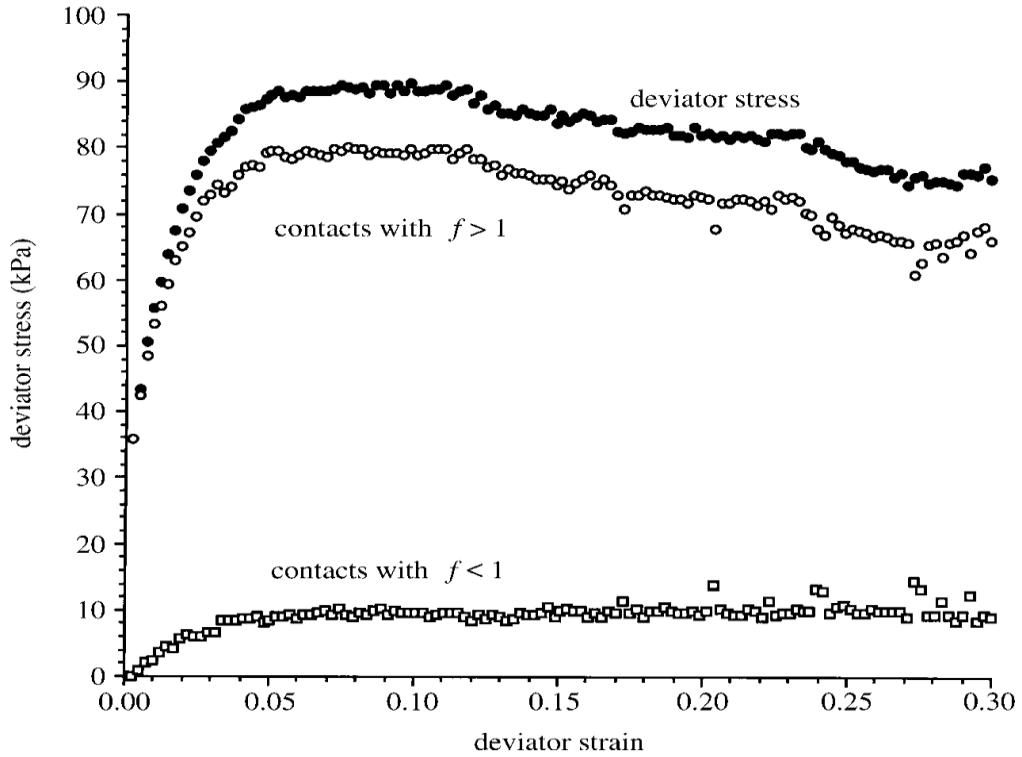

Figure 2.17 The contribution of strong and weak networks to the deviator stress presented against axial strain for the dense sample (Thornton and Antony, 1998).

Sliding of the contact force in granular materials.

The investigation of the contact network, encompassing both strong and weak networks, has been a longstanding subject of research interest. As the strong contacts (or strong force chains) are responsible for carrying most of the deviator stress in the granular materials system, many researchers have focused on the stability of the strong network. They have found that the stability of the strong force network influences the strength of the granular materials (Tordesillas et al., 2011, Zhang et al., 2017). The failure model for granular materials has primarily focused on the concept of sliding along a failure plane. Many researchers, such as Horne (1969) and Rowe (1962), have considered sliding at the contacts as the principal mechanism responsible for the failure of granular materials. Thornton and Antony (1998) evaluated the sliding of the contact networks with different interparticle friction. They found that as the interparticle friction increased the contact networks become more stable and the ratio of contact sliding decreased (Figure *2.18*). Similar results were observed by Göncü and

Luding (2013) and Suiker and Fleck (2004). However, there was no examination of how the contact networks slid during the whole shearing prosses. Tordesillas et al. (2014) found that the mechanical response of dense granular materials subjected to indentation by a rigid flat punch is highly related to force chain stability. Liu et al. (2019a) conducted a study to examine the influence of sliding contacts on shear banding in granular materials. They utilised a quasi-2D biaxial test and used DEM simulations to model the mechanical behaviour and formation of shear bands. Shear bands refer to localised zones within the material where significant shear deformation occurs when subjected to shear forces, such as compression or shearing. The numerical simulation involved a model consisting of a single layer of 20,000 spheres within a rectangular domain, with particle sizes following a uniform distribution. In their study, they consider that sliding between connected spheres occurred when the tangential contact force attained its maximum value, which was limited by the normal force and the friction angle. They calculated the sliding ratio, as the number of sliding contacts divided by the total number of contacts, to analyse the sliding behaviour. Figure *2.19* presents their findings regarding the sliding ratio, which was divided into two parts: inside and outside the shear band. Initially, the proportion of sliding contacts gradually increased until reaching State C, which indicated the maximum rearrangements of the bulk material. After reaching the peak value of the sliding ratio, the probability of sliding decreased gradually. When a single shear band eventually formed, the sliding ratio stabilised at around 0.007. During this period, the magnitudes of sliding ratios inside and outside the shear band exhibited distinct patterns. The majority of sliding contacts were concentrated within the shear band area, while only a small proportion of sliding contacts occurred outside this area.

Several studies have focused on evaluating the buckling of the force chain (strong contact) (Guo, 2012, Tordesillas, 2007, Tordesillas et al., 2011, Tordesillas and Muthuswamy, 2009). Buckling refers to deformation or instability that occurs in a structural element or a force transmission path when subjected to compressive loads. It is a mode of failure that typically involves a sudden lateral deflection or bending of the structure or force chain. Buckling occurs when the compressive load exceeds the critical buckling load, leading to a loss of stability and a change in the shape or behaviour of the element or force chain. According to Zhang et al. (2017), a force chain is described as a connection of at least three particles that align

approximately in a linear manner and endure stresses greater than the average value. The failure of force chains is identified by the occurrence of buckling. Force chain buckling is defined based on changes in the geometry of the particles within the chain. For instance, at time t, a three-chain-particle segment is present, and at time t + δt, as shown in Figure *2.20*. Tordesillas (2007) used 2D DEM simulations to study force chain buckling, unjamming transitions and shear banding in dense granular assemblies. They found that the initiation of global unjamming occurs as a result of force chain buckling. Initially, buckling is localised within a limited number of force chains in a small area of the band. However, it rapidly propagates along the band, leading to elastic unloading of the outer regions on both sides. The dynamic particle rearrangements triggered by buckling and the subsequent collapse of force chains are responsible for non-affine motion and serve as the mechanisms for energy dissipation at two distinct length scales: friction at the contact scale and irreversible structural rearrangements at the mesoscopic scale.

Zhang et al. (2017) investigated the role of the force chain in granular materials in 2D and 3D DEM simulations. They found that the development of the force chain leads to an increase in the strength of granular materials and that a decrease in strength is due to the buckling of the force chain (i.e. it is the buckling of force chains that is primarily responsible for the shear resistance of granular materials). Furthermore, they studied the relationship between deviator stress, the development of kinetic energy and buckling events. Figure 2.21 shows that, as the deviator stress reaches its peak and starts decreasing, the buckling of the force chain will start building up and, as the buckling of the force chain occurs, the kinetic energy also increases which is illustrated in the figure by the dotted line that linking the three figures. Figure 2.21 also shows that the sliding or buckling is responsible for the strength of the sample as well as the release of kinetic energy.

However, it is important to note that these studies have a specific focus on force chains, which represent strong contacts, often overlooking the significant contribution of weak contacts to sliding behaviour. According to the hypotheses proposed by Radjai et al. (1997), all sliding occurs within the weak contacts, while the strong contacts remain non-sliding. Nevertheless,

it is crucial to highlight that there is currently insufficient evidence available to substantiate this hypothesis

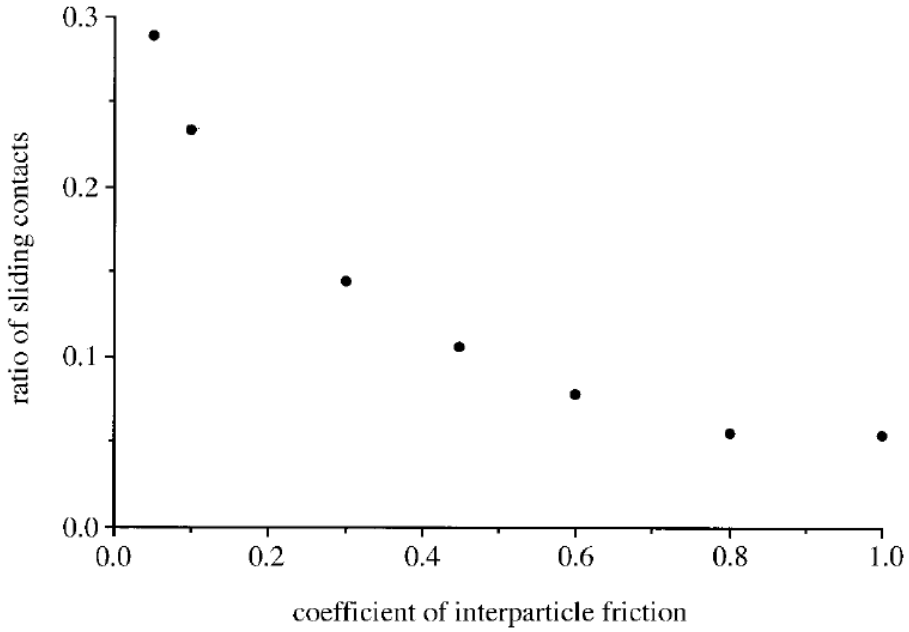

Figure 2.18 Effect of interparticle friction on sliding ratio (Thornton and Antony, 1998).

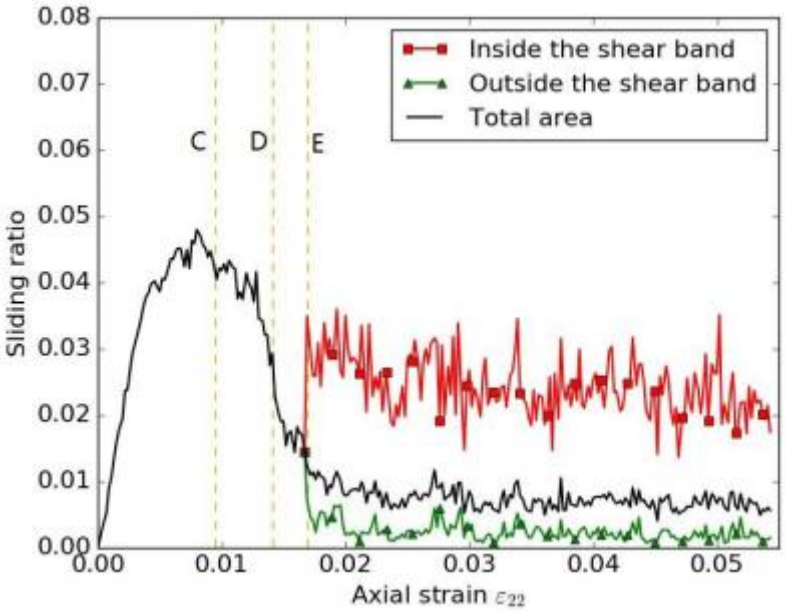

Figure 2.19 Sliding ratio against axial strain (Liu et al., 2019a).

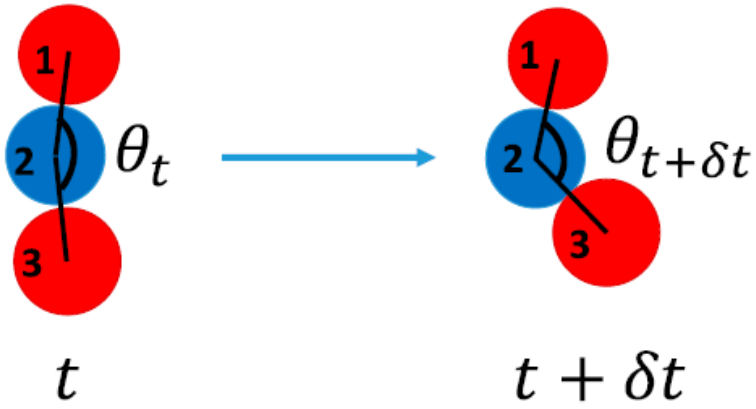

Figure 2.20 Geometry change of force chain buckling between two timesteps (Zhang et al., 2017).

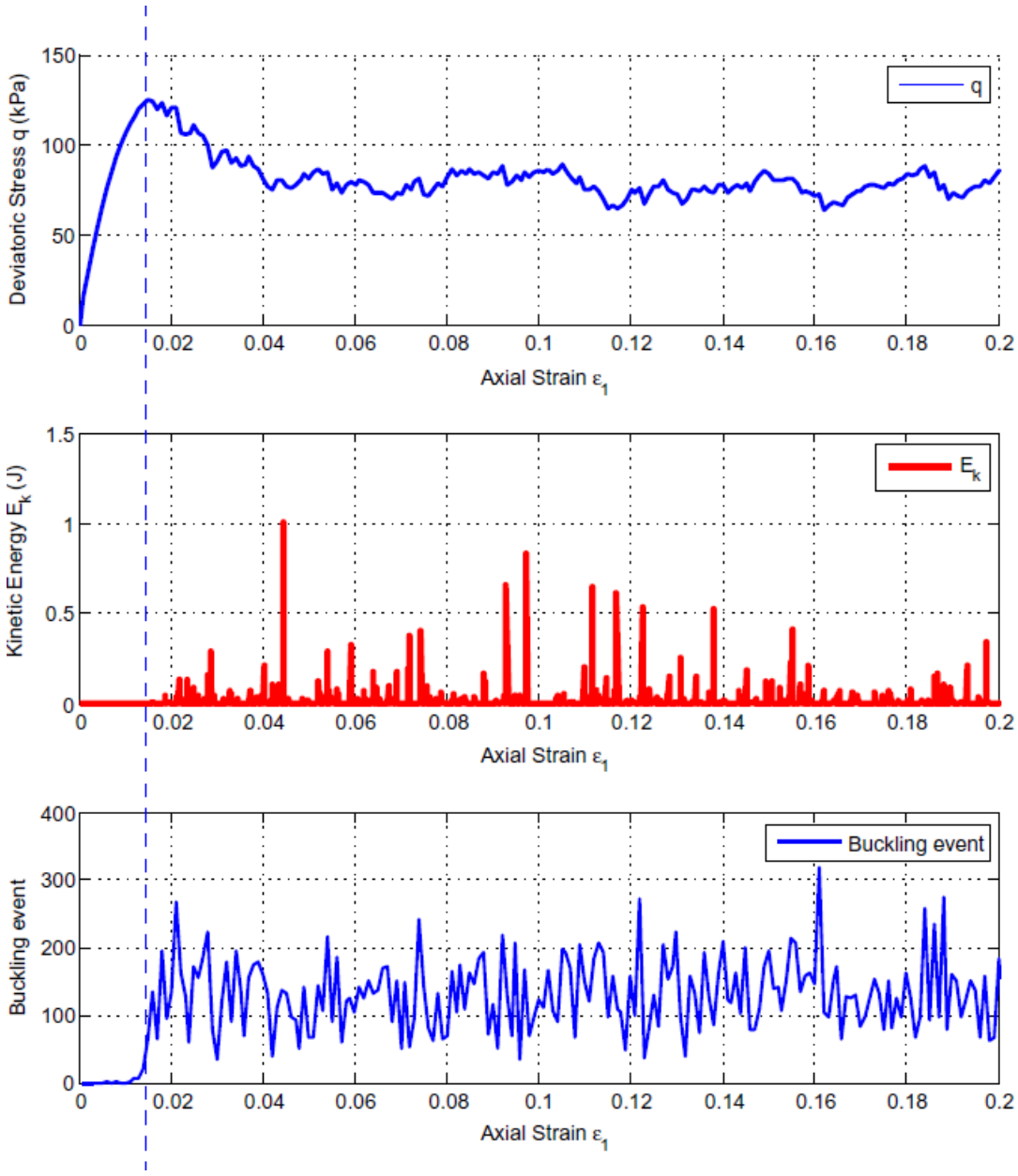

Figure 2.21 Evaluating kinetic energy and buckling event (Zhang et al., 2017).

2.3 DEM investigation of energy dissipation in granular materials

Monitoring energy dissipation both improves the knowledge of how particles interact at a microscopic level and offers a technique through which it can better comprehend the mechanics behind the macroscale stress-strain relationship. Energy dissipation in granular media has been a topic of interest for a very long time, and researchers have either

investigated this phenomenon theoretically or via the use of DEM modelling. When the load is applied to granular materials, it will be transferred across the network of contacts, and the energy in these contacts, as a result, will partly be dissipated within the networks as they slide. Several studies employed DEM modelling to track energy dissipation in granular materials.

Asmar et al. (2003) used a sophisticated energy analysis approach and applied it to the DEM simulation of vibrating particles, which records the kinetic energy, gravitational potential energy, spring strain energy, dissipated energy related to damping and gross frictional sliding, and boundary wall work. Their key finding is that energy is mostly lost through normal damping and gross sliding when utilising conventional friction and damping coefficients. Furthermore, they also found that the friction coefficient has a moderate effect on the proportion of dissipated energy components, but it has no effect on the maximum rate of energy dissipation. The particle stiffness has a very minor impact on the proportion of dissipated energy components, but it does affect the maximum rate of energy dissipation.

Kozicki et al. (2012) investigated the effects of grain roughness on strength, volume changes, and elastic and dissipated energies during quasi-static homogeneous triaxial compression using DEM simulation. They found that simulations of a homogeneous triaxial compression test indicate that DEM is capable of reproducing the most essential macroscopic characteristics of cohesionless granular materials. They also observed that grain roughness increases energy and energy rate fluctuations. El Shamy and Denissen (2012) used DEM modelling to conduct a microscale analysis of energy dissipation in granular materials subjected to cyclic loading. They conducted undrained cycle triaxial tests across a wide range of relative densities. The models were also subjected to cyclic loadings at a variety of frequencies and shear strain amplitudes. They found that the majority of energy is dissipated due to inter-particle frictional sliding, the amount of which rises with increasing shear strain level and packing density. Their findings indicate that microscale energy dissipation calculated from DEM simulation is similar to macroscale energy dissipation calculated from the area under the deviator stress-axial strain loops, as can be seen in Figure *2.22*.

Wang and Yan (2012) have investigated energy dissipation in crushable soils using DEM simulation. They found that the simulation findings demonstrate that the initial specimen density and crushability have a significant impact on the energy distribution of the soil at both small and high strains. They also found that particle breakage only dissipates a small proportion of the input energy. However, it plays a significant role in the formation of soil fabric changes that promote the dissipation caused by interparticle friction. Mukwiri et al. (2016) examined energy dissipation during a one-dimensional normal compression test with a three-dimensional DEM simulation. The link between energy dissipation and particle size distribution was examined. They discovered that when the uniformity of particle size distribution increased, more energy is dissipated.

Hanley et al. (2018) investigated energy dissipation during drained triaxial shearing using DEM modelling. They used numerical samples consisting of 101,623 unbreakable spherical particles with a particle size distribution comparable to Dunkirk sand. Additionally, they utilised three distinct initial densities. The difference between the samples is based on their initial state parameters ψ_0, which adheres to the definition proposed by Been and Jefferies (1986). Specifically, ψ_0 represents the disparity between the initial void ratio and the critical state void ratio. As shown in Figure *2.23*, for all the samples the majority of the internal energy is dissipated by contact network friction sliding, which is also independent of the initial density during shearing.

Kruyt and Rothenburg (2006) studied the influence of the coefficient of friction μ on the shear strength, dilatancy and energy dissipation. They used a two-dimensional DEM simulation to perform a biaxial test for a granular sample containing 50,000 particles. Figure *2.24* illustrates the variation of $\mathrm{d}U$ (strain energy), δW (total work), and δD (dissipation) (in non-dimensional form) as strain is applied, considering three different values of μ. Initially, there is a positive change in strain energy, indicating an increase in strain energy. Subsequently, the energy change approaches zero rapidly, indicating a stabilisation of energy levels. The work done on the assembly, δW, quickly reaches a constant value. The dissipation, δD, start small, representing elastic behaviour. However, it rapidly increases until, at higher strains. The qualitative dissipative characteristics observed in the extreme cases of $\mu \rightarrow 0$ and $\mu \rightarrow$

∞ are similar to those observed when μ has a "normal" value of 0.5. Notably, even in the limit cases of $\mu \rightarrow 0$ and $\mu \rightarrow \infty$ where there is no frictional dissipation at the contact level, the dissipation remains substantial.

Keishing et al. (2020) conducted a parametric investigation using undrained cyclic triaxial discrete-element method simulations. They used cuboidal samples that contain 28,309 unbreakable, spherical particles to determine energy terms for five factors: void ratio, initial mean effective stress, mean deviator stress, deviator stress amplitude, and compressive/extensive initial loading. They found that only the void ratio substantially influences the relationship between excess pore water pressure and unit dissipated energy. Through the information provided at the microscale, they determined a preferable contact orientation for frictional dissipation of 30 to 40 degrees. In addition, they concluded that following a shear reversal, all simulations exhibit a negligible frictional dissipation at around 0.04% axial strain. They also concluded that incorporating mean deviator stress into the commonly used energy-based model for evaluating soil liquefaction potential could considerably improve its predictive accuracy.

The previous studies in this field primarily focused on investigating the overall energy dissipation in granular materials and the influence of different material behaviours on energy dissipation. However, there is a significant gap in understanding the microscale behaviour of energy dissipation. It is crucial to explore the relationship between the sliding of contact forces and energy dissipation because sliding contacts play a major role in the dissipation process. Through a meticulous examination of this relationship, valuable insights can be obtained into the underlying mechanisms that govern energy dissipation in granular materials. Based on the hypothesis made by Radjai et al. (1997), suggest that the majority of energy dissipation takes place within weak contact networks as they slid more. These hypotheses have been formulated based on the average force network partitioning method, which takes into account the magnitudes of contact forces (Radjai et al., 1997). Later theoretical investigations conducted by Collins and Kelly (2002) and Collins and Hilder (2002) have further advanced the hypothesis that energy dissipation in normal compaction is

primarily driven by the plastic deformation (sliding) of strong contact networks. Conversely, weak contacts will store energy, as they lack the sufficient stress levels needed to induce plastic deformation (sliding). However, they additionally demonstrated that in shear processes, energy dissipation predominantly takes place within weak contacts.

While the relationship between energy dissipation and contact networks has been the subject of numerous studies, the specific contribution of sliding contact networks to energy dissipation remains inadequately understood. Previous hypotheses have not thoroughly examined this aspect, and their development relied on the average force network partitioning method. It remains uncertain how the utilisation of alternative partitioning methods might impact the relationship between energy dissipation and contact networks. Further research is necessary to elucidate these aspects and enhance our comprehension of energy dissipation mechanisms in granular materials.

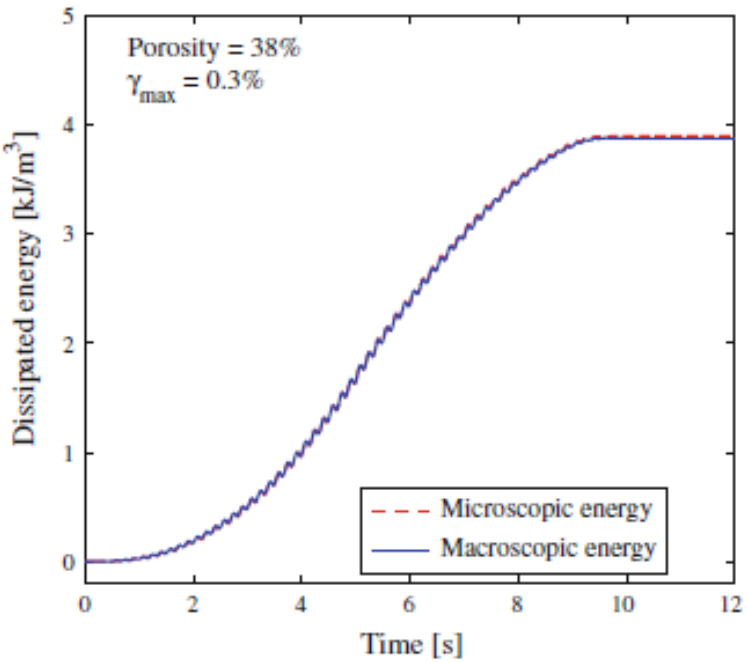

Figure 2.22 Comparison of microscopic and macroscopic energy dissipated cumulatively (El Shamy and Denissen, 2012).

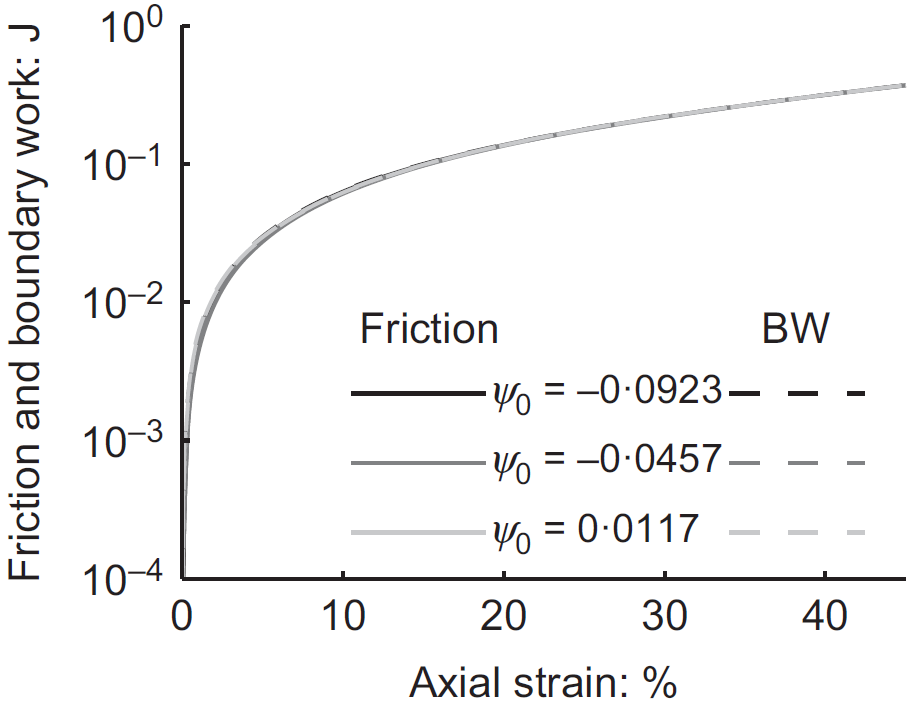

Figure 2.23 The evolution of friction dissipation and boundary work against axial strain (Hanley et al., 2018).

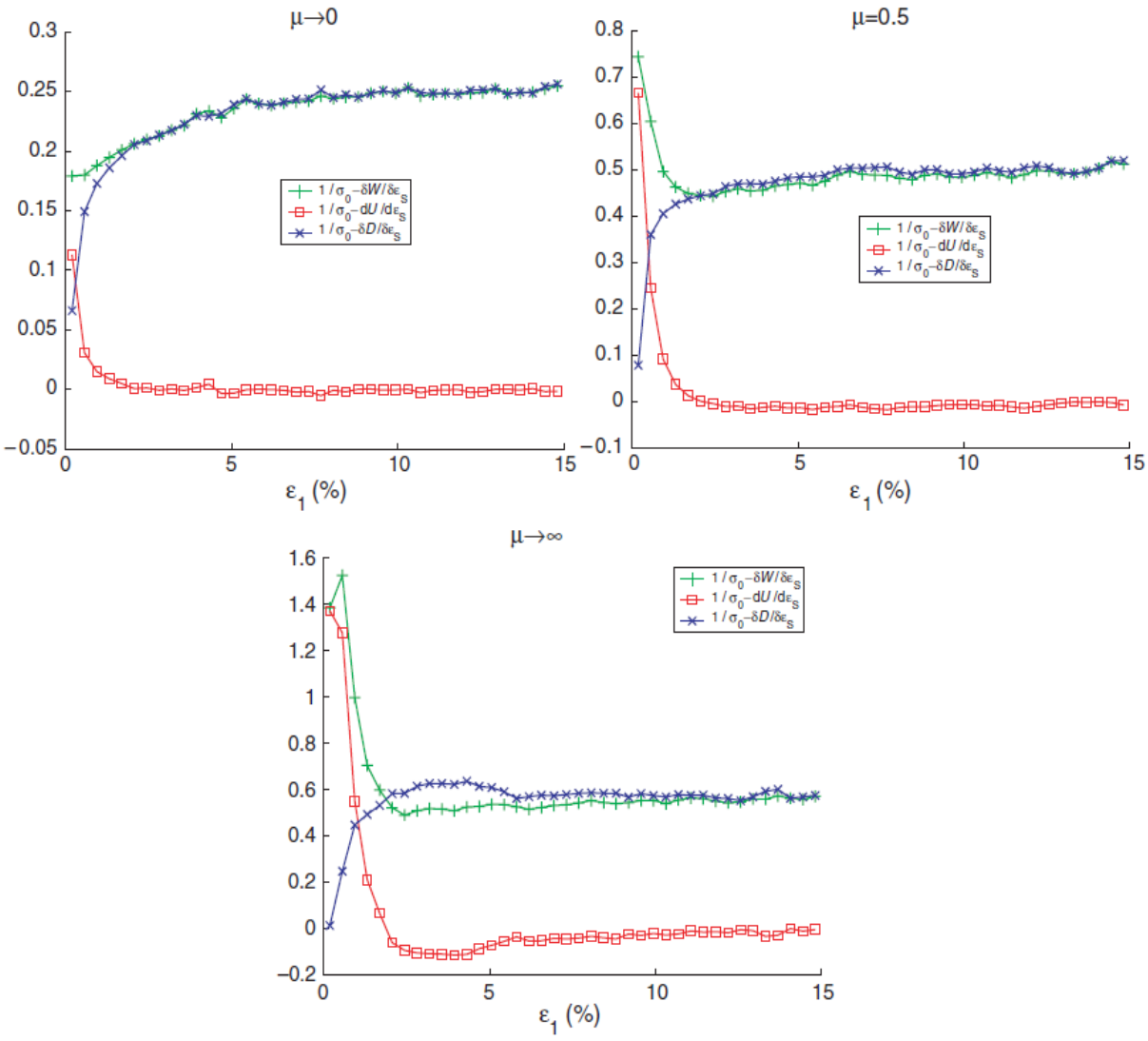

Figure 2.24 Effect of interparticle friction on input work δW, dissipation δD and strain energy dU against axial strain (Kruyt and Rothenburg, 2006).

2.4 Stored plastic work

Energy is a key consideration when describing the behaviour of sand. In particular, energy dissipation has been widely used to explain the mechanical behaviour of soils. However, there was a common misconception about plastic work and energy dissipation. It has been pointed out by Collins and Hilder (2002), that the misconception was created decades ago, where all the plastic deformation was assumed to contribute to the friction sliding between particles, and therefore all plastic work is dissipated (Okada and Nemat-Nasser, 1994, Luong, 1986). Subsequently, Collins and his co-workers revisited this misconception and suggested

that a portion of the plastic work within a granular system should be stored instead of being entirely dissipated. The stored plastic work or frozen plastic energy is the difference between the plastic work and the energy dissipation in the soil. The stored plastic work has been mentioned in the context of several elastic-plastic materials (Ulm and Coussy, 2003, Mróz, 1973, Maugin, 1992). Furthermore, the stored plastic work was also mentioned in soil mechanics by some of the early work by Houlsby (1981) who first applied thermomechanical principles to soil mechanics. Jefferies (1997) also noted the possibility of some plastic work being stored. Collins and his co-workers highlighted theoretically the importance of including the stored plastic work for constitutive modelling of sand (Collins and Hilder, 2002, Collins and Muhunthan, 2003, Collins and Kelly, 2002). Afterwards, Collins (2005) explains the concept of stored plastic work at both macro and micro levels and also provided a comprehensive discussion about the consequences of including the concept of stored plastic work. A thermodynamic framework for the constitutive modelling of soils has been established based on their research, in which the stored plastic work is considered. However, there is little understanding of the mechanism of stored plastic work in sand. For instance, The works by El Shamy and Denissen (2012) and Kruyt and Rothenburg (2006) studied energy dissipation, however, there is no information was provided regarding the stored plastic. Hanley et al. (2018) examined the work equations for both Cam Clay and Modified Cam Clay. They also examined the work equation developed by Collins and Hilder which is based on a thermomechanical approach. Figure *2.25* shows the difference between the work equations and frictional dissipation in different sample densities. The legend '' Equation 25'' indicates the thermomechanical work equation proposed by Collins and Hilder $\delta\Psi + \delta\Phi$ in which the total plastic work is the sum of stored plastic work and energy dissipation. They concluded that all work equations provide a good representation of the total frictional dissipation that occurs during shearing for loose samples. Nevertheless, differences grow as sample density increases. The modified Cam Clay work equation significantly overestimates the frictional dissipation for the densest sample. However, they showed that the thermodynamically work equation (Collins & Hilder, 2002) matches the actual frictional dissipation almost perfectly. However, the approach they employed to estimate elastic strains in the system, which assumes that the shear modulus is constant throughout shearing, differs from what can be determined by the experiment. Although it is possible that this function might overestimate

or underestimate the amount of stored plastic work, they have not provided a calculation of the actual plastic work that is stored in the system during the simulation.

In their study, Yang et al. (2018) conducted a thorough analysis of energy dissipation in elastic-plastic materials, focusing on thermodynamic formulations. They particularly emphasised the significance of stored plastic energy through theoretical formulations. Additionally, they applied this formulation to finite element method (FEM) simulations, where they found that the amount of stored plastic work was not particularly significant. Nonetheless, they stressed that including this stored plastic work is essential to uphold the fundamental principles of thermodynamics. Despite substantial efforts to theoretically explain the concept of stored plastic work in the system, there remains much to explore regarding the underlying mechanisms. One of the unresolved questions is the amount of plastic work that is stored during a triaxial test.

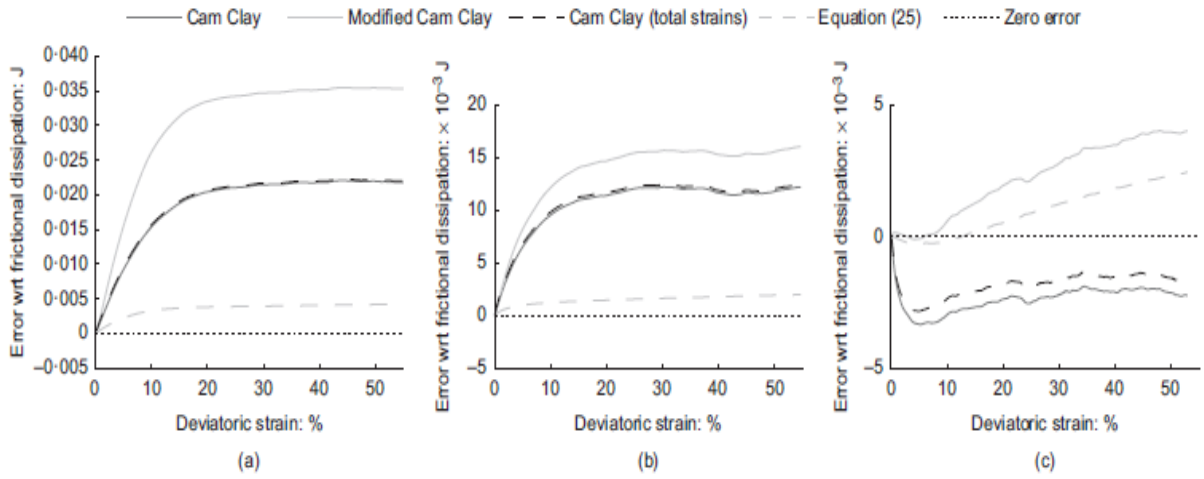

Figure 2.25 Difference between the work equations and frictional dissipation as a function of deviatoric strain For ψ_0 of; a) -0.0923, b) -0.0457 and c) 0.0117. A positive error indicates an overestimation of energy dissipation. (Hanley et al., 2018).

2.5 Constitutive modelling of granular materials based on energy consideration

Numerous constitutive models for geomaterials have been formulated based on fundamental mechanical concepts such as work, recoverable and irrecoverable energy, and dissipation. These models primarily emerged during the period spanning from the 1940s to the 1970s. After this period there were several developments using the principles of thermodynamics. The general theories of thermomechanics can be found in the work by Ziegler, summarised in his book Ziegler (1983) and the paper by Ziegler and Wehrli (1987). One example of these theories applies to rate-independent, elastic-plastic material PSD distributions s especially soils, which was described by Houlsby and Puzrin (2000) and Collins and Houlsby (1997). A key aspect of this approach is that the constitutive behaviour of soil can be completely determined when both free energy and dissipation function is specified (Collins and Kelly, 2002). These two energy equations can be used to determine the yield function and flow rule.

The interest in modelling the plastic component of free energy in granular materials has grown significantly. In these approaches, the notion of plastic-free energy is introduced during the development of constitutive models to ensure compliance with the second law of thermodynamics. Moreover, plastic-free energy serves as a valuable tool for distinguishing between plastic work and energy dissipation, where plastic work represents a combination of energy dissipation and plastic-free energy. Subsequently, the term "stored plastic work" or "frozen energy" was coined by Collins in 2005 to refer to plastic-free energy. This terminology helps to emphasise the role of this stored energy in the material's behaviour, reflecting the changes that occur during plastic deformation. The incorporation of stored plastic work into constitutive models has enhanced our understanding and ability to accurately describe the behaviour of granular materials, particularly in the context of irreversible deformations and energy dissipation processes.

Furthermore, adequate knowledge about free energy and energy dissipation functions is capable of determining elasticity law, yield function, flow rule and hardening rule (Collins, 1997, Collins, 2002, Collins and Houlsby, 1997, Collins and Kelly, 2002, Collins and Hilder,

2002, Houlsby, 1981). Although understanding free energy and energy dissipation functions is crucial for developing any model based on the concept of thermomechanics, the development of these function are mainly focused on the theoretical formulation and none was supported by quantitative results. Kruyt and Rothenburg (2006) used DEM simulation and 2D modelling to examine energy dissipation, proposing a new dissipation function based on the link between stress and dilatancy. However, they ignored the stored plastic work as they assumed that all plastic work is dissipated.

2.5.1 The thermomechanical process that is used to determine elastic-plastic constitutive laws

Initially, the influence of thermodynamic principles on plasticity models was primarily focused on models applicable to metals. However, as time progressed, these thermodynamic concepts began to equally impact models applicable to soil, rocks, and concrete. Numerous studies in the field of geomaterials have discussed the development of soil models based on thermodynamic principles. This process typically involves formulating plasticity theory, including yield surfaces, plastic potentials, and hardening functions and subsequently incorporating thermodynamic laws.

Another approach involves starting with thermodynamic hypotheses related to free energy and energy dissipation and deriving the plasticity theory from these hypotheses. Figure 2.26 illustrates this process, simplifying it through a flowchart that demonstrates how plasticity can be derived from free energy and dissipation functions (Collins and Hilder, 2002). This methodology provides a systematic way to integrate thermodynamics into the development of plasticity models for various geomaterials. Figure 2.26 illustrates that after creating the free energy function, it can be utilised to derive both the elastic law and shift stress. The elastic law characterises the relationship between stress and strain within the elastic range of a material, capturing its behaviour when subjected to small deformations and returning to its original shape upon load removal. On the other hand, shift stresses refer to stresses that cause a translation of yield surfaces without altering their shape. These shift stresses are significant in linear, anisotropic, and kinematic hardening models as they represent the stress at the "centre" of the shifted yield surface (Collins and Kelly, 2002, Puzrin and Houlsby, 2001).

Whereas the dissipation function can be used for the yield condition and the flow rule. In geotechnical engineering, the yield condition is a critical criterion that marks the transition from elastic to plastic behaviour in soils. It signifies the stress state at which the material undergoes plastic deformation. The yield condition is typically expressed in terms of the principal stresses or deviatoric stresses acting on the material. Several yield criteria have been proposed, including the well-known Mohr-Coulomb criterion, Drucker-Prager criterion, and Cam-Clay model, each characterised by its unique mathematical formulation and associated parameters. The selection of a specific yield condition depends on the particular behaviour exhibited by the soil under consideration.

Concurrently, the flow rule in geotechnical engineering elucidates the correlation between the incremental plastic strain rates and the stress state during plastic deformation. It provides valuable insights into how the material deforms plastically in response to applied stresses. At its core, the flow rule is grounded in the principle that plastic deformation transpires along the path of the maximum plastic potential gradient. This rule governs both the magnitude and direction of the incremental plastic strains experienced by the material. By comprehending and incorporating the yield condition and the flow rule into geotechnical analyses, engineers gain a deeper understanding of the complex behaviour exhibited by soils. These concepts serve as fundamental pillars within geotechnical constitutive models, enabling engineers to accurately predict and simulate the mechanical response of soils under various loading and deformation conditions.

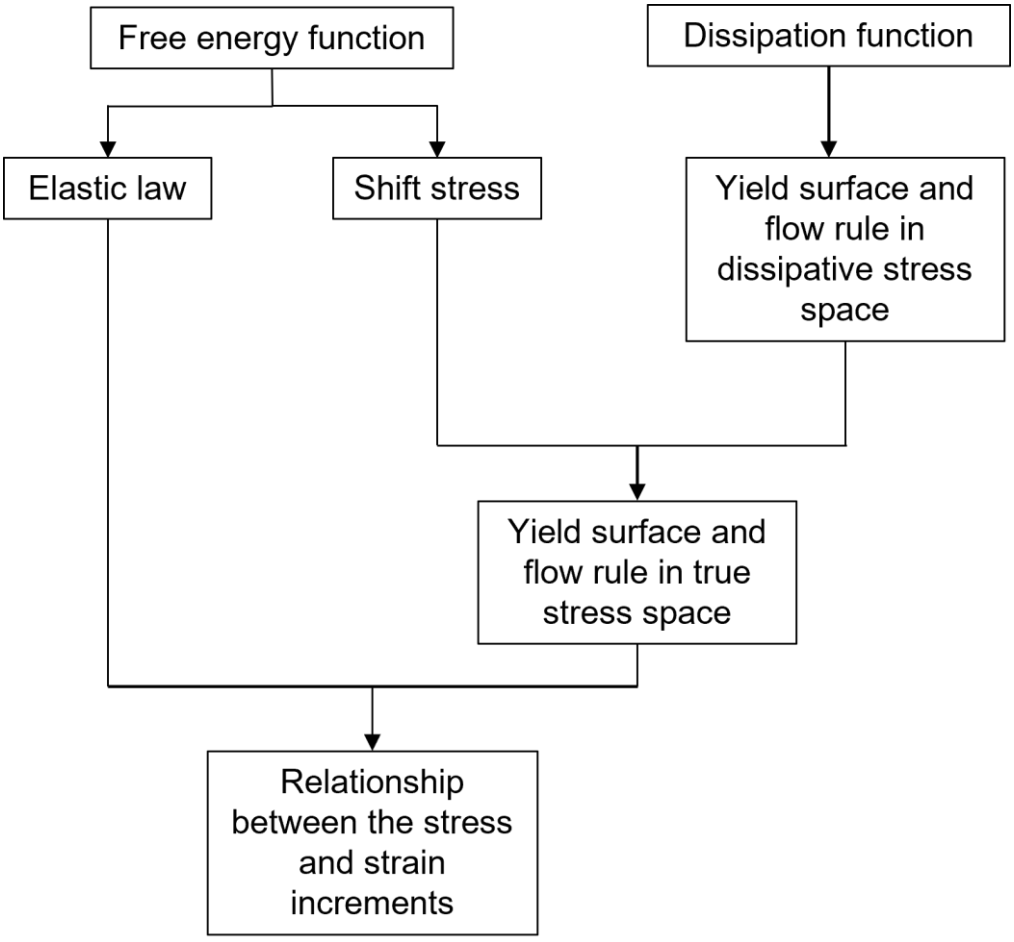

Figure 2.26 The proposed approach involves the development of a model by incorporating the concepts of free energy and dissipation function, as originally suggested by Collins and Kelly (2002).

The fundamental method for obtaining constitutive laws for rate-independent materials, starting with thermodynamic principles, will be described here. Several publications by Collins (2002), Collins and Houlsby (1997), Houlsby and Puzrin (2000), Collins and Kelly (2002) contain an explanation of the procedure of using thermodynamics to develop constitutive models suitable for geomechanics. These procedures will be detailed below using notation adequate for analysing triaxial testing. In isothermal deformations, the incremental work due to the applied stresses is the sum of the free energy function Ψ and the dissipation function Φ. Note that these functions are defined per unit volume. According to the fundamental energy relation, the incremental work that is accomplished as a result of the applied mean effective

p and deviator stress q is equivalent to the increase in free energy plus the energy that is dissipated:

$$p\delta\varepsilon_v + q\delta\varepsilon_q = \delta\Psi + \delta\Phi, \text{ where } \delta\Phi \geq 0 \quad (2.5)$$

Where $\delta\varepsilon_v$ and $\delta\varepsilon_q$ are the increment volumetric strain and increment deviator strain respectively. This inequality is the expression of the second law of thermodynamics that is suitable for use with isothermal deformations. This law strictly required $\delta\Phi$ to be positive whenever any irreversible plastic deformation occurs (Dugdale, 1996, Wilmanski, 1998).

The free energy is determined by the observable variables that are present in the kinematic state, for example, the total strains $\varepsilon_v, \varepsilon_q$ and plastic strains $\varepsilon_v^p, \varepsilon_q^p$. Instead of employing these volumetric strains, one might utilise the logarithm of the total and plastic-specific volumes (Collins and Kelly, 2002). However, strains will be used as the independent variables in this study. Therefore, the increment of the free energy will be as

$$\delta\Psi = (\partial\Psi/\partial\varepsilon_v)\delta\varepsilon_v + (\partial\Psi/\partial\varepsilon_q)\delta\varepsilon_q + (\partial\Psi/\partial\varepsilon_v^p)\delta\varepsilon_v^p + (\partial\Psi/\partial\varepsilon_q^p)\delta\varepsilon_q^p \quad (2.6)$$

The dissipation function is not a state function as it should only depend on the increments of plastic strains. It cannot depend on the total strain increments because if it does, a perfectly elastic deformation would result in energy dissipation. Therefore, the incremental dissipation function is in the form of $\delta\Phi\left(\varepsilon_v^p, \varepsilon_q^p; \delta\varepsilon_v^p, \delta\varepsilon_q^p\right)$. This function is homogenous of degree 1 in the plastic strain increments when applied to rate-independent, elastic/plastic materials. Collins and Kelly (2002) wrote about this function as

$$\delta\Phi = (\partial(\delta\Phi)/\partial(\delta\varepsilon_v^p))\delta\varepsilon_v^p + (\partial(\delta\Phi)/\partial(\delta\varepsilon_q^p))\delta\varepsilon_q^p \quad (2.7)$$

Collins and Houlsby (1997) have shown that in the case of frictional materials, $\delta\Phi$ depends also on the effective pressure. As stated by Collins and Kelly (2002) this has no influence on

the validity of Equation (2.7), however, by equating the four independent strain increment terms and eliminating the free energy and dissipation functions between Equations (2.2) – (2.7), the fundamental relations can be obtained

$$\mathrm{p} = \partial\Psi/\partial\varepsilon_{\mathrm{v}} \text{ and } \mathrm{q} = \partial\Psi/\partial\varepsilon_{\mathrm{q}} \tag{2.8}$$

$$\pi = -\partial\Psi/\partial\varepsilon_{\mathrm{v}}^{\mathrm{p}} = \partial(\delta\Phi)/\partial\left(\delta\varepsilon_{\mathrm{v}}^{\mathrm{p}}\right) \text{ and } \tau = -\partial\Psi/\partial\varepsilon_{\mathrm{q}}^{\mathrm{p}} = \partial(\delta\Phi)/\partial\left(\delta\varepsilon_{\mathrm{q}}^{\mathrm{p}}\right) \tag{2.9}$$

The effective stresses can be derived from the free-energy function, as shown by Equations (2.8), In addition, Equations (2.9) describe the dissipative (thermodynamic or generalised) effective pressure π, and dissipative shear invariant τ in terms of the free energy function and demonstrate that they can also be obtained from the dissipation function. More discussion is provided in papers by Collins and Houlsby (1997) and Collins and Kelly (2002) regarding the validity of Equations (2.8) and (2.9).

Distinguishing between dissipation and plastic work is crucial. Equations (2.7) and (2.9) can be used to obtain the incremental dissipation, as shown below.

$$\delta\Phi = \pi\delta\varepsilon_{\mathrm{v}}^{\mathrm{p}} + \tau\delta\varepsilon_{\mathrm{q}}^{\mathrm{p}} \tag{2.10}$$

whereas the plastic work increment is defined as

$$\delta W^{\mathrm{p}} = \mathrm{p}\delta\varepsilon_{\mathrm{v}}^{\mathrm{p}} + \mathrm{q}\delta\varepsilon_{\mathrm{q}}^{\mathrm{p}} \tag{2.11}$$

as mentioned earlier $\delta\Phi$ function is homogeneous of degree 1 in the plastic strain increment, hence, both derivatives of $\delta\Phi$ in Equation (2.9) are homogeneous of degree zero: which means that they only depend on the ratio of the plastic strain increment, also known as the plastic dilation (Collins and Kelly, 2002):

$$\delta^{\mathrm{p}} = -\delta\varepsilon_{\mathrm{v}}^{\mathrm{p}}/\delta\varepsilon_{\mathrm{q}}^{\mathrm{p}} \tag{2.12}$$

Collins and Kelly (2002) stated that if the ratio in Equation 2.13 is eliminated from Equations (2.6) and (2.7), it provides a relationship between π and τ which is the yield condition in dissipative stress space more details regarding this derivation can be found in the works by Collins and Houlsby (1997), Houlsby and Puzrin (2000), Maugin (1992) and Maugin (1999). In addition, the general theory demonstrates that the plastic strain increments in this stress space are always presented by the normal flow rule. The link between the dissipative stresses and the true stresses depends on the form of the free-energy function. For example, if the free energy function depends only on the elastic strain, then the true stresses and dissipative stresses are identical. Consequently, the yield surface and flow rule can be easily converted to the true stress space (Collins and Kelly, 2002). Nevertheless, Collins and Houlsby (1997) proved, however, that for the exceptional situation of frictional materials, when the dissipation function and therefore the yield function in dissipative stresses space rely directly on p, the normality aspect of the flow rule vanishes when transferred to real stress space. In the case of decoupled materials, the free energy function will depend on elastic and plastic strains.

$$\Psi\left(\varepsilon_{ij}^{e},\ \varepsilon_{ij}^{p}\right) = \Psi^{e}\left(\varepsilon_{ij}^{e}\right) + \Psi^{p}\left(\varepsilon_{ij}^{p}\right) \tag{2.14}$$

where $\Psi\left(\varepsilon_{ij}^{e},\ \varepsilon_{ij}^{p}\right)$ is the total free energy, $\Psi^{e}\left(\varepsilon_{ij}^{e}\right)$ is the elastic part of the free energy, and $\Psi^{p}\left(\varepsilon_{ij}^{p}\right)$ is the plastic part of the free energy. $\varepsilon_{ij}^{e},\ \varepsilon_{ij}^{p}$ are the elastic and plastic strain tensors respectively. Collins and Kelly (2002) stated that using Equations (2.8) and (2.9) provide the relation between the two sets of stress variables, which are as follows:

$$\mathrm{p} = \rho + \pi \text{ and } \mathrm{q} = \xi + \tau, \text{where } \rho = \partial\Psi^{p}/\,\partial\varepsilon_{v}^{p} \text{ and } \xi = \partial\Psi^{p}/\,\partial\varepsilon_{q}^{p} \tag{2.15}$$

where ρ and ξ are termed shift stresses. These stresses work on transferring the yield surfaces without changing their shape. In linear, anisotropic, and kinematic hardening models, these shifts (or back) stresses are very important because they show the stress at the "centre" of the shifted yield surface (Lemaitre and Chaboche, 1990, Puzrin and Houlsby, 2001). On the other hand, it does not seem that it has been completely recognised that they also play an essential role in the process of creating isotropic models of geomaterials with

varying strengths in tension and compression, as will be illustrated in the following paragraphs.

These shift stresses may be thought of as resulting from recoverable (elastic) deformations, which are only activated when plastic strains are present. As explained in Puzrin and Houlsby (2001), they may be conceptualised as a spring that is placed in parallel with the plastic slider. Walton and Braun (1986) were the ones who came up with the idea of developing such models to characterise the elastic/plastic deformations of the contacts that occur between individual granular particles. However, the conceptual models that are detailed in the books written by Mróz (1973) and Besseling and Van Der Giessen (1994) may provide a more satisfactory explanation for the natural occurrence of such shift stresses. Both authors' works are pertinent to the study of geomaterials. Although it is assumed that a macro-continuum element is plastically deforming, it is acknowledged in this model that certain micro-elements contained within this continuum element will not be subjected to plastically stressed but will still be elastically deforming. This is because some of these micro-elements will have a different stress state. This recoverable energy, which is 'locked' into the macro-deformation, is what create to the second free energy function, as well as the shift stress that relates to it. This energy can only be released it the plastic strain are reversed. More details are provided in chapter 5 regarding the second part of the free energy.

2.6 Conclusion

In conclusion, Discrete Element Method (DEM) is a powerful approach for modelling granular materials by considering the interaction between rigid particles. DEM employs contact models to calculate contact forces between neighbouring particles, allowing for the simulation of inter-particle contact, breakage of existing contacts, and formation of new contacts. By using a simplified representation of particle shapes and adopting a basic contact model, DEM simulations can capture the key mechanical response characteristics of granular materials. This enables the analysis of systems containing a large number of particles while still capturing the essential behaviour of soil.

DEM simulations provide valuable insights into the macroscale response of granular materials, including the stress-strain relationship. They enable the analysis of state-dependent behaviours, such as strain softening, dilation, and hardening, and help understand the influence of parameters like interparticle friction and particle size distribution on the material's behaviour. In addition. DEM simulations can provide valuable insights into the critical-state behaviour of granular materials, confirming the existence of a unique CSL and investigating the influence of factors such as initial densities, and confining pressures on the critical void ratio. These findings contribute to the understanding of granular material behaviour and can be applied in various engineering and geotechnical applications.

DEM provides researchers with a powerful tool to study granular materials at the microscale, offering valuable insights into their mechanical behaviour, flow properties, and structural characteristics. In particular, DEM simulations can shed light on the energy dissipation mechanisms within granular materials. While previous studies have focused on the overall energy dissipation resulting from particle friction or internal mechanisms like particle crushability, there is a need for more detailed information regarding the internal mechanisms of energy dissipation. Specifically, there is a lack of a quantitative link between the sliding of the contact network (i.e., particle interactions) and the energy dissipated within the granular material. By quantifying the sliding behaviour of the contact network and relating it to the energy dissipated, can establish a more detailed and precise understanding of the energy dissipation mechanisms. This knowledge is crucial for optimising the design and performance of granular systems in various applications, such as geotechnical engineering, material processing, and industrial processes.

Furthermore, this chapter addresses a common misconception concerning the distinction between plastic work and energy dissipation. Theoretical analysis has revealed that a portion of the plastic work within a granular system is stored rather than entirely dissipated. This stored plastic work is a significant aspect to consider. Despite substantial efforts dedicated to elucidating this concept, there remains a considerable amount to explore regarding the characteristics of stored plastic work. For instance, previous studies have not offered

quantitative results to represent the amount and behaviour of the energy stored in a granular system.

In this chapter, the development of constitutive modelling based on thermodynamic laws was examined. This process relies on two important functions: the dissipation function and the free energy function. Although various dissipation functions have been developed, however, their development is only limited to the theoretical formulation and similarly for a free energy function. Nevertheless, the development of constitutive modelling for granular materials could be greatly simplified by providing quantitative studies on both the free energy and dissipation functions. By conducting empirical investigations and obtaining quantitative data, researchers can enhance their understanding of these functions and facilitate their practical application in constitutive modelling. This would enable a more accurate representation of the thermodynamic behaviour of granular materials and contribute to the development of more reliable and robust models.

Chapter 3: Methodology

This chapter describes the DEM simulation that will be used throughout this study. The chapter focuses on describing the methods required to perform DEM simulation, including a description of the contact model, servo-control, periodic boundaries, and the selection of simulation parameters used throughout simulations. In addition, this chapter will describe the approach used in this study to monitor energy dissipation during DEM simulations.

3.1 The open-source code LAMMPS

The DEM simulations during this study were carried out using a modified version of LAMMPS (Plimpton, 1995). LAMMPS is the abbreviation of Large-scale Atomic/Molecular Massively Parallel Simulator. LAMMPS simulations can be performed on multiprocessor machines with distributed memory. A Message Passing Interface is used to parallelise these simulations (MPI). The parallel capability of LAMMPS may be used on multi-core desktop computers as well as massively parallel high-performance systems. In LAMMPS, simulations are run using an input script. In this study, all simulations were run on high-performance computers.

3.2 Contact model

A simplified Hertz-Mindlin contact model is used (Itasca Consulting Group2008, Hanley et al., 2018, Huang, 2014). The simplified Hertz-Mindlin contact model combines the normal and tangential forces to describe the overall contact behaviour. It accounts for the elastic deformation under the normal force and the frictional resistance to tangential motion. This model is commonly used in simulations and calculations involving granular materials, as it provides a simplified yet effective representation of the contact forces between particles. The simplified Hertz-Mindlin contact model strikes a balance between computational efficiency

and accuracy, making it a popular choice in DEM studies for a wide range of applications in geotechnical engineering (Cundall, 1988, Hanley et al., 2018, Huang, 2014, O'Sullivan, 2011)

This model uses Hertzian theory for the normal direction, for two overlapping sphere particles as presented in Figure 3.1 the normal component of the contact force is given by.

$$F_n = \frac{4Gr_g}{3(1-v)}\alpha_n^{3/2}\boldsymbol{n} \tag{3.1}$$

and the 'no-slip' Mindlin theory for calculating the tangential contact force incrementally as

$$F_t^{\beta} = F_t^{\beta-1} + k_t \Delta s \tag{3.2}$$

$$k_t = \frac{4Gr_g}{2-v}\sqrt{\alpha_n} \tag{3.3}$$

where G is the shear modulus of particles, v is the particle's Poisson ratio, α_n is the interparticle overlap, $r_g = \sqrt{r_a r_b/(r_a + r_b)}$ where r_a and r_b are the radius of two overlapping particles, $\boldsymbol{n}$ is a unit vector along the line joining the sphere centres, β is the timestep, and k_t is the shear tangent stiffness and Δs is the increment of relative tangential displacement. By calculating the tangential force incrementally and considering the limiting condition, the Hertz-Mindlin contact model in DEM simulations can capture the gradual development and evolution of tangential forces during particle sliding, allowing for a more accurate representation of the frictional behaviour between particles (O'Sullivan, 2011).

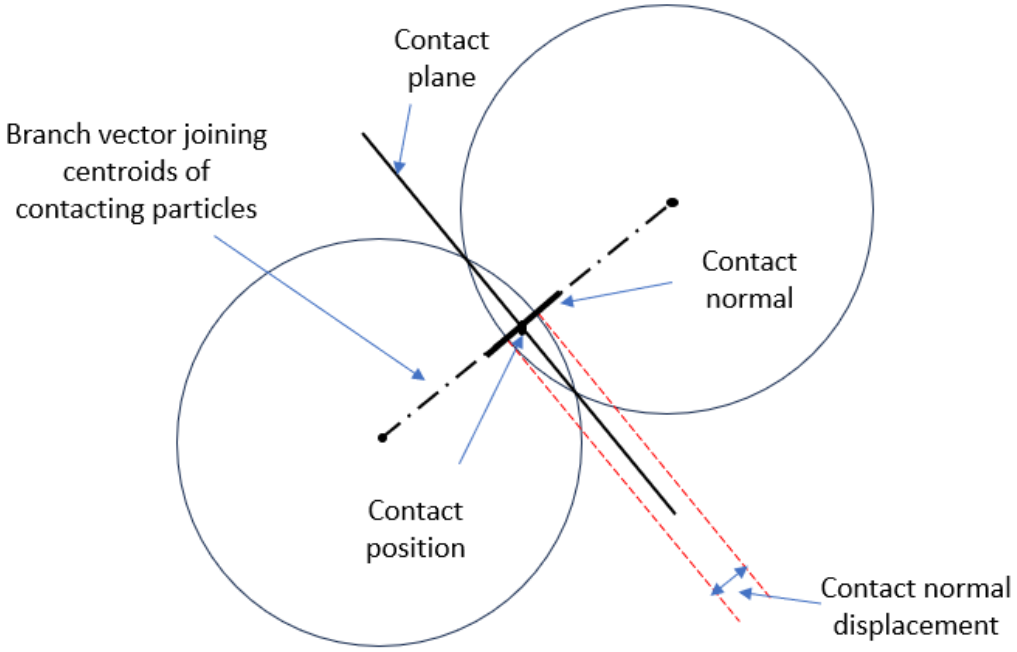

Figure 3.1 Diagram of two-particle in contact (O'Sullivan, 2011).

3.3 Servocontrol using periodic boundaries.

Periodic boundaries (PB) are used during this study. As shown in Figure 3.2, the periodic boundary condition presents the actual sample with multiple repeated structures surrounding the sample representative volume elements (REV). Periodic boundaries are used in DEM simulations to simulate an infinite system by creating a periodic repetition of a finite simulation domain. These boundaries allow particles to exit one side of the domain and re-enter from the opposite side, simulating continuous motion without encountering physical walls (Cundall, 1988). The use of periodic boundaries allows DEM simulations to be free of boundary effects that may considerably influence the material responses (Thornton, 2000).

In a simulation involving a strain field, the positions of particles within the simulation domain are continuously monitored as the simulation progresses. This tracking allows for the determination of the relative motion between particles and their interactions with the boundaries. As particles move within the simulation domain, their displacements are carefully observed to assess their motion relative to each other and the boundaries. This information

is essential for accurately understanding and modelling the behaviour of the system under strain. Additionally, when calculating the contact forces between particles, it is crucial to consider the influence of the periodic cell deformation rate. In cases where the periodic cell undergoes deformation, the relative motion between particles becomes a combination of two components. Firstly, the relative motion is determined based on the dynamic equilibrium considerations, which involve calculating velocities according to the forces acting on the particles. This accounts for the interactions and equilibrium of forces within the system. Secondly, relative motion is also affected by the velocity related to the periodic space. As described by Cundall (1988), when a periodic cell deforms, this velocity component contributes to the overall relative motion between particles. It captures the effects of the periodic nature of the system and the changes occurring due to the deformation of the cell. By considering both components of relative motion, the simulation can accurately capture the complex dynamics of the system under strain. This comprehensive approach ensures that the effects of particle displacements, relative motion, and the deformation of the periodic cell are properly accounted for, leading to more accurate and realistic simulations. It was also found that these boundaries eliminate inhomogeneities at the sample's periphery (Huang et al., 2014b).

3.3.1 Stress-controlled periodic boundary

The DEM simulation achieves stress-controlled loading conditions by continuously adjusting the boundary locations according to Equation (3.4). This allows triaxial simulations to be carried out using a variety of stress paths.

$$\dot{\varepsilon} = \frac{2\dot{\varepsilon}_{max}}{\sigma' required}(\sigma'_{required} - \sigma'_{measured}) \tag{3.4}$$

where $\dot{\varepsilon}$ is the strain rate, $\dot{\varepsilon}_{max}$ is the maximum allowable strain rate, $\sigma'_{measured}$ is the current stress within the assembly, and $\sigma'_{required}$ is the target stress. The first part of the equation $\frac{2\dot{\varepsilon}_{max}}{\sigma'_{required}} = g$, where g is the gain parameter which controls the speed of convergence between the target $\sigma'_{required}$ and the current stresses within a numerical assembly $\sigma'_{measured}$. Huang (2014) implemented this definition for the gain parameter in

LAMMPS, where it is generally calculated by trial and error. Utilising Equation (3.4) has several benefits. It quickly converges when the measured stress is much less than the required stress. This is very helpful during the first stage of isotropic compression when particles have little interaction, and the sample is in a condition of zero stress. Furthermore, the strain rate will decrease as the measured stress approaches the required stress.

If a reasonable $\dot{\varepsilon}_{max}$ has been established in one parametric study, the same $\dot{\varepsilon}_{max}$ can be utilised for other samples even with the different initial states; hence, there is no need for further trial and error. Selecting the proper gain parameter is essential. When g is too small, the simulation will take a long time to attain the target stress, and the steady-state stress is much greater than the target stress. When g is very big, oscillations may arise, which degrade the quality of the servo control and may cause instability if the oscillation amplitude increases over time.

In this study on triaxial compression, two different stress path loading conditions are performed:

- Drained triaxial shearing with constant radial stress. Shearing in Z-direction while $\sigma_x = \sigma_y$ and mean effective stress p = variable.
- Drained triaxial shearing with constant p. shearing in Z-direction while $\sigma_x = \sigma_y$ and p = constant.

To simulate these triaxial stress path conditions, a particular method is used. These methods were built using the 'fix multistress' command in LAMMPS code (Huang, 2014). To produce triaxial shearing while maintaining constant radial stress, the movement of the lateral boundaries must be controlled by the following:

$$\dot{\varepsilon}_{i,t} = \frac{2\dot{\varepsilon}_{max}}{\sigma'_{i,required}}(\sigma'_{i,required} - \sigma'_{i,measured}) \tag{3.5}$$

where $\dot{\varepsilon}_{i,t}$ is the strain rate of boundaries normal to the i th axis at the current time step, t. In addition, the 'constantp' option is added to the LAMMPS 'fix multistress' command line to produce drained triaxial shearing with constant p. If the strain-controlled is applied in the Z-direction while keeping the stress in the other direction equal, an estimate of the target stresses for the next timestep may be found at each timestep as follows:

$$p = \frac{1}{3}\left(\sigma_x + \sigma_y + \sigma_z\right) \rightarrow \sigma_x = \sigma_y = \frac{1}{2}(3p - \sigma_z) \quad (3.6)$$

Because the timesteps are small, the change in σ_z from t to $t + \Delta t$ is approximately equal to the change from $t - \Delta t$ to t when the load is applied in the Z-direction. Consequently, the stress at $t + \Delta t$ can be estimated as follows:

$$\sigma_{z,t+\Delta t} = \sigma_{z,t} + (\sigma_{z,t} - \sigma_{z,t-\Delta t}) \quad (3.7)$$

Hence, the target stresses in the x and y directions at $t + \Delta t$ can be calculated as follows:

$$\sigma_{x,t+\Delta t} = \quad \sigma_{y,t+\Delta t} = \frac{1}{2}(3p - \quad \sigma_{z,t+\Delta t}) \quad (3.8)$$

There is further information regarding the servocontrol equations that can be found in Huang's PhD thesis (Huang, 2014). These servo-control algorithms have been used in a number of different publications to investigate the behaviour of granular materials when subjected to triaxial test conditions (Hanley et al., 2018, Huang et al., 2014a, Huang et al., 2014b, Huang et al., 2017b). Therefore, these servo-control methods have been chosen for use in this investigation.

3.4 DEM simulation parameters and number of particles

The computational cost restricts the number of particles in DEM simulations. Typically, physical laboratory tests are conducted on a larger scale, with a sample size to particle size ratio of at least six times greater. For example, ASTM (2011) recommends that the diameter of a cylindrical sample for triaxial compression tests should not be less than 33 mm, which is at least 30 times the characteristic size (i.e.,D_{50}) of ordinary sands. Head (1980) proposed that the thickness of samples in shear box testing should be at least 10 times the largest particle diameter. It is difficult to adhere to these principles while doing DEM simulations, especially when real particle size is utilised since a huge number of small particles need to be simulated for every bigger particle. The existence of these smaller particles not only increases the total number of degrees of freedom of the system but also requires very small timesteps to maintain numerical stability (Huang, 2014). The sample size, the number of particles, and the

particle size distributions that were utilised for this investigation are presented in Chapters 4 and 5. To select the appropriate simulation parameters for this study, a thorough review of existing literature was conducted, as shown in Table 3.1. The relevance of these studies lies in their utilisation of similar simulation procedures, such as employing periodic boundary conditions and employing comparable contact models. Notably, the coefficient of friction ranges from 0.25 to 0.5 across these studies. Moreover, the contact model parameters were examined, which include a range of values for the shear modulus (1.46 GPa to 29.17 GPa), Poisson's ratio (0.12 to 0.3), and particle density (2570 kg/m³ to 2670 kg/m³). These parameters play a significant role in characterising the behaviour of the granular material. The values presented in Table 3.2 are used in the present study.

Table 3.1 Summary of some DEM parameters used in previous studies

Published work	Coefficient of friction μ	Contact model parameters	Number of particles	Boundary condition
(Hanley et al., 2018)	0.25	G = 29.17GPa ν = 0.2 ρ = 2670kg/m^3	101,623	Periodic boundaries
(Shire et al., 2014)	0.3	G = 27GPa ν = 0.3 ρ = 2670kg/m^3	304,205	Periodic boundaries
(Huang et al., 2017b)	0.25	G = 29GPa ν = 0.12 ρ = 2670kg/m^3	20,164	Periodic boundaries
(Keishing et al., 2020)	0.25	G = 1.46GPa ν = 0.2 ρ = 2650kg/m^3	28,309	Periodic boundaries
(Thornton, 2000)	0.3	G = 26.92GPa ν = 0.3 ρ = 2650kg/m^3	3,620	Periodic boundaries
	0.3-0.5	G = 28.68GPa ν = 0.22	4,000	Periodic boundaries

(Barreto and O'Sullivan, 2012)		$\rho = 2570 \text{kg/m}^3$		

Table 3.2 DEM simulation parameters used in this study

Parameter type	Parameter value
Shear modulus G	25 GPa
Poisson's ratio ν	0.2
Particle density ρ	2,670 kg/m^3

The ever-increasing computational power has greatly facilitated the exploration of polydisperse systems (Da Cruz et al., 2005, Radjai, 2009). Additionally, algorithmic advancements in contact detection (Andreotti et al., 2013, Perez et al., 2016) have significantly improved the efficiency of simulations in this field. Despite these advancements, challenges persist, especially when simulating systems with long timescales. Many real-world processes and standard laboratory tests, such as geomechanical element testing, involve the application of extremely low strain rates over prolonged durations, leading to quasi-static shearing phenomena. However, replicating such conditions in DEM simulations with reasonable computational costs is impractical. To overcome this limitation, simulated strain rates are artificially magnified by several orders of magnitude. To maintain correspondence with reality, the granular material is loaded quasi-statically, ensuring that loading occurs at a sufficiently slow rate to neglect inertial effects. The dimensionless inertial number serves as a key parameter to discern the boundary between the quasi-static regime and the inertial or dense-flow regimes. This inertial number quantifies the ratio of inertial force to the applied force and a small value of I indicates the quasi-static regime (Da Cruz et al., 2005). I defined as below:

$$I = \dot{\varepsilon} d \sqrt{\frac{\rho}{p'}} \tag{3.9}$$

where $\dot{\varepsilon}$ is strain rate, d is the diameter of the maximum particles, ρ is the density of the particle and p' is the mean effective stress. According to Da Cruz et al. (2005), it has been determined that the practical threshold for the quasi-static regime is set at an inertial number $I \leq 10^{-3}$. For this study, the inertial number used is $I \leq 10^{-4}$ based on established literature (Hanley et al., 2018, Huang et al., 2017b). This specific value is adopted to ensure consistency with previous research and maintain compatibility with the expected behaviour of the simulated system. In this study, the simulation timestep was established by adapting relationships from PFC3D (Itasca Consulting Group2008), which were derived from considerations of the critical timestep for spring-mass systems:

$$T_{crit} = \sqrt{\frac{M}{K^n}} \tag{3.10}$$

$$T_{sim} = \frac{T_{crit}}{FOS} \tag{3.11}$$

where T_{crit} and T_{sim} represent the critical and simulation timestep respectively; M is the mass of the smallest particle; K^n is the normal tangent contact stiffness. PFC3D calculates the critical time step (T_{crit}) for each particle at every timestep and selects the minimum T_{crit} value. In the non-linear Hertz-Mindlin contact model, the normal contact stiffness (K^n) depends on the overlap between two contacting particles, which changes throughout the simulation. Consequently, T_{crit} also varies during the simulation. PFC3D follows an explicit time integration scheme. In LAMMPS, a fixed timestep is used, necessitating assumptions for Equation 3.12. Given the limited understanding of polydisperse system behaviour in DEM, a conservative approach has been adopted here. Equation 3.13 utilises the mass and stiffness of the smallest particle in the system, with stiffness calculated conservatively using a maximum allowable overlap of 2%. To ensure further conservatism, Equation 3.14 incorporates a conservative factor of safety (FOS = 10) (Shire, 2014),

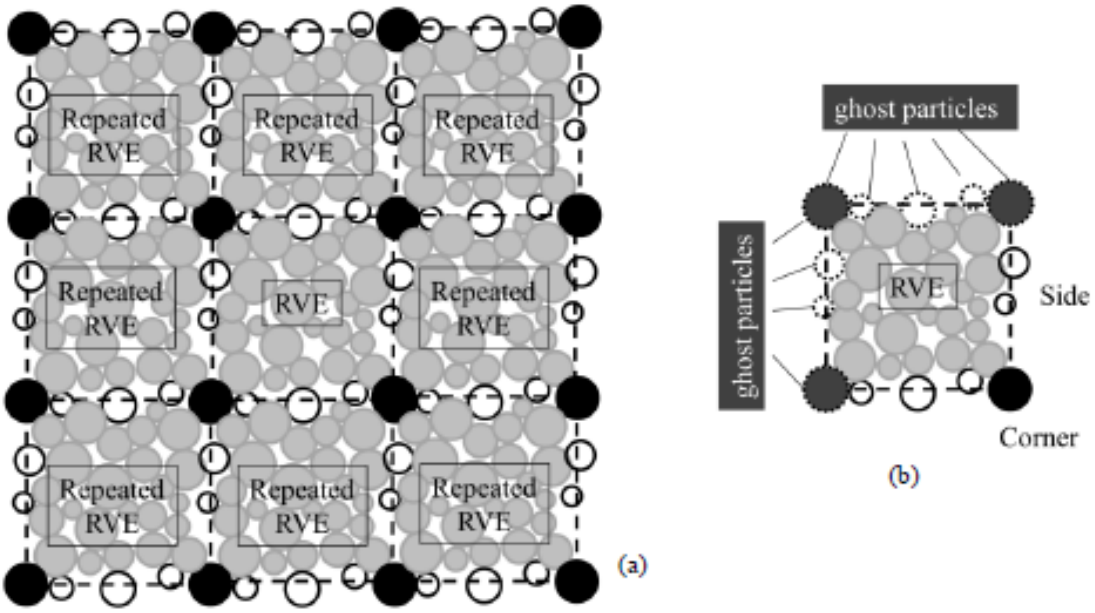

Figure 3.2 Periodic boundary (Huang, 2014).

3.5 DEM-based energy modelling

This DEM study employs the energy tracing technique that has been applied to granular LAMMPS by (Hanley et al., 2018). This technique is used to simulate spherical particles without numerical damping, rolling resistance or grain crushing. The DEM code contains calculations of energy and work terms. The energy dissipation across all contact sliding is calculated as

$$W_f^{c,t} = \sum_{c=1}^{N_{c_{sliding}}} W_f^{c,t-\Delta t} + F_s^c \Delta s^{c,t-\Delta t \to t} \tag{3.15}$$

where $W_f^{c,t-\Delta t}$ and $W_f^{c,t}$ are the energy dissipated by friction up to time $\Delta t - t$ and time t respectively, F_s^c the shear component of the contact force before rescaling it in accordance to $F_n \times \mu$. $\Delta s^{c,t-\Delta t \to t}$ is the incremental tangential displacement at the sliding contact between time $t - \Delta t$ and t. The total translational kinetic energy W_{kt} at any point in the particle system is given by

$$W_{kt} = \frac{1}{2}\sum_{p=1}^{N_p} m_p v_p^2 \tag{3.16}$$

where N_p is the number of particles in the system, v_p is the translation speed for particle p and m_p is the mass of particle p. The rotational kinetic energy is given by:

$$W_{kr} = \frac{1}{2}\sum_{p=1}^{Np} I_p \omega_p^2 \tag{3.17}$$

where I_p and ω_p are the moment of inertia and rotational speed of particle p respectively. Translational kinetic energy in granular materials is the energy associated with the linear motion of individual grains, arising from their movement and collisions. Rotational kinetic energy in granular materials emerges from the collective rotational motion of grains, contributing to macroscopic behaviour.

The normal component of strain energy is found to be the area underneath the normal component of the contact normal force $\left| F_n \right|$ against interparticle overlap α_n (Hanley et al., 2018).

$$W_{sn} = \int_0^{\alpha_n} \left| F_n \right| \mathrm{d}\alpha_n = \frac{4G_p r_g}{3(1-\nu)} \left| \boldsymbol{n} \right| \int_{\mathbf{0}}^{\alpha_n} \alpha_n^{\frac{3}{2}} \mathrm{d}\alpha_n = \frac{\mathbf{2}}{\mathbf{5}} \left| F_n \right| \alpha_n \tag{3.18}$$

In contrast to the normal component of strain energy, the calculation of the tangential component involves an incremental approach. This calculation is performed after the magnitude of the tangential force is rescaled to $\mu \left| F_n \right|$. Following the rescaling, the incremental calculation of the tangential component is conducted using the adjusted magnitude of the tangential force.

$$\delta W_{st} = \frac{\left| F_t^{\beta-1} + F_t^{\beta} \right|}{2} \frac{\left| F_t^{\beta} - F_t^{\beta-1} \right|}{k_t} \tag{3.19}$$

To confirm that the source of energy dissipated during the simulation has been correctly defined and implemented in DEM code, the margin of error in the energy at any timestep can be calculated using Equation (3.17) (Hanley et al., 2018),

$$\Delta E = W_{sn}^0 + W_{st}^0 + W_{kt}^0 + W_{kr}^0 + W^{\beta} - W_f^{\beta} - W_{sn}^{\beta} - W_{st}^{\beta} - W_{kt}^{\beta} - W_{kr}^{\beta} \tag{3.20}$$

The energy balance equation represents the conservation of energy, ensuring that the system maintains an energy balance without any spurious generation of energy due to numerical

instability. In this equation, W^{β} represents the total work done in the system, specifically referring to boundary work. The first part of the equation corresponds to the initial energies at the start of shearing, denoted by the subscript 0. Conversely, the second part of the equation represents the energies at different time steps, indicated by the subscript β.

3.6 Stress-strain calculation used in this study

The stress quantities used in this study include the mean effective stress p and deviator stress q which are defined as

$$q = \sqrt{\frac{1}{2}[(\sigma_1 - \sigma_2)^2 + (\sigma_2 - \sigma_3)^2 + (\sigma_3 - \sigma_1)^2]} \tag{3.21}$$

$$p = \frac{1}{3}(\sigma_1 + \sigma_2 + \sigma_3) \tag{3.22}$$

$$\eta = \frac{q}{p} \tag{3.23}$$

where σ_1 , σ_2 and σ_3 represent the major, intermediate, and minor principal stress, respectively; η is the stress ratio.

The normal strain component is defined as

$$\varepsilon_i = \int \frac{\Delta L_i}{L_i} \tag{3.24}$$

where ΔL_i is the change in length and L_i is the current length, i is representing the axial and radial strain. The shear strain and volumetric strain are defined below respectively.

$$\delta\varepsilon_q = \frac{2}{3}(\delta\varepsilon_a - \delta\varepsilon_r) \tag{3.25}$$

$$\delta\varepsilon_v = \delta\varepsilon_a + 2\,\delta\varepsilon_r \tag{3.26}$$

where $\delta\varepsilon_a$ is the axial strain and $\delta\varepsilon_r$ is the radial strain.

Chapter 4: The relationship between contact network and energy dissipation in granular materials

4.1 Introduction

The mechanical behaviour of sand (e.g., shear strength and dilatancy) at the macro-scale is dependent on the interaction between sand particles at the micro-scale (Zhao and Guo, 2013, Collins, 2005, Li and Li, 2009, Thornton and Antony, 1998). There has been extensive research on bridging the gap between the micro and macro responses of sand (Shire et al., 2014, Masson and Martinez, 2001, Li and Li, 2009, Arevalo et al., 2009, Liu et al., 2020). In particular, it is found that the energy dissipation in granular materials which occurs at the sand particle level is closely related to the macroscale response, such as shear strength, critical state and dilatancy (Mukwiri et al., 2017, Kruyt and Rothenburg, 2006, Collins and Muhunthan, 2003, Collins, 2005).

While some theoretical research has explored the relationship between energy dissipation and the behaviour of sand, our understanding of the microscale mechanism of energy dissipation remains limited (Zhao et al., 2008, Wang and Huang, 2014, Wang and Yan, 2012, Hanley et al., 2018, El Shamy and Denissen, 2010). It is widely recognised that frictional sliding between contact forces predominantly contributes to energy dissipation in granular materials (El Shamy and Denissen, 2010, Hanley et al., 2018). However, the role of contact networks during shearing in granular materials and their connection to energy dissipation has not been thoroughly investigated.

As discussed in Chapter 2, an important aspect that requires attention is establishing a quantitative relationship between the sliding behaviour of the contact network (i.e., particle interactions) and the dissipated energy within granular materials. By accurately quantifying the sliding behaviour of the contact network and its correlation with the dissipated energy, we can develop a more precise and comprehensive understanding of the mechanisms

underlying energy dissipation. Therefore, the primary objective of this chapter is to investigate, through DEM simulations, the quantitative relationship between energy dissipation and contact networks in granular materials.

4.2 DEM simulations

DEM samples were created containing 8262 spherical particles with a minimum diameter of 0.1 mm and a maximum diameter of 0.14 mm. Figure 4.1 shows the particle size distribution (PSD). The number of particles was varied to ensure a representative volume element (RVE) was obtained. Figure 4.2 compares the stress-strain relationship for the sample used in this chapter with a bigger sample that contains 21663 particles. It is evident that both samples yield comparable results. The larger sample displays a smoother curve, which can be attributed to its higher particle count compared to the smaller sample. Therefore, 8262 particles will be employed in this chapter to reduce computational time. As explained in Chapter 3, A simplified Hertz–Mindlin contact model and periodic boundaries were used. Two samples were produced in loose and dense states. The loose samples were first prepared by placing the particles randomly as a non-touching cloud in the periodic cell and then the cell was isotopically compressed to the target mean normal stress p_0 = 250, 500 and 1000 kPa with a friction coefficient μ of 0.3. Once the target stress was reached the samples were allowed to equilibrate. The dense sample was prepared using the two-step process (Hanley et al., 2014). The particles were placed randomly in a periodic cell and the sample was equilibrated with μ = 0 to reach the target p_0. The μ was then set to 0.3 and the sample was left to equilibrate again. Drained triaxial compression tests were then carried out, following two different stress paths, one with constant radial stress σ_r and the other with constant mean effective stress p. Loading was controlled by moving the upper boundary while the lower boundary was fixed. The shear rate was constant with the inertial number of $I = 1 \times 10^{-4}$, which indicates quasi-static loading. In line with the work conducted by Huang (2014), a local damping coefficient of 0.3 was selected and implemented during the preparation phase of this study. This local damping is utilised to facilitate the dissipation of kinetic energy, allowing the system to reach equilibrium efficiently within a reasonable number of calculation cycles (Huang, 2014). However, it should be noted that during shearing, the local damping was

specifically set to 0 to ensure that the dissipation is solely attributed to interparticle friction during triaxial compression. It is worth mentioning that any energy dissipation resulting from rolling friction or resistance has been excluded from consideration due to an ongoing dispute surrounding its impact.

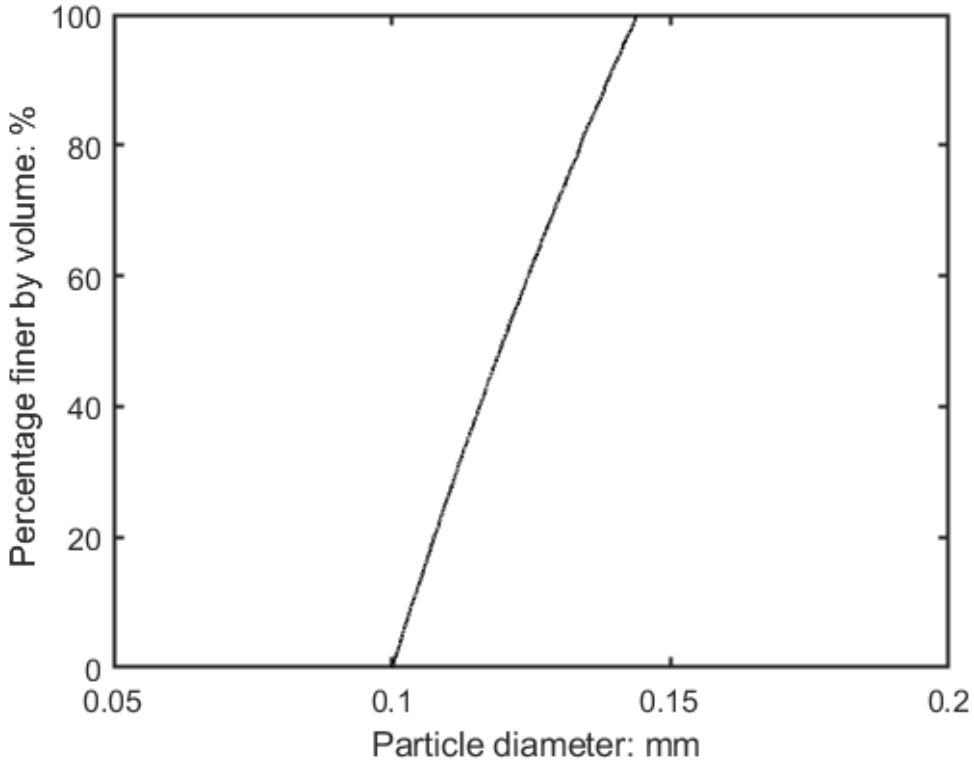

Figure 4.1 Particle size distribution (PSD).

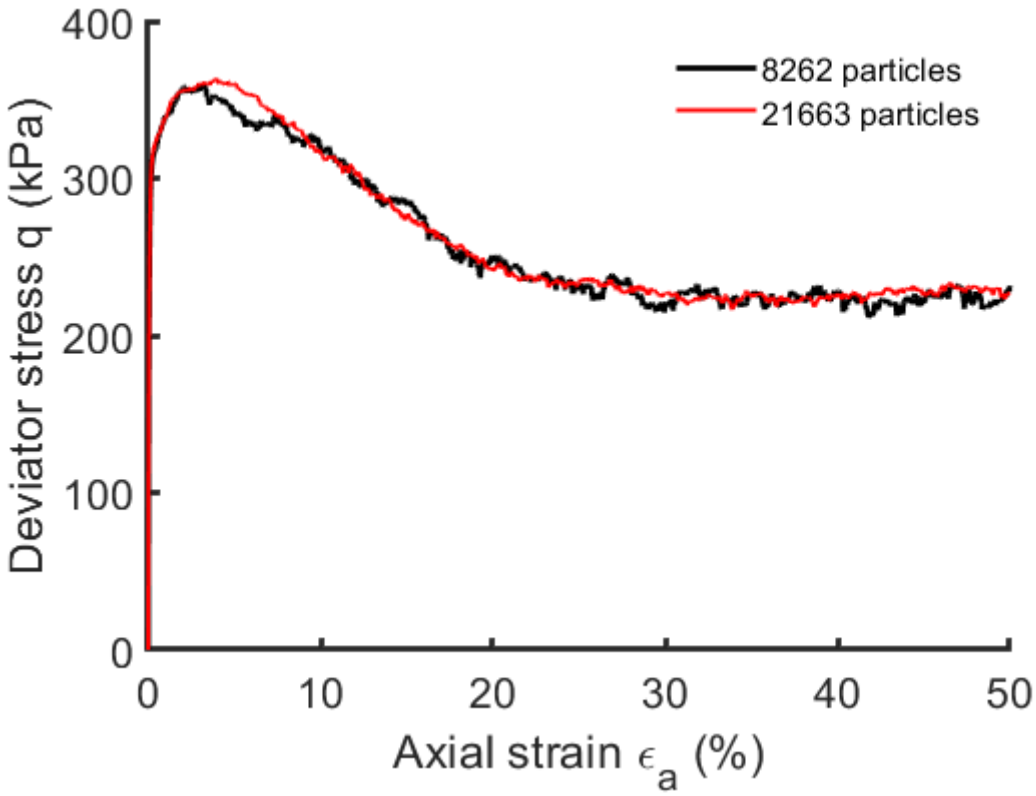

Figure 4.2 Effect of the particle number on the relationship between axial strain and deviator stress

4.2.1 Method for evaluating the contribution of contact networks to energy dissipation.

Throughout the simulation, LAMMPS identifies sliding contacts at each timestep, as seen in Figure 4.3. Then, the quantity of energy dissipation induced by each sliding contact will be measured. The energy dissipation will be outputted at both macro and micro levels. At the macroscale, LAMMPS outputs the total energy dissipation at a certain timestep generated by all sliding networks, with no information about the contribution of strong and weak contacts to energy dissipation. At the microscale, however, LAMMPS output energy dissipation due to the sliding networks at a specific timestep for each sliding network separately. The data provided at the microscale allows the contribution of weak and strong contact to be investigated. For instance, in a single timestep, both the weak and strong contact sliding and energy dissipation can be distinguished, as seen in Figure 4.4. To precisely quantify the amount of energy dissipated at the microscale, the output data must be printed at each timestep. Otherwise, some information will be lost between timesteps as contacts build and

collapse. Figure 4.5 gives an example of how some information will be lost. In the example, the data is printed out every 100 timesteps, as shown in the figure. If contact is lost at timestep 50, there will be no information about it at timestep 100 when the data is printed out. Therefore, To correctly estimate energy dissipation, the data should be printed at each timestep, as shown by this example. Nonetheless, printing data at each timestep would generate a massive data file of around 40GB for 8262 particles. This is impractical to store and analyses.

In order to streamline the computation process while ensuring a precise assessment of the contribution of contact networks to energy dissipation, a simplified approach has been adopted. This method provides an accurate and efficient means of evaluating energy dissipation, thereby reducing computational complexity. This research utilised a probing test method. First, information about the sample during the simulation is stored at different strain levels which in this work are stored at every 1% axial strain, as shown in Figure 4.6. At each specific location, represented by the red dot, the probe test is done by applying a small strain increment $\Delta\varepsilon_a = 1 \times 10^{-5}$ and the data is printed out for all contacts at every timestep. This provided information about dissipation at specific points ("snapshots") in the simulation without losing information. After applying the probe test method for each point shown in Figure 4.6. MATLAB code is used to analyse the results of each probe test. A flow chart illustrating and describing the technique used by the MATLAB code to determine microscale energy dissipation between two timesteps is shown in Figure 4.7. The MATLAB code is summarised in the following equations.

$$\delta E_{c,fd}^{\beta} = E_{c,fd}^{\beta} - E_{c,fd}^{\beta-1} \tag{4.1}$$

$$\delta E_{tot}^{\beta} = \sum_{C,fd=1}^{N_c} E_{c,fd}^{\beta} \tag{4.2}$$

$$\emptyset E_{tot}^{\beta} = \delta E_{tot}^{\beta-1} + \delta E_{tot}^{\beta} \tag{4.3}$$

where $E_{c,fd}^{\beta}$ is friction dissipation per single contact at timestep β, $E_{c,fd}^{\beta-1}$ is friction dissipation per single contact at timestep β-1, δE_{tot}^{β} is total increment energy dissipation across all contact in timestep β, and $\emptyset E_{tot}^{\beta}$ is total cumulative energy dissipation at timestep β. To validate the MATLAB code, the results of both Equations (4.2) - (4.3) have to be compared with the DEM simulations. However, validating Equations (4.1) and (4.2) are time-consuming,

and therefore, only Equation (4.3) has been validated. The results computed by the code (Equation (4.3)) should match the sum of energy dissipation outputted by the DEM simulation; however, this validation cannot be performed on a large sample including a large number of particles. Therefore, a sample containing just 15 particles was prepared. This sample was simulated for around 600 timesteps, which is sufficient for the contact to begin dissipating energy. The data was outputted at every timestep during the simulation. The MATLAB code was then used to analyse energy dissipation for each contact network during the 600 timesteps, and the findings were compared to DEM results at the macroscale as shown in Figure 12. Both outcomes are identical, indicating that the code is running correctly.

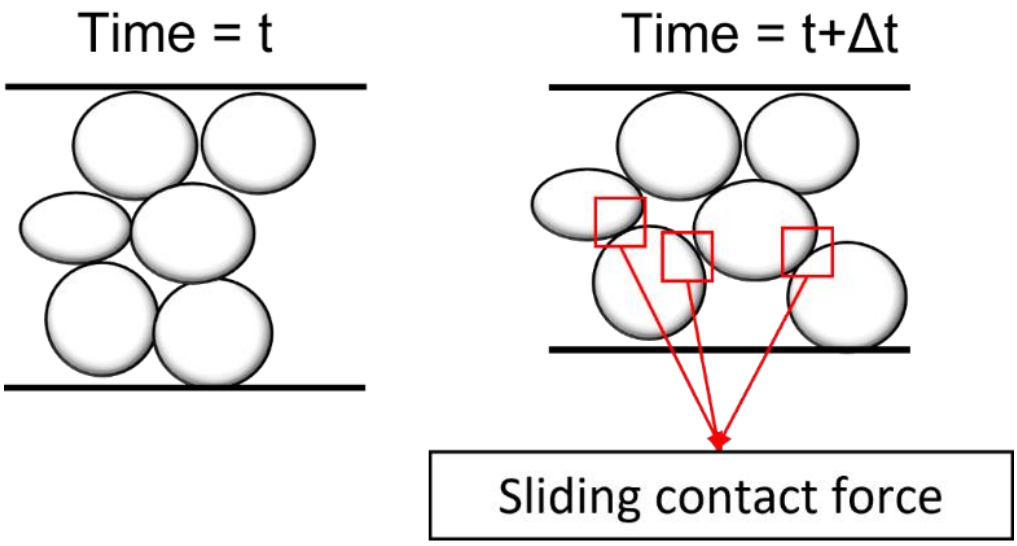

Figure 4.3 Example of sliding contacts at specific timestep

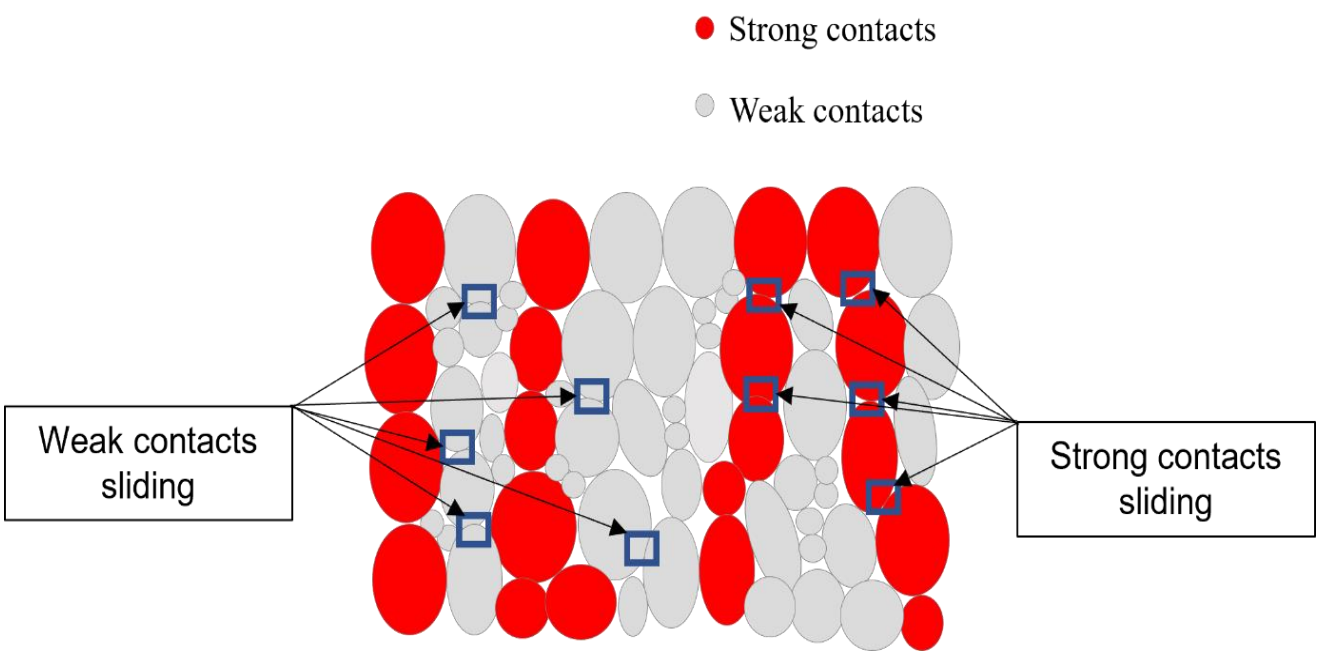

Figure 4.4 Example of identifying the weak and strong sliding contacts at a single timestep during the simulation.

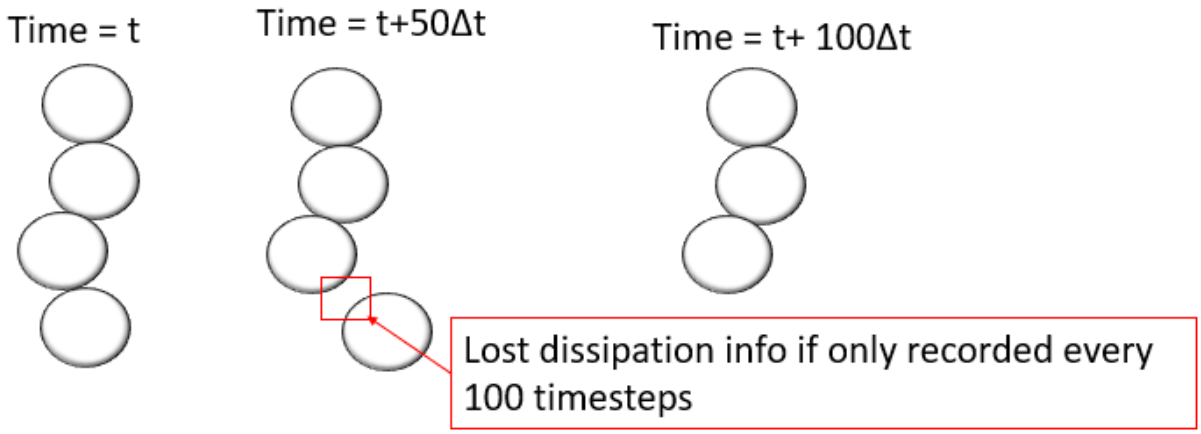

Figure 4.5 Example of how energy dissipation information is lost if only recorded every 100 timesteps

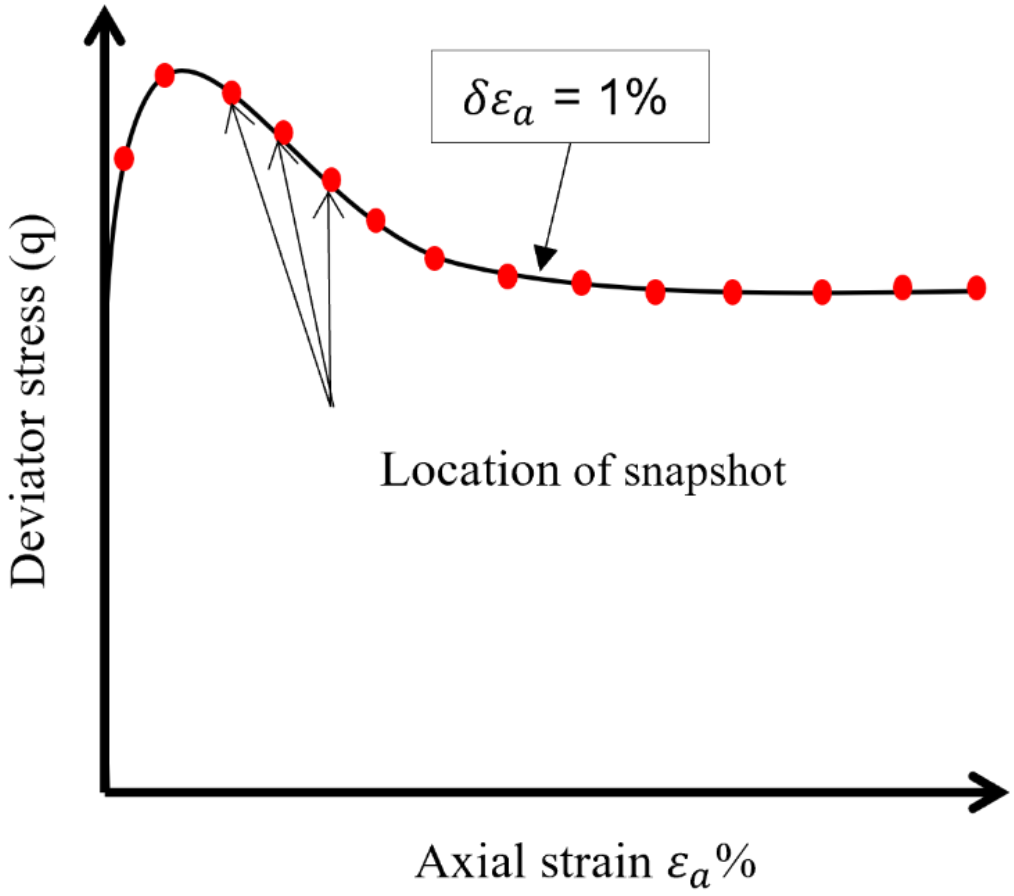

Figure 4.6 Schematic representation of data snapshots

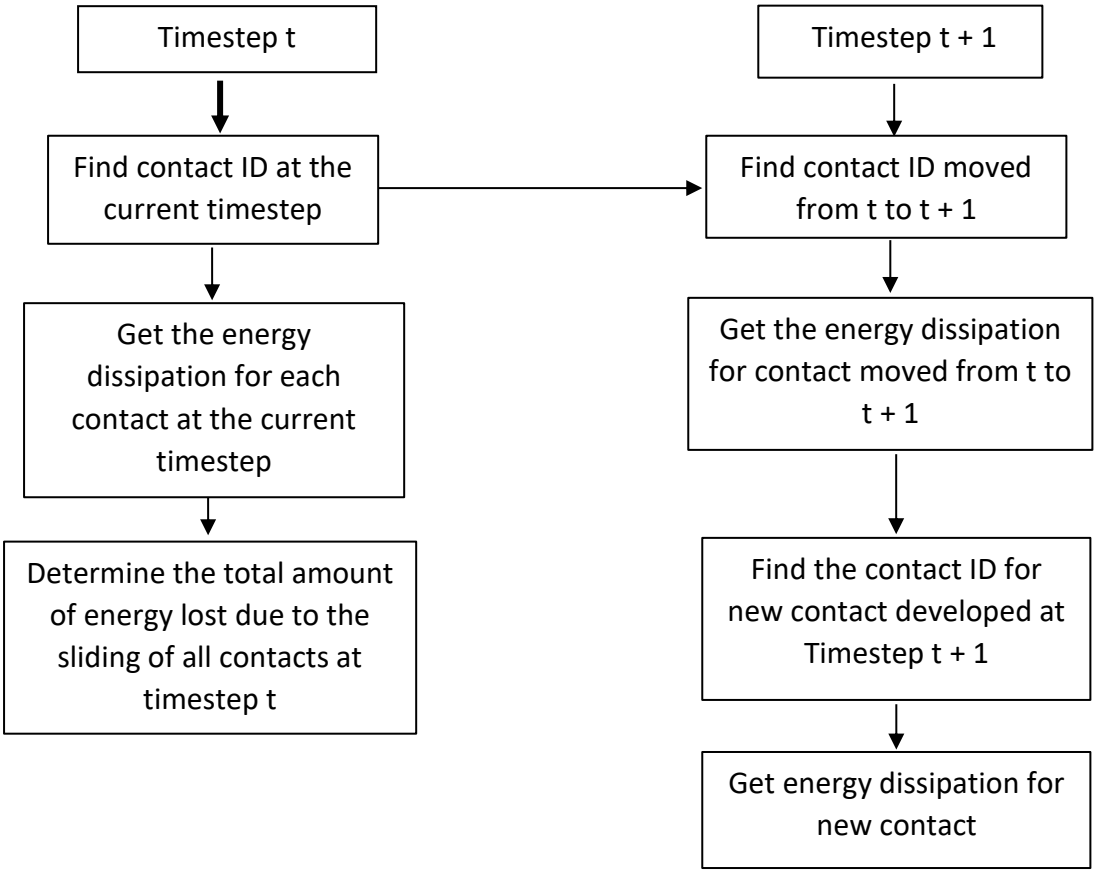

Figure 4.7 flow chart describes the steps that the MATLAB code follows to calculate energy dissipation at the microscale

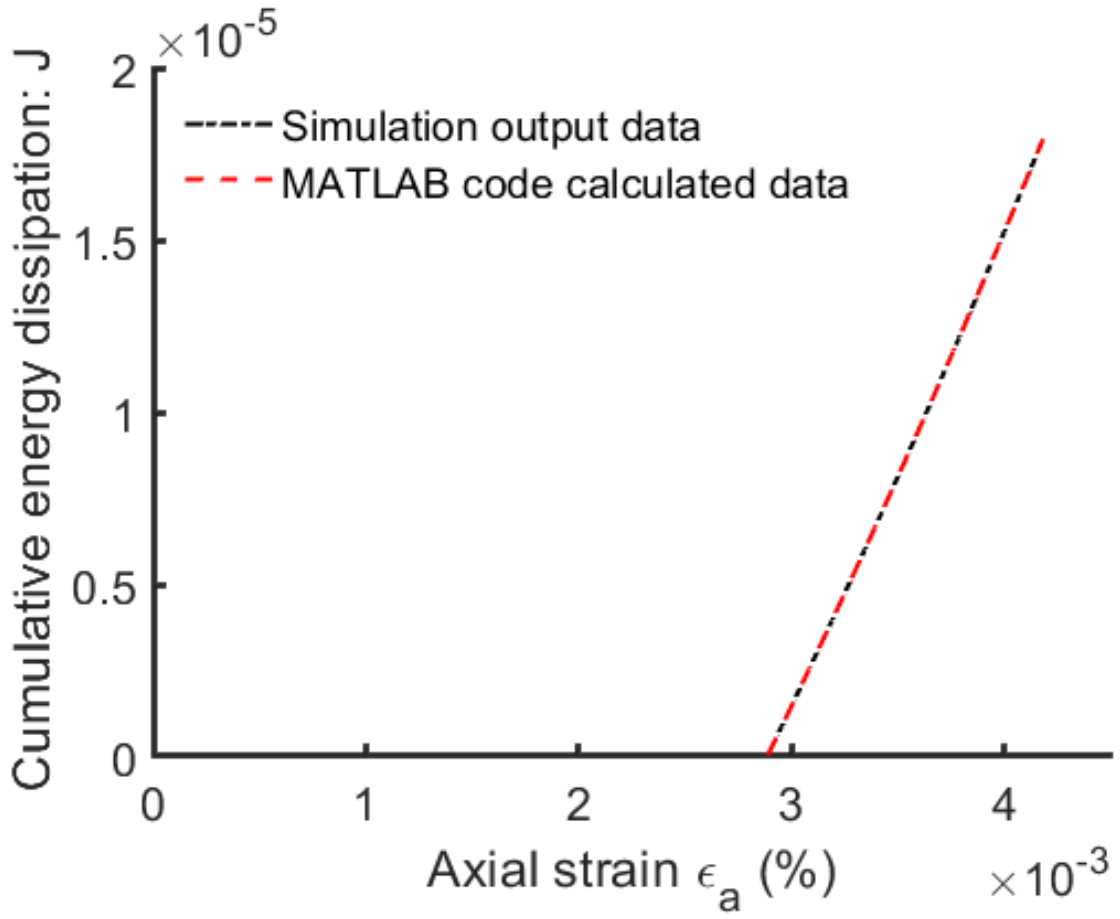

Figure 4.8 Energy dissipation results calculated at the macroscale (simulation output) and at the microscale (using MATLAB code)

4.3 Results

4.3.1 Stress-strain relationship

Figure 4.9 and Figure 4.10 show the stress-strain relationship of dense and loose sand. The dense sand shows strain softening and volume expansion while the loose sand shows strain hardening and volume contraction during the tests. Note that the true strain is used in this study. Furthermore, Figure 4.11 shows the stress ratio against axial strain, it can be noticed that regardless of the stress path applied, there is a unique relationship between ε_a and q/p when the initial void ratio is the same.

Figure 4.12 shows the critical state line (CSL) in the $e - log(p)$ plot and $q - p$ plot. To obtain a broader Critical State Line (CSL) in both $-log(p)$ plot and $q - p$ space, additional simulations were conducted. These simulations maintained a constant σ_3 stress path and

utilised two initial density conditions (loose and dense). Various values of the main effective stress were employed in these simulations. It is observed that the critical state stress ratio, denoted as M, is equal to 0.7. The CSL is nonlinear in the $e - log(p)$ plot, which is consistent with previous results (Hanley et al., 2018, Perez et al., 2016, Peña et al., 2009, Huang et al., 2014a). It can be seen that the critical state void ratio is almost constant when p < 1000 kPa, which is different from that for real sand. There are several possible reasons for this. First, spherical particles cannot represent the shape and movement of real sand particles in the 3D space (Ng, 2009b). Secondly, it should be acknowledged that the contact model utilised in this study may not accurately represent the true contact behaviour between sand particles. Additionally, it is important to note that excessively high mean effective stress, such as reaching 10^4 kPa, can result in significant overlap between particles, potentially leading to unrealistic outcomes.

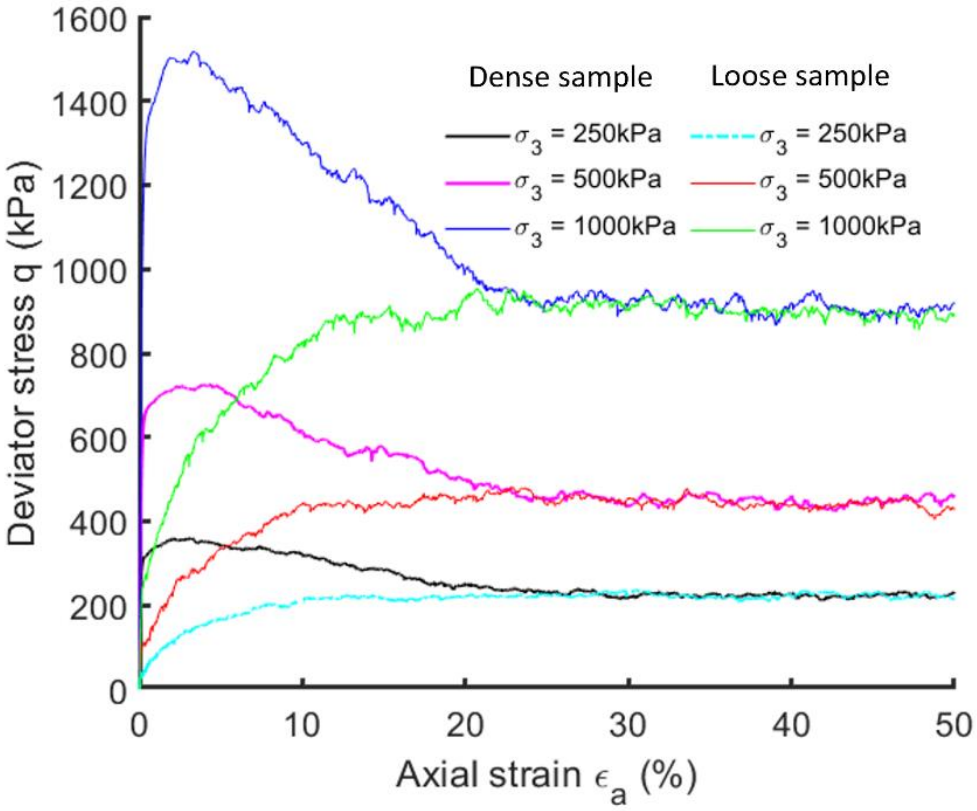

(a)

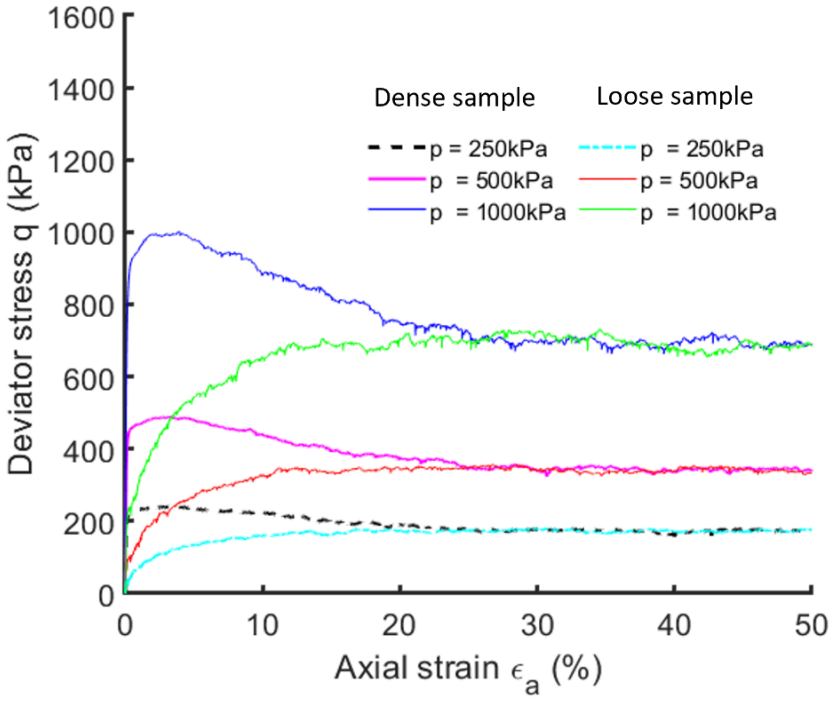

(b)

Figure 4.9 Stress-strain relationship for dense and loose sand during drained triaxial tests with different stress paths a) constant σ_r; b) constant p.

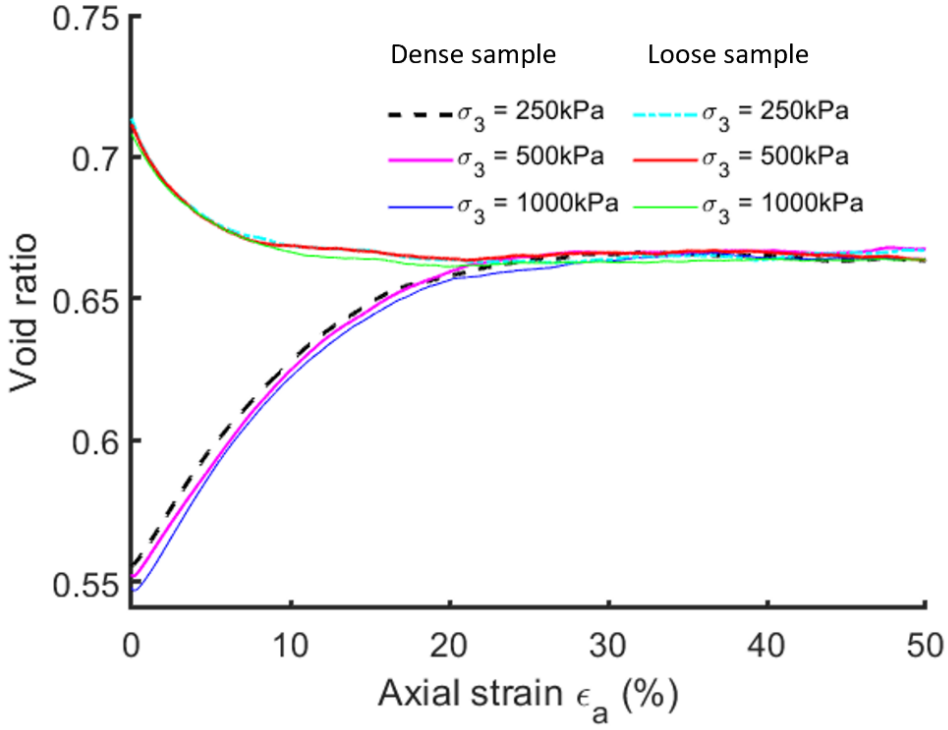

(a)

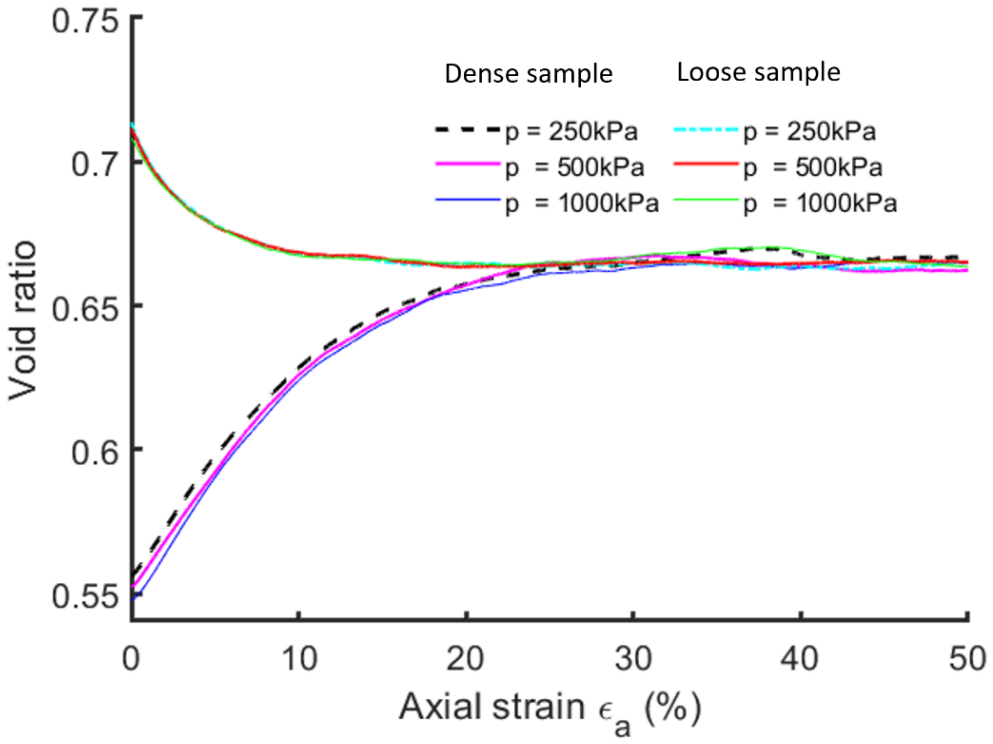

(b)

Figure 4.10 Dilatancy behaviour for dense and loose sand during drained triaxial simulation test with different stress paths a) constant σ_r; b) contstant p.

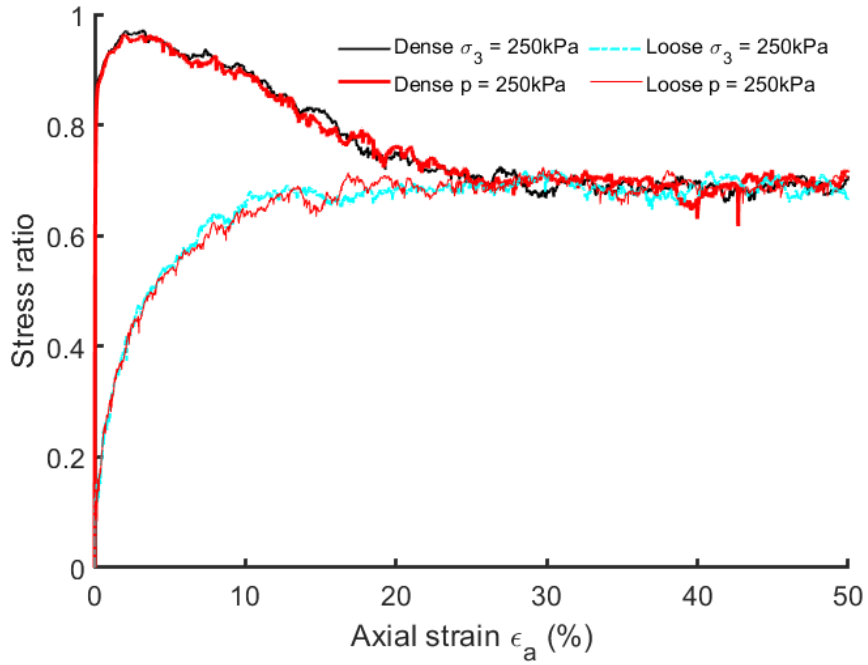

Figure 4.11 stress ratio against the axial strain for triaxial shearing with different stress paths and soil density.

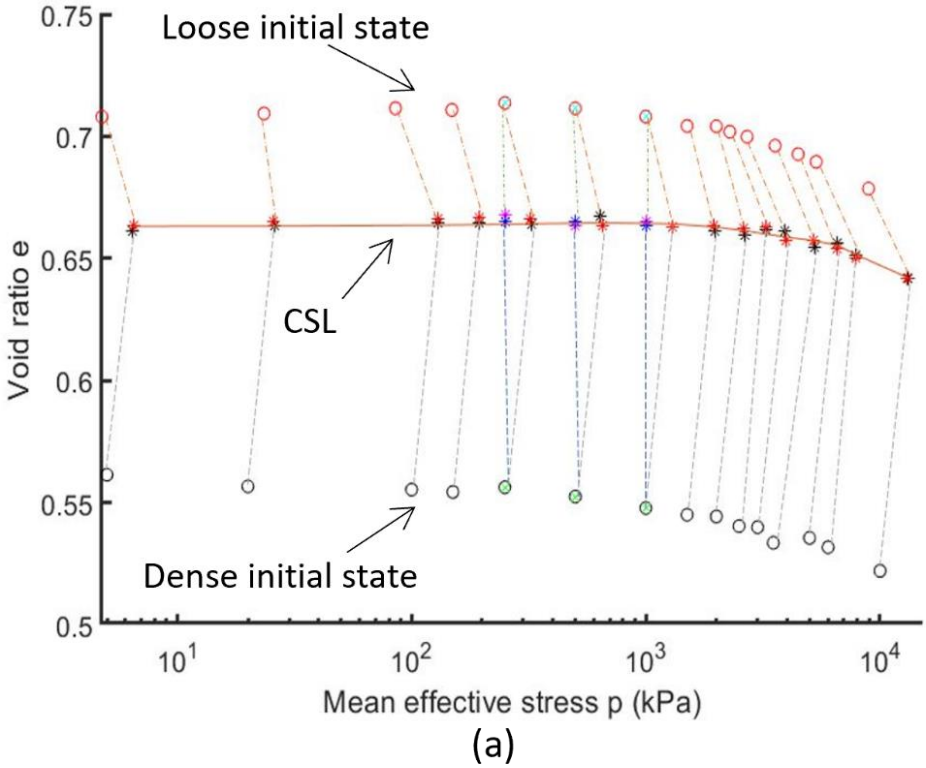

(a)

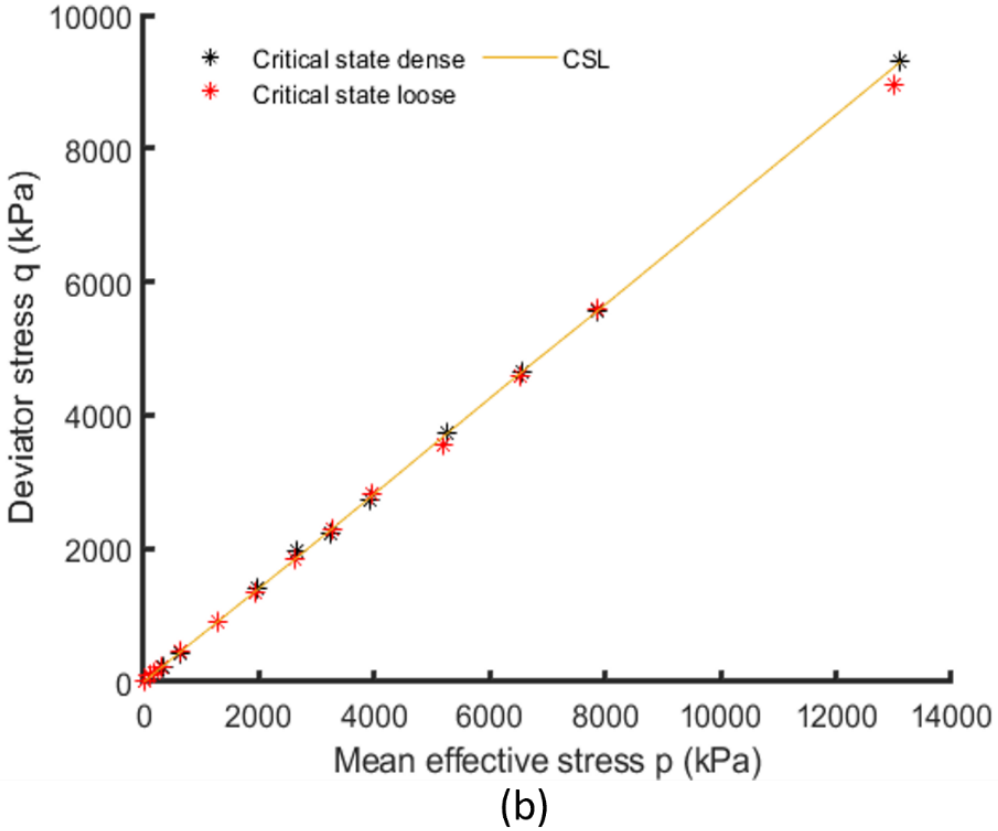

(b)

Figure 4.12 Critical state lines in the a) $e - log\ (p)$ and b) $q - p$ spaces.

4.3.2 Energy dissipation

In this study, the energies were traced using the method implemented in Granular LAMMPS by (Hanley et al., 2018). The error in the energy balance during the simulation is examined by using Equation 4.4 as described in (Hanley et al., 2018). The error in the energy balance during triaxial compression is illustrated in Figure 4.13a and Figure 4.13b. The error is quantified as a percentage of the boundary work and is consistently negligible throughout the simulation, demonstrating the absence of spurious energy generation caused by numerical instability. It is worth noting that, at the outset of the simulations, the errors may appear relatively higher compared to the subsequent stages, primarily due to the boundary work being zero during the initial shearing phase. These findings are consistent with the observations reported by Hanley et al. (2018).

It is well known that interparticle sliding in granular materials is the main source of energy dissipation (El Shamy and Denissen, 2012). Other sources of energy, such as strain energy and kinetic energy, are negligible in the system due to quasi-static loading conditions (Hanley et al., 2018, El Shamy and Denissen, 2012, El Shamy and Denissen, 2010). In this study, the main focus is on the energy dissipation associated with sliding within the contact networks. During loading, the energy dissipation is continuously monitored. When sliding occurs, the increment of energy dissipation δW_f^{β} is calculated using the equation below

$$\delta W_f^{\beta} = \frac{1}{V}\sum_{c=1}^{N_{c_{sliding}}} F_s^c \Delta s^{\beta \leftarrow \beta-1} \tag{4.5}$$

where β denotes a time step, $\Delta s^{\beta \leftarrow \beta-1}$ is the incremental tangential displacement at the sliding contact between timestep $\beta \leftarrow \beta - 1$. F_s^c is the tangential component of the contact force of sliding contacts; V is the volume of the sample and N_c is the number of sliding contact in the system. Note that the energy increment has been normalised by the total volume because the response of a representative soil element is considered. The total frictional energy dissipation as accumulation is

$$W_f^{\beta} = W_f^{\beta-1} + \delta W_f^{\beta} \tag{4.6}$$

The energy dissipation results in this work are presented per unit volume and expressed as a rate of energy and the unit of the energy dissipation is converted to kPa. This offers valuable

insights into the behaviour and stability of the systems being studied. By adopting this approach, a more comprehensive understanding of the processes of energy dissipation during triaxial shearing can be provided. Figure 4.14a displays the incremental energy dissipation, while Figure 4.14b illustrates the cumulative energy dissipation. These figures show the energy dissipation for various soil densities and stress paths. However, it is important to highlight that the results presented in Figure 4.14 solely represent the dissipation of all contact sliding, without providing specific information about the contribution of weak and strong contacts to energy dissipation. The subsequent discussion will introduce a method for determining the respective contributions of strong and weak contacts to energy dissipation. In Figure 4.14a it is observed that the energy dissipation stabilises at a constant rate when the critical state is reached. The initial void ratio and stress path have minimal influence on the energy dissipation mechanism, except for cases where samples are sheared with a constant σ_r , resulting in higher energy dissipation. Figure 4.14b shows the cumulative energy dissipation compared to the boundary work, revealing a close correspondence, particularly when the samples reach the critical state. These findings align with previous studies by El Shamy and Denissen (2012) and Hanley et al. (2018).

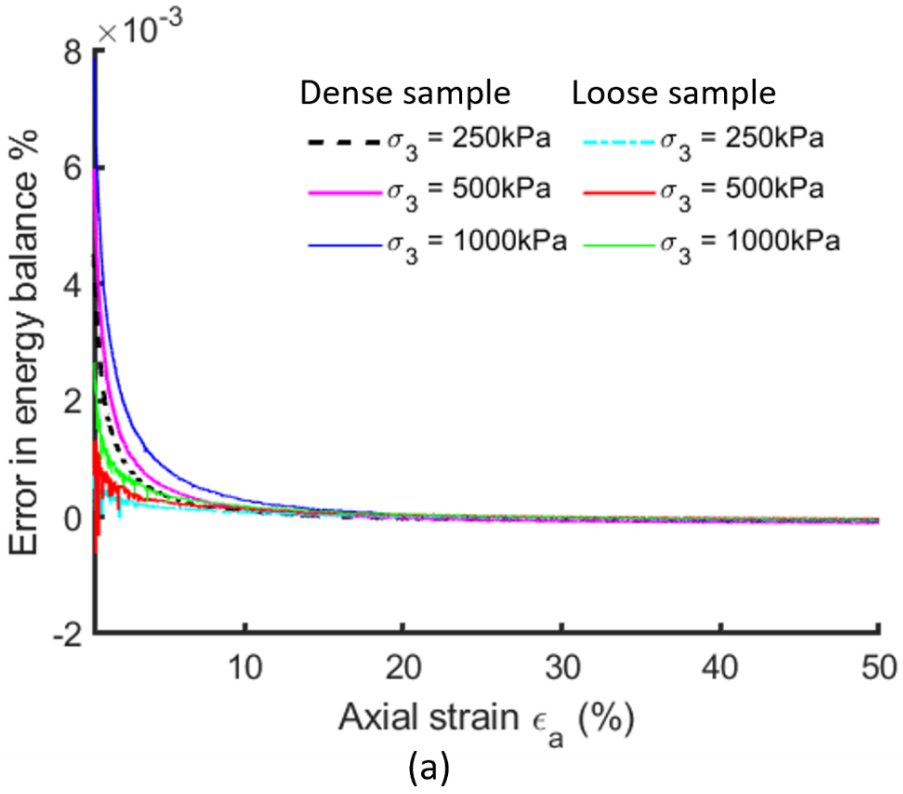

(a)

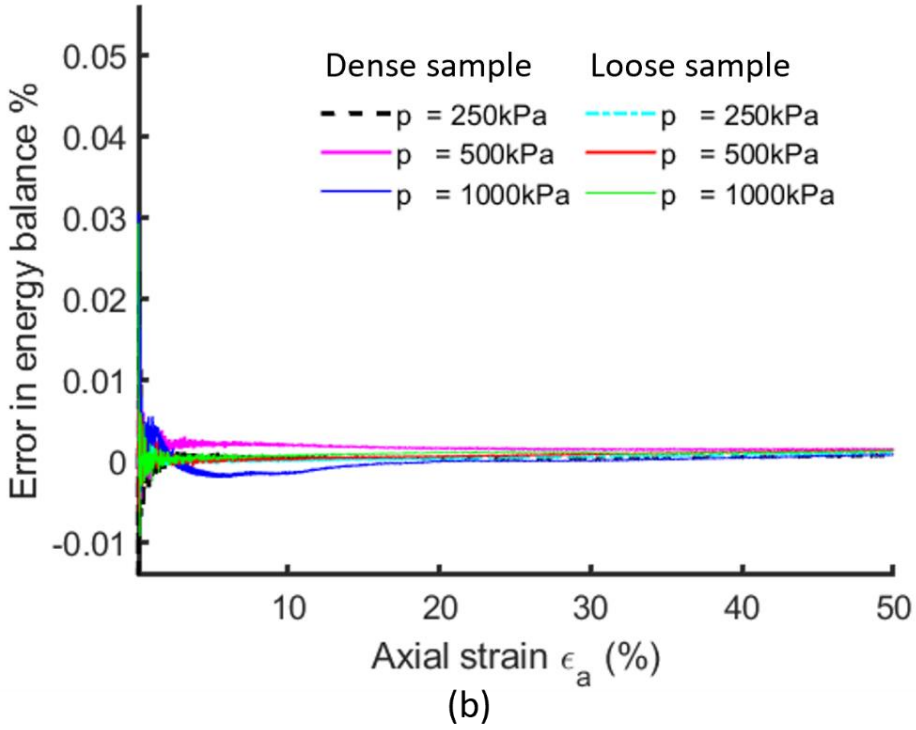

Figure 4.13 Error in energy balance as percentage of boundary work for dense and loose sand during a drained triaxial simulation test; a) constant σ_r; b) constant p.

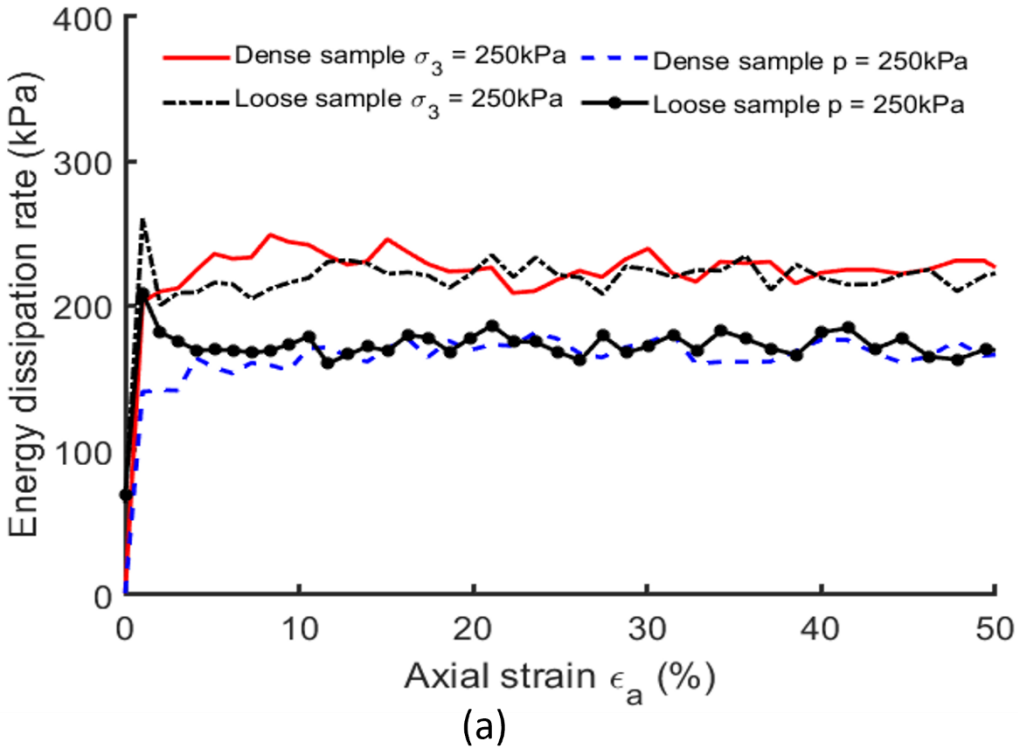

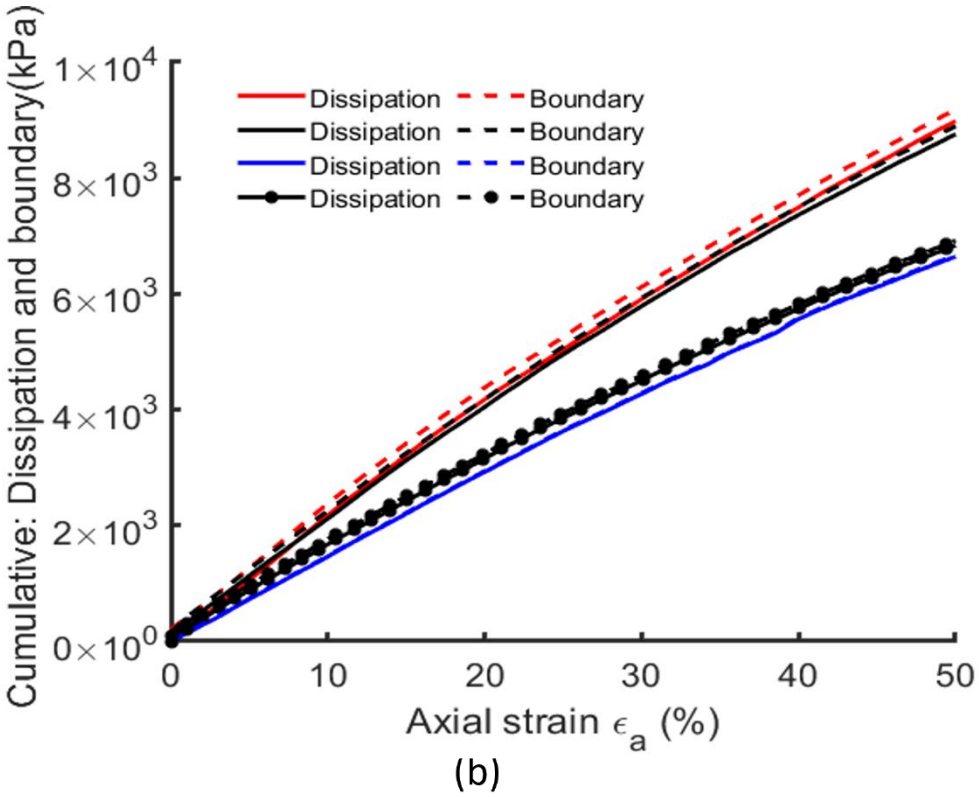

Figure 4.14 Energy dissipation during drained triaxial compression for dense and loose sand with different stress paths; a) evaluation of energy dissipation; b) cumulative energy dissipation.

4.3.3 Partitioning of contact networks

This chapter utilised two methods for partitioning contact networks. The first method is based on average normal force magnitude (Radjai et al., 1997), and the second is based on the contribution of contact networks to deviator stress (Huang et al., 2017). Though the average contact force partitioning method is widely used, it was not considered a robust method when the contribution to global deviator stress is considered for 3D modelling (Huang et al., 2017b). To illustrate this, this work examines the average contact force partitioning method based on how the contact network contributes to deviator stress.

The deviator stress is calculated from the contact force, where the stresses are obtained based on the stress tensor equation in (Bagi, 1996)

$$\sigma_{ij} = \frac{1}{V}\sum_{c=1}^{N_c} f_i^c \, l_j^c \tag{4.7}$$

where V is the volume of the domain considered f_i^c is the component of the contact force acting on the particle and l_j^c is the component of the branch vector from the centre of the contacting neighbour to the centre of the particle and N_c is the number of contacts. To determine the contribution of weak and strong networks to total deviator stress, the total average stress tensor can be decomposed into contributions from the strong $(\frac{1}{V}\sum_{c=1}^{N_c^S} f_i^s \, l_j^s)$ and weak contacts $(\frac{1}{V}\sum_{c=1}^{N_c^W} f_i^w \, l_j^w)$ in which f_i^s and f_i^w are the components of the contact force of strong and weak contacts, l_j^s and l_j^w are the components of the branch vector of strong and weak contacts, and N_c^S and N_c^w are the number of strong and weak contacts respectively.

Figure 4.15 depicts the cumulative contribution of the contact force to deviator stress as a function of the normalised contact force, where f_n is the magnitude of normal contact force and $\langle f_n \rangle$ is the average magnitude of normal contact force. The figure evaluates the contribution in several positions during the test: near peak (2%, 3% and 5% axial strain) and the critical state (30% axial strain and 50% axial strain). To generate this figure, the contacts are arranged in ascending order based on the magnitude of the normalised force. The contribution of each contact to the value of q is calculated using Equation 4.8. It is evident that the weak contacts (contact force below average) also contribute to deviator stress, with approximately half of the weak contacts contributing to the overall deviator stress which is in agreement with the findings by (Huang et al., 2017b). In addition, it can be noticed from

Figure 4.15 that approximately half the mean normal contact force $(f_n/\langle f_n \rangle = 0.5)$ gives a reasonable separation for the contact network contribution to the overall deviator stress at all strain levels. Therefore, $f_n/\langle f_n \rangle = 0.5$ is used as the second partitioning method in this study. This partitioning definition is based on the assumption that weak contacts do not contribute to deviator stress and strong contacts are responsible for carrying out all deviator stress. This method will thus be called a deviator stress partitioning method. As shown in Figure 4.16, the value of $f_n/\langle f_n \rangle = 0.5$ used for the deviator stress partitioning is valid for all the tests with different initial densities and stress paths. Therefore, the value of $f_n/\langle f_n \rangle =$

0.5 is used for partitioning the force networks based on contribution to the deviator stress in a 3D system. Figure 4.17 illustrates the contribution of the strong and weak force networks to the total deviator stress and compares both partitioning methods (Thornton and Antony, 1998). It is apparent from the figure that all deviator stress is carried by strong contacts when the deviator partition method is used, which confirms that the load will be transferred via the strong contact only. However, when the average force partition method is used it is apparent that some of the weak contacts also contribute to deviator stress. The contribution of weak and strong contact to deviator stress is analysed for loose and dense samples under 500 kPa using both partitioning approaches, as seen in Figure *4.18*. Consistent relationships are observed, indicating that the findings are independent of variable densities and confining pressure. Given this similarity, the remaining figures are included in Appendix A for reference.

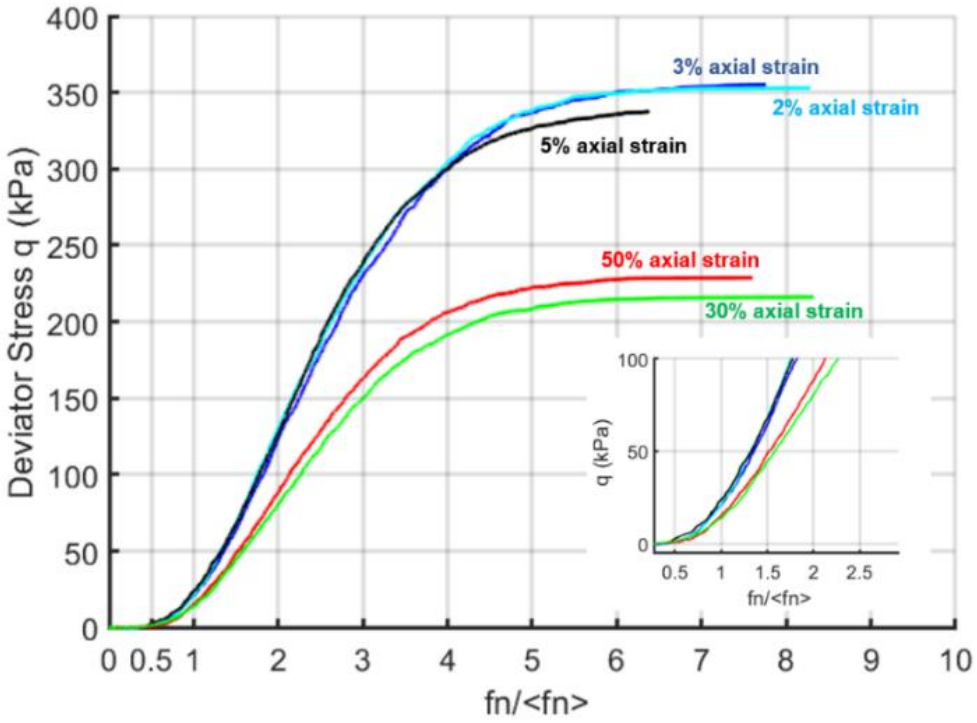

Figure 4.15 Accumulated deviator stress as a function $f_n/\langle f_n \rangle$ at peak and at the critical state.

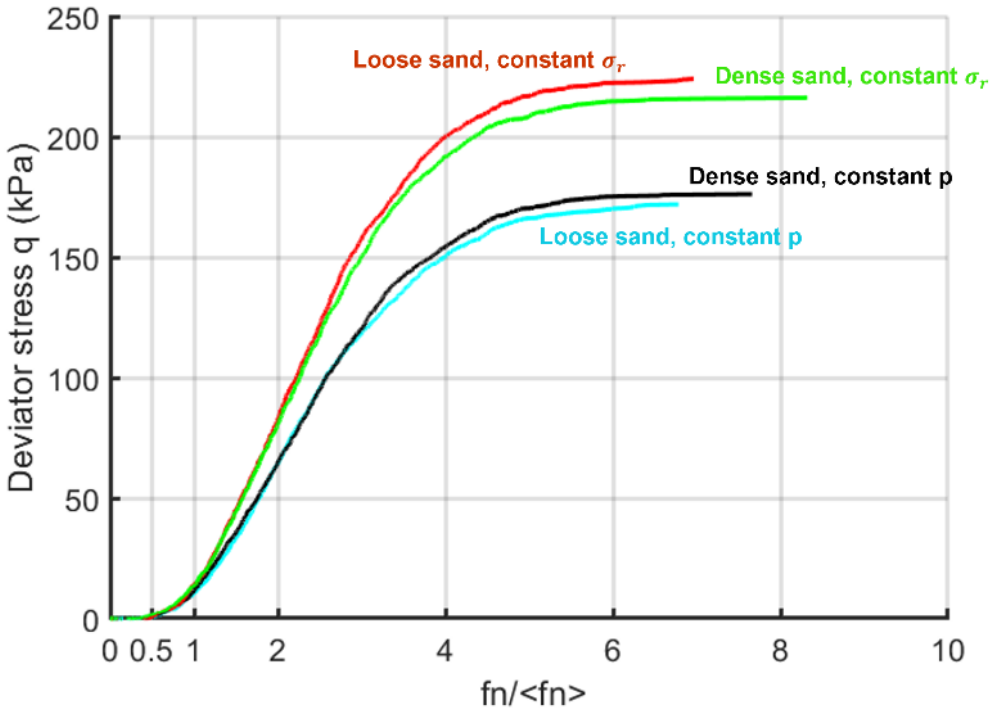

Figure 4.16 Accumulated deviator stress as a function $f_n/\langle f_n \rangle$ for different stress paths and densities at the critical state (30% axial strain).

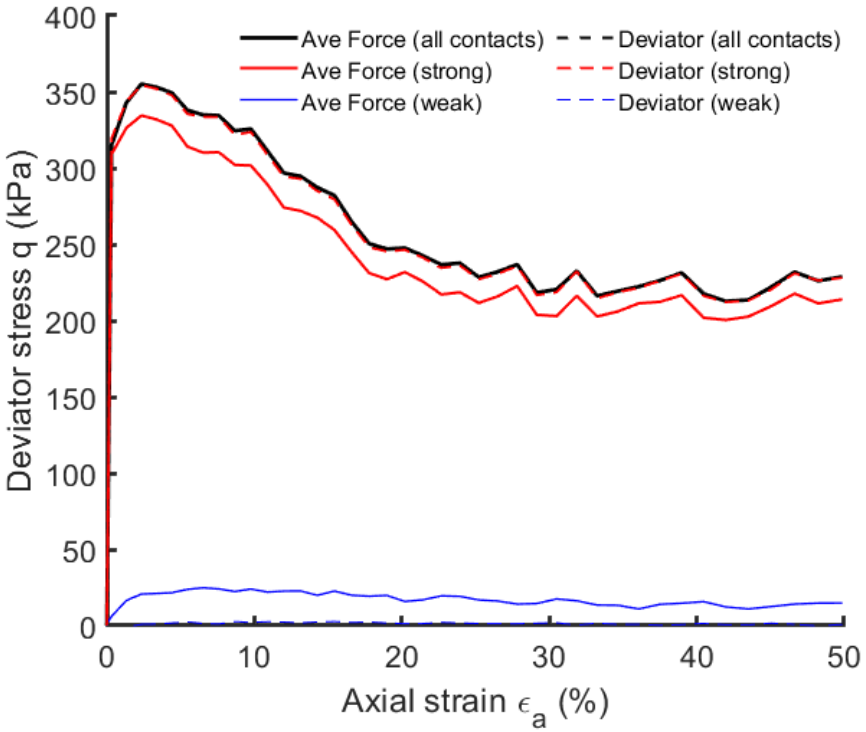

Figure 4.17 Contribution of weak and strong contact networks to the deviator stress when average force and deviator stress partitioning methods are used sheared with 250 kPa and constant σ_r.

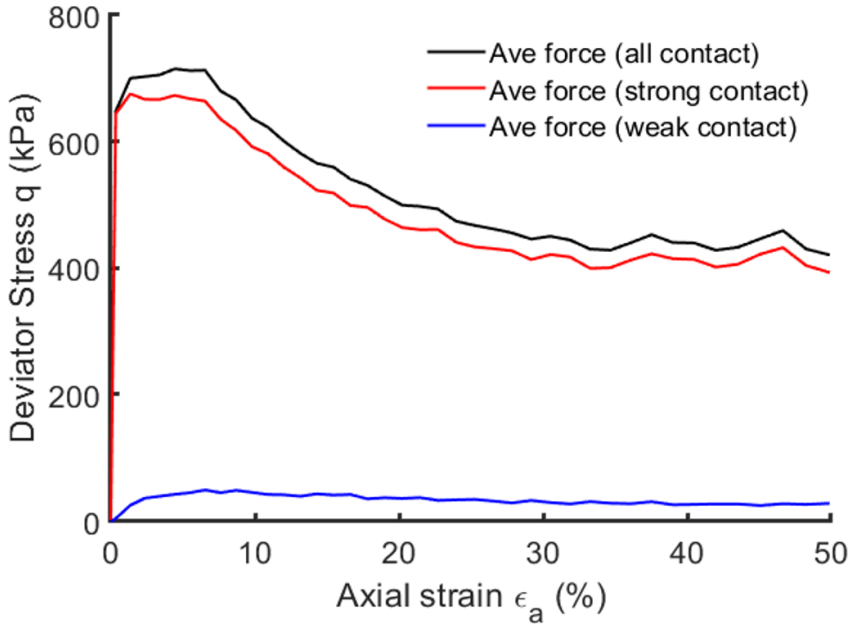
Ave force (all contact)
Ave force (strong contact)
Ave force (weak contact)
Deviator Stress q (kPa)
Axial strain ϵ_a (%)
0
200
400
600
800
0
10
20
30
40
50

(a)

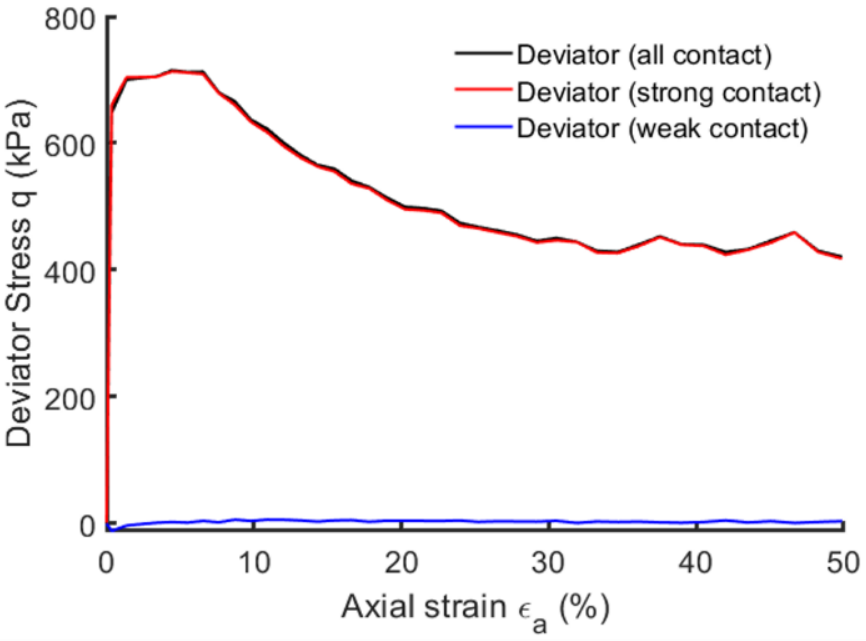
Deviator (all contact)
Deviator (strong contact)
Deviator (weak contact)
Deviator Stress q (kPa)
Axial strain ϵ_a (%)
0
200
400
600
800
0
10
20
30
40
50

(b)

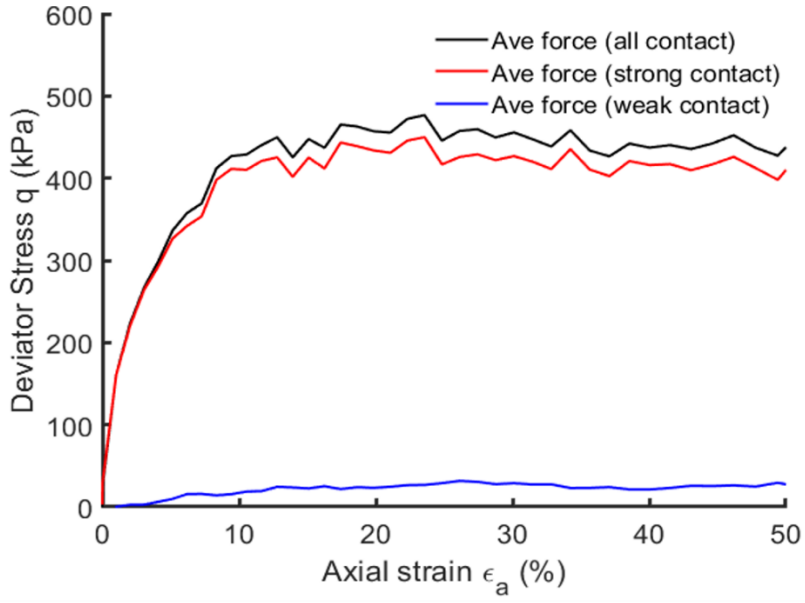

(c)

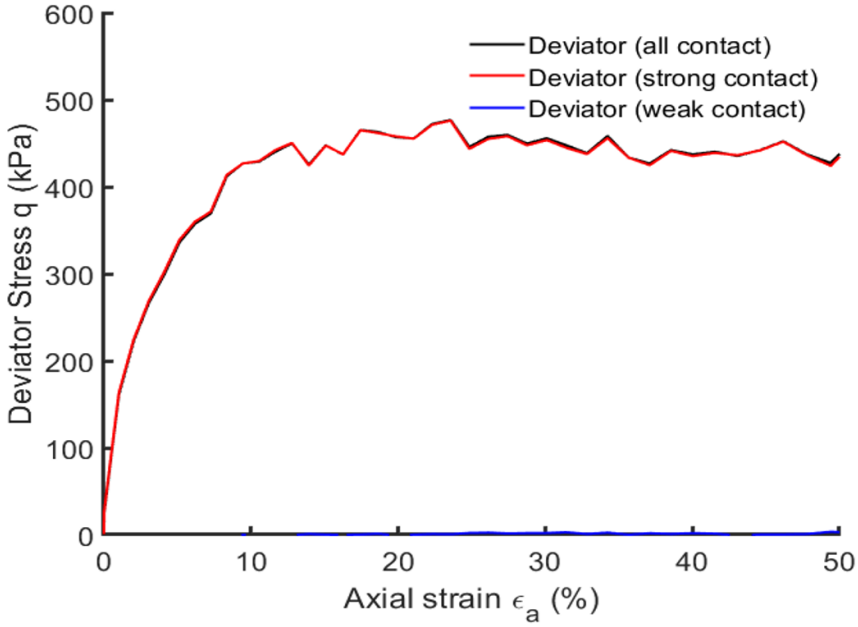

(d)

Figure 4.18 Contribution of weak and strong contact networks to the deviator stress when average force and deviator stress methods are used. Loose and dense samples sheared with 500 kPa and constant σ_r: a) dense sample average force partition, b) dense sample deviator partition, c) loose sample average force partition, d) loose sample deviator partition.

4.3.4 Relationship between contacts network and energy dissipation

To understand the relationship between energy dissipation and contact networks, results at the microscale are needed. In this study, the objective is to identify the amount of energy dissipated by each type of contact network (strong and weak) separately. Therefore, the method explained in section 4.2.1 is used here. Since all the energy is dissipated by the sliding of contact networks, it is initially convenient to assess the percentage of contacts that are sliding during the shearing process. In this study, the particles considered to be sliding if $F_t \leq |f_n|\mu$ where F_n is the normal contact force, F_t tangential force and the tolerance used for this calculation is 0.999. The contribution of strong and weak networks to the proportion of total contact sliding is illustrated in Figure 4.19 for dense samples sheared with 250 kPa and constant σ_r. The figure also compares both partitioning methods used in this study. The results reveal that the majority of sliding occurs in weak contacts, but a portion of strong contacts also exhibit sliding behaviour. This behaviour is consistent when employing both partitioning methods. However, it is noteworthy that the use of the deviator stress partitioning method leads to an increase in the proportion of sliding observed in strong contacts, from approximately 18% to around 29%. Additionally, there is an increase in the proportion of sliding observed in weak contacts, from 55% to around 65%. Previous studies have suggested that all sliding occurs in weak contacts, while non-sliding contacts are classified as strong contacts (Radjai et al., 1997). In contrast, the present study demonstrates that the sliding occurring at strong contacts is not negligible, challenging the notion that sliding is solely confined to weak contacts. Additionally, the data used to create Figure 4.19 are presented in Table 4.1 and Table *4.2* which show the total number of contacts categorised as total, weak, and strong, the total number of contacts sliding also categorised as total, weak, and strong networks, along with the corresponding percentage of sliding observed in each category. The categorisation is based on the average force and deviator stress partitioning methods. The data pertains to dense samples subjected to shearing with 250 kPa stress and constant σ_r. An observable difference is observed when utilising the deviator stress partitioning method, as it results in an increase in the number of strong contacts. Consequently, this leads to a corresponding increase in the number of sliding contacts within

the strong contacts. Furthermore, a similar relationship is observed for the proportion of sliding across various confining pressures and densities (Figure 4.20). The remaining results, encompassing different stress paths, confining pressures, and densities, are included in Appendix A, and they consistently exhibit similar behaviours.

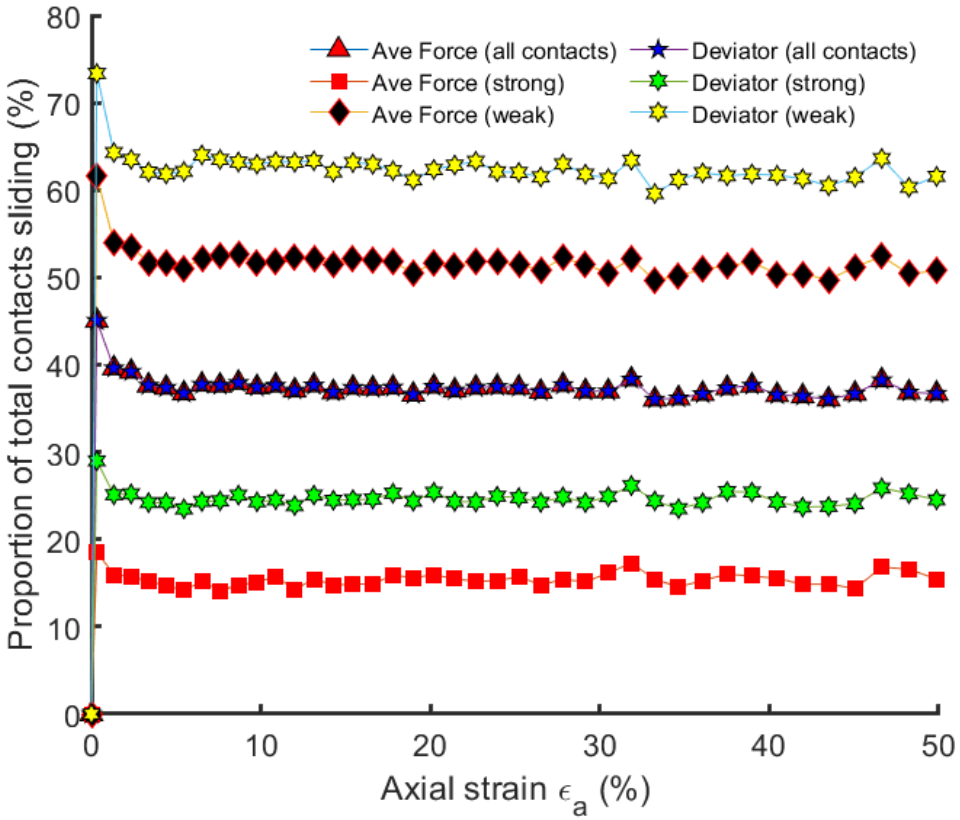

Figure 4.19 Proportion of sliding contacts for the average contact force magnitude and deviatoric partitioning methods for dense samples sheared with 250 kPa and constant σ_r.

Table 4.1 The distribution of contacts categorised as total, weak, and strong, along with the corresponding percentage of sliding observed in each category divided based on the average force partitioning method, for dense samples sheared with 250 kPa and constant σ_r.

Axial strain %	Number of total contacts	Number of weak contacts	Number of strong contacts	Number of total contacts sliding	Number of weak contacts sliding	Number of strong contacts sliding	Total contacts sliding %	Weak contacts sliding %	Strong contacts sliding %
1%	20503	12596	7907	9233	7763	1470	45	62	19
2%	18869	11747	7122	7473	6337	1136	40	54	16
3%	18754	11646	7108	7353	6233	1120	39	54	16
4%	18560	11406	7154	6984	5899	1085	38	52	15
5%	18622	11428	7194	6958	5898	1060	37	52	15
6%	18628	11393	7235	6841	5817	1024	37	51	14
7%	18639	11380	7259	7031	5929	1102	38	52	15
8%	18703	11458	7245	7037	6015	1022	38	52	14
9%	18823	11526	7297	7140	6060	1080	38	53	15
10%	18704	11436	7268	7000	5905	1095	37	52	15
11%	18789	11392	7397	7070	5903	1167	38	52	16
12%	18676	11215	7461	6921	5857	1064	37	52	14
13%	18643	11265	7378	7016	5875	1141	38	52	15

14%	18526	11130	7396	6826	5733	1093	37	52	15
15%	18593	11232	7361	6948	5854	1094	37	52	15
16%	18570	11229	7341	6924	5830	1094	37	52	15
17%	18502	11090	7412	6918	5738	1180	37	52	16
18%	18590	11168	7422	6800	5642	1158	37	51	16
19%	18736	11299	7437	7024	5838	1186	37	52	16
20%	18658	11204	7454	6913	5758	1155	37	51	15
21%	18638	11297	7341	6967	5853	1114	37	52	15
22%	18672	11362	7310	6999	5882	1117	37	52	15
23%	18516	11198	7318	6920	5770	1150	37	52	16
24%	18481	11358	7123	6821	5767	1054	37	51	15
25%	18551	11216	7335	6990	5859	1131	38	52	15
26%	18393	11062	7331	6799	5689	1110	37	51	15
27%	18467	11168	7299	6823	5644	1179	37	51	16
28%	18654	11259	7395	7148	5871	1277	38	52	17
29%	18483	11126	7357	6659	5524	1135	36	50	15
30%	18480	11200	7280	6684	5624	1060	36	50	15

31%	18497	11099	7398	6781	5650	1131	37	51	15
32%	18464	11143	7321	6893	5720	1173	37	51	16
33%	18601	11292	7309	6998	5843	1155	38	52	16
34%	18437	11117	7320	6737	5600	1137	37	50	16
35%	18510	11216	7294	6736	5652	1084	36	50	15
36%	18461	11213	7248	6654	5576	1078	36	50	15
37%	18372	11138	7234	6740	5700	1040	37	51	14
38%	18461	11107	7354	7058	5821	1237	38	52	17
39%	18368	11000	7368	6766	5544	1222	37	50	17
40%	18473	11111	7362	6778	5640	1138	37	51	15

Table 4.2 The distribution of contacts categorised as total, weak, and strong, along with the corresponding percentage of sliding observed in each category divided based on the deviator stress partitioning method, for dense samples sheared with 250 kPa and constant σ_r.

Axial strain %	Number of total contacts	Number of weak contacts	Number of strong contacts	Number of total contacts sliding	Number of weak contacts sliding	Number of strong contacts sliding	Total contacts sliding %	Weak contacts sliding %	Strong contacts sliding %
1%	20503	7414	13089	9233	5438	3795	45	73	29
2%	18869	6982	11887	7473	4489	2984	40	64	25
3%	18754	6855	11899	7353	4353	3000	39	64	25
4%	18560	6579	11981	6984	4083	2901	38	62	24
5%	18622	6512	12110	6958	4027	2931	37	62	24
6%	18628	6379	12249	6841	3963	2878	37	62	23
7%	18639	6286	12353	7031	4024	3007	38	64	24
8%	18703	6323	12380	7037	4015	3022	38	63	24
9%	18823	6351	12472	7140	4014	3126	38	63	25
10%	18704	6354	12350	7000	4000	3000	37	63	24
11%	18789	6354	12435	7070	4020	3050	38	63	25
12%	18676	6266	12410	6921	3959	2962	37	63	24
13%	18643	6120	12523	7016	3877	3139	38	63	25

14%	18526	6092	12434	6826	3782	3044	37	62	24
15%	18593	6174	12419	6948	3899	3049	37	63	25
16%	18570	6136	12434	6924	3863	3061	37	63	25
17%	18502	6066	12436	6918	3774	3144	37	62	25
18%	18590	6172	12418	6800	3774	3026	37	61	24
19%	18736	6130	12606	7024	3822	3202	37	62	25
20%	18658	6159	12499	6913	3871	3042	37	63	24
21%	18638	6260	12378	6967	3962	3005	37	63	24
22%	18672	6306	12366	6999	3915	3084	37	62	25
23%	18516	6263	12253	6920	3884	3036	37	62	25
24%	18481	6285	12196	6821	3865	2956	37	61	24
25%	18551	6236	12315	6990	3928	3062	38	63	25
26%	18393	6236	12157	6799	3855	2944	37	62	24
27%	18467	6111	12356	6823	3747	3076	37	61	25
28%	18654	6090	12564	7148	3862	3286	38	63	26
29%	18483	6104	12379	6659	3638	3021	36	60	24
30%	18480	6205	12275	6684	3798	2886	36	61	24

31%	18497	6101	12396	6781	3781	3000	37	62	24
32%	18464	6054	12410	6893	3731	3162	37	62	25
33%	18601	6236	12365	6998	3856	3142	38	62	25
34%	18437	6041	12396	6737	3727	3010	37	62	24
35%	18510	6247	12263	6736	3829	2907	36	61	24
36%	18461	6170	12291	6654	3732	2922	36	60	24
37%	18372	6192	12180	6740	3806	2934	37	61	24
38%	18461	6045	12416	7058	3845	3213	38	64	26
39%	18368	6074	12294	6766	3663	3103	37	60	25
40%	18473	6067	12406	6778	3735	3043	37	62	25

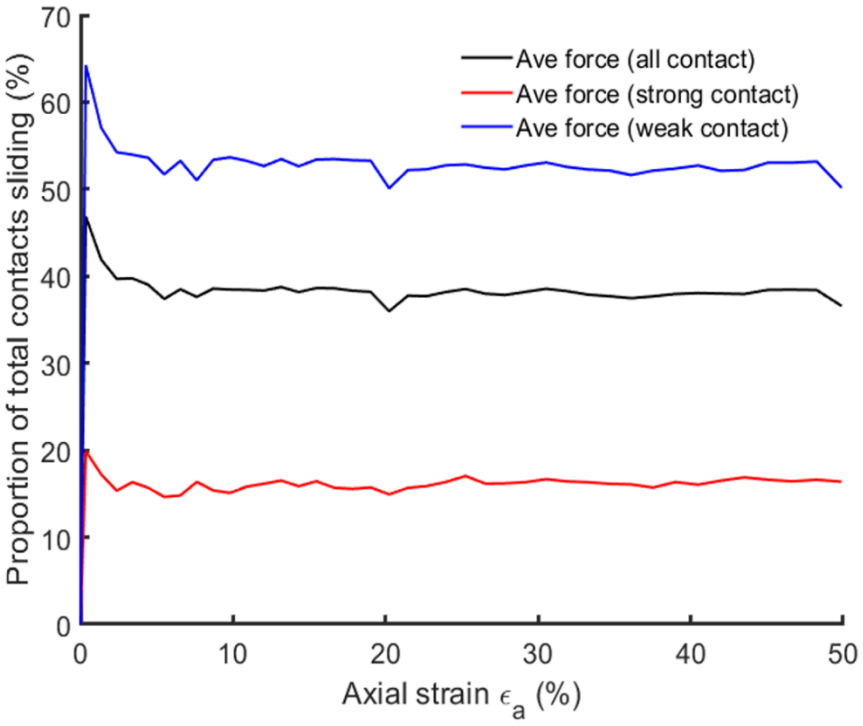
Ave force (all contact)
Ave force (strong contact)
Ave force (weak contact)
Proportion of total contacts sliding (%)
Axial strain ϵ_a (%)
0
10
20
30
40
50
60
70

(a)

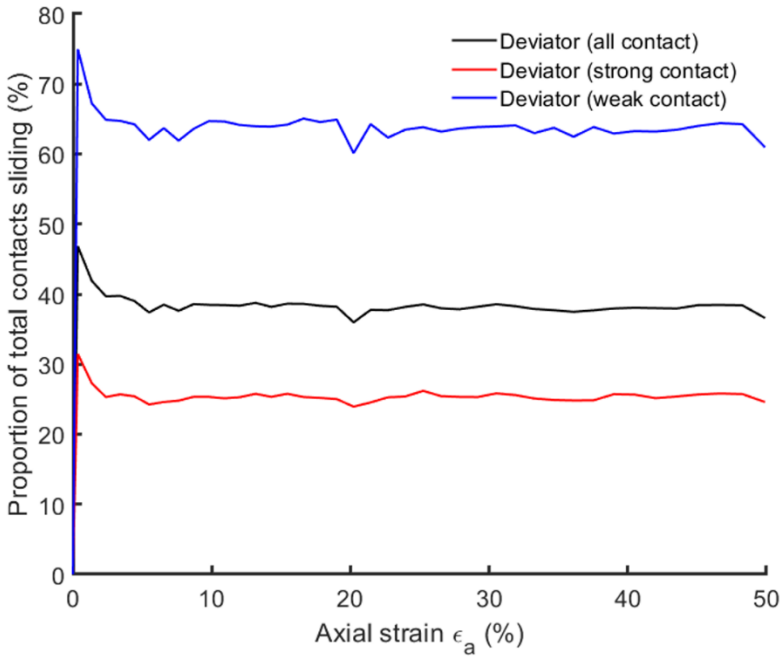
Deviator (all contact)
Deviator (strong contact)
Deviator (weak contact)
Proportion of total contacts sliding (%)
Axial strain ϵ_a (%)
0
10
20
30
40
50
60
70
80

(b)

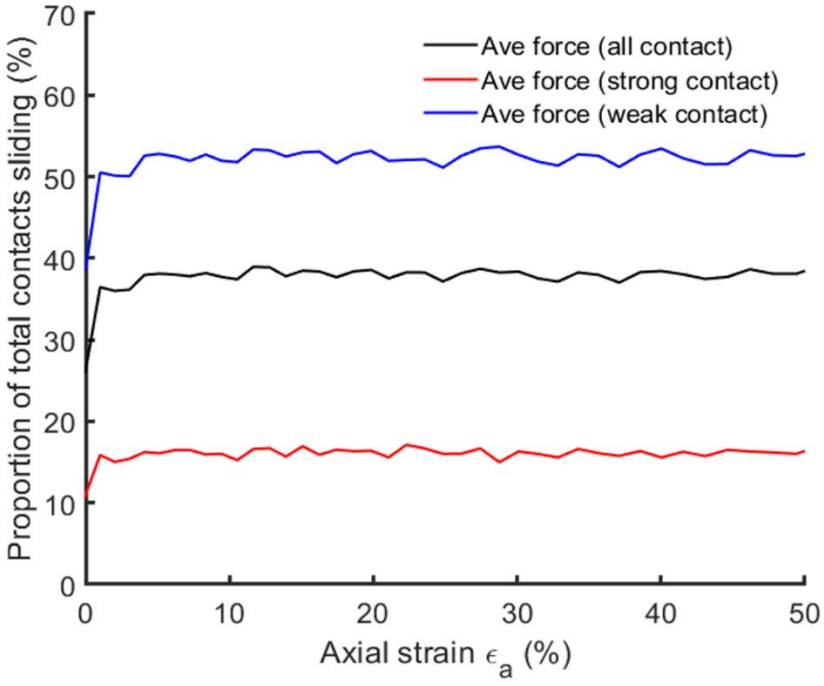

(c)

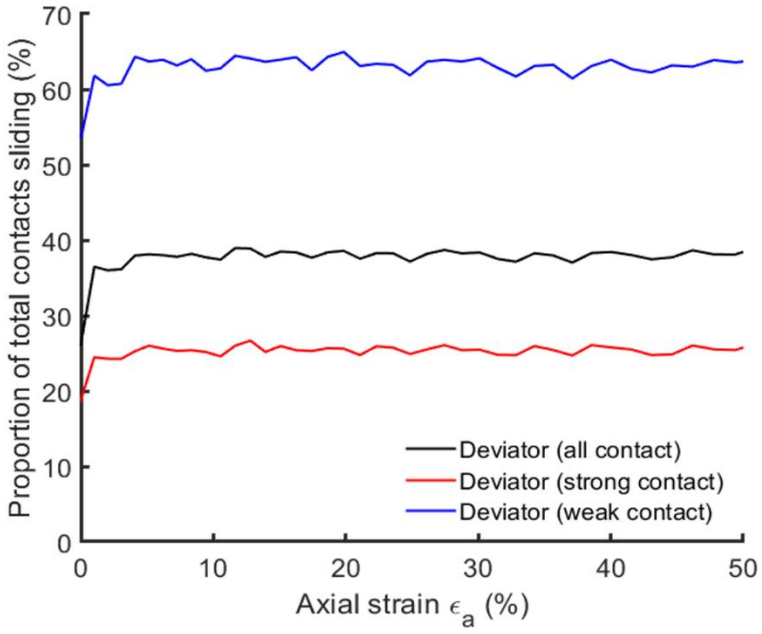

(d)

Figure 4.20 Proportion of sliding contacts when average force and deviator stress methods are used. Loose and dense samples sheared with 500 kPa and constant σ_r : a) dense sample average force partition, b) dense sample deviator partition, c) loose sample average force partition, d) loose sample deviator partition.

Energy dissipation was traced for both the strong and weak contact networks separately. As depicted in Figure 4.23, the contribution of the strong and weak contacts to the total energy dissipation was analysed using the average force partitioning method. Notably, around 70% of the dissipation occurs in weak contacts, with the remaining 30% in strong contacts. The results highlight that the dissipation in strong contacts is not negligible, indicating that the strong contacts dissipate more energy per sliding contact network. To provide further insight, Figure *4.22* shows the dissipation per sliding contact network at various locations during the simulation. The results demonstrate that strong networks dissipate approximately two times more energy per sliding contact network compared to weak contact networks. However, when the deviator stress partitioning method is used, the relationship appears differently, Figure 4.23 shows that the energy dissipation occurs more in the strong contact with approximately 65%, while the weak contact is approximately 35%.

Table 4.3 shows the split of energy dissipation at different strain levels for a dense sample. Note that the portion of sliding contacts is calculated with reference to a specific contact network (e.g., strong or weak). Contribution to energy dissipation is defined as the ratio of energy dissipation in a contact network and the total dissipation in the sample. The examination is specifically located before and after the critical state at 2%,3%,5%,30% and 50% axial strain. The table shows that although strong contact sliding was around 15% when the average force partitioning method was used, this caused around 30% of total energy dissipation. Around 53% of weak contacts slide when applying the average force partitioning method, causing around 70% of the total energy dissipation. Using the deviator stress partitioning method leads to an increase in the proportions of strong contacts sliding to around 25%, which results in their contribution to energy dissipation being around 65% of the total dissipation.

Additionally, using deviator stress partitioning increased the proportion of sliding in weak contacts significantly. However, the contribution of weak contacts to energy dissipation decreased to around 35%. The results show that the relationship between energy dissipation and contact networks is not influenced only by the number of sliding contacts but also by how much force each contact network carries. When the normal and tangential components of contact force in a strong contact network are large, the dissipation during sliding becomes

greater. The remaining results, encompassing different stress paths, confining pressures, and densities, are included in Appendix A, and they consistently exhibit similar behaviours.

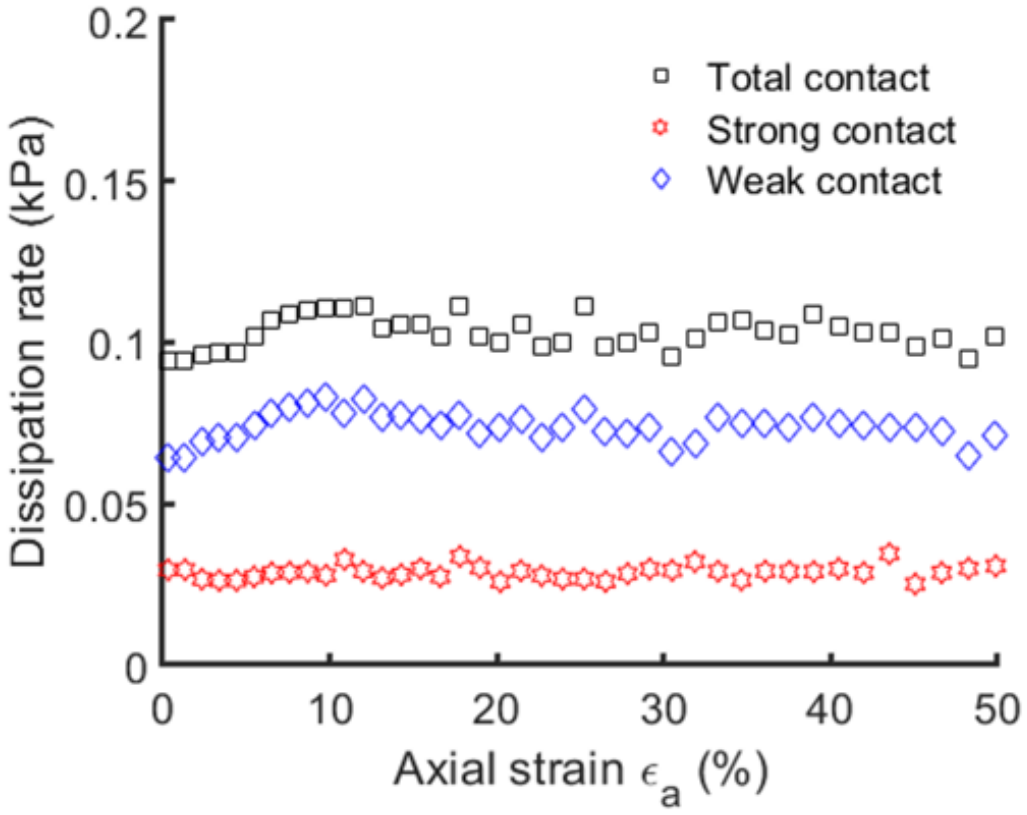

Figure 4.21 Contribution of weak and strong networks to the energy dissipation based on average force partition from probe test for dense sample sheared with constant σ_r. (σ_3 = 250 kPa).

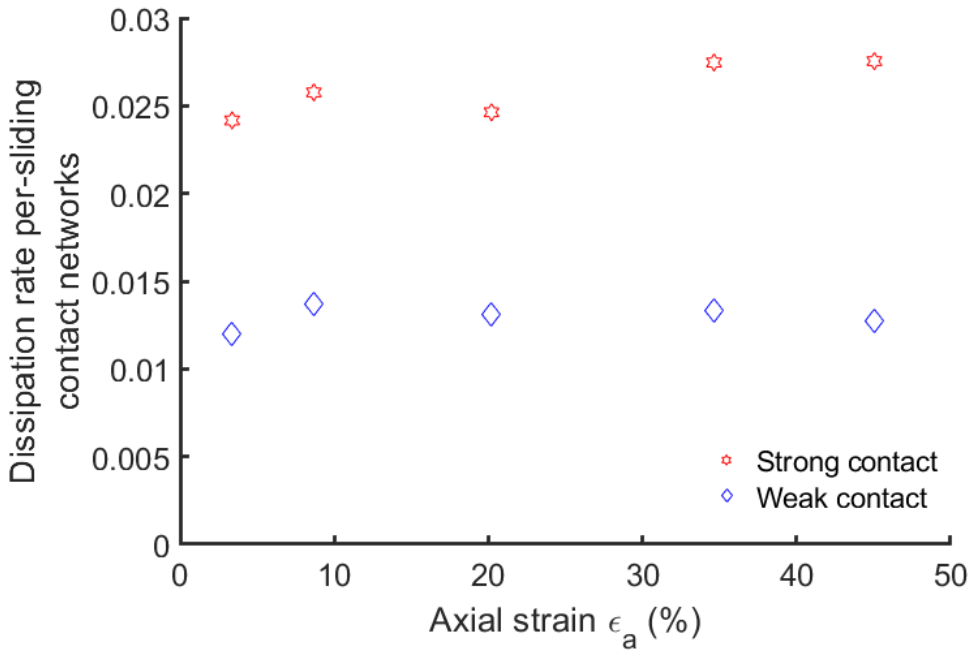

Figure 4.22 Dissipation rate per-sliding contact networks for dense sample sheared with constant σ_r (σ_3 = 250 kPa) and using average force partitioning method.

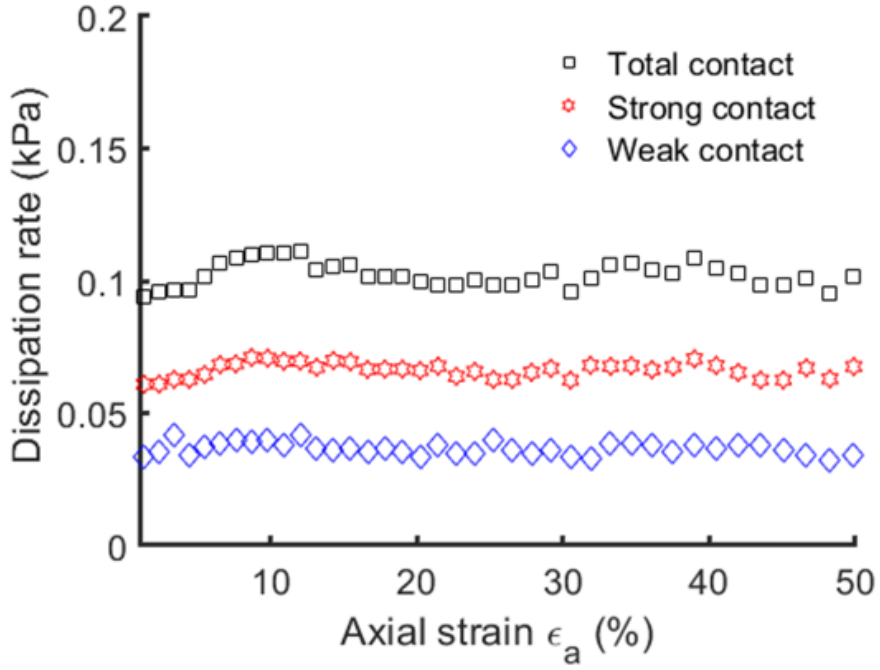

Figure 4.23 Contribution of weak and strong networks to the energy dissipation from probe test for dense sample sheared with constant σ_r (σ_3 = 250 kPa); a) average force partition; b) deviator stress partition.

Table 4.3 The percentage contribution of weak and strong networks to the energy dissipation and sliding from probe test for dense sample sheared with constant σ_r (σ_3 = 250 kPa) using the average force and deviatoric partitioning methods.

Axial strain %	Average force partitioning				Deviator stress partitioning			
	Portion of sliding contacts (%)		Contribution to total energy dissipation (%)		Portion of sliding contacts (%)		Contribution to total energy dissipation (%)	
	Strong	Weak	Strong	Weak	Strong	Weak	Strong	Weak
2	19	62	29	71	29	73	64	36
3	16	54	26	74	25	64	63	37
5	15	52	27	73	24	62	62	38
30	15	50	29	71	24	60	66	34
50	15	51	28	72	25	62	64	36

The presence of substantial energy dissipation is apparent in both the strong and weak networks when employing both partitioning methods. This observation underscores the significance of exploring energy dissipation in contact networks according to their normal force magnitude. To examine this, it is convenient to begin by examining the distribution of the contacts network based on $f_n/\langle f_n \rangle$. Figure *4.24* shows the distribution of contact forces at the critical state using the probability density function PDF. Though there is an exponential decay after the peak, the number of contacts with $f_n/\langle f_n \rangle$ between 1 and 3 is not negligible. Figure 4.25 shows the energy dissipation per contact network for contacts with different ranges of $f_n/\langle f_n \rangle$ near peak (5% axial strain) and critical state (30% axial strain). To create these figures, the contact networks are arranged in ascending order according to the magnitude of the normalised normal force $f_n/\langle f_n \rangle$. Then, the networks are grouped based on different ranges of the magnitude of the normalised normal force $f_n/\langle f_n \rangle$. The energy dissipation is summed up for each contact group. It is worth noting that the unit used to present these results is Joule, as it specifically describes the energy dissipation at a specific location during the simulation. It is evident that the energy dissipation rate is much higher when $f_n/\langle f_n \rangle \leq 2$.

Figure 4.26 depicts the cumulative energy dissipation for several contact groups throughout the simulation. Similar results to are found, with the majority of energy dissipation occurring at the contact $f_n/\langle f_n \rangle \leq 2$. Furthermore, Table 3 shows the portion of sliding contacts and energy dissipation for contacts with $f_n/\langle f_n \rangle \leq 2$ and $f_n/\langle f_n \rangle > 2$. It can be seen that the

majority of energy dissipation (>93%) occurs in contact with $f_n/\langle f_n \rangle \leq 2$. The primary reason is that the portion of sliding contacts is much higher when $f_n/\langle f_n \rangle \leq 2$ (Table 3).

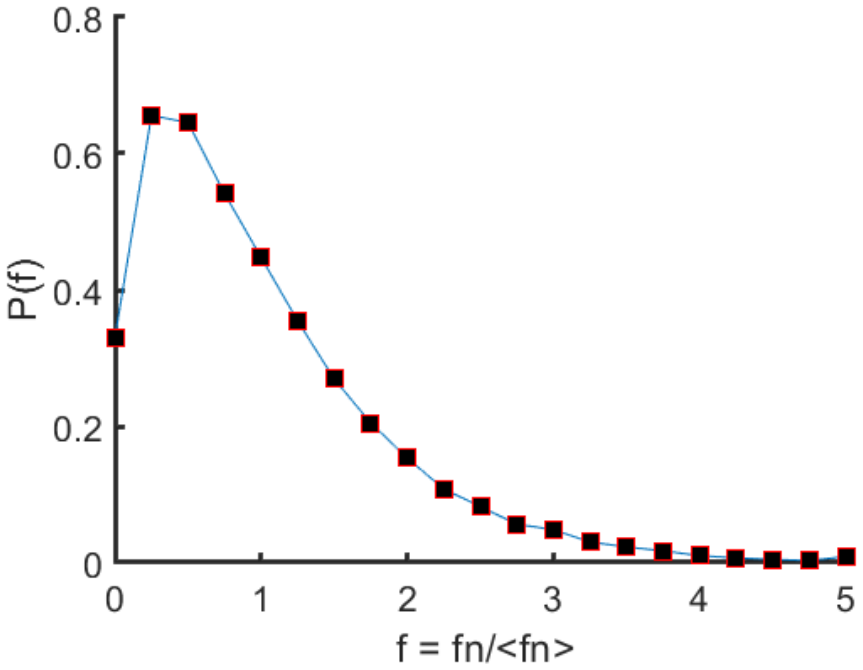

Figure 4.24 The distribution of contact forces at the critical state.

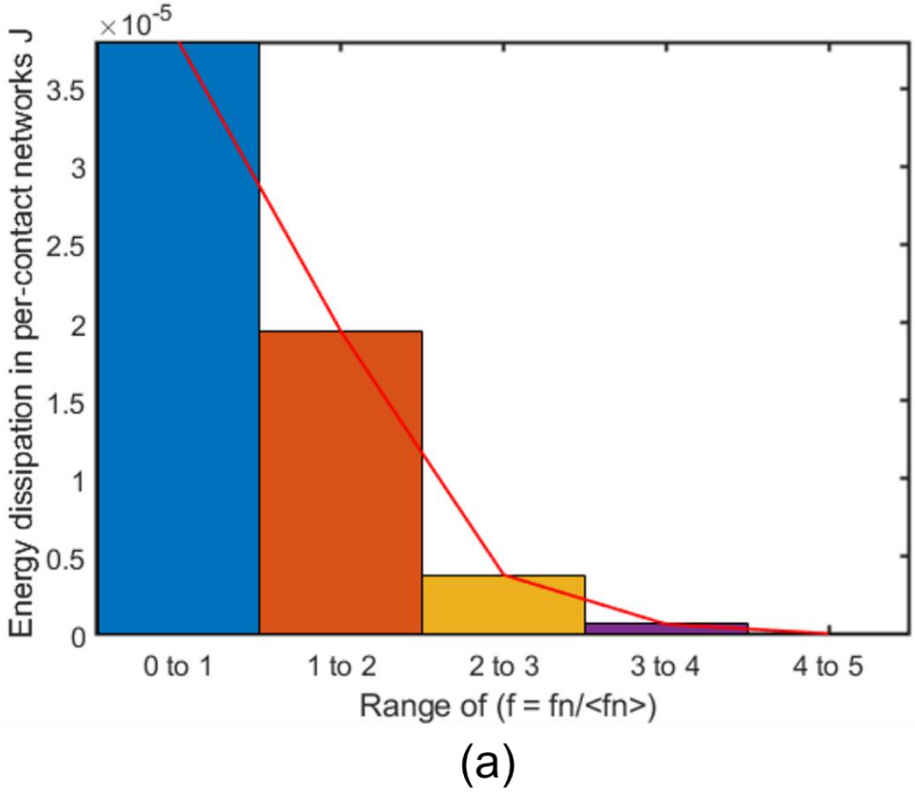

(a)

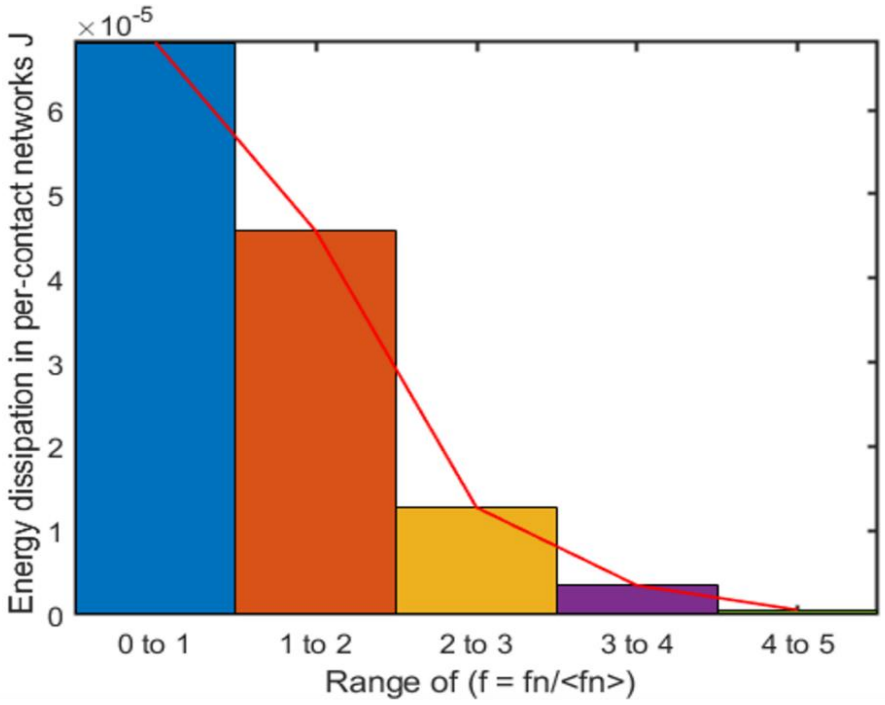

(b)

Figure 4.25 Energy dissipation per-contact networks at different contact groups: a) peak (5% axial strain); b) critical state (30% axial strain).

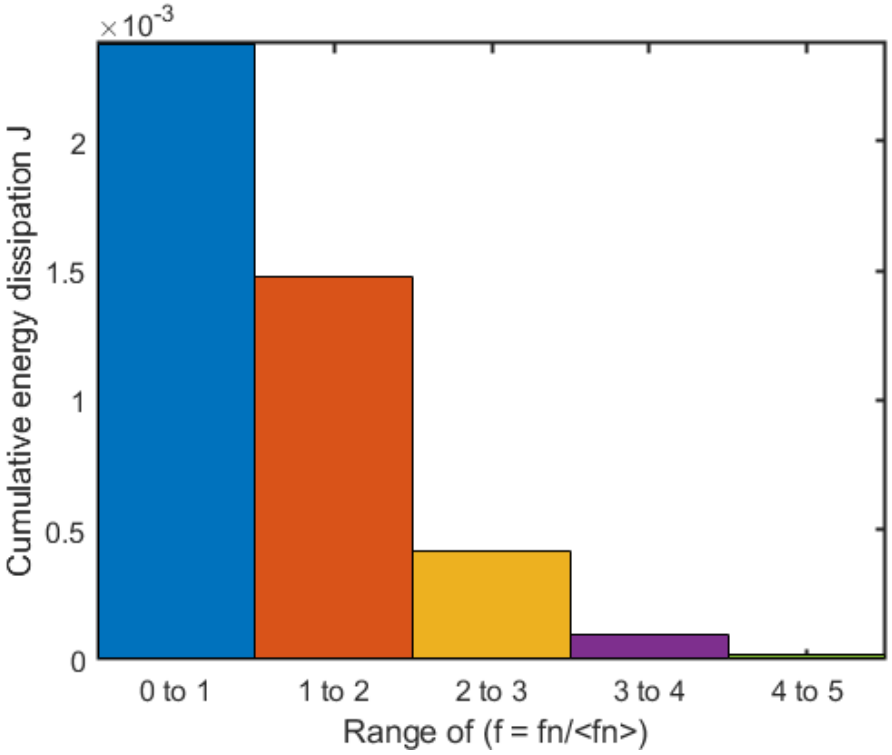

Figure 4.26 Cumulative energy dissipation per-contact networks at different contact groups.

Table 4.4 Sliding and energy dissipation in contacts with different normal contact forces (dense sample with constant σ_r of 250 kPa)

Axial strain %	Portion of sliding contacts (%)		Contribution to total energy dissipation (%)	
	$f_n/\langle f_n\rangle > 2$	$f_n/\langle f_n\rangle \leq 2$	$f_n/\langle f_n\rangle > 2$	$f_n/\langle f_n\rangle \leq 2$
5	5	42	4	96
30	5	40	8	92
50	5	40	7	93

4.4 Conclusion

In this study, a DEM-based investigation is conducted to investigate the mechanism of energy dissipation in granular materials. The relationship between contact networks and energy dissipation is investigated for dense and loose sand in drained triaxial compression with different stress paths.

- Two partitioning methods for the contact force networks were used. The first partition method is based on the contact force magnitude and the second is based on the contribution to global deviator stress.
- When the average contact force partitioning method is used, more interparticle sliding and energy dissipation occur in the weak networks. However, the strong contact network has a two times higher energy dissipation per sliding contact due to higher contact forces.
- When the deviator stress partitioning method is used the sliding still occurs more in the weak contact. Nonetheless, there has been a slight increase in the proportion of strong contact sliding compared to the average contact force partitioning results. This increase of sliding in strong contacts has led to more energy dissipation in the strong contacts.
- It is observed that the energy dissipation that occurs in both strong and weak contacts is not negligible when both partitioning methods are used. Therefore, A new threshold of $f_n/\langle f_n\rangle$ for partitioning the contact network has been identified. Specifically, $f_n/\langle f_n\rangle = 2$ can be used to determine if the contact contributes to energy dissipation. Over 93% of the total energy dissipation occurs in contact with $f_n/\langle f_n\rangle \leq 2$.

The results of this study confirm that both the proportion of sliding contacts and the magnitude of tangential contact force between particles play a significant role in the relationship between contact networks and energy dissipation. For simplicity, this work has used only a uniform particle size distribution. Mukwiri et al. (2016) demonstrated that particle size distribution influences the total amount of energy dissipation. It is expected that the particle size distribution does not have a significant influence on the conclusions of this study.

Chapter 5: Stored plastic work and energy dissipation in granular materials

5.1 Introduction

In granular materials, the concept of stored plastic work has emerged as a significant and interesting aspect. Granular materials, such as sand, exhibit complex behaviours that are essential to understand in various engineering and geotechnical applications. The distinction between plastic work and energy dissipation in such materials has been a subject of theoretical analysis and investigation(Collins, 2005, Collins and Houlsby, 1997, Collins and Kelly, 2002, Collins and Hilder, 2002, Houlsby, 1981). The stored plastic work refers to a phenomenon in which the plastic work during plastic deformation is not completely dissipated by interparticle friction; rather, a portion of it is stored in the system. This conserved energy can play an important role in the mechanical behaviour and development of constitutive models for granular materials. Despite the fact that several works have highlighted the significance of stored plastic work, there is still a lot to explore about this concept.

The main objective of this chapter is to investigate the evolution of stored plastic work and energy dissipation in granular materials using 3D DEM simulation. The investigation will be carried out using different particle size distributions and drained triaxial compression tests. To calculate both the plastic work and the stored plastic work the elastic stiffness of the samples will be measured.

5.2 Theoretical and computational formulations

The basic energy equation is expressed as

$$\delta W = \delta W^e + \delta W^p = \delta \Psi + \delta \Phi \tag{5.1}$$

where δW is the incremental applied work, δW^e is the increment elastic work, δW^p is the increment plastic work, $\delta \Psi$ is the free energy, which describes the energy stored in the

representative elementary volume (REV) and can be recovered; and $\delta\Phi$ is the increment of energy dissipation in the system. Based on the second law of thermodynamics $\delta\Phi$ must always be positive, whereas the $\delta\Psi$ is not restricted by a sign which can be either positive or negative. In the past, it was assumed that free energy is equal to elastic work, which is very small and is often ignored ($\delta W^e = \delta\Psi$). This means that the entire work in the system dissipates, and for this reason, Equation (5.1) becomes as:

$$\delta W^p = \delta\Phi \tag{5.2}$$

As noted by Collins (2005) if this assumption is employed, modelling unloading conditions will be difficult. This is due to the increment of the plastic work and energy dissipation becoming negative during unloading, which violates the second law of thermodynamics. This problem can be solved if the formulation of the free energy depends on both elastic and plastic strains (Collins, 2002, Collins, 2005, Collins and Houlsby, 1997).

$$\Psi\left(\varepsilon_{ij}^e,\ \varepsilon_{ij}^p\right) = \Psi^e\left(\varepsilon_{ij}^e\right) + \Psi^p\left(\varepsilon_{ij}^p\right) \tag{5.3}$$

where $\Psi\left(\varepsilon_{ij}^e,\ \varepsilon_{ij}^p\right)$ is the total free energy, $\Psi^e\left(\varepsilon_{ij}^e\right)$ is the elastic part of the free energy, and $\Psi^p\left(\varepsilon_{ij}^p\right)$ is the plastic part of the free energy. In addition, the basic work equation can be rewritten also as follow.

$$\delta W = \delta W^e + \delta W^p = \delta\Psi^e + \delta\Psi^p + \delta\Phi \tag{5.4}$$

If the elastic contribution is cancelled from both sides of the equation. The plastic work equation can be rewritten as follow.

$$\delta W^p = \delta\Psi^p + \delta\Phi \tag{5.5}$$

5.3 Conceptual explanation of the stored plastic work

The mechanism of energy dissipation and stored plastic work has been explained in previous studies (e.g., Collins, 2005). Figure *5.1* shows a 1D example for illustrating this, which consists of a spring and slider. The model is commonly used in granular media (Collins, 2005, Iwan, 1967, Puzrin and Houlsby, 2001). This model can be used to simulate elastic perfectly plastic

stress-strain behaviour which consists of two parts. The first contains one spring, which represents the elastic deformation. The second contains a spring and slider, which represents the plastic deformation. During loading before the load reaches the value that moves the slider, the behaviour is linearly elastic, and only spring A is affected. At this stage, there will be some elastic energy stored in spring A which is represented as

$$\Psi_A = \frac{1}{2} K_A (\varepsilon^e)^2 \tag{5.6}$$

where Ψ_A is the energy stored in spring A, K_A is the stiffness of spring A, and ε^e is the amount of deformation that occurs in spring A. As soon as the load is removed, the spring will return to its original position, releasing all the elastic energy that was stored. However, if the model is loaded until spring B and the slider gets into action. In this stage, both elastic and plastic strains will occur, as well as energy is stored in springs A and B and energy dissipate as the block slides. The total energy in the model can be represented as

$$W = \frac{1}{2} K_A (\varepsilon^e)^2 + \frac{1}{2} K_B (\varepsilon^p)^2 + F_k \Delta s \tag{5.7}$$

where K_B is the stiffness of spring B, ε^p is the amount of deformation that occurs in spring B, F_k friction force due to the movement of the slider and Δs is the amount of displacement of the slider. The second part of Equation (5.7) represents the amount of energy stored in spring B, whereas the last part of Equation (5.7) represents the energy dissipation due to the movement of the slider. When the load is removed, spring A will return to its initial state in which both the elastic strain and the elastic stored energy are recovered. However, in the second part of the model, the slider will prevent spring B from returning to its initial position. Therefore, the remaining energy in the system is the total plastic energy, represented as

$$W^p = \frac{1}{2} K_B (\varepsilon^p)^2 + F_k \Delta s \tag{5.8}$$

The two parts in Equation (5.8) represent the stored plastic work in spring B and the energy dissipation caused by the movement of the slider, which is similar to Equation (5.5). In order for this energy to be released, the load must be reversed, which will return the slider to its original position and let the spring release its stored energy. In summary, the elastic and

plastic parts of the free energy differ significantly which the elastic part is released during unloading, whereas the plastic part needs reverse loading to be released.

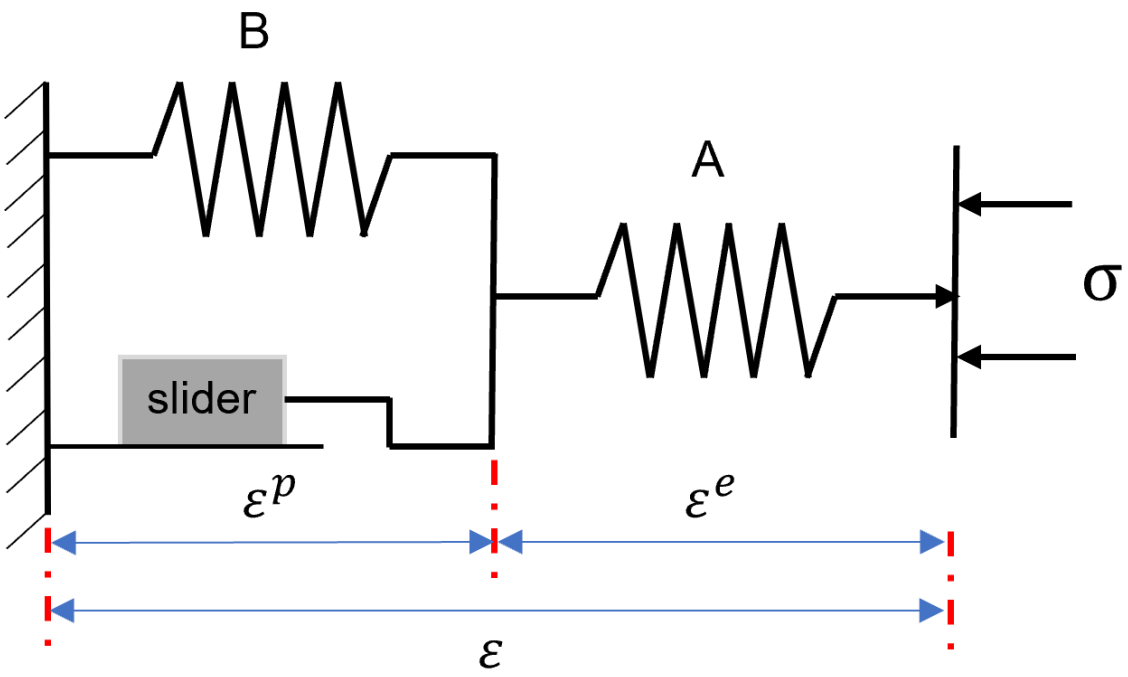

Figure 5.1 Spring and slider model representing a deformation in REV, also showing plastic work storage during plastic deformation.

The plastic work stored within granular materials is associated with the particles that are trapped and unable to release their energy (Collins, 2005, Collins and Kelly, 2002, Collins and Muhunthan, 2003, Iwan, 1967, Puzrin and Houlsby, 2001). This hypothesis is illustrated using the schematic particle diagrams shown in *Figure 5.2.* In this example, particle A is tracked during a loading-unloading cycle. At state (a) sample is at the initial state, and particle A is in contact with particles B, C, and F. Upon loading at state (b), particle B will start transferring the load, which will push particle A down. At this stage, particle A will be surrounded by particles B, C, D, E, and F. If the sample is unloaded as shown in state (c) some of the compressed particles will be able to release their stored elastic energy and go back to their initial state. But particle A will be trapped between particles C, D, E, and F, which will prevent it from returning to its initial state. The energy stored in particle A is the plastic part of the free energy which is only released by reversing the stress direction (Collins, 2005)

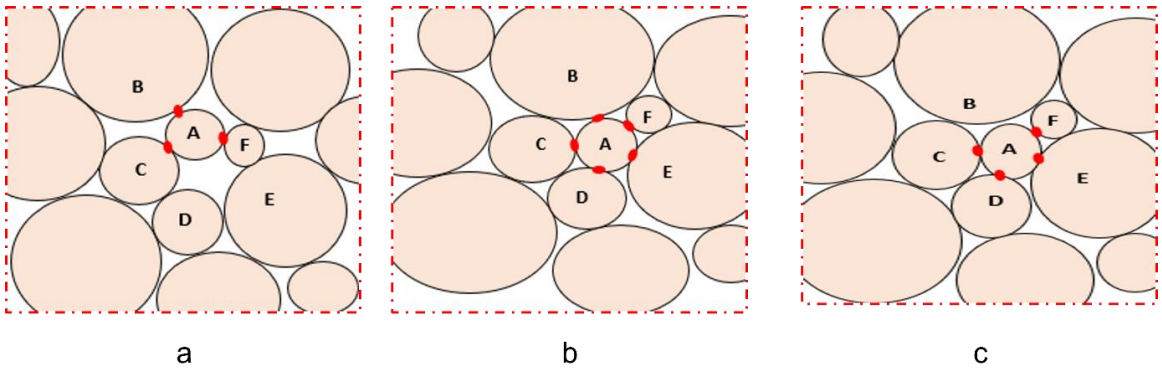

Figure 5.2 2D schematic diagrams of particle rearrangement during: (a) Initial state; (b) Loading; (c) Unloading.

Furthermore, the development of stored plastic work in granular materials is associated with the force chain network in granular materials (Yang et al., 2018). Strong force chain formation and collapse have a direct effect on the dilatancy of sand, where the buckling of the strong force chains will lead to volumetric contraction (Cundall and Strack, 1979, Li and Li, 2009, Oda et al., 1982). Meanwhile, the collapse of strong force chains is associated with interparticle sliding, which leads to energy dissipation. On the other hand, the formation of the strong force chains as shown in Figure 5.3 will lead to more particles getting trapped in the weak force networks, which causes the accumulation of stored plastic work.

Collins (2005) proposed a hypothesis linking the stored plastic work in granular materials to the volumetric strain. This hypothesis can be better understood through the behaviour of dense sand subjected to shearing. At the start of shearing, as the dense sand experiences compression, the particles come closer together, leading to a change in volume. During this phase, the applied load is transferred, resulting in the formation of a strong force network. Some contacts between particles start sliding and dissipate energy, while others become trapped and store some of the applied energy. As shearing continues and reaches its peak, the sample starts to dilate, causing a change in the stored energy associated with the change in the sample volume. During this dilation, the force chains within the granular assembly break and reform, releasing some stored plastic energy. This process leads to a reduction in material density and a decrease in strength and stiffness. Upon reaching the critical state, there is no further change in volume or stored plastic work.

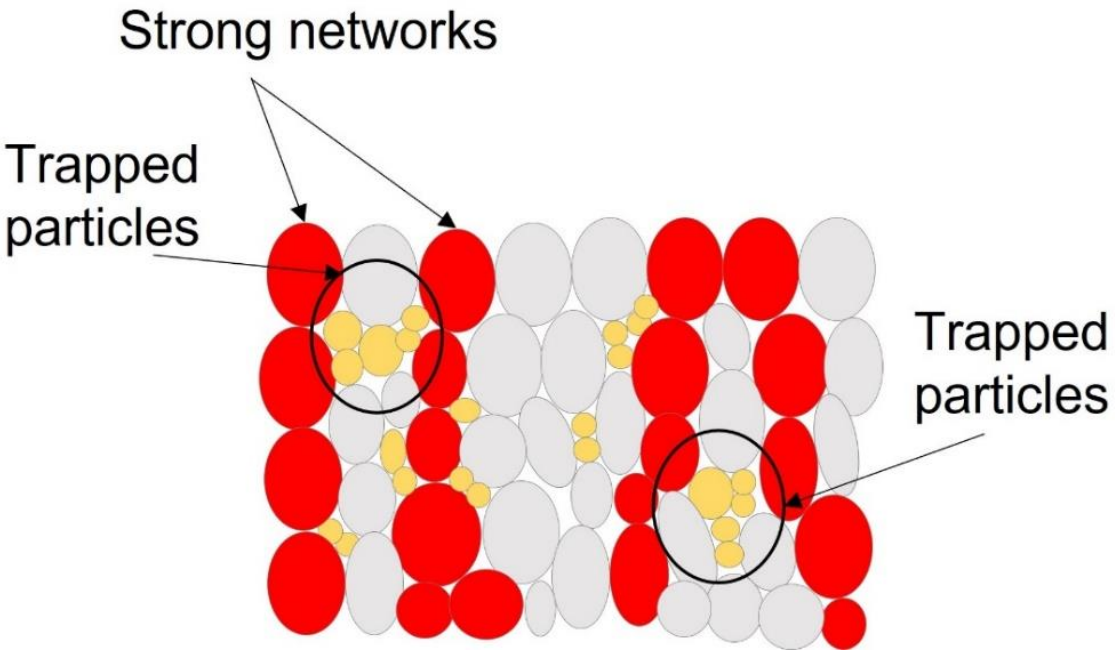

Figure 5.3 Schematic diagrams of the particle system.

5.4 DEM simulations

5.4.1 Sample preparation and shearing

DEM samples were generated using three different particle size distributions (PSD). The first sample has a PSD representative of Dunkirk sand with 40150 spherical particles. The second sample has a PSD representative of Toyoura sand with 27961 spherical particles, while the third sample has a uniform PSD containing 21663 spherical particles with a minimum diameter of 0.1 mm and a maximum diameter of 0.14 mm. Figure 5.4 shows the DEM particle size distributions match the PSD distributions from the experiment. The experimental data were measured by the authors using a plot digitizer (Alshibli and Cil, 2018, Liu et al., 2019b). Drained triaxial simulations were performed on these samples. A dense sample was created for each PSD type. These samples were prepared using a two-step process (Hanley et al., 2014). To begin, the particles were randomly placed into the periodic cell, which was then isotopically compressed to the target mean normal stress p_0 = 250 kPa with a friction coefficient μ = 0 to reach the target p_0. Then μ was set to 0.3 and the sample was left to

equilibrate again. When samples reach the target stress, they are subjected to drained triaxial compression to the critical state with constant radial stress σ_r. The upper boundary was moved to control loading, while the lower boundary remained fixed. The samples were sheared with a constant inertial number of $I = 1 \times 10^{-4}$, which indicates quasi-static loading. Local damping of 0.3 was used during the preparation but set to 0 during shearing, which ensures that all dissipation is due to interparticle friction during triaxial compression. Table *5.1* shows the codes generated for samples tested in this study based on their PSD type.

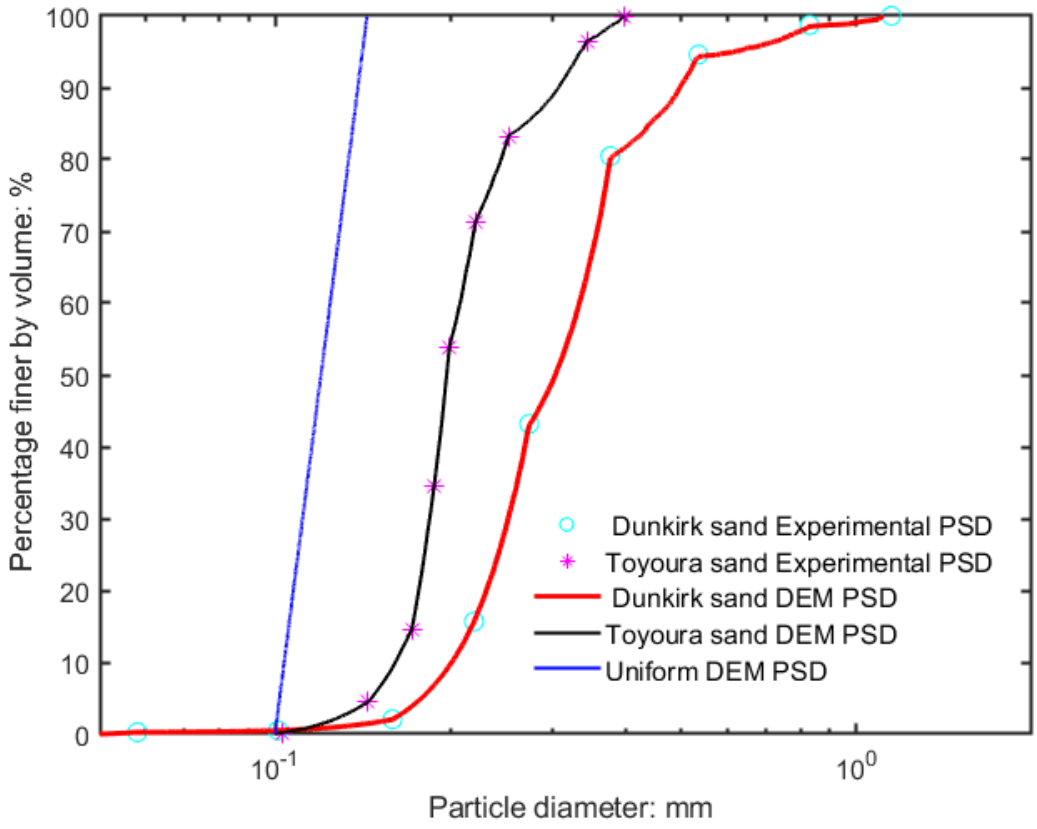

Figure 5.4 Particle size distribution (PSD).

Table 5.1 Sample codes used in this study based on their PSD type and density.

Sample type	Void ratio at end of isotropic compression	Confining pressure	Stress path	Sample code
Dunkirk sand	0.479	250 kPa	Constant σ_r	DS-1-D

Toyoura sand	0.522	250 kPa	Constant σ_r	TS-1-D
Uniform PSD	0.553	250 kPa	Constant σ_r	US-1-D

5.4.2 Measurement of stored plastic work

The measurement of the stored plastic work requires the measurement of both the total plastic work and energy dissipation. As previously demonstrated, energy dissipation can be determined directly from DEM simulation. To compute the plastic work, it is necessary to measure plastic strains throughout the simulation. The plastic work may then be determined based on $\mathrm{p}\delta\varepsilon_{\mathrm{v}}^{\mathrm{p}} + \mathrm{q}\delta\varepsilon_{\mathrm{q}}^{\mathrm{p}}$. This work proposes a technique for estimating plastic strains. In this approach, simulation is performed in two phases. In the first stage, the simulations are run until the critical state (50% axial strain), during which the state of the samples is stored at different strain levels, as shown in Figure *5.5*a. In the second stage, stress probe tests are done at each strain level to get the elastic bulk modulus K and shear modulus G.

$$G = \frac{\delta q}{3\delta\varepsilon_q} \tag{5.9}$$

$$K = \frac{\delta p}{\delta\varepsilon_v} \tag{5.10}$$

where $\delta\mathrm{q}$ is the increment of deviator stress, $\delta\varepsilon_{\mathrm{q}}$ is the incremental deviatoric strain, $\delta\mathrm{p}$ is the incremental main effective stress, and $\delta\varepsilon_{\mathrm{v}}$ is the incremental volumetric strain. The probe test is performed by applying a small strain increment $\Delta\varepsilon$ in the axial direction whereas the lateral stress is controlled based on the stress path (e.g, constant p or σ_{r}) until the increment of shear strain $\delta\varepsilon_{\mathrm{q}}$ reaches 10^{-6}. During the probe test, the coefficient of friction μ is set infinite to prevent sliding, this will ensure the deformation is linearly elastic and there is no plastic deformation (Cundall, 1989). Figure *5.5*b shows schematic diagrams of a probe test at a specific location during the simulation (point A), and it will produce a linear stress-strain relationship as shown in Figure *5.5*c.

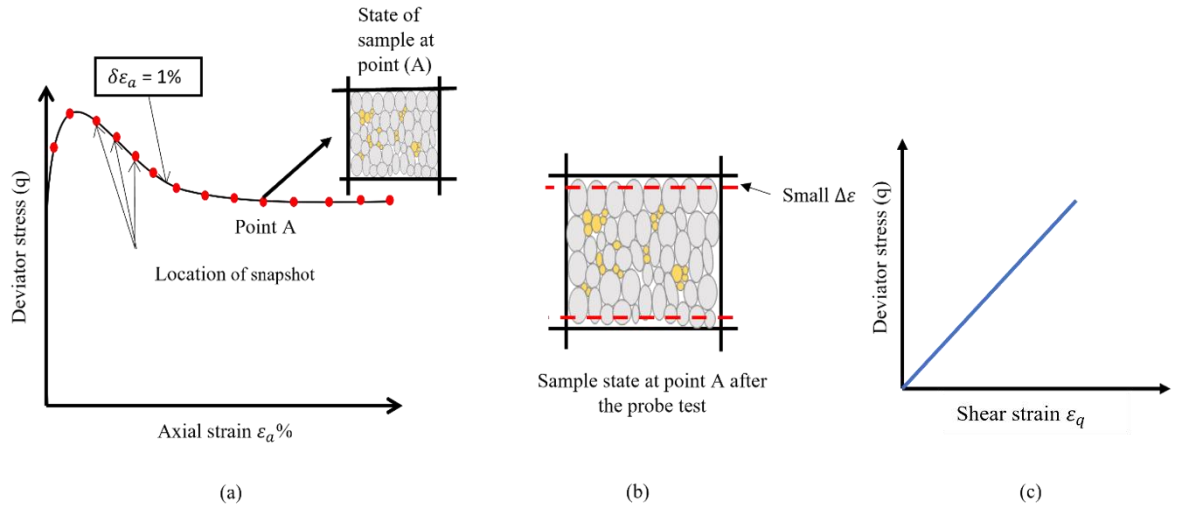

Figure 5.5 Schematic diagrams of probe test for calculating elastic stiffness in the DEM simulation.

The elastic modulus obtained during this study is used to calculate the elastic shear strain increment $\delta\varepsilon_q^e$ and elastic volumetric strain increment $\delta\varepsilon_v^e$. In addition, the total shear strain increment $\delta\varepsilon_d$ and total volumetric strain increment $\delta\varepsilon_v$ can be calculated as below

$$\delta\varepsilon_d = \frac{2}{3}(\delta\varepsilon_a - \delta\varepsilon_r) \tag{5.11}$$

$$\delta\varepsilon_v = \delta\varepsilon_a + 2\delta\varepsilon_r \tag{5.12}$$

where $\delta\varepsilon_a$ is increment axial strain and $\delta\varepsilon_r$ is the increment radial strain. The plastic strain increment then can be calculated as

$$\delta\varepsilon_q^p = \delta\varepsilon_d - \delta\varepsilon_q^e \tag{5.13}$$

$$\delta\varepsilon_v^p = \delta\varepsilon_v - \delta\varepsilon_v^e \tag{5.14}$$

The following work increment can then be obtained as below

$$\delta W^e = q\delta\varepsilon_q^e + p\delta\varepsilon_v^e \tag{5.15}$$

$$\delta W^p = q\delta\varepsilon_q^p + p\delta\varepsilon_v^p \tag{5.16}$$

$$\delta W = q\delta\varepsilon_q + p\delta\varepsilon_v \tag{5.17}$$

The stored plastic work increment is then calculated based on Equation (5.5).

The small strain stiffness (e.g., shear modulus G and bulk modulus K) contributes significantly to many geotechnical problems, such as liquefaction, foundation mechanics and earthquake. Experimental tests are the most common method for measuring small strain properties. During laboratory tests, small stress is applied to measure elastic stiffness, but particles are not fixed, causing particle sliding and energy dissipation. In DEM probe tests, however, the stress probe is applied, and particle movement is fixed, which ensures no energy is dissipated during the test. Several recent studies have used DEM probe tests to investigate the elastic properties of granular materials (Gong et al., 2019, Gu et al., 2017, Gu et al., 2013).

The DEM probe tests utilised in this study undergo rigorous validation to ensure their reliability and accuracy. Multiple validation procedures are conducted to verify that this method yields results consistent with those obtained in previous studies. By subjecting the DEM probe tests to thorough validation, the credibility and validity of the results are upheld, providing confidence in the approach used. The first validation is done in accordance with the results of Cundall (1989). Cundall (1989) run a DEM simulation with 432 particles and particle diameters of 0.1075 and 0.1825. The sample sheared to 0.4% axial strain with 138 kPa. Additionally, he compared his results with a physical experiment (Chen et al., 1988). Chen et al. (1988) performed a laboratory experiment to measure the elastic properties of a sample made of glass spheres with two diameters of 0.300 to 0.425mm and 0.180 to 0.250. In this chapter, DEM simulation is carried out similarly to the simulation done by Cundall except for the number of particles used, where in this work the sample contains 21663 particles and Uniform PSD is used. The results are compared with Cundall and Chen's results in Figure *5.6* and Figure *5.7*.

Figure *5.6* and Figure *5.7* shows the shear modules against axial strain compared with Cundall and Chen's results. The results obtained in this work are indicated by "Validation data" while the other two are Cundall and Chen. The findings of this research are more similar to those of Chen et al. (1988) than they are to those of Cundall (1989). The initial shear modulus obtained in this study is 151MPa with a reduction of around 10% at 0.3% axial strain, while Chen et al. (1988) initial shear modulus 161MPa with a reduction of around 20% at 0.3% axial strain. The

initial shear modulus obtained by Cundall is 127MPa with a reduction of around 32% at 0.3% axial strain. A second validation was made with the study by Gu et al. (2013). Gu et al. (2013) carried out a DEM probe test to study the effect of stress ratio on small strain stiffness of granular materials. They evaluated the shear modulus at different isotropic stress states 250,500, and 1000 kPa. This work also performed similar simulations and evaluated shear modulus at three effective stresses 250,500, and 1000 kPa. The results are presented in Figure *5.7*, the results obtained in this work are indicated by "Validation data" as well. It can be noticed this validation also showed similar results to those found by Gu et al. (2013). Based on the validation done in this part, it is clear that the DEM probe tests used in this research are capable of producing accurate data that may be used to examine the chapter's goals.

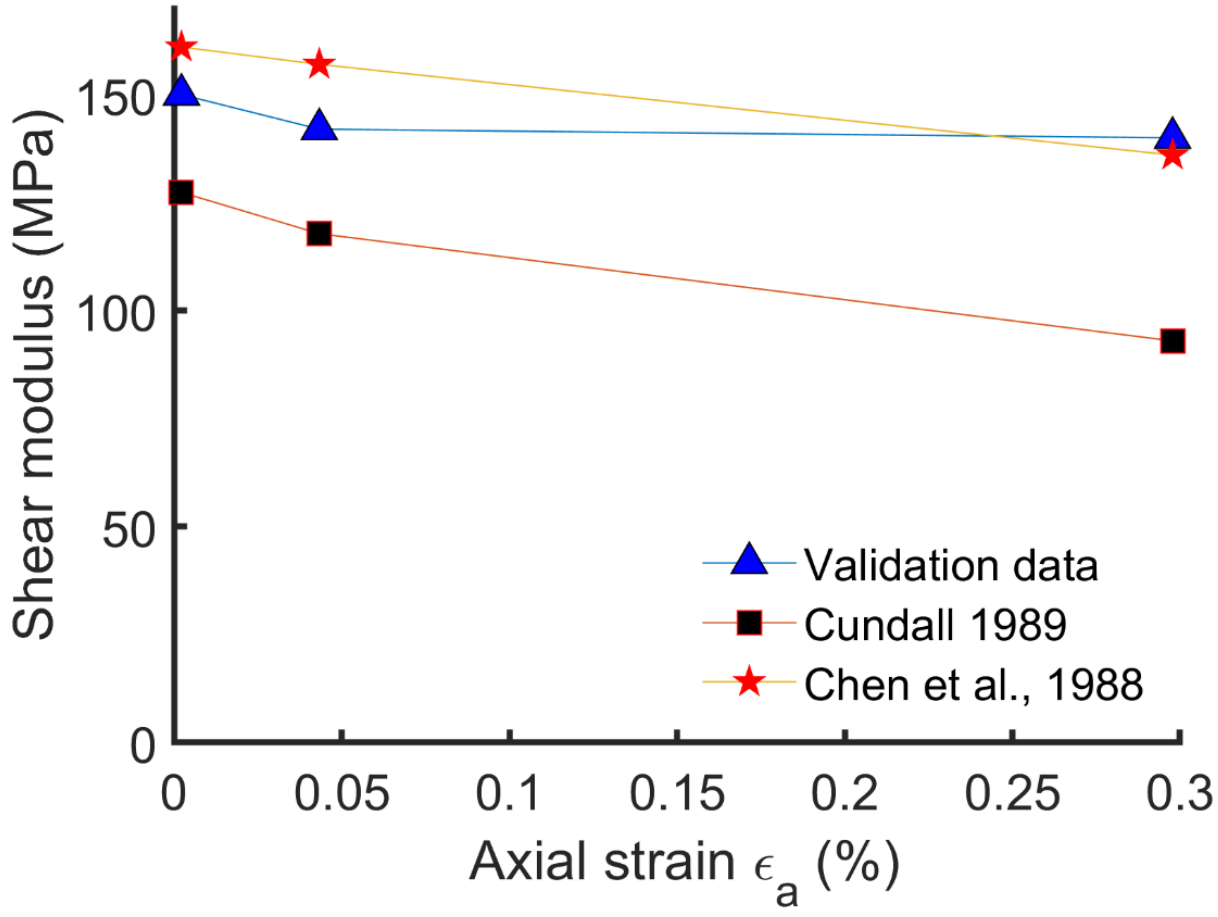

Figure 5.6 Validation for DEM probe test against Cundall (1989) DEM probe test.

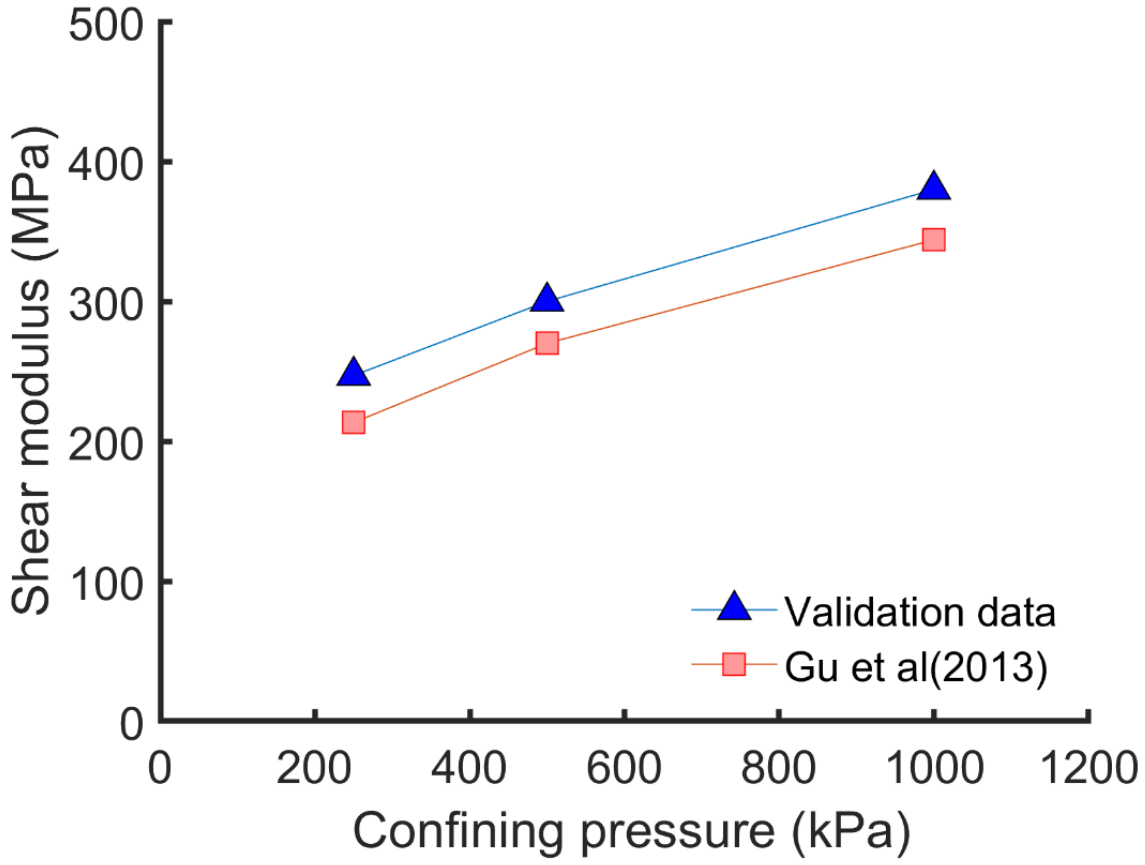

Figure 5.7 Validation for DEM probe test against Gu et al. (2013) DEM probe test data.

5.5 Stress-strain response

Figure *5.8* shows the stress-strain response for dense samples with different PSD. All samples show strain-softening and volume expansion throughout the simulation, which is consistent with the results of the experiment. Figure *5.8*a and Figure *5.8*b show the stress ratio and deviator stress against axial strain respectively. The deviator stress increases rapidly for all samples, reaching a peak at around 2.5% axial strain and then decreasing gradually until reaching a critical state at around 30% axial strain. It is interesting to see that all the samples reach the same critical state stress ratio, indicating that the critical state friction angle is insensitive to the PSD, which is consistent with previous studies (Voivret et al., 2009, Yang and Luo, 2018). In addition, as the samples are all prepared dense, their initial relative densities (or equivalently initial state parameters) are close, leading to close peak stress ratios

as well. Figure *5.8*c shows the void ratio against axial strain for all samples. Due to the different PSDs of the samples, it can be observed that the initial and critical state void ratios of each sample vary. US-1-D has the largest void ratios, while DS-1-D with the widest PSD span exhibits the lowest.

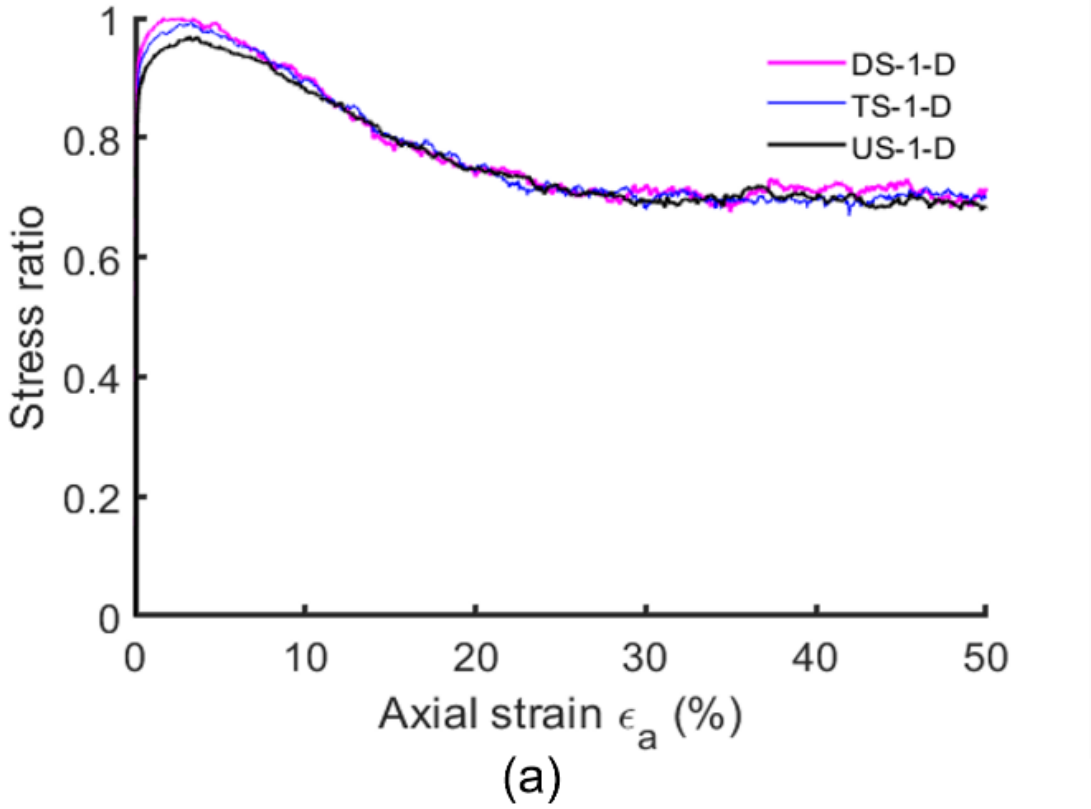

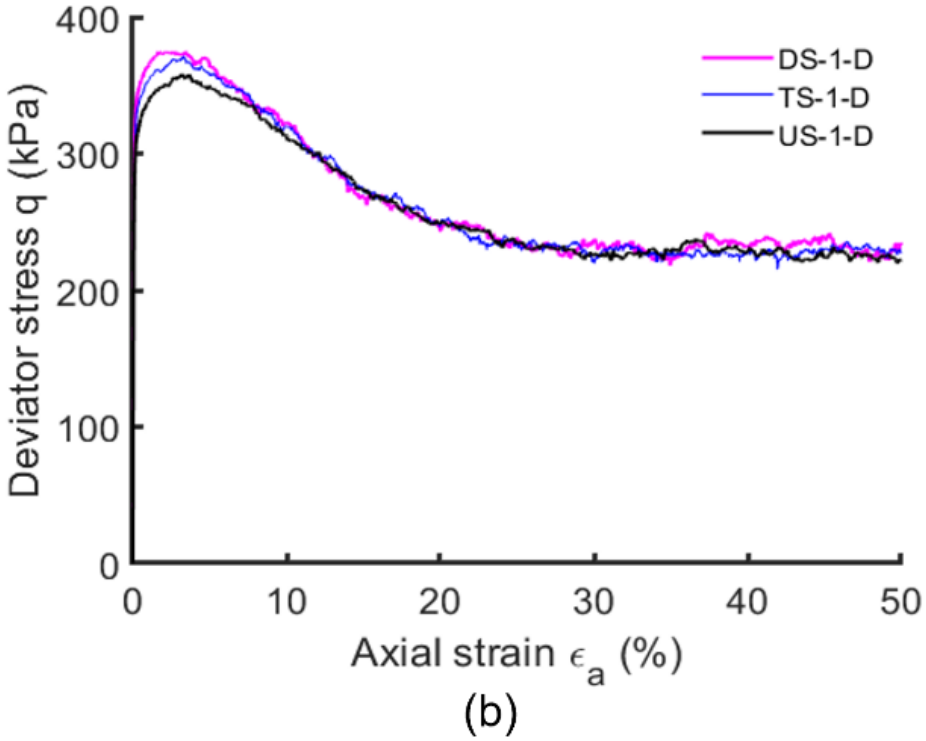

(b)

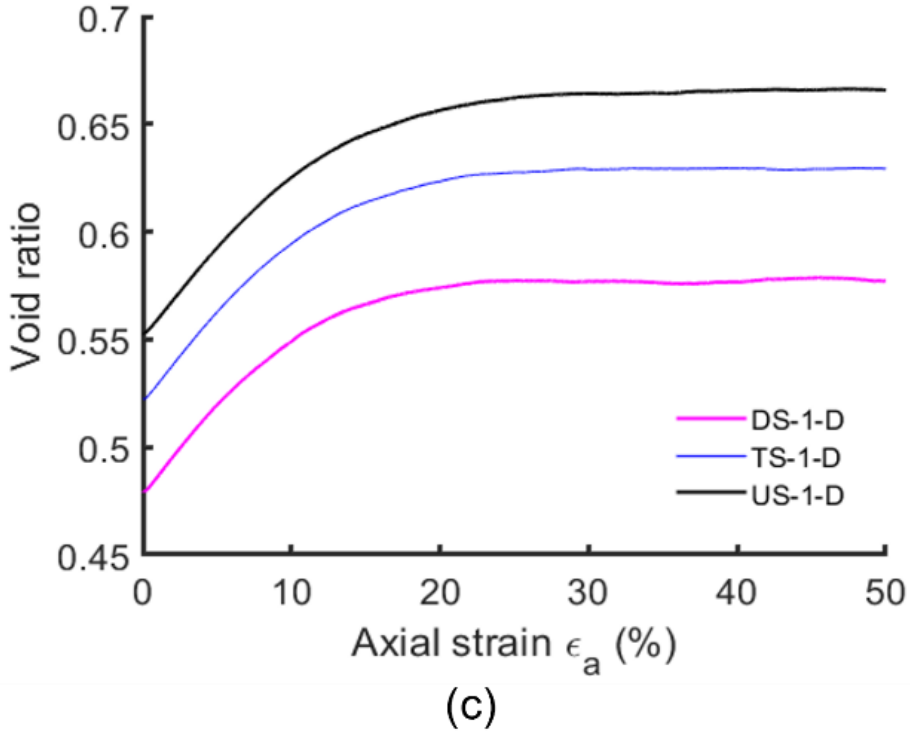

(c)

Figure 5.8 Comparison of the stress-strain behaviour of all samples; a) stress ratio against axial strain; b) deviator stress against axial strain; c) void ratio against axial strain.

5.6 Energy dissipation

The energy was traced in all simulations conducted in this chapter, employing the same method as elucidated in Chapter 3. Figure *5.9* shows the error in the energy balance as a percentage of the applied work. It is worth noting that, at the outset of the simulations, the errors may appear relatively higher compared to the subsequent stages, primarily due to the boundary work being zero during the initial shearing phase. These findings are consistent with the observations reported by (Hanley et al., 2018). The energy dissipation resulting from sliding friction is evaluated by computing the incremental energy dissipation and subsequently normalising it by the sample volume. This normalisation accounts for the response of a representative soil element, enabling a more accurate assessment of energy dissipation per unit volume within the granular material. Figure *5.10* shows the rate of energy dissipation against axial strain for all samples utilised in this investigation. The results show similar behaviour for all samples, except for a slight difference in the amount of dissipation. It is noted that the DS-1-D has the highest rate of energy dissipation and the US-1-D has the lowest. There are two main reasons for this: (a) DS-1-D has the most particles per unit volume, which causes the most interparticle sliding; (b) DS-1-D has the most heterogeneous force-chain structure due to its widest PSD. There is more interparticle sliding when the force-chain structure becomes more heterogeneous (Hanley et al., 2018). The dissipation rate is relatively low at the outset of shearing and rapidly increases afterwards. The maximum rate of energy dissipation is observed at about 5% axial strain. At the critical state, the rate of energy dissipation becomes constant. Figure *5.11* shows the cumulative energy dissipation for all samples with different PSDs. It can be seen that energy dissipation has accumulated rapidly since the simulations began. Additionally, the influence of the PSD on the amount of energy dissipation is observed in cumulative energy dissipation, with the largest accumulated dissipation recorded for the sample DS-1-D and the lowest for the sample US-1-D.

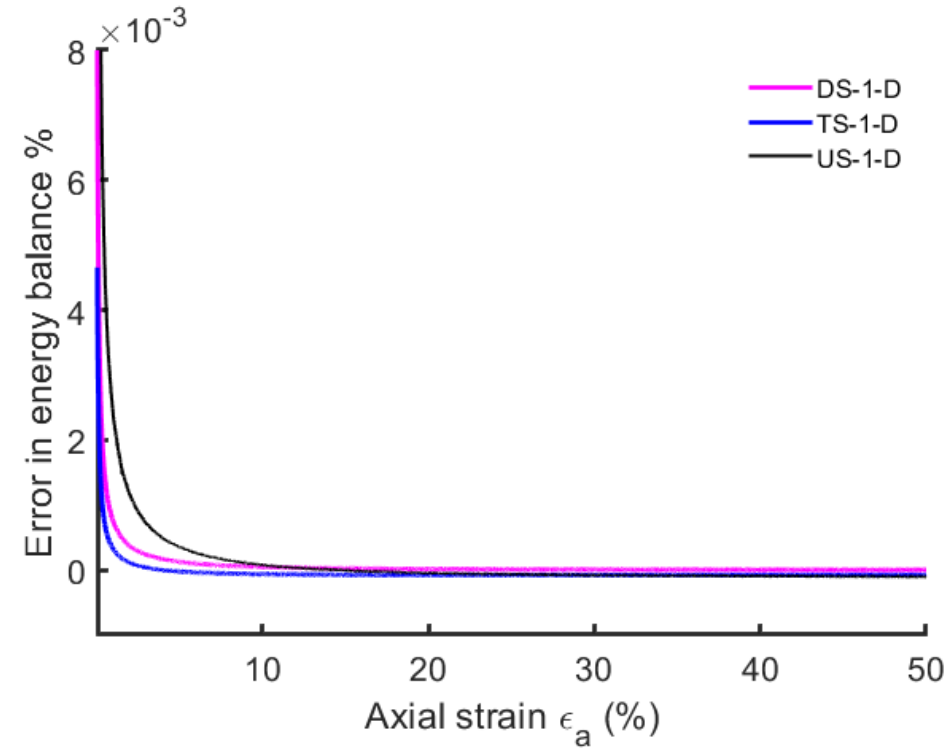

Figure 5.9 The error in the energy balance as percentage of the boundary work plotted against axial strain as a percentage of the boundary work for all simulations

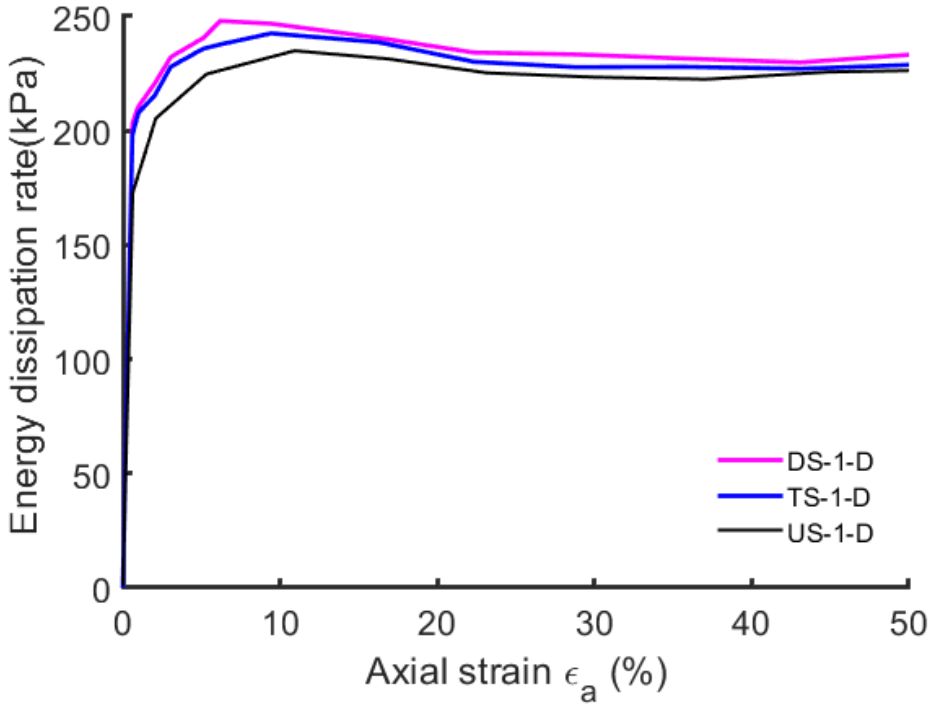

Figure 5.10 Evaluation of energy dissipation during the simulations with different PSD

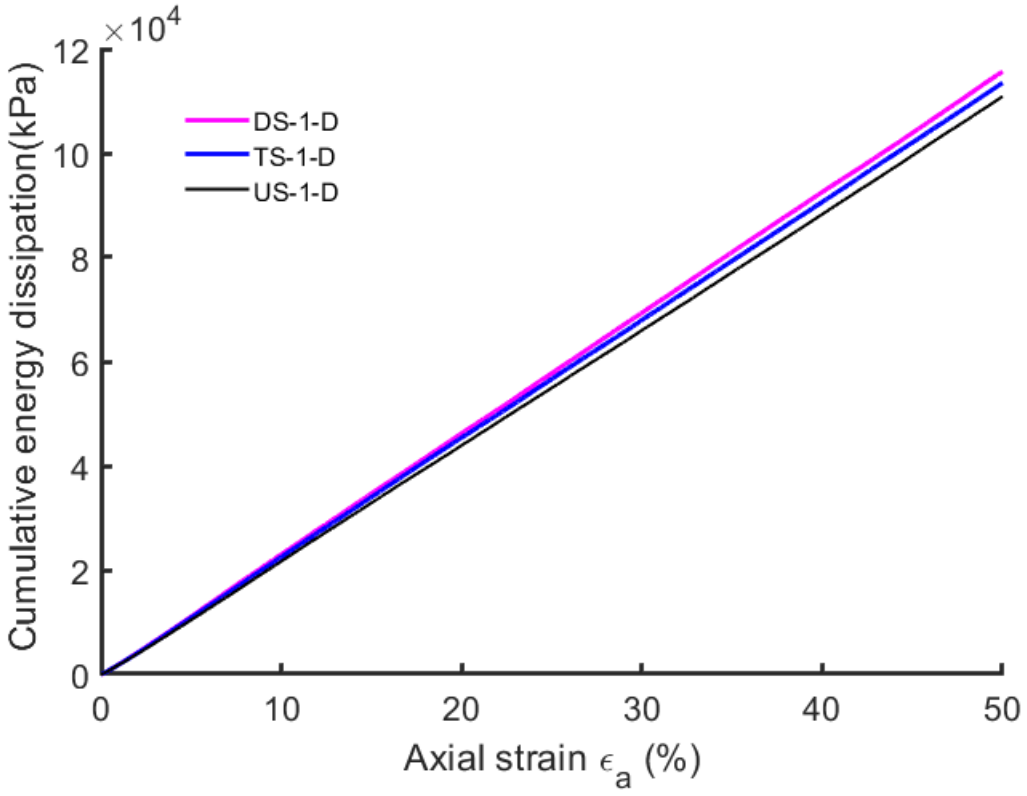

Figure 5.11 Cumulative energy dissipation during the simulations with different PSD.

5.7 Elastic behaviour

Using the probing test described earlier in section 5.4.2, the shear modulus G and bulk modulus K are determined throughout the simulation at different strain levels. Figure *5.12* illustrates the elastic modulus determined for each sample with a different PSD. It can be noticed from the results that the elastic modulus shows nonlinear behaviour at low strain levels for all samples. To investigate the difference in elastic modulus at a small strain level, the probe test was conducted more often before 1% axial strain. After 1% axial strain, the probe test was performed less frequently since no significant variation in the findings was seen. Figure *5.13* shows the evolution of shear modulus reduction $(\mathrm{G}/\mathrm{G}_0)$ for the three samples used, where G_0 is the initial or the maximum shear models at the start of shearing. It can be seen that the decrease occurs mostly before 1% axial strain; nevertheless, after the strain surpasses 1% axial strain, the modulus remains constant, which is consistent with the

results (Mair, 1993, Xu et al., 2014). These stiffness modulus are used to calculate the total elastic strains during the simulation as explained in 5.4.2.

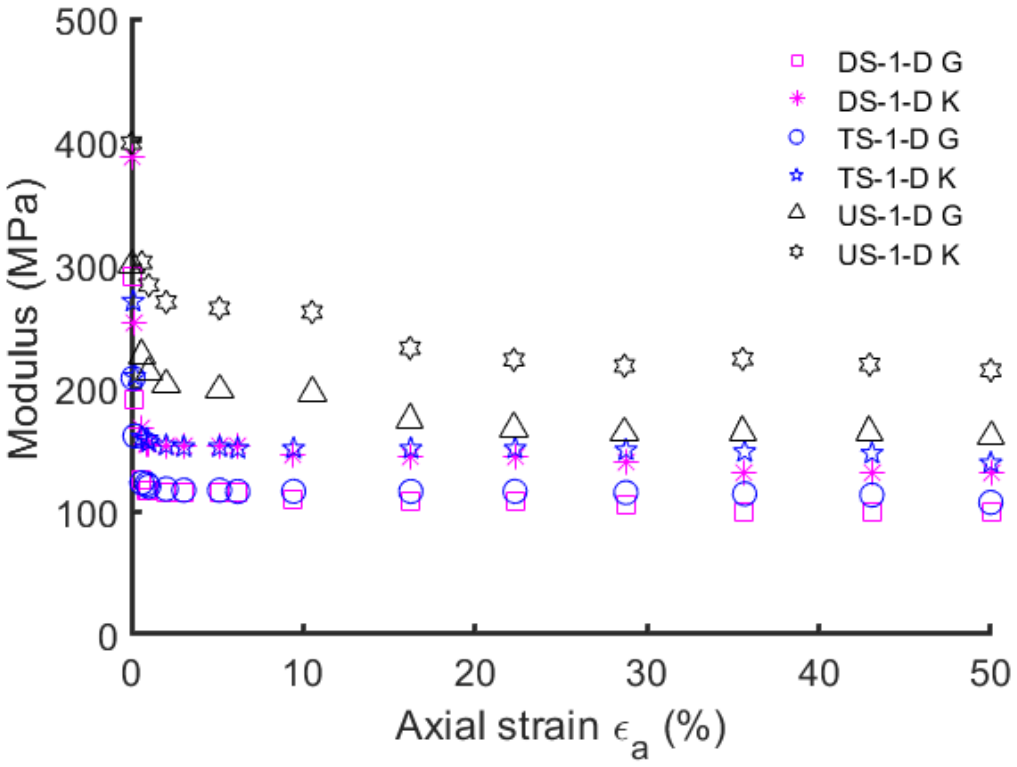

Figure 5.12 Properties of small strain stiffness G shear modulus and K bulk modulus vs axial strain.

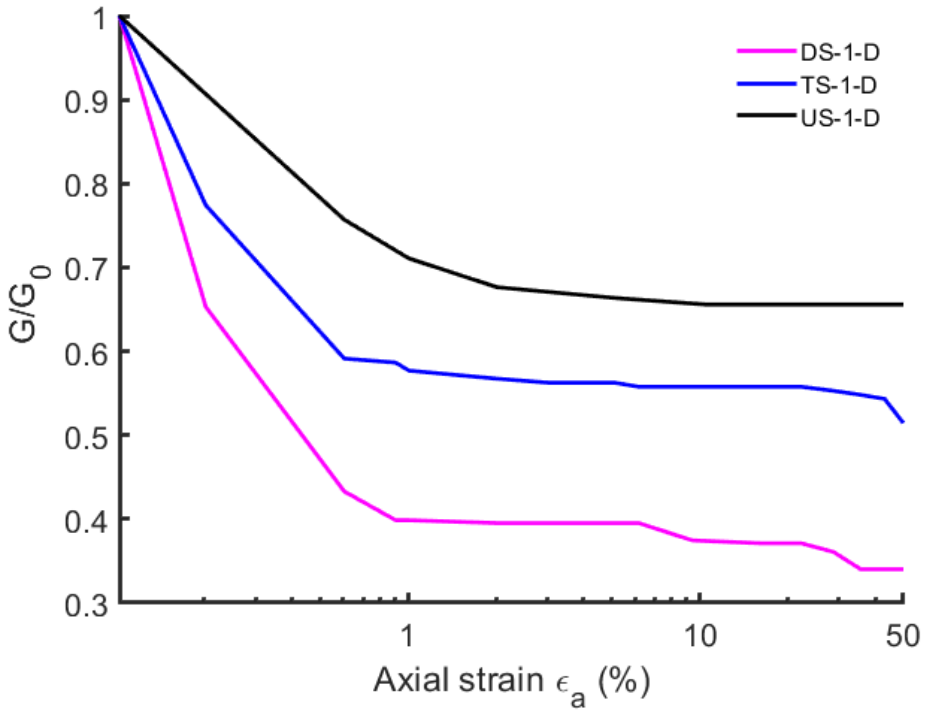

Figure 5.13 Comparison of the degradation curves of the normalised shear modulus.

5.8 Stored plastic work results

In this work, the stored plastic work is assumed to be zero at the start of shearing.

Figure 5.14 shows the evolution of different energy terms for all three samples. The elastic work rate is very small due to the small elastic strain in the samples. The plastic work is the summation of stored plastic work and dissipation. It is found that stored plastic work is much smaller than the dissipation in all samples (Fig. 7a-c). Note that the stored plastic work is assumed to be equal to zero at the beginning of shearing.

For DS-1-D, the stored plastic work rate exhibits fluctuation with negative values recorded at the beginning, which indicates the release of plastic work that is stored during isotropic compression. The rate of stored plastic work becomes positive after the axial strain reaches about 3% and reaches the peak at about 10% axial strain. This means that plastic work is being stored in this strain range Following that, the stored plastic work rate rapidly diminishes until it becomes almost zero at the critical state. This is consistent with the assumption by Collins

(2005) that the stored plastic work increment is dependent on the volumetric strain increment which is 0 at the critical state. Similar results have been observed for TS-1-D (

Figure 5.14b).

Figure 5.14c shows the results of US-1-D. The stored plastic work rate shows both negative and positive values for this sample as well. But there is respectively storage and release of plastic work at lower and higher axial strain, which is opposite to the trend observed in the other two samples. At a critical state, the stored plastic work is approximately zero, which is the same as the other two samples. Figure *5.15* shows the accumulative stored plastic work for the three samples. There is net plastic work storage for DS-1-D and TS-1-D, and net release for US-1-D. This indicates that PSD affects the evolution of stored plastic work. The DS-1-D sample shows more stored plastic work than the other two samples because it has the widest range of particle sizes. In granular materials, plastic work is stored when particles are trapped among the larger ones during loading. This is more likely to occur when there is a wider range of particle size. The US-1-D has the smallest range of particle size and net plastic work release is observed. A plausible reason is that the particle size is so close that none of the particles is trapped during triaxial compression. Instead, the volume expansion during triaxial compression causes the release of plastic work stored in isotropic compression.

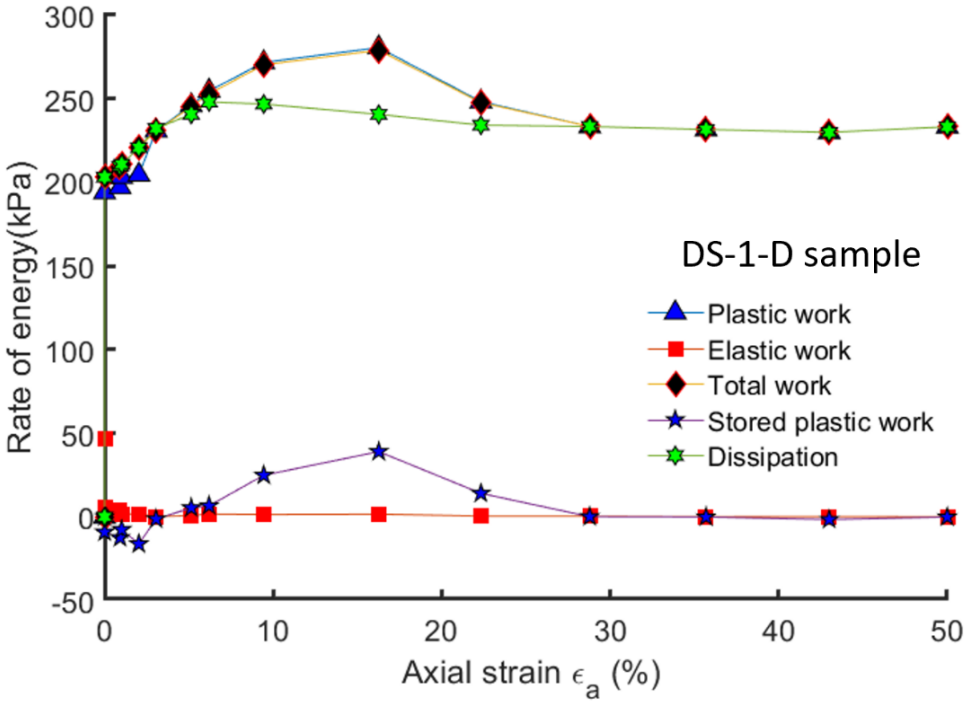
DS-1-D sample
Plastic work
Elastic work
Total work
Stored plastic work
Dissipation
Rate of energy(kPa)
Axial strain ϵ_a (%)
300
250
200
150
100
50
0
-50
0
10
20
30
40
50

(a)

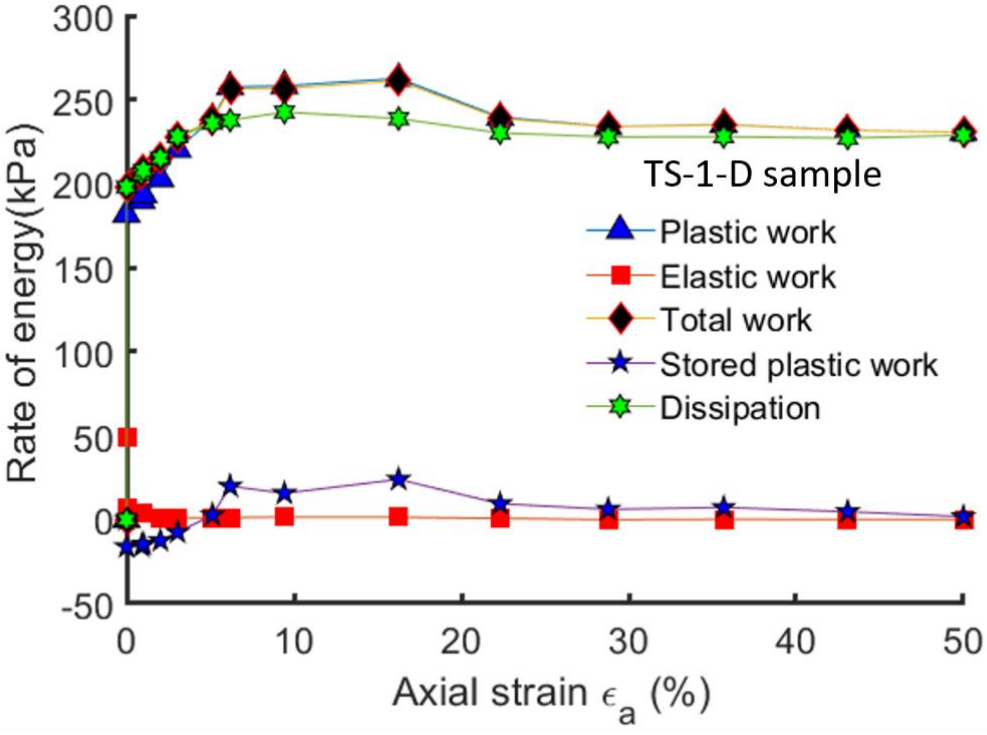
TS-1-D sample
Plastic work
Elastic work
Total work
Stored plastic work
Dissipation
Rate of energy(kPa)
Axial strain ϵ_a (%)
300
250
200
150
100
50
0
-50
0
10
20
30
40
50

(b)

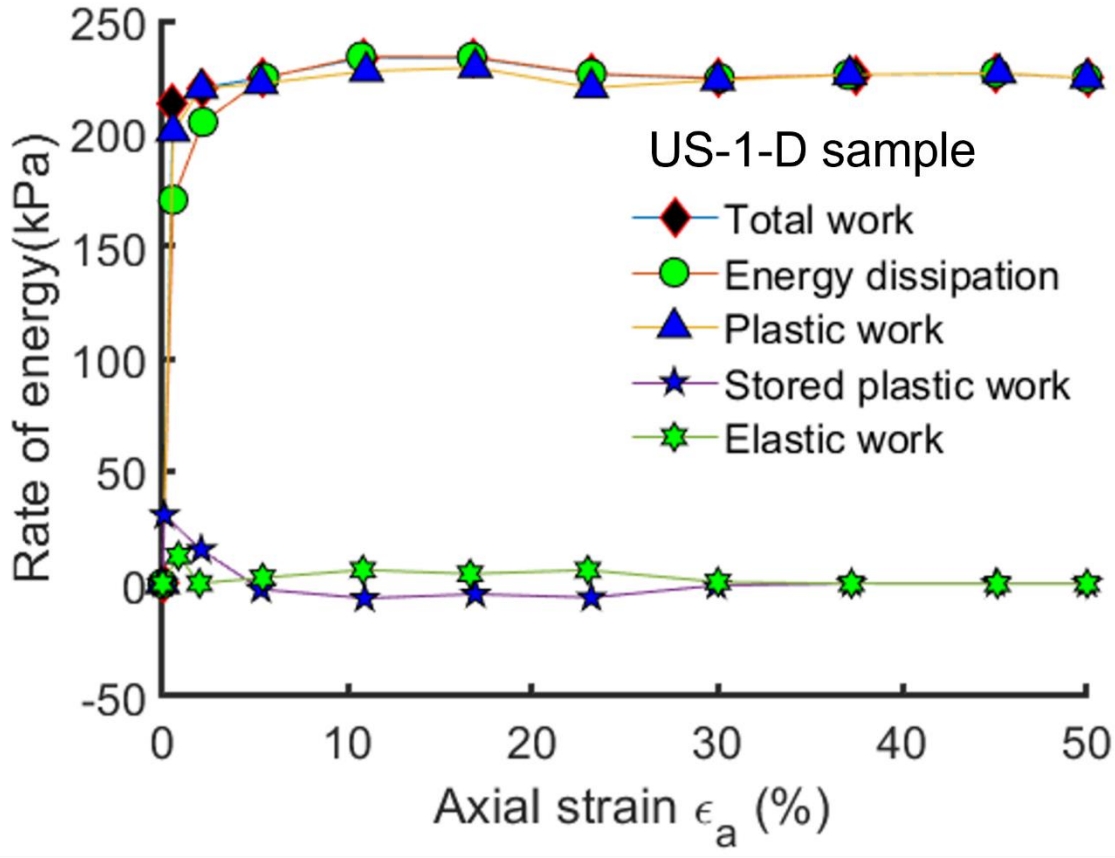

c

Figure 5.14 Energy rates for (a) DS-1-D (Dunkirk sand-PSD), (b)TS-1-D (Toyoura sand-PSD) and (c) US-1-D (Uniform-PSD).

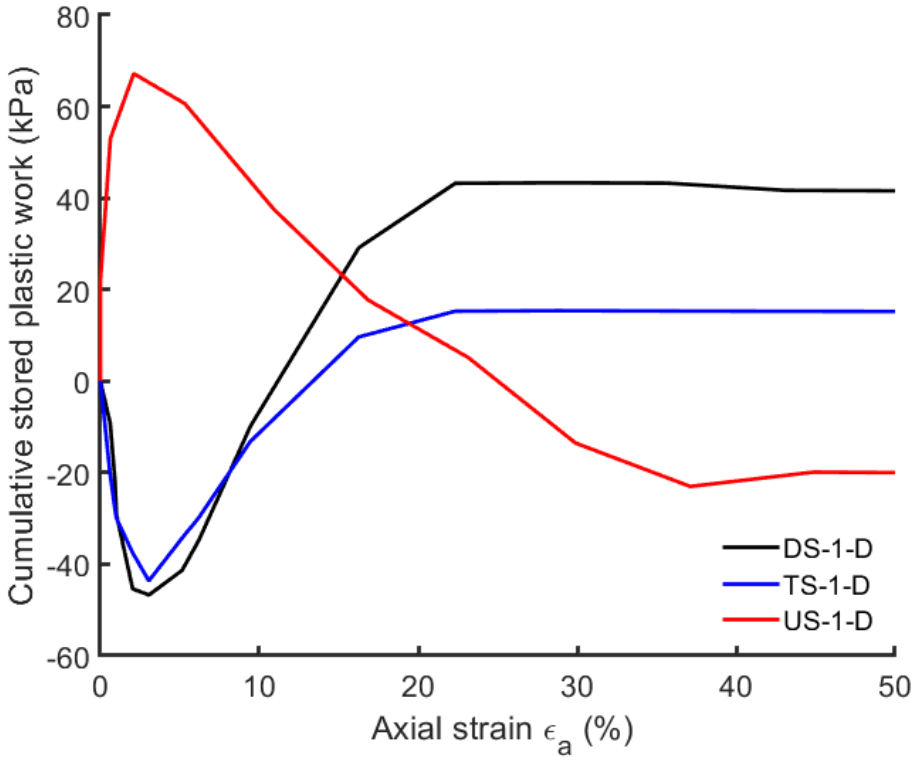

Figure 5.15 Cumulative stored plastic work against the axial strain with different PSDs.

5.9 Conclusion

This chapter provided a numerical investigation of energy dissipation and stored plastic work during triaxial shearing to a critical state. The effect of particle size distribution on both energy dissipation and stored plastic work is examined. Three separate PSDs were utilised to produce three different samples with various numbers of particles. These samples were produced and sheared to the critical state, a probe test technique was utilised to assess the elastic and plastic stresses of the samples during shearing. The key results of this chapter are:

- Some plastic work was stored during shearing, but only before the critical state. At the critical state, all plastic work is dissipated. It was also observed that the stored plastic work is not restricted by a sign which either negative or positive. It was also obvious that the varied PSDs utilised in this study affected the quantity of stored plastic work, with samples with finer particles exhibiting a larger amount of stored plastic work. Even though the quantity of stored plastic was not extremely high in general.

However, it is imperative to incorporate the stored plastic work in the development of constitutive models that involve energy analysis. By doing so, we ensure persistent adherence to the fundamental principles of thermodynamics throughout the any study.

- The energy dissipation results had a similar trend for all PSDs utilised in this research with slightly variable quantities of dissipation across samples.

Chapter 6: The development of energy dissipation and stored plastic work equations.

6.1 Introduction

As discussed in Chapter 2, the development of constitutive models based on the principles of thermodynamics requires assuming or constructing a dissipation function and free energy function that can be used to drive some relationships. Several dissipation functions have been proposed. Taylor (1948) found that part of the input energy is dissipated by a critical state friction component and part by the work needed to increase the volume of dense sand. Taylor utilised the relation $\tau x - \sigma y = \mu\sigma x$, where τ is applied shear stress, σ is the constraining normal stress, x and y are horizontal and vertical coordinates, and μ is a friction coefficient (Figure *6.1*). Later on Schofield (1999) elaborated on Taylor's relationship, stating that Taylor proposed that two variables contributed to the strength of soil: frictional resistance between particles as they slid during a shear distortion and a phenomenon he termed interlocking, which the required work needed to increase the volume. Thurairajah (1962) carried out triaxial shear tests on kaolin sand and clay. He found that during plastic deformation the rate of energy dissipation is equal to the product of mean effective stress p, with M the slope of the critical state line, and the increment of shear strain. These finding were later reviewed by Muhunthan and Olcott (2002) and Schofield (2000). Accordingly, Taylor's equation can be rewritten for triaxial test notation as

$$p\delta\varepsilon_v^p + q\delta\varepsilon_q^p = Mp\delta\varepsilon_q^p = \Phi \tag{6.1}$$

where $\delta\varepsilon_q^p$ and $\delta\varepsilon_v^p$ are the increment of shear and volumetric components of the plastic strain respectively. The right-hand side of the equation is the increment of plastic dissipation, which expressed as $Mp\delta\varepsilon_q^p$. Constitutive models of soil that developed based on the concept of work and dissipation made use of Equation (6.1) and a similar form of the Reynolds stress-dilatancy relationship. Consider, for instance, Equation (6.1) can be rewritten as

$$\eta = d + M, \text{ or } \tan\phi = \tan\psi + \tan\phi_c \tag{6.2}$$

where

$$\eta \equiv \tan\phi \equiv q/p, d \equiv \tan\psi \equiv -\delta\varepsilon_v^p/\delta\varepsilon_q^p, \text{and } M = \tan\phi_c \tag{6.3}$$

where ϕ is the mobilised friction angle, ψ is the dilation angle and ϕ_c is critical state friction angle. The stress dilatancy relationship expressed by Equation (6.2) was used as the basis for the original Cam clay model (Schofield and Wroth, 1968a). They found that this relation can be used as an equation for plastic potential $g(p, q)$, which can be rewritten as follow:

$$\frac{q}{p} = -\frac{\partial g/\partial p}{\partial g/\partial q} + M \equiv \frac{dq}{dp} + M \tag{6.4}$$

this can be integrated to give:

$$q = Mp\ln(p_c/p) \tag{6.5}$$

Equation (6.5) can be also used as that of the yield surface, where p_c is normal consolidation pressure and can be calculated based on the assumption of an elliptical yield locus $p\frac{M^2+\eta^2}{M^2}$ (Muir Wood, 1990). Even though the above model is well known as an appropriate model for modelling plastic shearing behaviour at the critical state line, it does not accurately represent the isotropic compression of soils. Consequently, Burland (1965) and Roscoe and Burland (1968) introduced a modified energy dissipation function replacing Equation (6.1) as

$$p\delta\varepsilon_v^p + q\delta\varepsilon_q^p = p\sqrt{\delta\varepsilon_v^{p\,2} + M^2\delta\varepsilon_q^{p\,2}} = \Phi \tag{6.6}$$

which now the increment of volumetric plastic strain also contributes to dissipation function. Collins and Muhunthan (2003) rewrite Equation (6.6) as a stress-dilatancy equation as follow:

$$d = \frac{\eta^2 - M^2}{2\eta} \tag{6.7}$$

this relationship can also be integrated, giving the yield functions for modified Cam clay (Muir Wood, 1990):

$$q^2 - M^2p(p_c - p) = 0 \tag{6.8}$$

This procedure differs from the original model by Taylor, the difference is not only associated with volume change induced by shearing but also due to dilation and isotropic compaction. Collins and Muhunthan (2003) have also pointed out that this approach has serious internal inconsistencies in the logical steps that lead from Equation (6.6) to Equation (6.8). Additionally, they noted that Equation (6.6) cannot truly represent the work equation of modified Cam clay. The derivation of both the true plastic work equation and the dissipation function associated with modified Cam clay is first discussed by (Houlsby, 1981) and further discussed in later studies (Collins and Houlsby, 1997, Collins and Kelly, 2002, Collins and Hilder, 2002). Building on Equation (6.8) as representative of the yield functions of modified Cam clay, the associated plastic volumetric and shear strains can be expressed as follows:

$$\delta\varepsilon_v^p = -\delta\lambda M^2(p_c - 2p) \text{ and } \delta\varepsilon_q^p = \delta\lambda 2q \tag{6.9}$$

where λ is the slope of the normal consolidation line. If the p and q are eliminated between Equations (6.8) and (6.9) will give the following equation for proportional constant $\delta\lambda$.

$$\delta\lambda = \frac{\sqrt{\delta\varepsilon_v^{p^2} + M^2\delta\varepsilon_q^{p^2}}}{M^2 p_c} \tag{6.10}$$

Therefore the stress invariants can be expressed using Equation (6.9) as follow:

$$p = \frac{1}{2}p_c + \frac{\frac{1}{2}p_c\ \delta\varepsilon_v^p}{\sqrt{\delta\varepsilon_v^{p^2} + M^2\delta\varepsilon_q^{p^2}}} \text{ and } q = \frac{\frac{1}{2}M^2 p_c \delta\varepsilon_q^p}{\sqrt{\delta\varepsilon_v^{p^2} + M^2\delta\varepsilon_q^{p^2}}} \tag{6.11}$$

and hence the true plastic work equation is expressed:

$$\delta W^p \equiv p\delta\varepsilon_v^p + q\delta\varepsilon_q^p = \frac{1}{2}\ p_c\ \delta\varepsilon_v^p + \frac{1}{2}\ p_c\sqrt{\delta\varepsilon_v^{p^2} + M^2\delta\varepsilon_q^{p^2}} \tag{6.12}$$

The first term in Equation (6.12) on the right is integrable and can be positive or negative, and it represents the amount of stored plastic work that can be recovered during a reversing loading. The second term in Equation (6.12) is not integrable because it contains a shear strain. If plastic strain occurs, this term should be always positive, which represents the dissipation part of plastic work. Therefore, the modified dissipation function expressed as

$$\delta\Phi = \frac{1}{2}\ p_c\sqrt{\delta\varepsilon_v^{p^2} + M^2\delta\varepsilon_q^{p^2}} \tag{6.13}$$

As pointed out by Collins and Hilder (2002) any dissipation function expressed as

$$\delta\Phi = p\sqrt{\delta\varepsilon_v^{p\,2} + M^2\delta\varepsilon_q^{p\,2}} \quad \text{or} \quad \delta\Phi = \sqrt{(p\delta\varepsilon_v^p)^2 + (q\delta\varepsilon_q^p)^2} \tag{6.14}$$

is not correct since this kind of function defines purely frictional materials (Coulomb type), and to develop models with a close yield surface, the dissipation function should be defined in terms of the consolidation pressure. Almost all these functions are derived from theoretical formulations without numerical evidence to support them. The prediction of these functions to energy dissipation at different strain levels is still not clear. In addition, any dissipation function should depend on the plastic strains in the system, and any function that relies on the total strain is incorrect. If the dissipation function depends on the total strain, then any purely elastic deformation will generate energy dissipation (Collins, 1997, Collins and Kelly, 2002). This also raises the difficulty of evaluating these functions, and any work which examines these functions should also calculate the plastic strain in the system at the outset.

The main objective of this chapter is to use DEM simulation to investigate some of the suggested dissipation functions and stored plastic work functions. In addition, a proposal for alternate equations of dissipation and stored plastic work will be developed based on the DEM data.

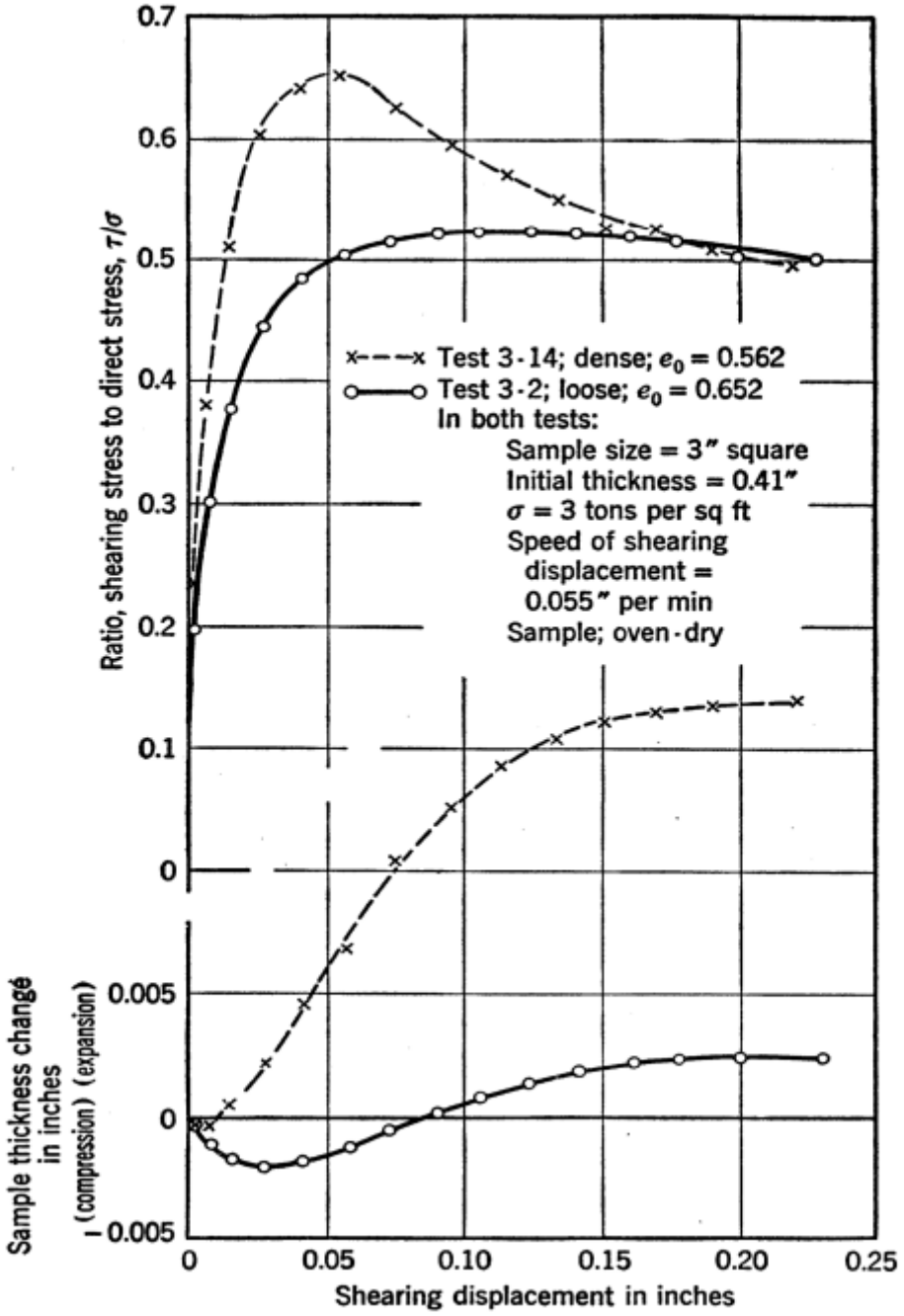

Figure 6.1 Typical direct shear testing plotted on Ottawa sand (Taylor, 1948).

6.2 DEM simulation

The DEM simulation used in this chapter is similar to the simulations described in chapter 5. In this investigation, three samples with different particle size distributions are used. The

plastic strains measured in Chapter 5 are also used in this chapter to evaluate the dissipation function and stored plastic work functions

Table 6.1 Sample code used in this study based on their PSD and density

Sample type	Void ratio at end of isotropic compression	Confining pressure	Stress path	Sample code
Dunkirk sand	0.479	250 kPa	Constant σ_r	DS-1-D
Toyoura sand	0.522	250 kPa	Constant σ_r	TS-1-D
Uniform PSD	0.553	250 kPa	Constant σ_r	US-1-D

6.3 Evaluation of existing energy dissipation functions

Figure 6.2a, b and c demonstrate the difference between the dissipation from DEM simulations with the prediction of the dissipation functions for samples DS-1-D, TS-1-D and US-1-D respectively. All the dissipation functions overestimate the amount of energy dissipation before the critical state. The modified Cam-Clay equation produces the biggest overestimation, whereas the Taylor equation and the Collins and Hilder equation give comparable results. Figure *6.3* a, b and c show the prediction error of the dissipation functions as a percentage of DEM energy dissipation for samples DS-1-D, TS-1-D and US-1-D respectively. The vast majority of errors occur before the critical state, with a positive error indicating an overestimation. The prediction of the modified Cam-Clay equation has the highest error, which is roughly 80%. The other equations have an error that is about 60%. At the critical stage, however, these errors rapidly reduce until they are close to zero.

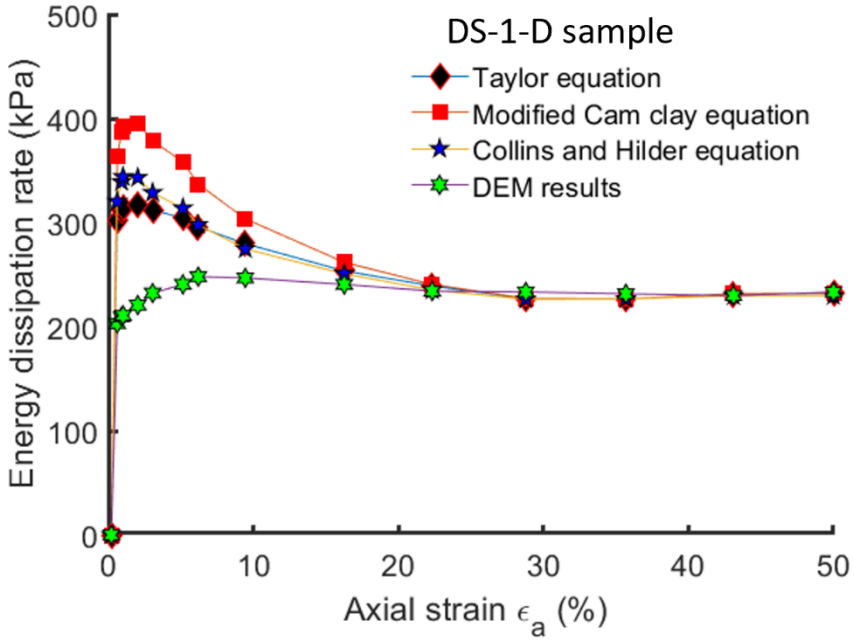
DS-1-D sample
Taylor equation
Modified Cam clay equation
Collins and Hilder equation
DEM results
Energy dissipation rate (kPa)
Axial strain ϵ_a (%)
0
100
200
300
400
500
0
10
20
30
40
50

(a)

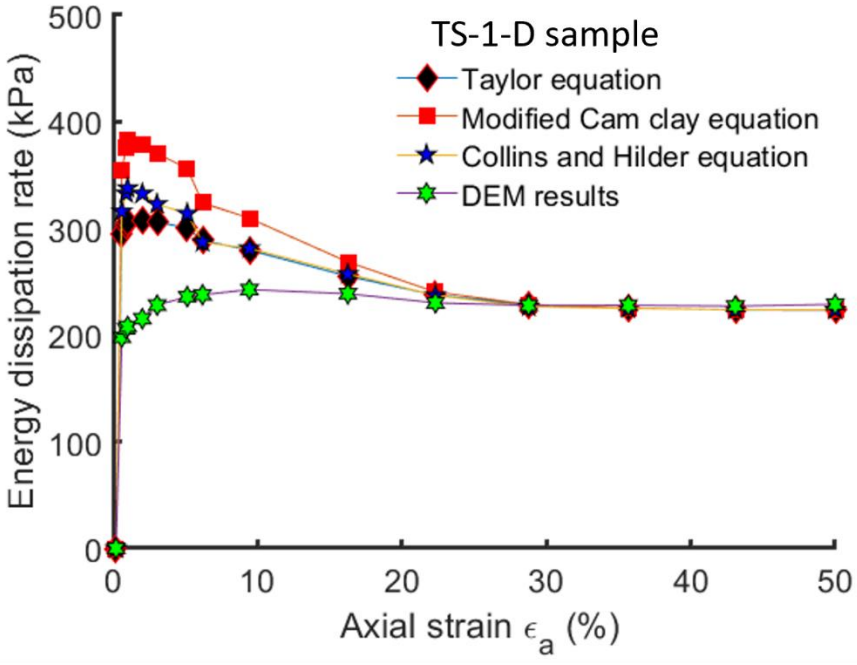
TS-1-D sample
Taylor equation
Modified Cam clay equation
Collins and Hilder equation
DEM results
Energy dissipation rate (kPa)
Axial strain ϵ_a (%)
0
100
200
300
400
500
0
10
20
30
40
50

(b)

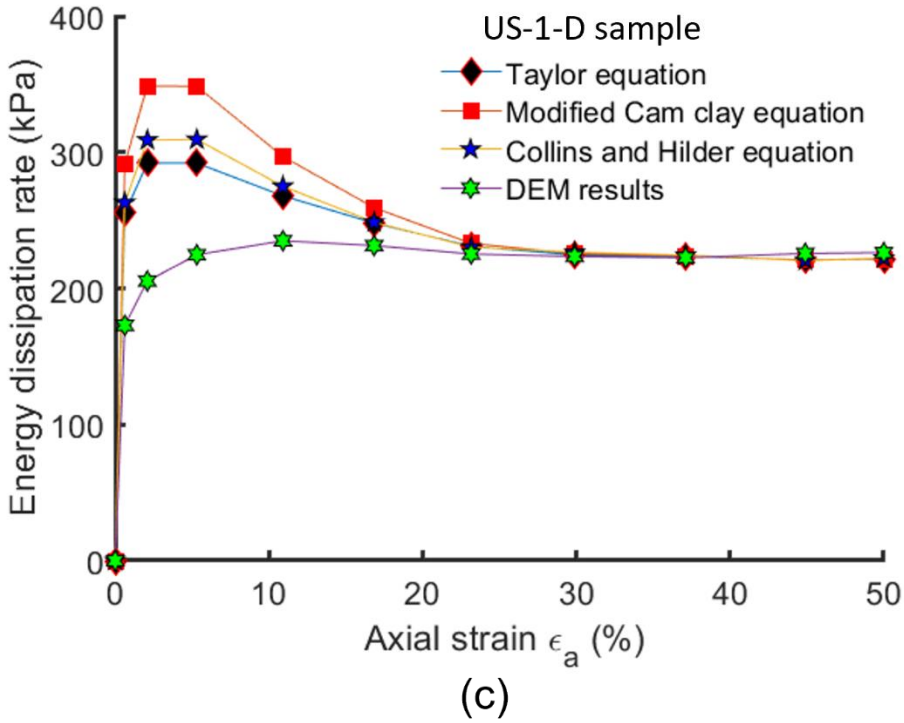

Figure 6.2 Compare energy dissipation from DEM for all samples and dissipation according to dissipation functions (Equations 6.1, 6.6 and 6.13); a) sample DS-1-D (Dunkirk sand-PSD); b) sample TS-1-D (Toyoura sand-PSD); c) sample US-1-D (Uniform-PSD).

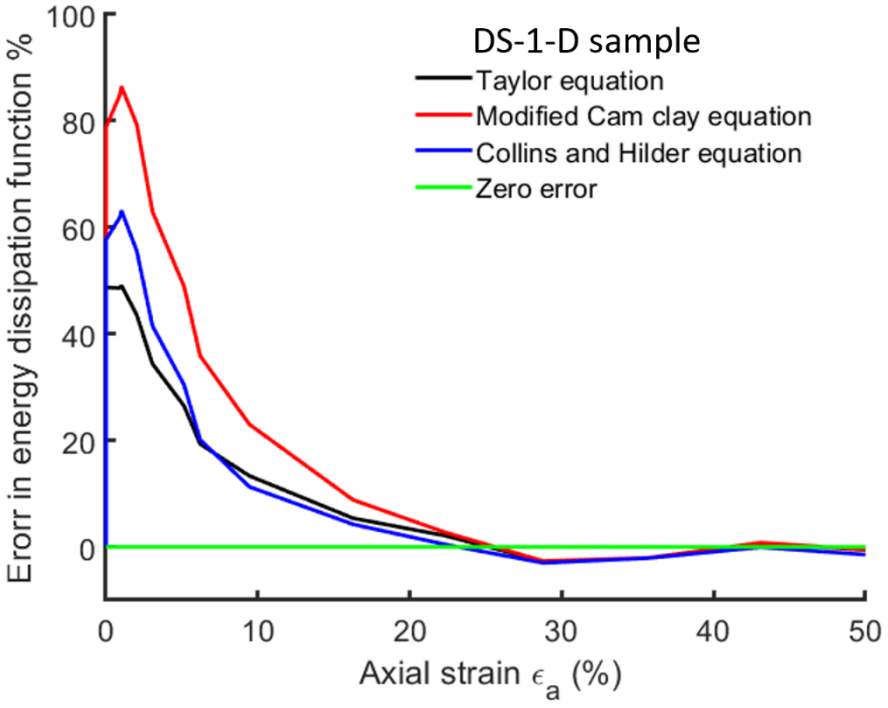
DS-1-D sample
Taylor equation
Modified Cam clay equation
Collins and Hilder equation
Zero error
Erorr in energy dissipation function %
Axial strain ϵ_a (%)
100
80
60
40
20
0
0
10
20
30
40
50

(a)

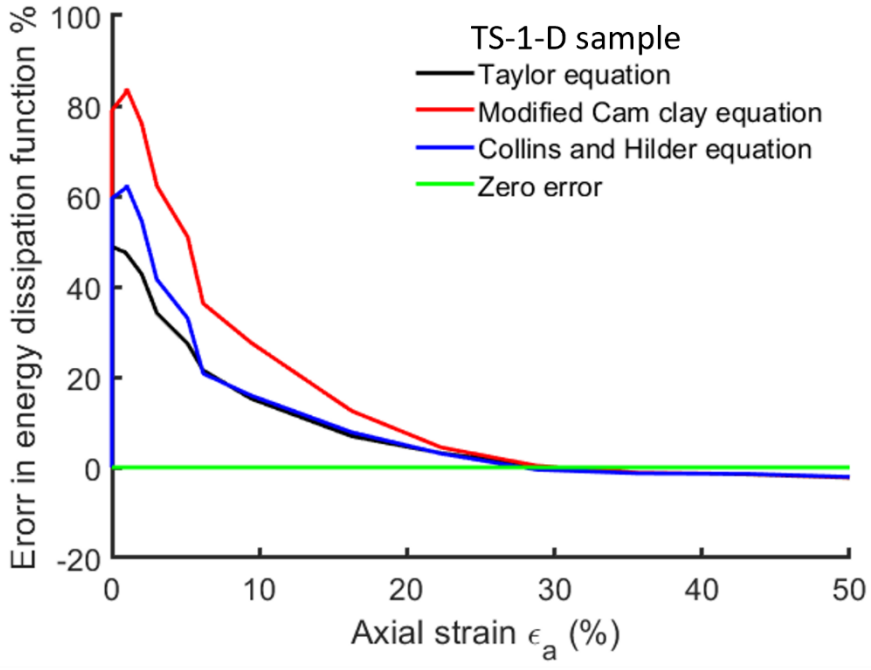
TS-1-D sample
Taylor equation
Modified Cam clay equation
Collins and Hilder equation
Zero error
Erorr in energy dissipation function %
Axial strain ϵ_a (%)
100
80
60
40
20
0
-20
0
10
20
30
40
50

(b)

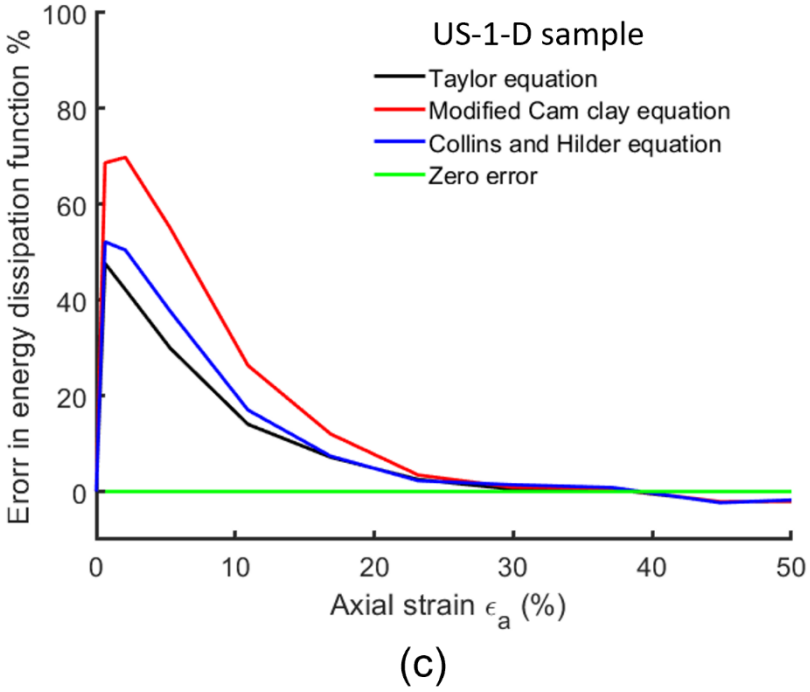

Figure 6.3 Error of the dissipation function as a percentage of DEM energy dissipation, positive error means over-prediction; a) sample DS-1-D (Dunkirk sand-PSD); b) sample TS-1-D (Toyoura sand-PSD); c) sample US-1-D (Uniform-PSD).

6.4 Proposed dissipation function based on DEM results

The analysis presented in the previous section demonstrates that none of the existing dissipation functions can provide a reasonable prediction for the DEM results and more error is observed before the critical state. The prediction is good at the critical state when there is no increment of volumetric strain. It is therefore inferred that the volumetric strain increment term should be revised in these equations. Even though the equation by Taylor does not include the contribution of the volumetric strain, it does produce results similar to the equation by Collins and Hilder that include the volumetric strain contribution. In this work, the modification of energy dissipation focuses primarily on the contribution of volumetric strain to the dissipation function. Based on the results of this study, a modified dissipation function is proposed as follows:

$$\delta\Phi = p\sqrt{\left(M\delta\varepsilon_q^p\right)^2 - \left(\delta\varepsilon_v^p\right)^2} \tag{6.15}$$

This function differs from both the modified Cam Clay model function and the thermomechanical function (Collins and Hilder, 2002, Roscoe and Burland, 1968, Taylor, 1948) in several aspects. Firstly, while the modified Cam Clay model function and the thermomechanical function are developed based on theoretical formulations, this function is developed through curve fitting. Secondly, this function aligns with the modified Cam Clay model function by using 'p' instead of 'p_c'. This is because using p_c' in the equation leads to an overestimation of the energy dissipation. Although Collins recommends that any energy dissipation function should rely on consolidation pressure, this can result in an overestimation of the actual amount of energy dissipation. Finally, the contribution of plastic volumetric strain in this function deviates from both the modified Cam Clay model function and the thermomechanical function. However, it has been observed that incorporating this contribution yields the most accurate fitting of the curve to the DEM results. Figure 6.4 a, b and c show comparisons between the prediction of Equation (6.15) and the DEM result for samples DS-1-D, TS-1-D, and US-1-D respectively. The results show that the modified dissipation function provides a good prediction of energy dissipation measured in DEM simulations for samples with different PSDs.

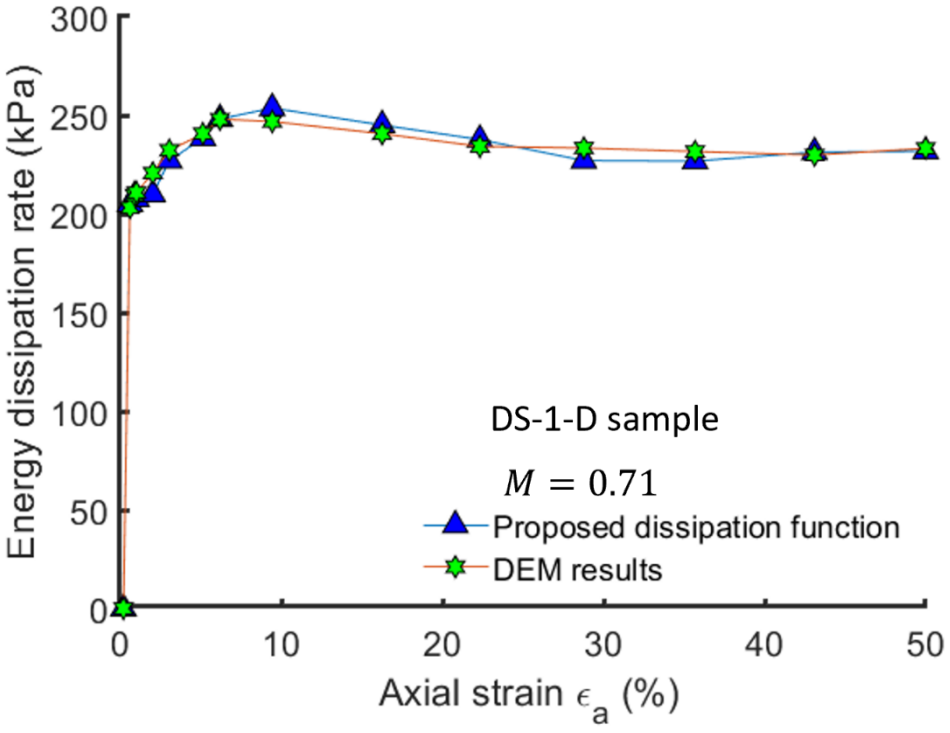
Energy dissipation rate (kPa)
300
250
200
150
100
50
0
0
10
20
30
40
50
Axial strain ϵ_a (%)
DS-1-D sample
$M = 0.71$
Proposed dissipation function
DEM results

(a)

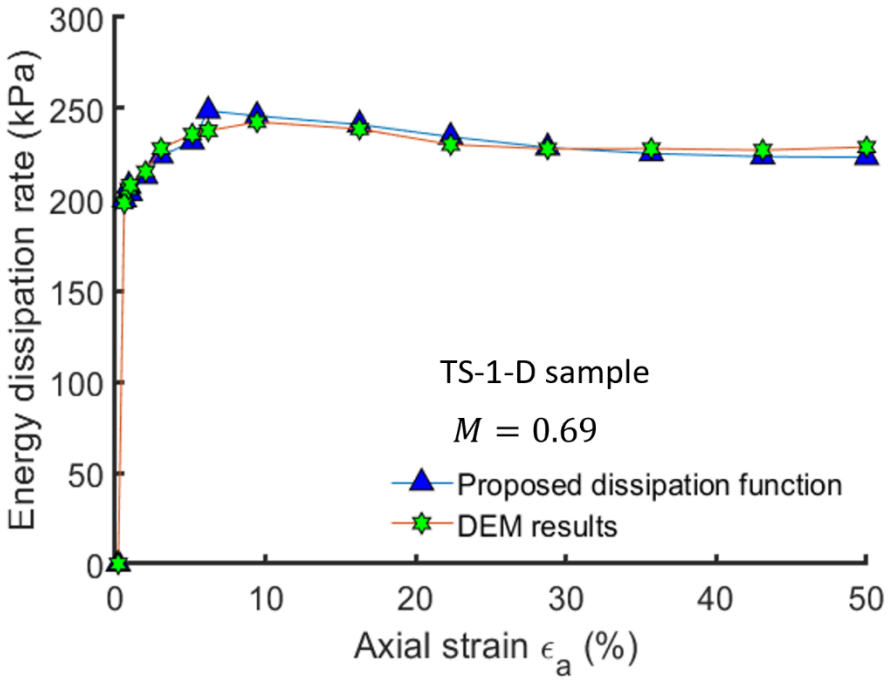

(b)

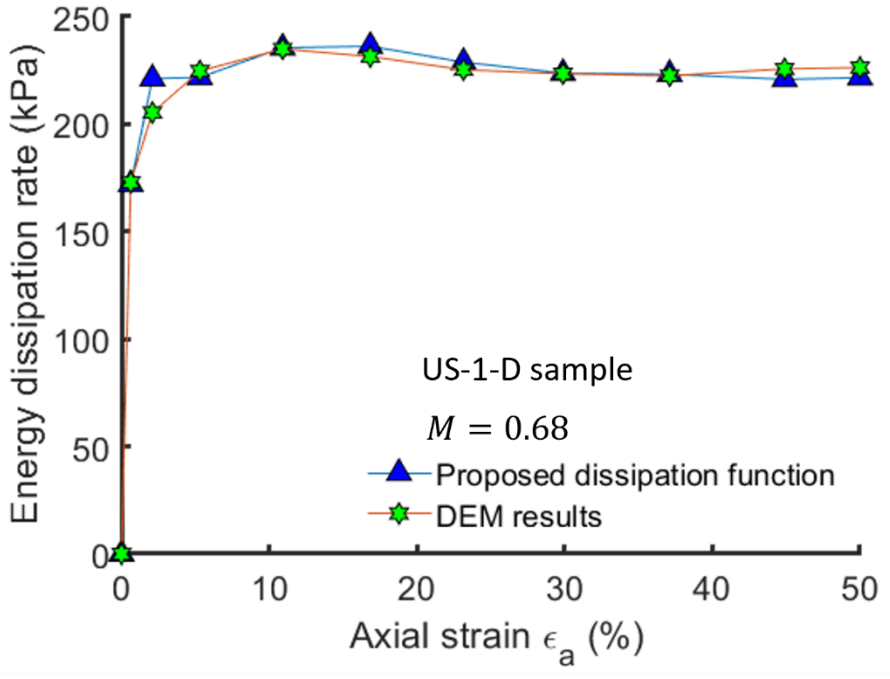

(c)

Figure 6.4 Compare the prediction of new modified dissipation functions with the energy dissipation obtained from DEM simulations; a) sample DS-1-D (Dunkirk sand-PSD); b) sample TS-1-D (Toyoura sand-PSD); c) sample US-1-D (Uniform-PSD).

6.5 Stored plastic work equation.

The investigation reveals that the stored plastic work is significantly smaller than the dissipated energy and remains constant once the critical state is attained. Therefore, it is reasonable to consider expressing the stored plastic work rate in terms of the volumetric strain increment, which is zero at the critical state, as proposed by Collins (2005).

However, the stored plastic function suggested by Collins, 2005 exhibits a noteworthy issue of excessively overpredicting the stored plastic work. This is demonstrated in Figure *6.5*, where the predictions deviate from the actual values. Additionally, the findings in chapter 5 indicate that the evolution of stored plastic work is influenced by the particle size distribution (PSD).

In this study, the stored plastic work equation is proposed as below:

$$\delta\Psi^p = (\delta p/\alpha)\delta\varepsilon_v^p \tag{6.16}$$

where α is a parameter that is dependent on the PSD. Note that δp is typically much smaller than p or p_c which are used in the energy dissipation equations. This eventually makes the stored plastic work rate much smaller than the energy dissipation rate, which has been observed in the DEM simulations. A comparison is made between the prediction of this function and the measured stored plastic work in Figure *6.6*. This analysis is carried out for each of the PSDs that were used for this investigation. The results demonstrate that Equation 16 offers a good prediction for all samples. The α value varies with the PSD of the samples, with $\alpha = 0.1$, $\alpha = 0.2$ and $\alpha = -0.2$ for DS-1-D, TS-1-D and US-1-D, respectively.

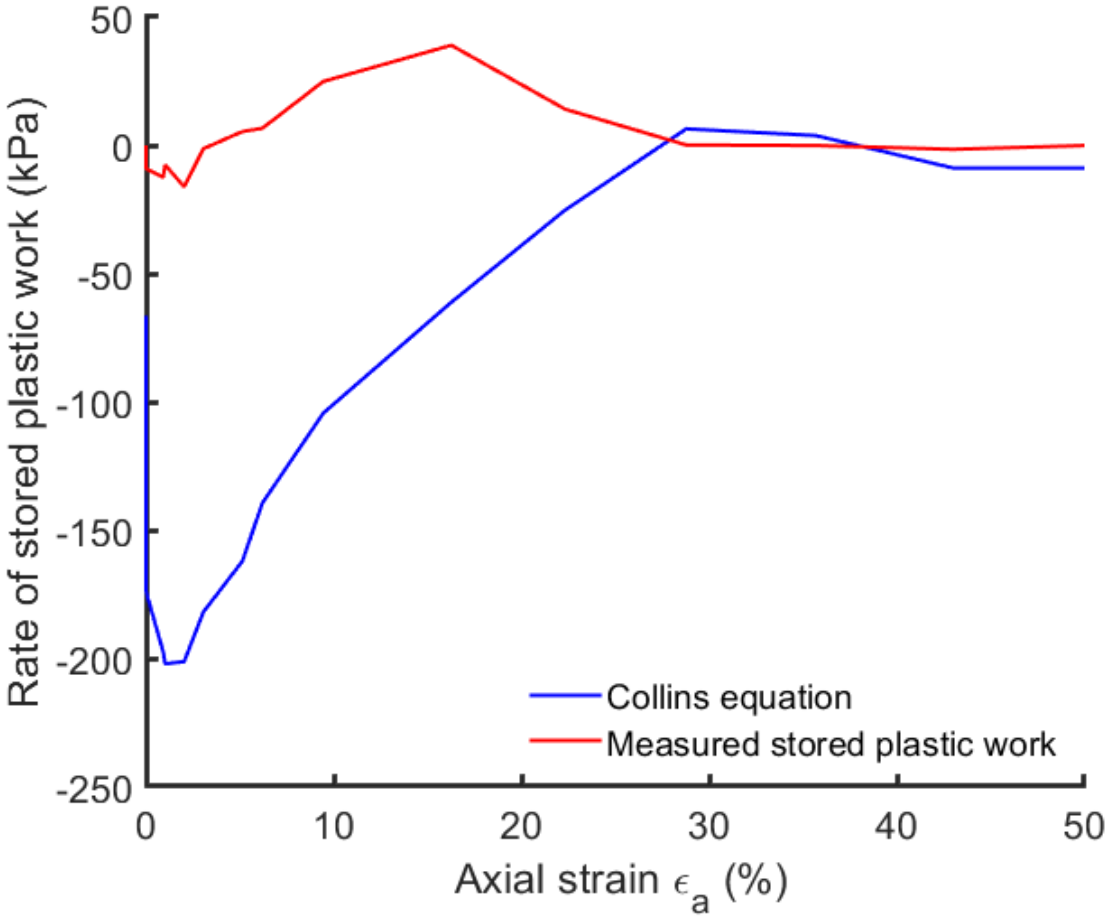

Figure 6.5 Comparison between the measured stored plastic work with the prediction of Collins equation for the sample DS-1-D (Dunkirk sand-PSD).

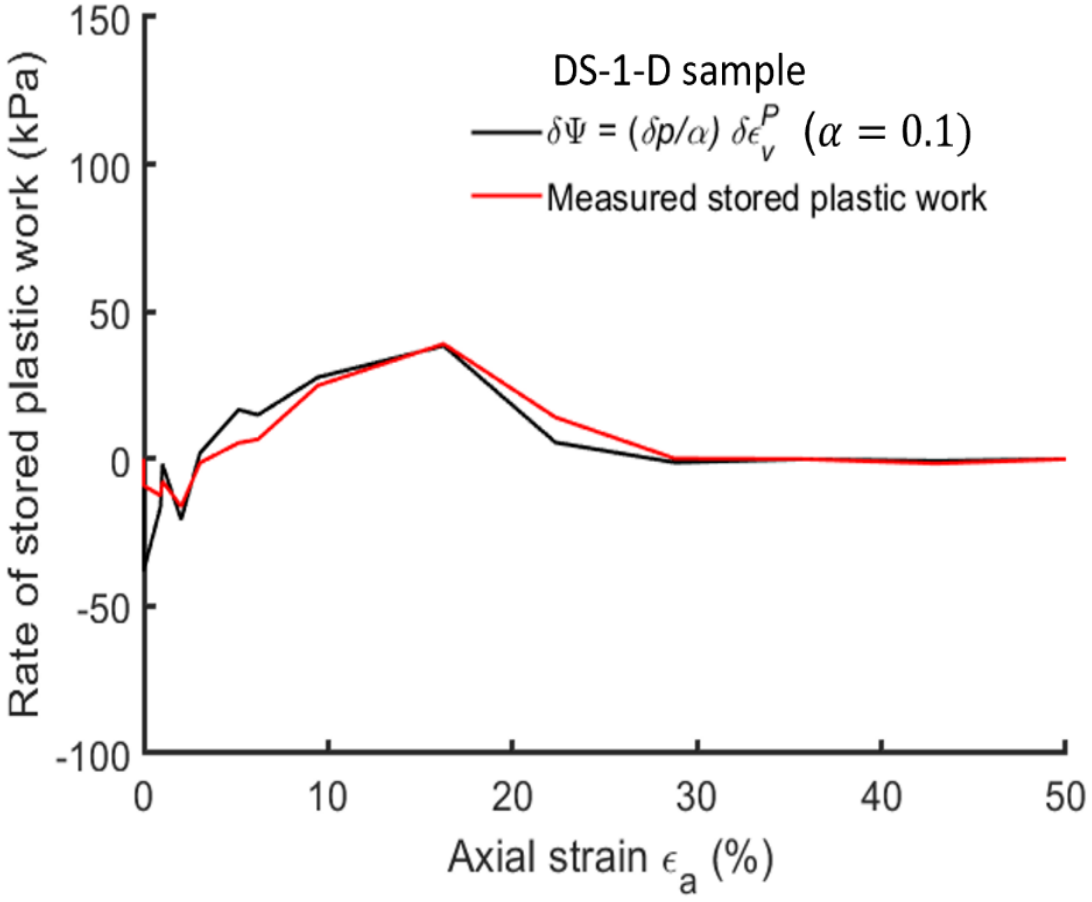
DS-1-D sample
$\delta\Psi = (\delta p/\alpha)\ \delta\epsilon_v^P \quad (\alpha = 0.1)$
Measured stored plastic work
Rate of stored plastic work (kPa)
150
100
50
0
-50
-100
0
10
20
30
40
50
Axial strain ϵ_a (%)

(a)

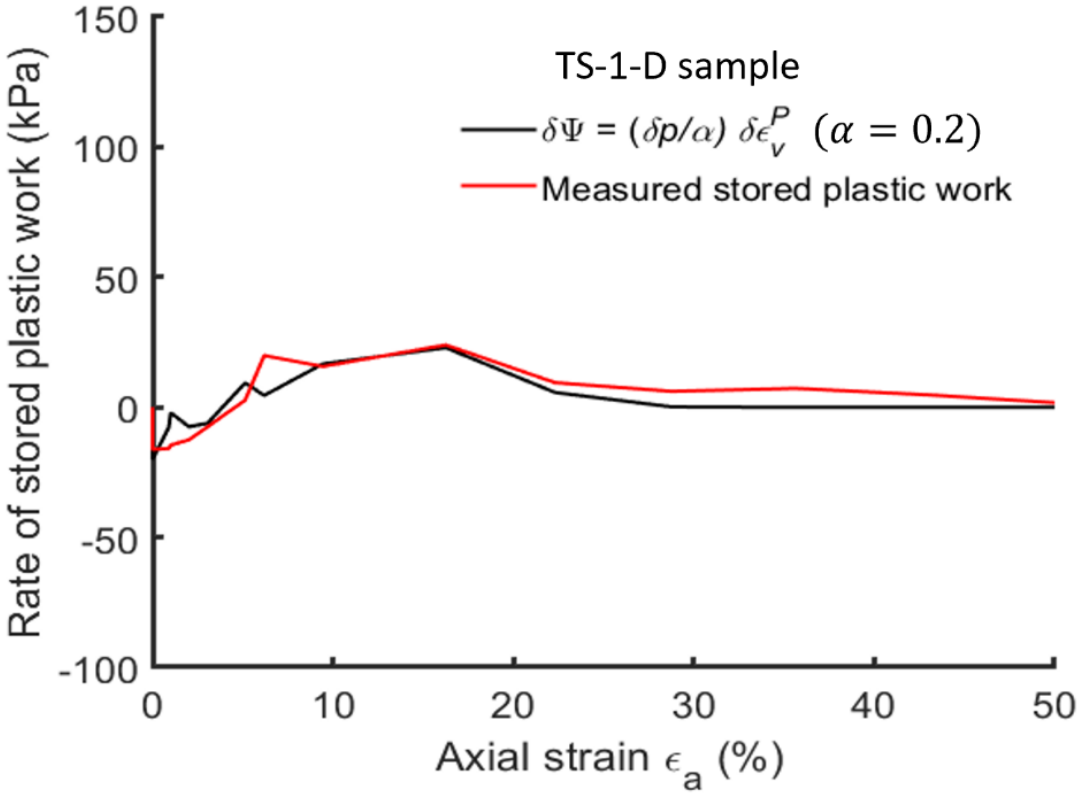
TS-1-D sample
$\delta\Psi = (\delta p/\alpha)\ \delta\epsilon_v^P \quad (\alpha = 0.2)$
Measured stored plastic work
Rate of stored plastic work (kPa)
150
100
50
0
-50
-100
0
10
20
30
40
50
Axial strain ϵ_a (%)

(b)

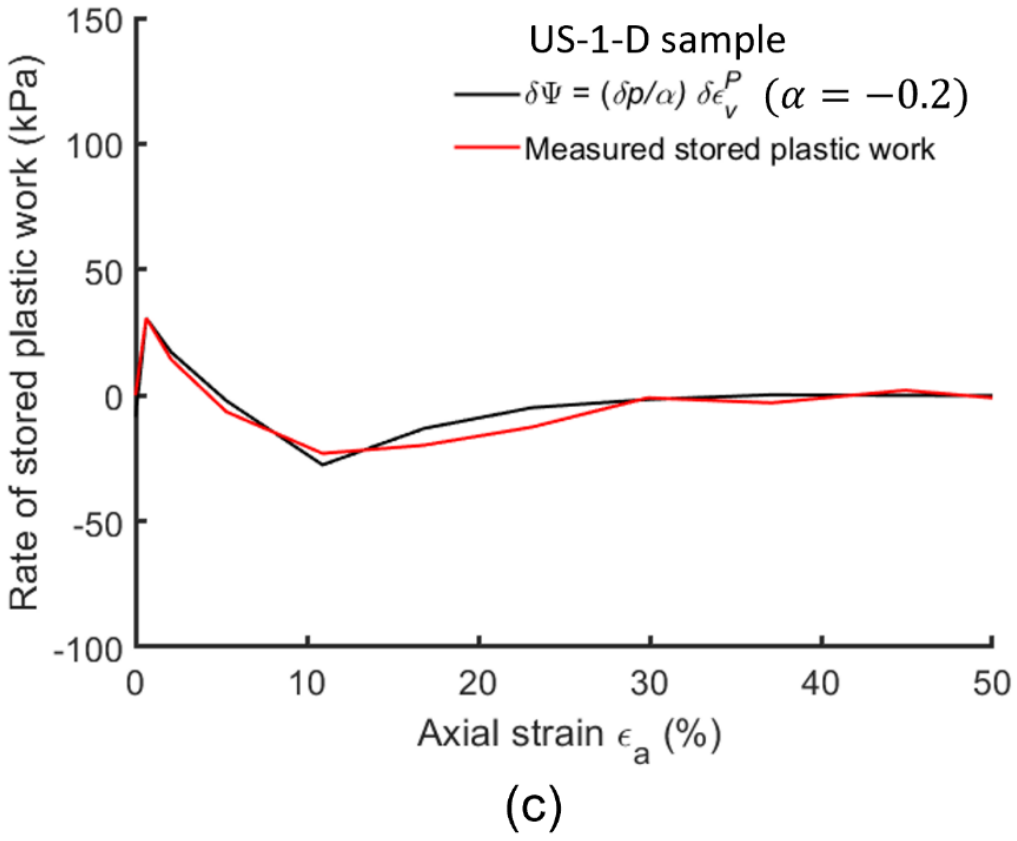

Figure 6.6 Compare the measured stored plastic work with the prediction of the proposed function for the stored plastic work; a) sample DS-1-D (Dunkirk sand-PSD); b) sample TS-1-D (Toyoura sand-PSD); c) sample US-1-D (Uniform-PSD).

6.6 Conclusions

This chapter discusses and evaluated multiple functions for energy dissipation that have been suggested in prior research. Nonetheless, these functions have not been quantitatively confirmed. Using DEM simulation, this chapter examines some of the dissipation functions. And provide some modifications for the dissipation function to provide a good prediction for the energy dissipation. The findings of this chapter are summarised as follows:

- Most of the dissipation functions overestimated the amount of energy dissipation, especially before the critical state. However, At the critical state, all these functions provide good results that match the DEM simulation results.
- It has been found that the error of the energy dissipation functions (Taylor equation, modified Cam Clay equation and Collins and Hilder equation) is not negligible, ranging from 60 to 80%. Due to this error, a new modified dissipation function has been proposed which provides good prediction even with different particle distributions.
- The development of a new stored work plastic function was analysed. As the quantity of stored plastic is quite little, the appropriate work function for stored plastic should rely on the pressure increment rather than the total. An equation stored plastic work was proposed. It has been discovered that function is capable of providing satisfactory results when dealing with actual particle size distribution.

Chapter 7: Conclusion

7.1 Summary

The overall objective of this research is to study the mechanical behaviour of energy dissipation under three-dimensional loading conditions using DEM. The work primarily aimed to accomplish three main objectives. First, studying the interparticle behaviour of the energy dissipation by analysing the relationship between energy dissipation and contact networks. Secondly, this work investigates the difference between energy dissipation and plastic work by studying the stored plastic work during triaxial shearing. Finally, this work evaluates some existing dissipation functions and stored plastic work functions. Additionally, based on the DEM data, alternative equations for dissipation and stored plastic work will be proposed. These objectives were split into three main chapters.

Chapter 4 of the thesis investigated the relationship between energy dissipation and contact networks. A series of drained triaxial tests have been carried out using a modified version of LAMMPS (Plimpton, 1995). DEM samples were created containing 8262 spherical particles with a minimum diameter of 0.1 mm and a maximum diameter of 0.14 mm. Two different initial density samples were created in dense and loose states. The sample sheared with different stress paths (constant σ_r and constant p) and different confining pressure (250,500 and 1000 kPa). The energy dissipation was analysed using two existing contact force network partitioning approaches, one based on the average contact force magnitude and the other on the contribution of contact forces to the global deviator stress. The contribution of contact networks to stress transmission was used to examine both partitioning techniques. In addition, the contribution of contact networks (strong and weak) to sliding and energy dissipation was evaluated based on both partitioning methods.

In chapter 5 an investigation of the stored plastic work in granular materials was provided. This work mainly focuses on clarifying a common misconception about plastic work and energy dissipation. This misconception was created long ago assuming that all plastic work is dissipated by friction. Using theoretical and computational formulations physical meaning of stored plastic work has been discussed. Using DEM modelling, this chapter conducted a

numerical analysis of energy dissipation and stored plastic work during triaxial shearing to a critical state. Investigating the influence of particle size distribution on energy dissipation and stored plastic work. Three distinct PSDs were used to generate three samples with varying particle counts. A probe test approach was used to evaluate the elastic and plastic strains of the specimens during shearing.

In Chapter 6, DEM simulations were utilised to investigate the prediction of some energy dissipation functions and stored plastic work described in prior research. In addition, the impact of the various PSDs on the prediction of these functions was assessed. Based on data DEM simulations, modification of the dissipation function and stored plastic work function is carried out.

7.2 Key finding

The primary findings that have emerged from the relationship between energy dissipation and contact networks (Chapter 4) are:

- Weak networks exhibit more interparticle sliding and energy dissipation when the average contact force partitioning method is used. Since strong contacts have higher contact forces, they dissipate five times more energy per sliding contact.
- When the deviator stress partitioning method is used, sliding is still more prevalent in weak contacts. However, the percentage of strong contact sliding has increased somewhat compared to the average contact force partitioning data. This increase in sliding in strong contacts has led to an increase in energy dissipation.
- It is observed that the strong and weak contacts both contribute significantly to the total amount of energy dissipation when both partitioning methods are utilised. Consequently, a new threshold of $f_n/\langle f_n \rangle$ is proposed for partitioning the contact network based on the contribution to energy dissipation. Specifically, it is observed that $f_n/\langle f_n \rangle = 2$ can be used to identify whether the contact contributes to the dissipation of energy or not, which contacts

with $f_n/\langle f_n \rangle \leq 2$ dissipate more than 93% of total energy dissipation

The findings that have emerged from the stored plastic work in granular materials (Chapter 5) are:

- This investigation confirms that some of the plastic work is being stored during the triaxial shearing. However, the stored plastic work was only observed before the critical state with its rate differing from negative to positive. At the critical state, the rate of stored plastic work becomes constant, and its mechanism no longer varies. At the critical point, the total applied work equals the total energy, which indicates that no more plastic work will be stored in the sample.
- It was also observed that the varied PSDs utilised in this study affected the quantity of stored plastic work, with samples with real PSD exhibiting a larger amount of stored plastic work. Even though the quantity of stored plastic is not extremely high in general. However, stored plastic work must always be included during the development of constitutive models that include energy analysis. To ensure that the fundamental concept of thermodynamics is constantly respected.
- There is a similar pattern of energy dissipation for all PSDs used in this study, although the amounts of dissipation varied slightly.

The findings that have emerged from the energy dissipation and stored plastic work functions in modelling granular materials. (Chapter 6)

- The majority of the dissipation functions that have been evaluated in this chapter showed an overestimation of the amount of energy dissipation, particularly before the critical state. Nevertheless, when the test reaches the critical state, all of these functions provide accurate results that agree with the DEM simulation findings.
- It has been shown that the estimated error for the evaluated functions ranges between 60 and 80 %. However, at the critical state, this error fell dramatically to almost zero. An alternative equation for dissipation has been suggested, and it has been shown that this function delivers a very excellent prediction for the energy dissipation, which is comparable to the results of the DEM simulation. It has also been discovered that this function produces correct results even when the PSD used is different.

- Analysis was provided to develop a new stored work plastic function. As the quantity of stored plastic is quite little, the appropriate work function for stored plastic should rely on the pressure increment rather than the total. An equation for stored plastic work was proposed. It has been discovered that function can provide good results for all the particle size distributions used in this investigation.

7.3 Future work

As with any research study, the study is not thorough, and the results indicate the need for more research. Following the main structure of the thesis, the suggestions for future study are categorised for each of the works presented in this thesis.

- The relationship between energy dissipation and contact network in granular materials (Chapter 4).

Explore how different particle shapes (non-spherical particles) impact the energy dissipation behaviour in granular materials. This could involve conducting DEM simulations with various particle shapes and comparing their energy dissipation patterns to understand shape-dependent effects. In addition, Investigate how variations in material properties affect energy dissipation and the evolution of contact networks.

- Stored plastic work and energy dissipation in granular materials (Chapter 5).

Although the scope of this current work has been accomplished, there is potential for further extension to investigate the impact of various particle shapes on the magnitude of stored plastic work.

- Energy dissipation and stored plastic work functions in modelling granular materials.

The suggested energy dissipation function and stored plastic work function have demonstrated remarkable predictive accuracy. However, their underlying physical significance remains uncertain, warranting further research to determine their applicability in

determining the elasticity law, yield function, flow rule, and hardening rule. While thermodynamic functions for both energy dissipation and stored plastic work may not yield results similar to DEM results, investigating the reasons behind this discrepancy should be considered as a potential area of future research. Furthermore, both functions proposed in this study were originally developed based on spherical particles. However, it is crucial to conduct further investigation to assess the predictive capability of these functions when applied to particles with different shapes. Understanding the limitations and potential improvements of these functions can enhance their effectiveness and broaden their applications in granular material analysis.

References

ASTM (2011) Standard Test Method for Consolidated Drained Triaxial Compression Test for Soils. doi:10.1520/D7181.

Alshibli, K. A. & Cil, M. B. (2018) Influence of particle morphology on the friction and dilatancy of sand. *Journal of Geotechnical and Geoenvironmental Engineering* **144(3)**:04017118.

Andreotti, B., Forterre, Y. & Pouliquen, O. (2013) *Granular media: between fluid and solid.* Cambridge University Press.

Arevalo, R., Zuriguel, I. & Maza, D. (2009) Topological properties of the contact network of granular materials. *International Journal of Bifurcation and Chaos* **19(02)**:695-702.

Asmar, B., Langston, P., Matchett, A. & Walters, J. K. (2003) Energy monitoring in distinct element models of particle systems. *Advanced Powder Technology* **14(1)**:43-69.

Bagi, K. (1996) Stress and strain in granular assemblies. *Mechanics of Materials* **22(3)**:165-177.

Barreto, D. & O'sullivan, C. (2012) The influence of inter-particle friction and the intermediate stress ratio on soil response under generalised stress conditions. *Granular Matter* **14(4)**:505-521.

Been, K. & Jefferies, M. (1986) Discussion: A state parameter for sands. *geotechnique* **36(1)**:123-132.

Berrill, J. & Davis, R. (1985) Energy dissipation and seismic liquefaction of sands: revised model. *Soils and Foundations* **25(2)**:106-118.

Besseling, J. F. & Van Der Giessen, E. (1994) *Mathematical modeling of inelastic deformation.* CRC Press.

Burland, J. (1965) Correspondence on The yielding and dilation of clay. *geotechnique* **15(2)**:211-214.

Capozza, R. & Hanley, K. J. (2021) A hierarchical, spherical harmonic-based approach to simulate abradable, irregularly shaped particles in DEM. *Powder technology* **378**:528-537.

Casagrande, A. (1936) Characteristics of cohesionless soils affecting the stability of slopes and earth fills. *J. Boston Society of Civil Engineers* **23(1)**:13-32.

Chen, Y.-C., Ishibashi, I. & Jenkins, J. (1988) Dynamic shear modulus and fabric: part I, depositional and induced anisotropy. *geotechnique* **38(1)**:25-32.

Cho, G.-C., Dodds, J. & Santamarina, J. C. (2006) Particle shape effects on packing density, stiffness, and strength: natural and crushed sands. *Journal of Geotechnical and Geoenvironmental Engineering* **132(5)**:591-602.

Collins, I. (1997) The use of Legendre transformations in developing the constitutive laws of geomechanics from thermodynamic principles. In *IUTAM Symposium on Mechanics of Granular and Porous Materials*.) Springer, pp. 151-159.

Collins, I. (2002) Associated and non-associated aspects of the constitutive laws for coupled elastic/plastic materials. *The International Journal Geomechanics* **2(2)**:259-267.

Collins, I. (2005) The concept of stored plastic work or frozen elastic energy in soil mechanics. *geotechnique* **55(5)**:373-382.

Collins, I. & Houlsby, G. (1997) Application of thermomechanical principles to the modelling of geotechnical materials. *Proceedings of the Royal Society of London. Series A: Mathematical, Physical and Engineering Sciences* **453(1964)**:1975-2001.

Collins, I. & Kelly, P. (2002) A thermomechanical analysis of a family of soil models. *geotechnique* **52(7)**:507-518.

Collins, I. & Muhunthan, B. (2003) On the relationship between stress–dilatancy, anisotropy, and plastic dissipation for granular materials. *geotechnique* **53(7)**:611-618.

Collins, I. F. & Hilder, T. (2002) A theoretical framework for constructing elastic/plastic constitutive models of triaxial tests. *International Journal for Numerical and Analytical Methods in Geomechanics* **26(13)**:1313-1347.

Cundall, P. (1988) Computer simulations of dense sphere assemblies. In *Studies in Applied Mechanics*.) Elsevier, vol. 20, pp. 113-123.

Cundall, P. A. (1989) Evolution of elastic moduli in a deforming granular assembly. *S ELECTE*:59.

Cundall, P. A. & Strack, O. D. (1979) A discrete numerical model for granular assemblies. *geotechnique* **29(1)**:47-65.

Da Cruz, F., Emam, S., Prochnow, M., Roux, J.-N. & Chevoir, F. (2005) Rheophysics of dense granular materials: Discrete simulation of plane shear flows. *Physical review E* **72(2)**:021309.

Dantu, P. (1957) A contribution to the mechanical and geometrical study of non-cohesive masses. In *Pros. 4th Int. Conf. Soil Mech. and Found. Eng.*), pp. 144-148.

De Josselin De Jong, G. (1969) Etude photoelastique d'un empilement de disques. *Cah. Grpe fr. Etud. Rheol.* **2**:73-86.

Dugdale, J. S. (1996) *Entropy and its physical meaning.* CRC Press.

El Shamy, U. & Denissen, C. (2010) Microscale characterization of energy dissipation mechanisms in liquefiable granular soils. *Computers and Geotechnics* **37(7-8)**:846-857.

El Shamy, U. & Denissen, C. (2012) Microscale energy dissipation mechanisms in cyclically-loaded granular soils. *Geotechnical and Geological Engineering* **30(2)**:343-361.

Estrada, N., Taboada, A. & Radjai, F. (2008) Shear strength and force transmission in granular media with rolling resistance. *Physical review E* **78(2)**:021301.

Ferellec, J.-F. & Mcdowell, G. R. (2010) A method to model realistic particle shape and inertia in DEM. *Granular Matter* **12(5)**:459-467.

Fu, P. & Dafalias, Y. F. (2011) Fabric evolution within shear bands of granular materials and its relation to critical state theory. *International Journal for Numerical and Analytical Methods in Geomechanics* **35(18)**:1918-1948.

Gajo, A. & Muir Wood, D. (1999) Severn–Trent sand: a kinematic-hardening constitutive model: the q–p formulation. *geotechnique* **49(5)**:595-614.

Gao, X., Yu, J., Portal, R. J., Dietiker, J.-F., Shahnam, M. & Rogers, W. A. (2022) Development and validation of SuperDEM for non-spherical particulate systems using a superquadric particle method. *Particuology* **61**:74-90.

Gens, A. & Potts, D. (1988) Critical state models in computational geomechanics. *Engineering Computations* **5(3)**:178-197.

Göncü, F. & Luding, S. (2013) Effect of particle friction and polydispersity on the macroscopic stress–strain relations of granular materials. *Acta Geotechnica* **8(6)**:629-643.

Gong, J., Wang, X., Li, L. & Nie, Z. (2019) DEM study of the effect of fines content on the small-strain stiffness of gap-graded soils. *Computers and Geotechnics* **112**:35-40.

Group, I. C. (2008) *PFC3D: particle flow code in three dimensions user's guide.* 4th edn edn. Minneapolis,MN, USA, Itasca Consulting Group.

Gu, X., Huang, M. & Qian, J. (2014) DEM investigation on the evolution of microstructure in granular soils under shearing. *Granular Matter* **16(1)**:91-106.

Gu, X., Lu, L. & Qian, J. (2017) Discrete element modeling of the effect of particle size distribution on the small strain stiffness of granular soils. *Particuology* **32**:21-29.

Gu, X., Yang, J. & Huang, M. (2013) DEM simulations of the small strain stiffness of granular soils: effect of stress ratio. *Granular Matter* **15(3)**:287-298.

Guo, N. & Zhao, J. (2013) The signature of shear-induced anisotropy in granular media. *Computers and Geotechnics* **47**:1-15.

Guo, P. (2012) Critical length of force chains and shear band thickness in dense granular materials. *Acta Geotechnica* **7(1)**:41-55.

Hanley, K. J., Huang, X. & O'sullivan, C. (2018) Energy dissipation in soil samples during drained triaxial shearing. *geotechnique* **68(5)**:421-433.

Hanley, K. J., Huang, X., O'sullivan, C. & Kwok, F. C. (2014) Temporal variation of contact networks in granular materials. *Granular Matter* **16(1)**:41-54.

Harmon, J. M., Karapiperis, K., Li, L., Moreland, S. & Andrade, J. E. (2021) Modeling connected granular media: Particle bonding within the level set discrete element method. *Computer Methods in Applied Mechanics and Engineering* **373**:113486.

Head, K. H. (1980) Permeability, shear strength and compressibility tests. *Manual of Soil Laboratory Testing* **2**:747p.

Horne, M. R. (1969) The behaviour of an assembly of rotund, rigid, cohesionless particles. Ill. *Proceedings of the Royal Society of London. A. Mathematical and Physical Sciences* **310(1500)**:21-34.

Houlsby, G. & Puzrin, A. (2000) A thermomechanical framework for constitutive models for rate-independent dissipative materials. *International journal of Plasticity* **16(9)**:1017-1047.

Houlsby, G. T. (1981) Study of plasticity theories and their applicability to soils.) University of Cambridge.

Huang, X. (2014) Exploring Critical-state Behaviour Using DEM.) Imperial College London London.

Huang, X., Hanley, K. J., O'sullivan, C. & Kwok, C. Y. (2014a) Exploring the influence of interparticle friction on critical state behaviour using DEM. *International Journal for Numerical and Analytical Methods in Geomechanics* **38(12)**:1276-1297.

Huang, X., Hanley, K. J., O'sullivan, C. & Kwok, F. C. (2014b) Effect of sample size on the response of DEM samples with a realistic grading. *Particuology* **15**:107-115.

Huang, X., Hanley, K. J., O'sullivan, C. & Kwok, C.-Y. (2017a) Implementation of rotational resistance models: a critical appraisal. *Particuology* **34**:14-23.

Huang, X., O'sullivan, C., Hanley, K. J. & Kwok, C.-Y. (2017b) Partition of the contact force network obtained in discrete element simulations of element tests. *Computational Particle Mechanics* **4(2)**:145-152.

Iwan, W. D. (1967) On a class of models for the yielding behavior of continuous and composite systems. *Journal of Applied Mechanics* **34(3)**:612-617.

Iwashita, K. & Oda, M. (1998) Rolling resistance at contacts in simulation of shear band development by DEM. *Journal of Engineering Mechanics* **124(3)**:285-292.

Jaeger, H. M., Nagel, S. R. & Behringer, R. P. (1996) Granular solids, liquids, and gases. *Reviews of modern physics* **68(4)**:1259.

Jefferies, M. (1993) Nor-Sand: a simle critical state model for sand. *geotechnique* **43(1)**:91-103.

Jefferies, M. (1997) Plastic work and isotropic softening in unloading. *geotechnique* **47(5)**:1037-1042.

Jefferies, M. & Shuttle, D. (2002) Dilatancy in general Cambridge-type models. *geotechnique* **52(9)**:625-638.

Jiang, M., Shen, Z. & Wang, J. (2015) A novel three-dimensional contact model for granulates incorporating rolling and twisting resistances. *Computers and Geotechnics* **65**:147-163.

Keishing, J., Huang, X. & Hanley, K. J. (2020) Energy dissipation in soil samples during cyclic triaxial simulations. *Computers and Geotechnics* **121**:103481.

Kozicki, J., Tejchman, J. & Mróz, Z. (2012) Effect of grain roughness on strength, volume changes, elastic and dissipated energies during quasi-static homogeneous triaxial compression using DEM. *Granular Matter* **14(4)**:457-468.

Kruyt, N. P. (2016) On weak and strong contact force networks in granular materials. *International journal of solids and structures* **92**:135-140.

Kruyt, N. P. & Rothenburg, L. (2006) Shear strength, dilatancy, energy and dissipation in quasi-static deformation of granular materials. *Journal of Statistical Mechanics: Theory and Experiment* **2006(07)**:P07021.

Langston, P., Ai, J. & Yu, H.-S. (2013) Simple shear in 3D DEM polyhedral particles and in a simplified 2D continuum model. *Granular Matter* **15(5)**:595-606.

Law, K. T., Cao, Y. & He, G. (1990) An energy approach for assessing seismic liquefaction potential. *Canadian Geotechnical Journal* **27(3)**:320-329.

Lee, S. J., Hashash, Y. M. & Nezami, E. G. (2012) Simulation of triaxial compression tests with polyhedral discrete elements. *Computers and Geotechnics* **43**:92-100.

Lemaitre, J. & Chaboche, J. (1990) Mechanics of Solid Materials University Press.) Cambridge.

Li, X. & Li, X.-S. (2009) Micro-macro quantification of the internal structure of granular materials. *Journal of Engineering Mechanics* **135(7)**:641-656.

Liu, J., Nicot, F., Wautier, A. & Zhou, W. (2019a) Role of sliding contacts in shear banding affecting granular materials. In *International Conference on Particle-Based Methods (Particles)-6. International Conference on Particle-Based Methods: fundamentals and applications (Particles 2019)*.) International Centre for Numerical Methods in Engineering, pp. 46-56.

Liu, J., Zhou, W., Ma, G., Yang, S. & Chang, X. (2020) Strong contacts, connectivity and fabric anisotropy in granular materials: a 3D perspective. *Powder technology* **366**:747-760.

Liu, T., Chen, H., Buckley, R. M., Quinteros, V. S. & Jardine, R. J. (2019b) Characterisation of sand-steel interface shearing behaviour for the interpretation of driven pile behaviour in sands. In *E3S Web of Conferences*.) EDP Sciences, vol. 92, pp. 13001.

Liu, Y., Yin, Z., Hicher, P., Wang, J. & Xia, X. (2013) Macro and micro analysis for grading-dependent mechanical behavior of granular materials. In *Poromechanics V: Proceedings of the Fifth Biot Conference on Poromechanics*.), pp. 1082-1089.

Luong, M. P. (1986) Characteristic threshold and infrared vibrothermography of sand. *Geotechnical Testing Journal* **9(2)**:80-86.

Maeda, K., Sakai, H., Kondo, A., Yamaguchi, T., Fukuma, M. & Nukudani, E. (2010) Stress-chain based micromechanics of sand with grain shape effect. *Granular Matter* **12**:499-505.

Mair, R. (1993) Developments in geotechnical engineering research: application to tunnels and deep excavations. In *Proceedings of institution of civil engineers: civil engineering*.), vol. 93, pp. 27-41.

Manzari, M. T. & Dafalias, Y. F. (1997) A critical state two-surface plasticity model for sands. *geotechnique* **47(2)**:255-272.

Masson, S. & Martinez, J. (2001) Micromechanical analysis of the shear behavior of a granular material. *Journal of Engineering Mechanics* **127(10)**:1007-1016.

Maugin, G. A. (1992) *The thermomechanics of plasticity and fracture.* Cambridge University Press.

Maugin, G. A. (1999) *The thermomechanics of nonlinear irreversible behaviours.* World scientific.

Mróz, Z. (1973) *Mathematical models of inelastic material behaviour.* Solid Mechanics Division, University of Waterloo.

Muhunthan, B. & Olcott, D. (2002) Elastic energy and shear work. *geotechnique* **52(7)**:541-544.

Muir Wood, D. (1990) *Soil behaviour and critical state soil mechanics.* Cambridge university press.

Mukwiri, R., Ghaffari Motlagh, Y., Coombs, W. & Augarde, C. (2016) Energy dissipation in granular material under 1D compression.) Cardiff University.

Mukwiri, R., Motlagh, Y. G., Coombs, W. & Augarde, C. (2017) Energy dissipation in granular materials in triaxial tests. In *Proceedings of the 25th UKACM Conference on Computational Mechanics*.), vol. 12, pp. 13.

Ng, T.-T. (2009a) Discrete element method simulations of the critical state of a granular material. *International Journal of Geomechanics* **9(5)**:209-216.

Ng, T. T. (2009b) Particle shape effect on macro ‐ and micro ‐ behaviors of monodisperse ellipsoids. *International Journal for Numerical and Analytical Methods in Geomechanics* **33(4)**:511-527.

O'sullivan, C. (2011) *Particulate discrete element modelling: a geomechanics perspective.* CRC Press.

Oda, M. & Konishi, J. (1974) Microscopic deformation mechanism of granular material in simple shear. *Soils and Foundations* **14(4)**:25-38.

Oda, M., Konishi, J. & Nemat-Nasser, S. (1982) Experimental micromechanical evaluation of strength of granular materials: effects of particle rolling. *Mechanics of Materials* **1(4)**:269-283.

Okada, N. & Nemat-Nasser, S. (1994) Energy dissipation in inelastic flow of saturated cohesionless granular media. *geotechnique* **44(1)**:1-19.

Pena, A., Lizcano, A., Alonso‐Marroquin, F. & Herrmann, H. J. (2008) Biaxial test simulations using a packing of polygonal particles. *International Journal for Numerical and Analytical Methods in Geomechanics* **32(2)**:143-160.

Peña, A. A., García‐Rojo, R., Alonso‐Marroquín, F. & Herrmann, H. J. (2009) Investigation of the critical state in soil mechanics using DEM. In *AIP Conference Proceedings*.) American Institute of Physics, vol. 1145, pp. 185-188.

Perez, J. L., Kwok, C., Huang, X. & Hanley, K. (2016) Assessing the quasi-static conditions for shearing in granular media within the critical state soil mechanics framework. *Soils and Foundations* **56(1)**:152-159.

Peters, J., Muthuswamy, M., Wibowo, J. & Tordesillas, A. (2005) Characterization of force chains in granular material. *Physical review E* **72(4)**:041307.

Plimpton, S. (1995) Fast parallel algorithms for short-range molecular dynamics. *Journal of computational physics* **117(1)**:1-19.

Puzrin, A. & Houlsby, G. (2001) Fundamentals of kinematic hardening hyperplasticity. *International journal of solids and structures* **38(21)**:3771-3794.

Radjai, F. (2009) Force and fabric states in granular media. In *AIP conference proceedings*.) American Institute of Physics, vol. 1145, pp. 35-42.

Radjai, F. (2015) Modeling force transmission in granular materials. *Comptes Rendus Physique* **16(1)**:3-9.

Radjai, F., Roux, S. & Moreau, J. J. (1999) Contact forces in a granular packing. *Chaos: An Interdisciplinary Journal of Nonlinear Science* **9(3)**:544-550.

Radjai, F., Wolf, D., Roux, S., Jean, M. & Moreau, J. J. (1997) Force networks in dense granular media. In *Powders & grains 97*.), pp. 211-214.

Roscoe, K., Schofield, A. & Thurairajah, A. (1963) Yielding of clays in states wetter than critical. *geotechnique* **13(3)**:211-240.

Roscoe, K. H. & Burland, J. (1968) On the generalized stress-strain behaviour of wet clay.

Roscoe, K. H., Schofield, A. & Wroth, A. P. (1958) On the yielding of soils. *geotechnique* **8(1)**:22-53.

Rowe, P. W. (1962) The stress-dilatancy relation for static equilibrium of an assembly of particles in contact. *Proceedings of the Royal Society of London. Series A. Mathematical and Physical Sciences* **269(1339)**:500-527.

Schofield, A. (1999) A note on Taylor's interlocking and Terzaghi's" true cohesion" error. *Geotechnical News*.

Schofield, A. & Wroth, P. (1968a) *Critical state soil mechanics.* McGraw-Hill London.

Schofield, A. N. (2000) *Behaviour of a soil paste continuum.* University of Cambridge, Department of Engineering.

Schofield, A. N. & Wroth, P. (1968b) *Critical state soil mechanics.* McGraw-hill London.

Shi, J., Guo, P. & Stolle, D. (2018) Noncoaxiality between fabric and stress in two-dimensional granular materials. *Journal of Engineering Mechanics* **144(9)**:04018092.

Shin, H. & Santamarina, J. C. (2013) Role of particle angularity on the mechanical behavior of granular mixtures. *Journal of Geotechnical and Geoenvironmental Engineering* **139(2)**:353-355.

Shire, T. (2014) Micro-scale modelling of granular filters.) Imperial College London.

Shire, T., O'sullivan, C., Hanley, K. & Fannin, R. J. (2014) Fabric and effective stress distribution in internally unstable soils. *Journal of Geotechnical and Geoenvironmental Engineering* **140(12)**:04014072.

Suiker, A. S. & Fleck, N. A. (2004) Frictional collapse of granular assemblies. *J. Appl. Mech.* **71(3)**:350-358.

Taylor, D. W. (1948) *Fundamentals of soil mechanics.* LWW.

Thornton, C. (2000) Numerical simulations of deviatoric shear deformation of granular media. *geotechnique* **50(1)**:43-53.

Thornton, C. & Antony, S. (1998) Quasi–static deformation of particulate media. *Philosophical Transactions of the Royal Society of London. Series A: Mathematical, Physical and Engineering Sciences* **356(1747)**:2763-2782.

Thurairajah, A. (1962) Some shear properties of kaolin and of sand.) University of Cambridge.

Tordesillas, A. (2007) Force chain buckling, unjamming transitions and shear banding in dense granular assemblies. *Philosophical Magazine* **87(32)**:4987-5016.

Tordesillas, A., Hunt, G. & Shi, J. (2011) A characteristic length scale in confined elastic buckling of a force chain. *Granular Matter* **13(3)**:215-218.

Tordesillas, A. & Muthuswamy, M. (2009) On the modeling of confined buckling of force chains. *Journal of the Mechanics and Physics of Solids* **57(4)**:706-727.

Tordesillas, A., Steer, C. & Walker, D. M. (2014) Force chain and contact cycle evolution in a dense granular material under shallow penetration. *Nonlinear Processes in Geophysics* **21(2)**:505-519.

Trifunac, M. (1995) Empirical criteria for liquefaction in sands via standard penetration tests and seismic wave energy. *Soil Dynamics and Earthquake Engineering* **14(6)**:419-426.

Ulm, F.-J. & Coussy, O. (2003) *Mechanics and durability of solids: Solid Mechanics.* Prentice Hall.

Voivret, C., Radjai, F., Delenne, J.-Y. & El Youssoufi, M. S. (2009) Multiscale force networks in highly polydisperse granular media. *Physical review letters* **102(17)**:178001.

Walton, O. R. & Braun, R. L. (1986) Viscosity, granular‐temperature, and stress calculations for shearing assemblies of inelastic, frictional disks. *Journal of rheology* **30(5)**:949-980.

Wang, J. & Yan, H. (2012) DEM analysis of energy dissipation in crushable soils. *Soils and Foundations* **52(4)**:644-657.

Wang, J. F. & Huang, R. Q. (2014) DEM study on energy allocation behavior in crushable soils. In *Advanced Materials Research*.) Trans Tech Publ, vol. 871, pp. 119-123.

Wang, S. & Ji, S. (2022) A unified level set method for simulating mixed granular flows involving multiple non-spherical DEM models in complex structures. *Computer Methods in Applied Mechanics and Engineering* **393**:114802.

Wei, D., Wang, J., Nie, J. & Zhou, B. (2018) Generation of realistic sand particles with fractal nature using an improved spherical harmonic analysis. *Computers and Geotechnics* **104**:1-12.

Wilmanski, K. (1998) *Thermomechanics of continua.* Springer Verlag, Berlin.

Xu, D.-S., Borana, L. & Yin, J.-H. (2014) Measurement of small strain behavior of a local soil by fiber Bragg grating-based local displacement transducers. *Acta Geotechnica* **9(6)**:935-943.

Yang, H., Sinha, S. K., Feng, Y., Mccallen, D. B. & Jeremić, B. (2018) Energy dissipation analysis of elastic–plastic materials. *Computer Methods in Applied Mechanics and Engineering* **331**:309-326.

Yang, J. & Luo, X. (2018) The critical state friction angle of granular materials: does it depend on grading? *Acta Geotechnica* **13(3)**:535-547.

Yang, J. & Wei, L. (2012) Collapse of loose sand with the addition of fines: the role of particle shape. *geotechnique* **62(12)**:1111-1125.

Zhang, L., Nguyen, N. G. H., Lambert, S., Nicot, F., Prunier, F. & Djeran-Maigre, I. (2017) The role of force chains in granular materials: from statics to dynamics. *European Journal of Environmental and Civil Engineering* **21(7-8)**:874-895.

Zhao, J. & Guo, N. (2013) Unique critical state characteristics in granular media considering fabric anisotropy. *geotechnique* **63(8)**:695.

Zhao, X. & Evans, T. (2011) Numerical analysis of critical state behaviors of granular soils under different loading conditions. *Granular Matter* **13(6)**:751.

Zhao, Z., Liu, C. & Brogliato, B. (2008) Energy dissipation and dispersion effects in granular media. *Physical review E* **78(3)**:031307.

Zheng, H., Wang, D. & Behringer, R. P. (2019) Experimental study on granular biaxial test based on photoelastic technique. *Engineering geology* **260**:105208.

Zhou, B. & Wang, J. (2017) Generation of a realistic 3D sand assembly using X‐ray micro‐computed tomography and spherical harmonic‐based principal component analysis. *International Journal for Numerical and Analytical Methods in Geomechanics* **41(1)**:93-109.

Zhou, B., Wang, J. & Zhao, B. (2015) Micromorphology characterization and reconstruction of sand particles using micro X-ray tomography and spherical harmonics. *Engineering geology* **184**:126-137.

Ziegler, H. & Wehrli, C. (1987) The derivation of constitutive relations from the free energy and the dissipation function. *Advances in applied mechanics* **25**:183-238.

Appendix. A

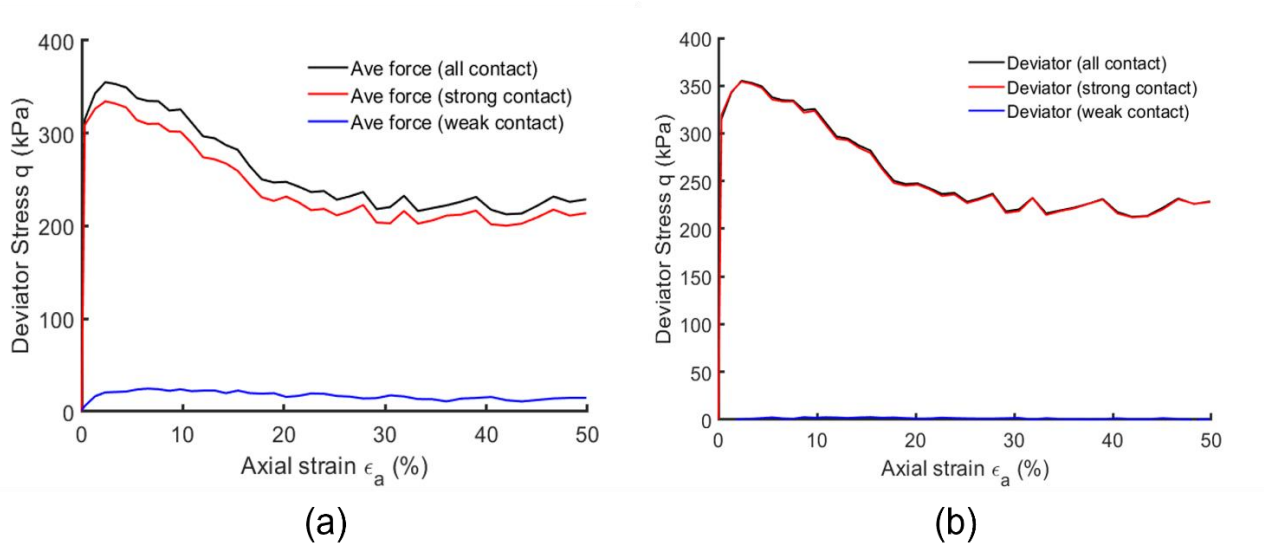

Figure A-1 Contribution of weak and strong contact networks to the deviator stress; a) when the average force partitioning method is used; b) when the deviator stress partitioning method is used. Dense sample sheared with 250 kPa and constant σ_r.

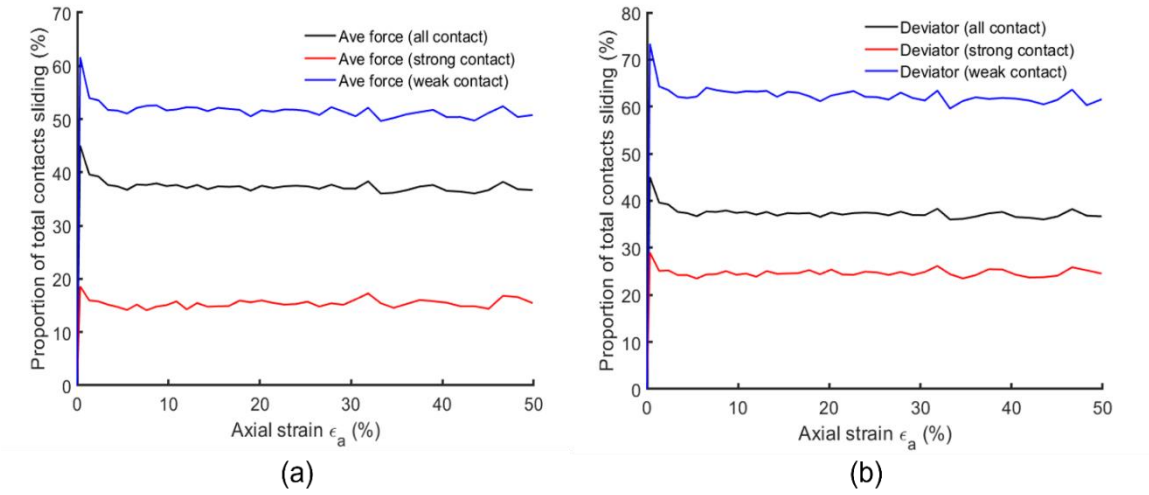

Figure A-2 Contribution weak and strong contact networks proportion of sliding contacts; a) when average force partitioning method is used; b) when deviator stress partitioning method is used. Dense sample sheared with 250 kPa and constant σ_r.

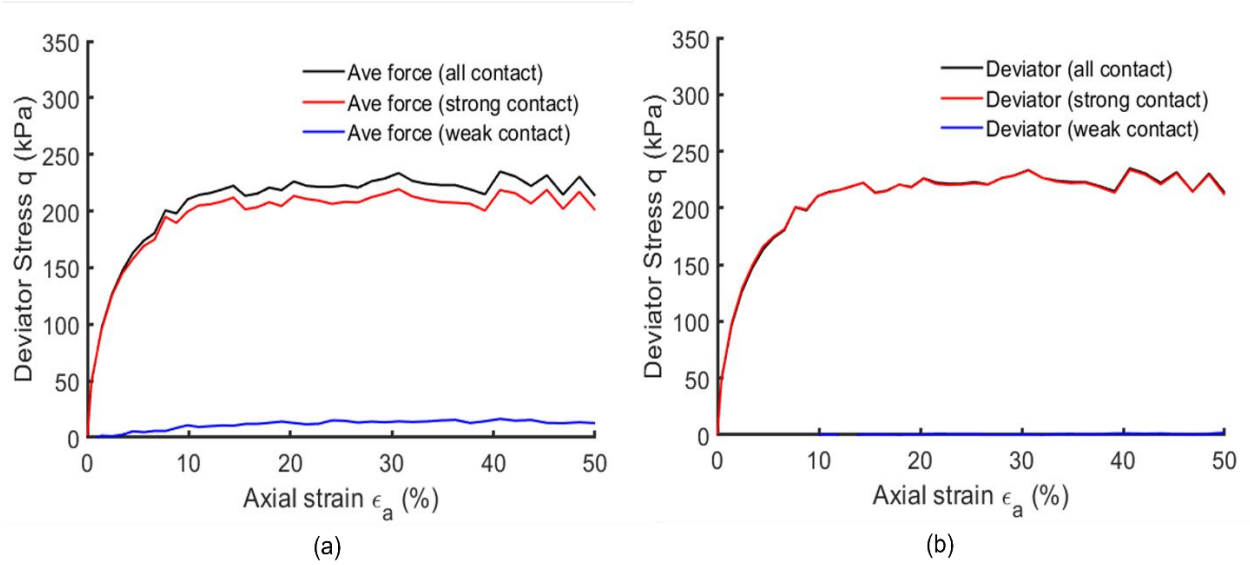

Figure A-3 Contribution weak and strong contact networks to the deviator stress; a) when average force partitioning method is used; b) when deviator stress partitioning method is used. Loose sample sheared with 250 kPa and constant σ_r.

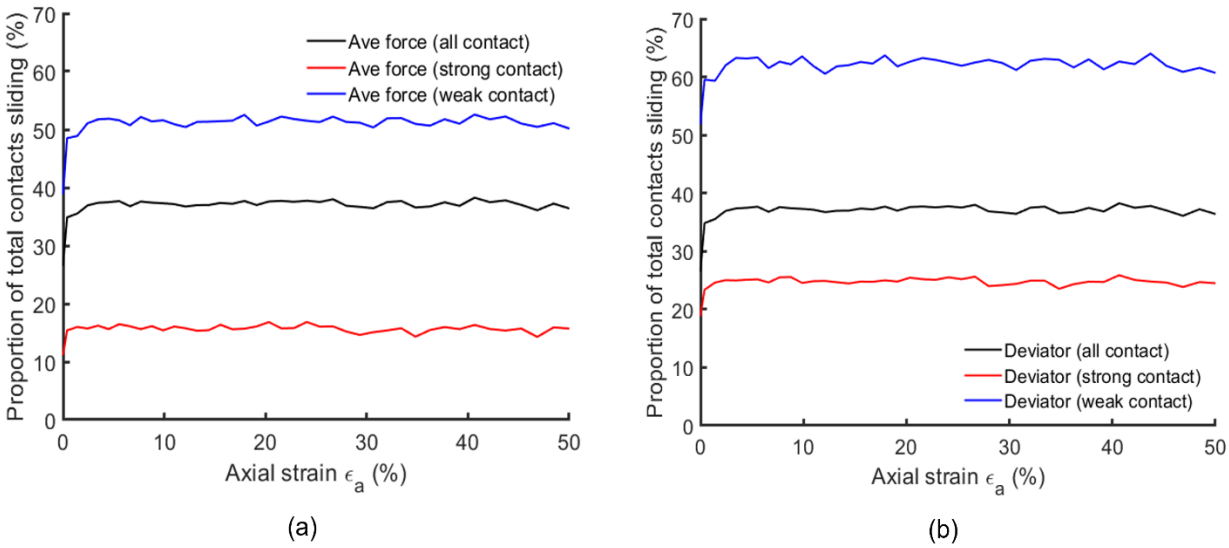

Figure A-4 Contribution weak and strong contact networks proportion of sliding contacts; a) when average force partitioning method is used; b) when deviator stress partitioning method is used. Loose sample sheared with 250 kPa and constant σ_r.

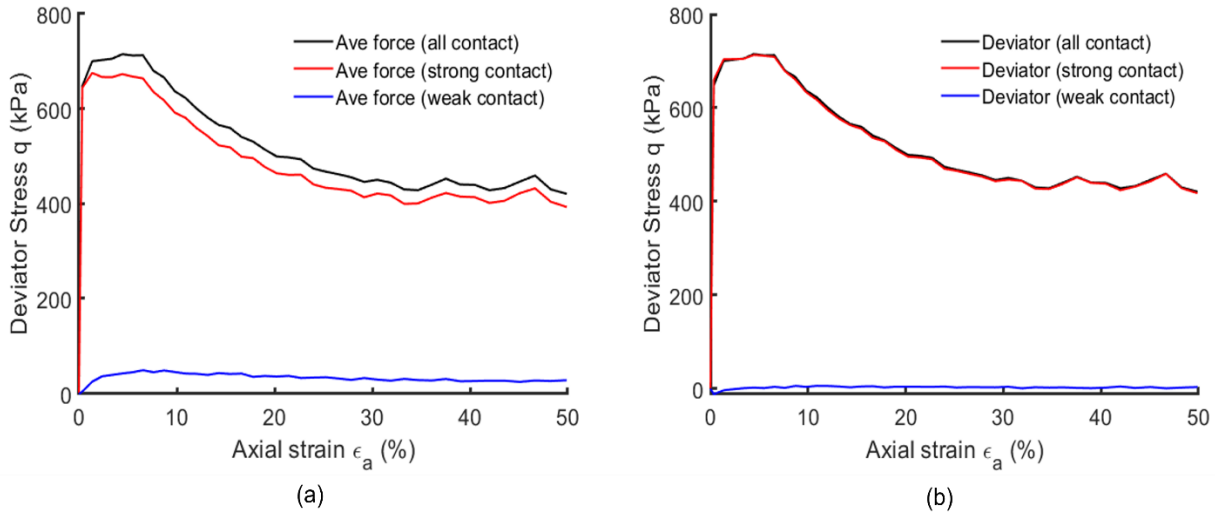

Figure A-5 Contribution weak and strong contact networks to the deviator stress; a) when average force partitioning method is used; b) when deviator stress partitioning method is used. Dense sample sheared with 500 kPa and constant σ_r.

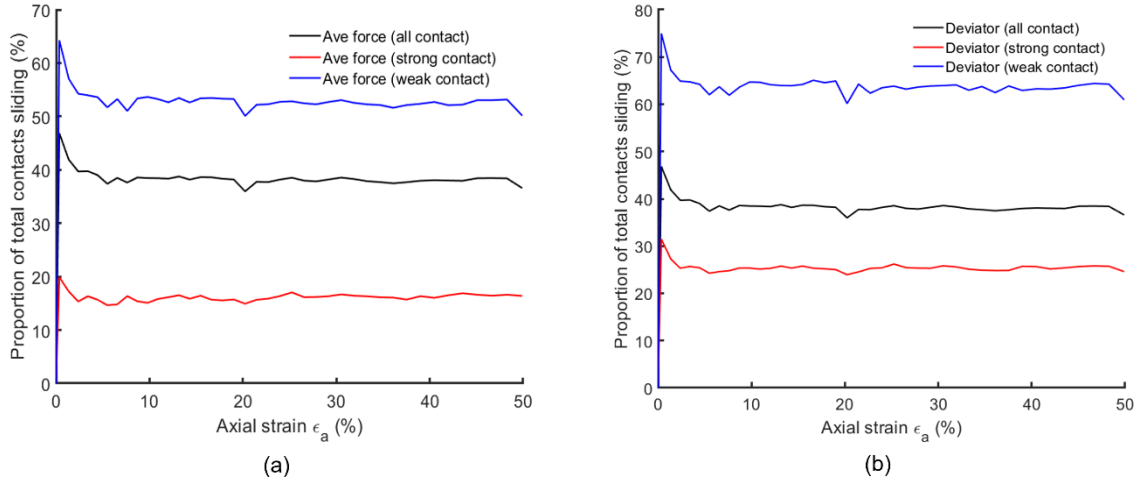

Figure A-6 Contribution weak and strong contact networks proportion of sliding contacts; a) when average force partitioning method is used; b) when deviator stress partitioning method is used. Dense sample sheared with 500 kPa and constant σ_r.

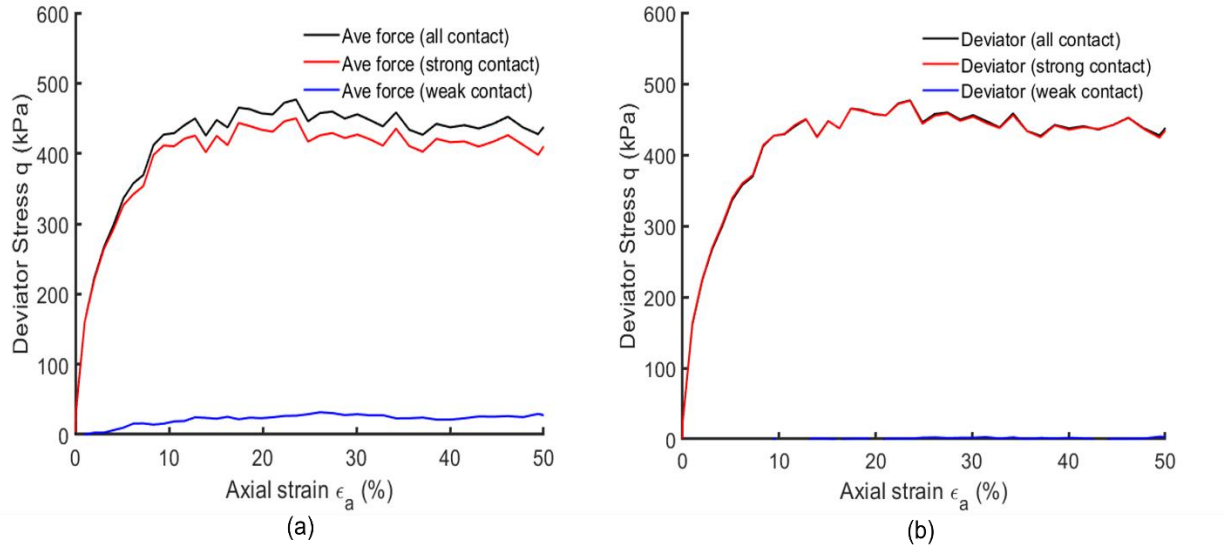

Figure A-7 Contribution weak and strong contact networks to the deviator stress; a) when average force partitioning method is used; b) when deviator stress partitioning method is used. Loose sample sheared with 500 kPa and constant σ_r.

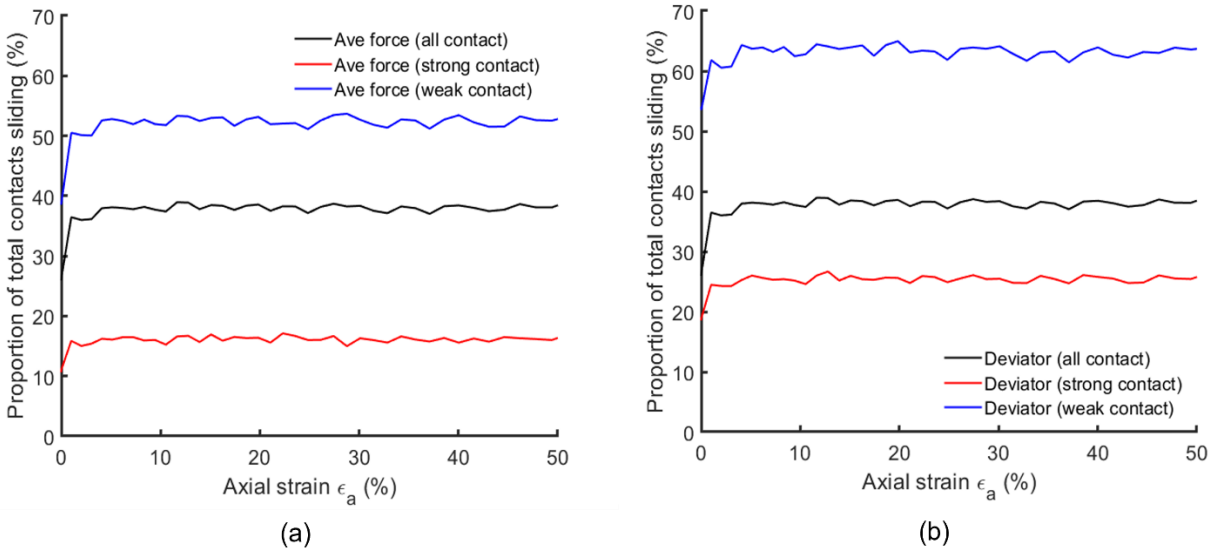

Figure A-8 Contribution weak and strong contact networks proportion of sliding contacts; a) when average force partitioning method is used; b) when deviator stress partitioning method is used. Loose sample sheared with 500 kPa and constant σ_r.

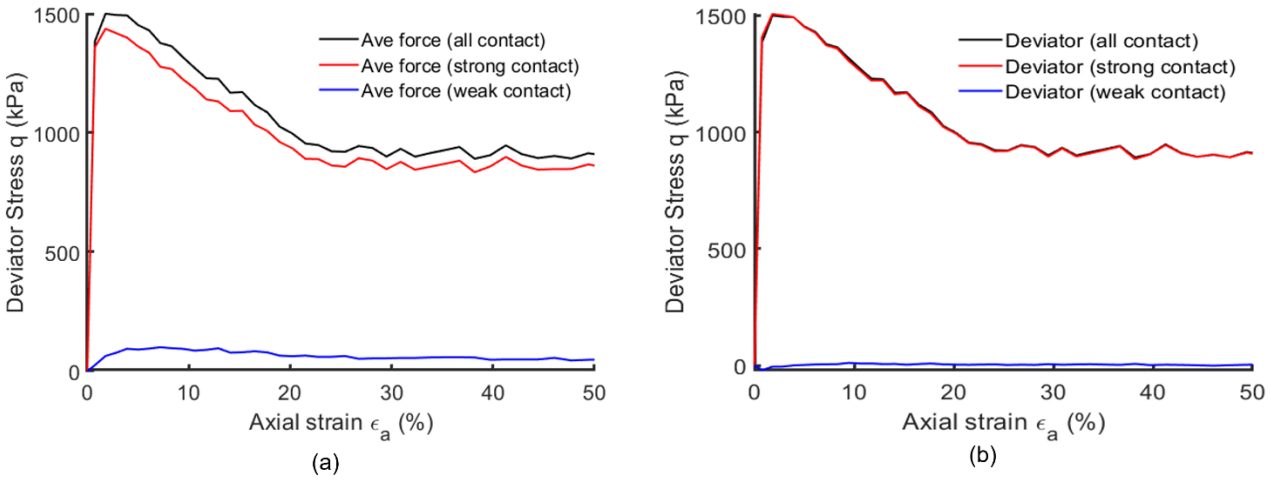

Figure A-9 Contribution weak and strong contact networks to the deviator stress; a) when average force partitioning method is used; b) when deviator stress partitioning method is used. Dense sample sheared with 1000 kPa and constant σ_r.

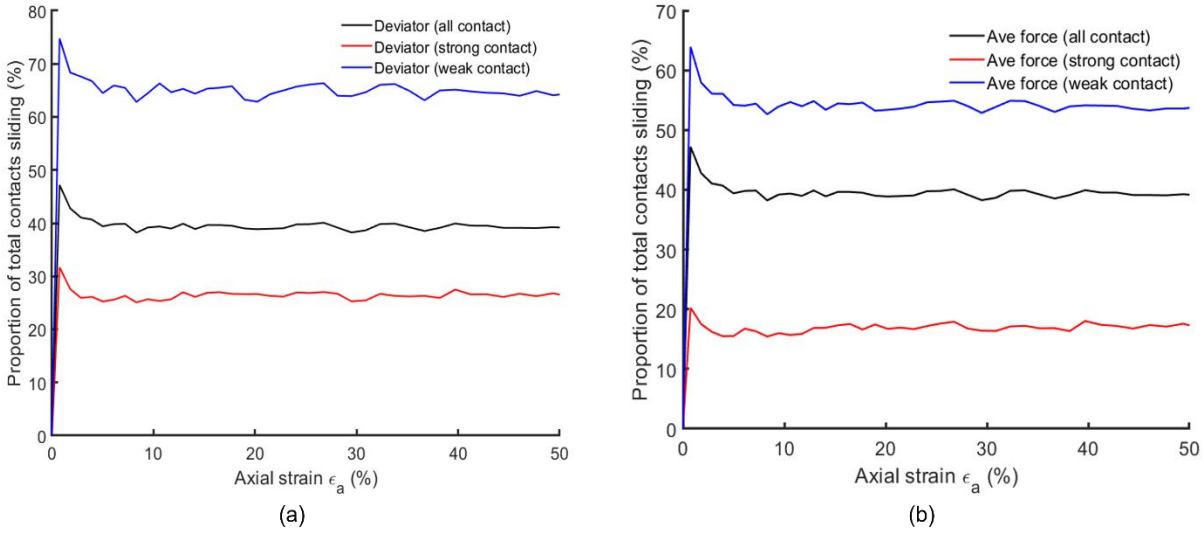

Figure A-10 Contribution weak and strong contact networks proportion of sliding contacts; a) when average force partitioning method is used; b) when deviator stress partitioning method is used. Dense sample sheared with 1000 kPa and constant σ_r.

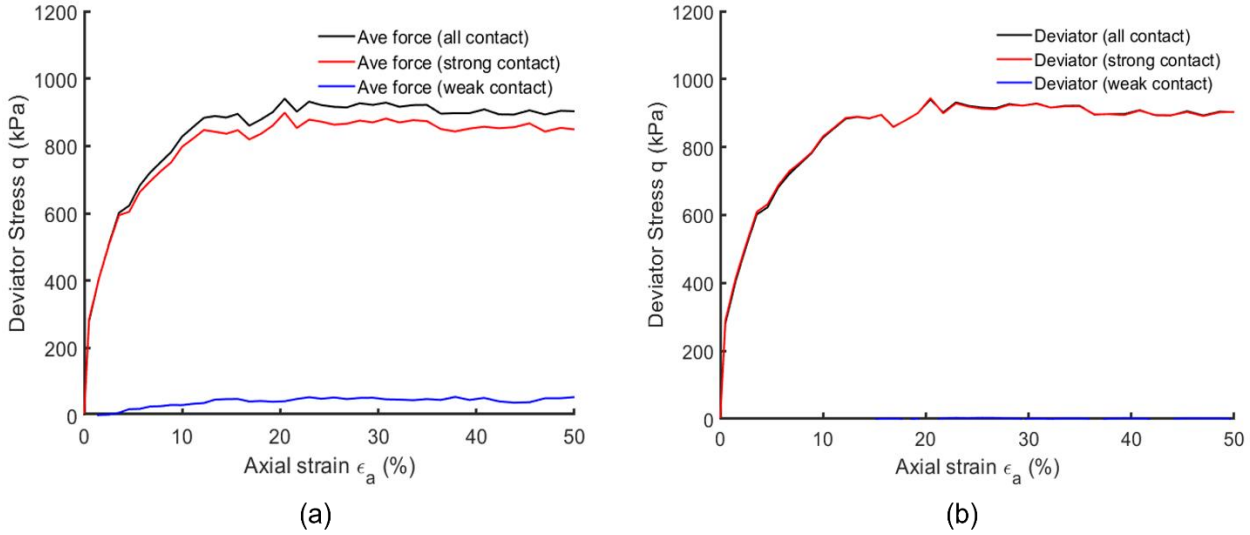

Figure A-11 Contribution weak and strong contact networks to the deviator stress; a) when average force partitioning method is used; b) when deviator stress partitioning method is used. Loose sample sheared with 1000 kPa and constant σ_r.

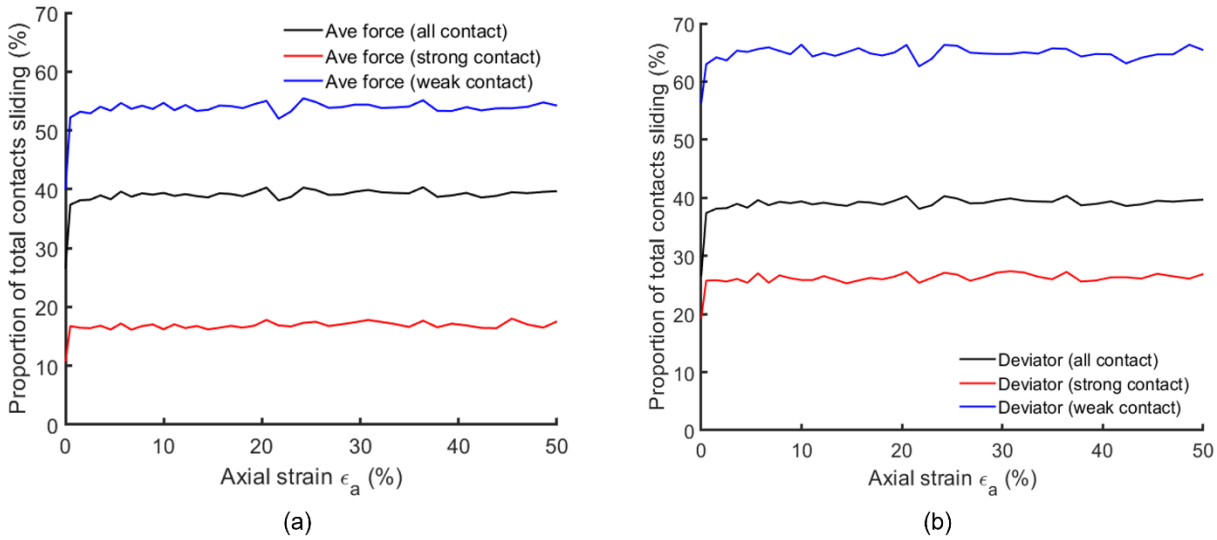

Figure A-12 Contribution weak and strong contact networks proportion of sliding contacts; a) when average force partitioning method is used; b) when deviator stress partitioning method is used. loose sample sheared with 1000 kPa and constant σ_r.

The results for constant p simulations

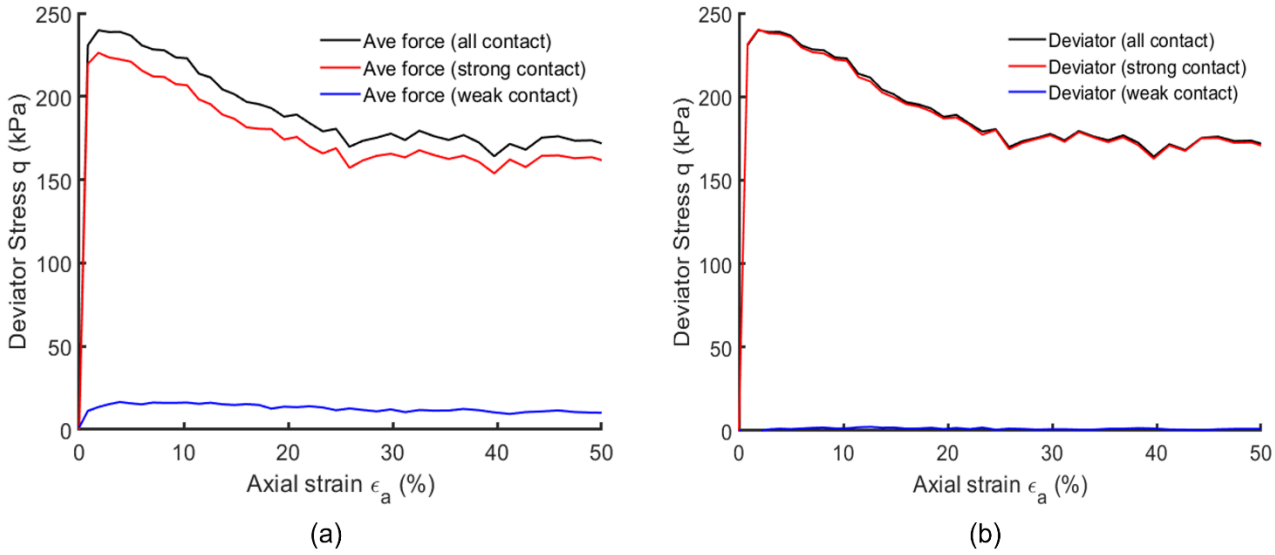

Figure A-13 Contribution weak and strong contact networks to the deviator stress; a) when average force partitioning method is used; b) when deviator stress partitioning method is used. Dense sample sheared with 250 kPa and constant p.

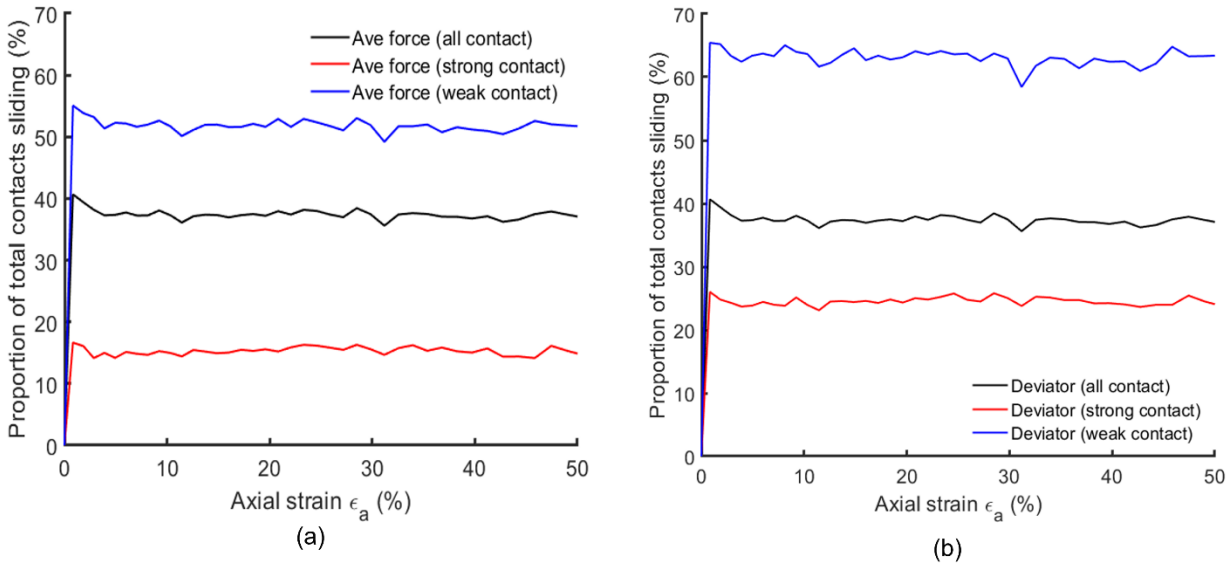

Figure A-14 Contribution weak and strong contact networks proportion of sliding contacts; a) when average force partitioning method is used; b) when deviator stress partitioning method is used. Dense sample sheared with 250 kPa and constant p.

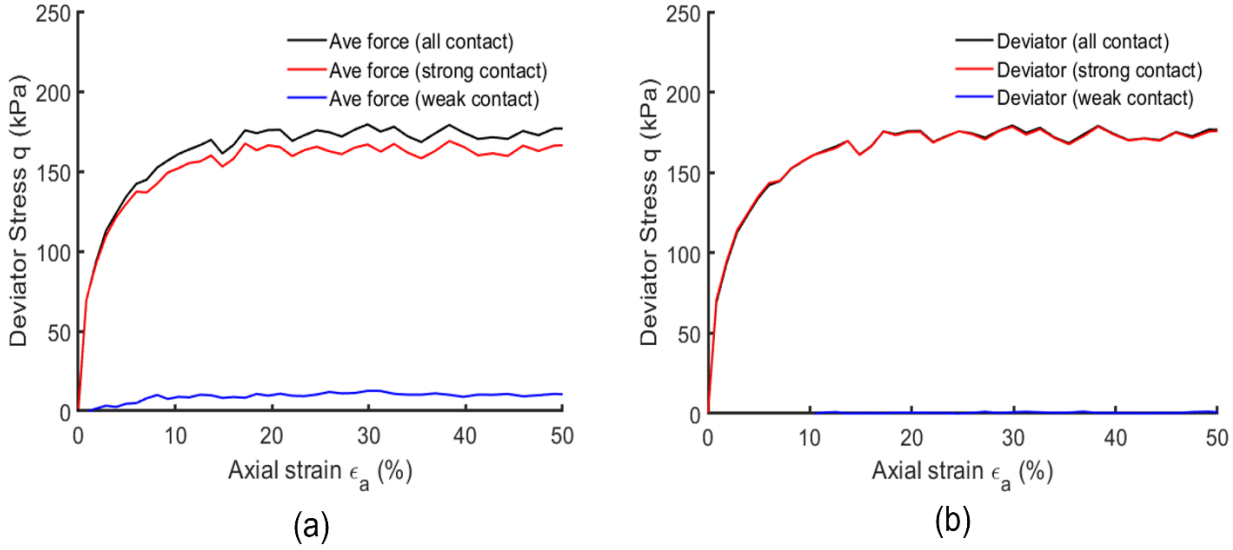

Figure A-15 Contribution weak and strong contact networks to the deviator stress; a) when average force partitioning method is used; b) when deviator stress partitioning method is used. Loose sample sheared with 250 kPa and constant p.

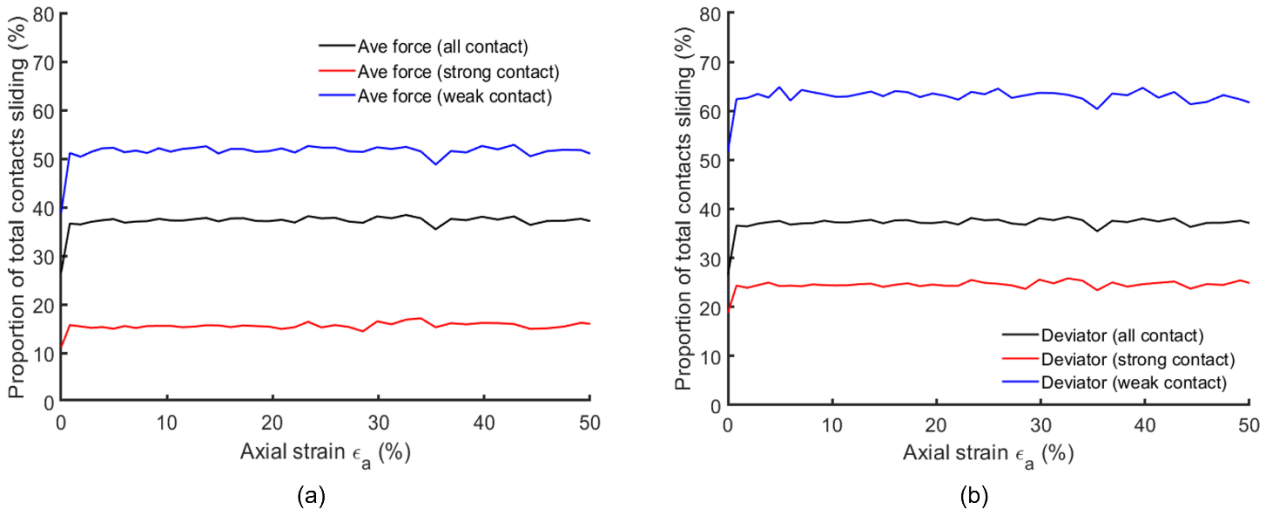

Figure A-16 Contribution weak and strong contact networks proportion of sliding contacts; a) when average force partitioning method is used; b) when deviator stress partitioning method is used. Loose sample sheared with 250 kPa and constant p.

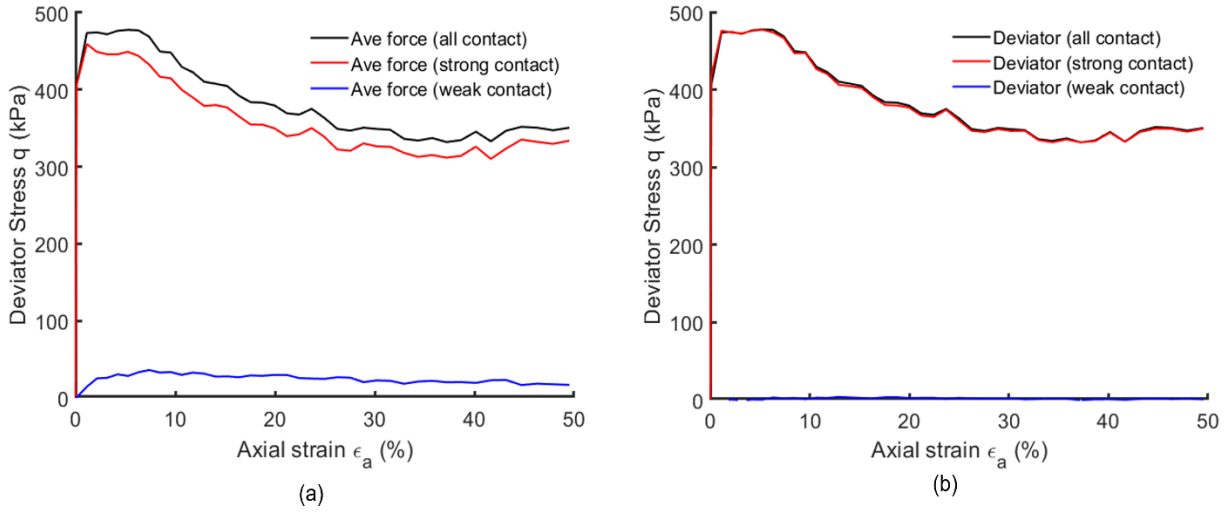

Figure A-17 Contribution weak and strong contact networks to the deviator stress; a) when average force partitioning method is used; b) when deviator stress partitioning method is used. Dense sample sheared with 500 kPa and constant p.

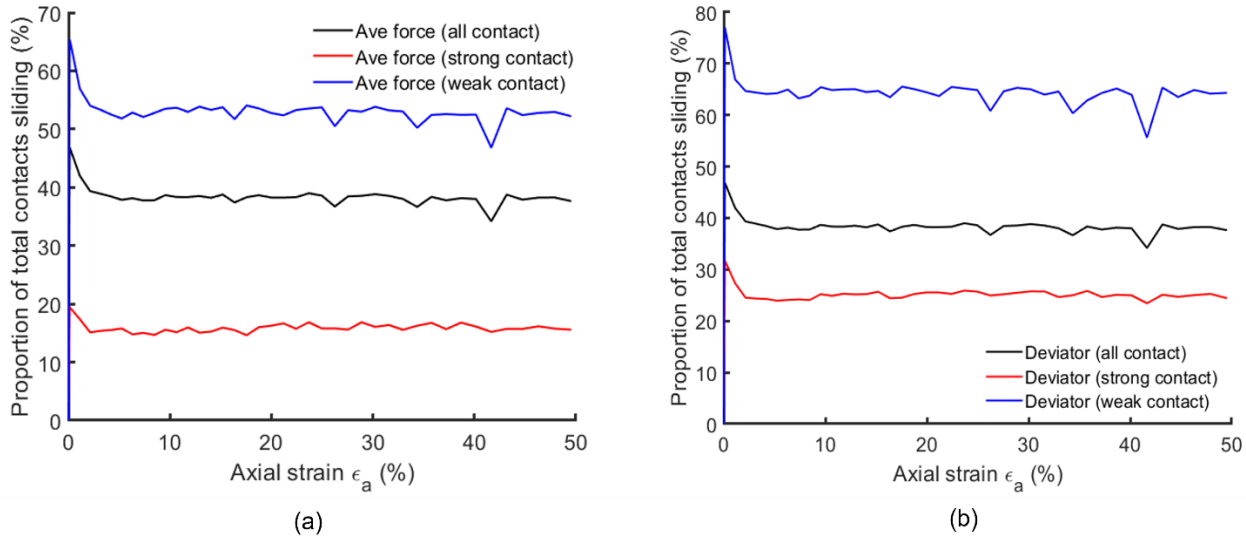

Figure A-18 Contribution weak and strong contact networks proportion of sliding contacts; a) when average force partitioning method is used; b) when deviator stress partitioning method is used. Dense sample sheared with 500 kPa and constant p.

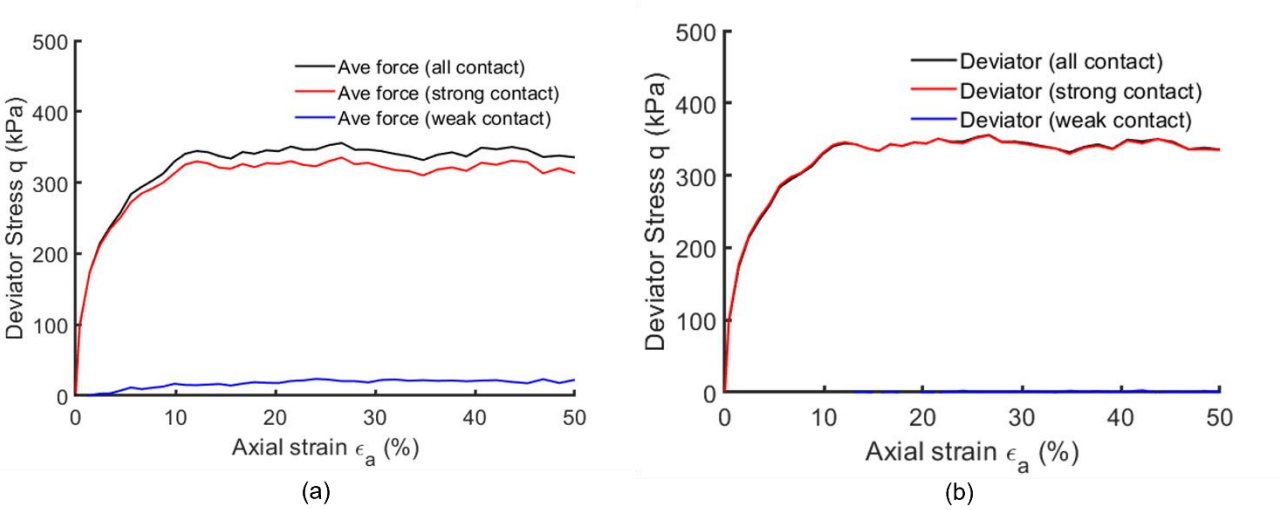

Figure A-19 Contribution weak and strong contact networks to the deviator stress; a) when average force partitioning method is used; b) when deviator stress partitioning method is used. Loose sample sheared with 500 kPa and constant p.

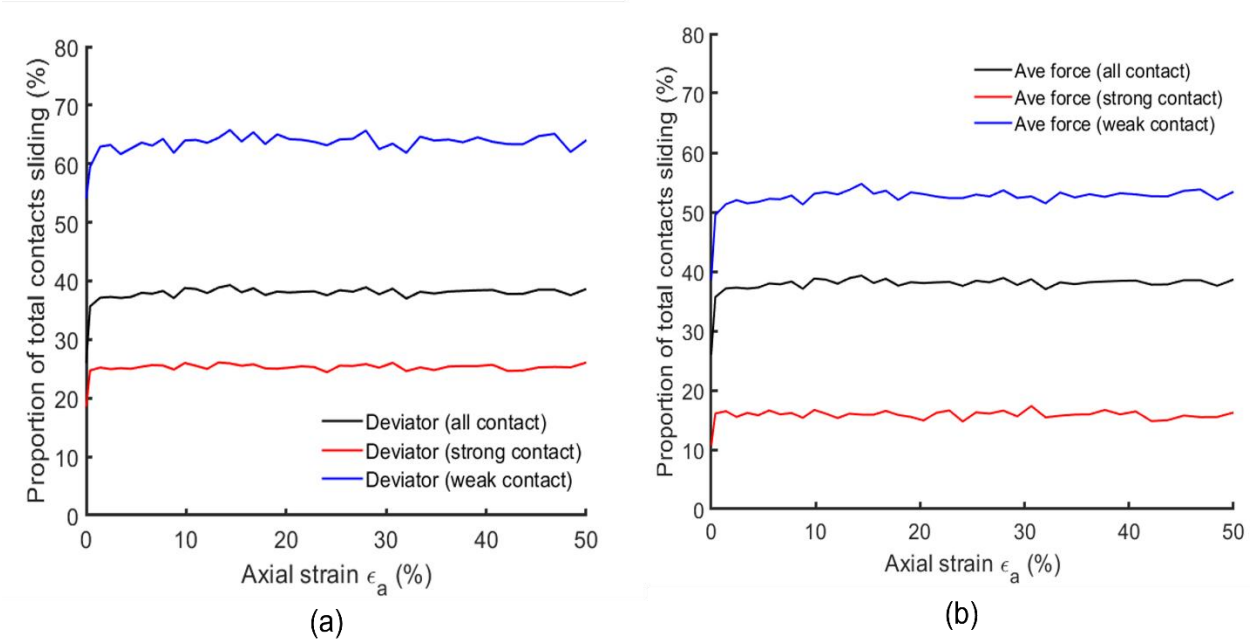

Figure A-20 Contribution weak and strong contact networks proportion of sliding contacts; a) when average force partitioning method is used; b) when deviator stress partitioning method is used. Loose sample sheared with 500 kPa and constant p.

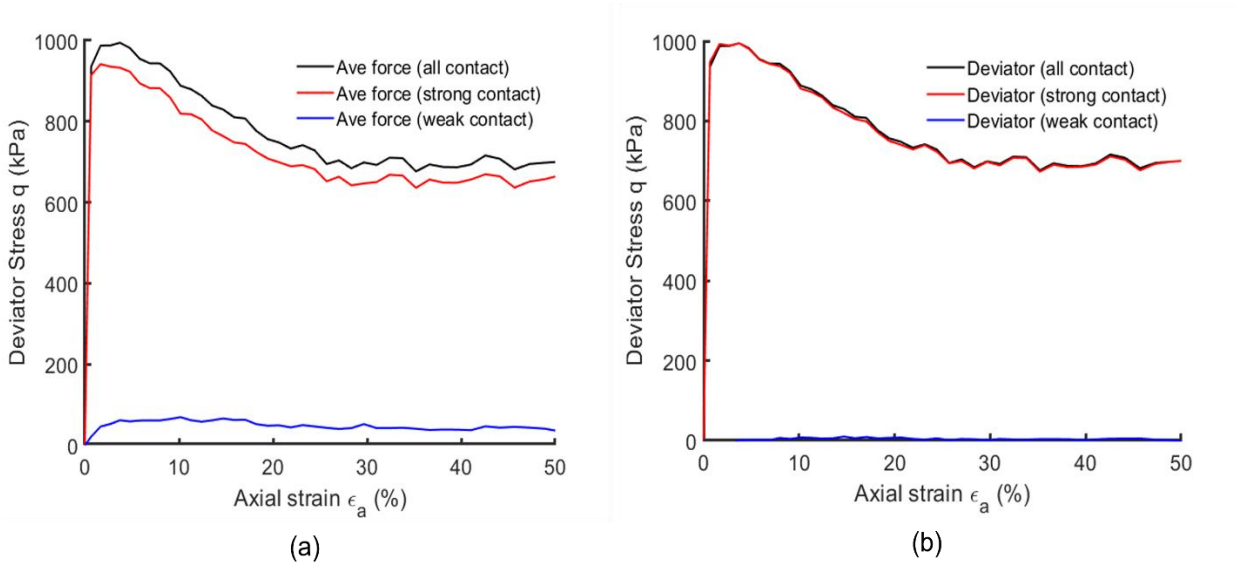

Figure A-21 Contribution weak and strong contact networks to the deviator stress; a) when average force partitioning method is used; b) when deviator stress partitioning method is used. Dense sample sheared with 1000 kPa and constant p.

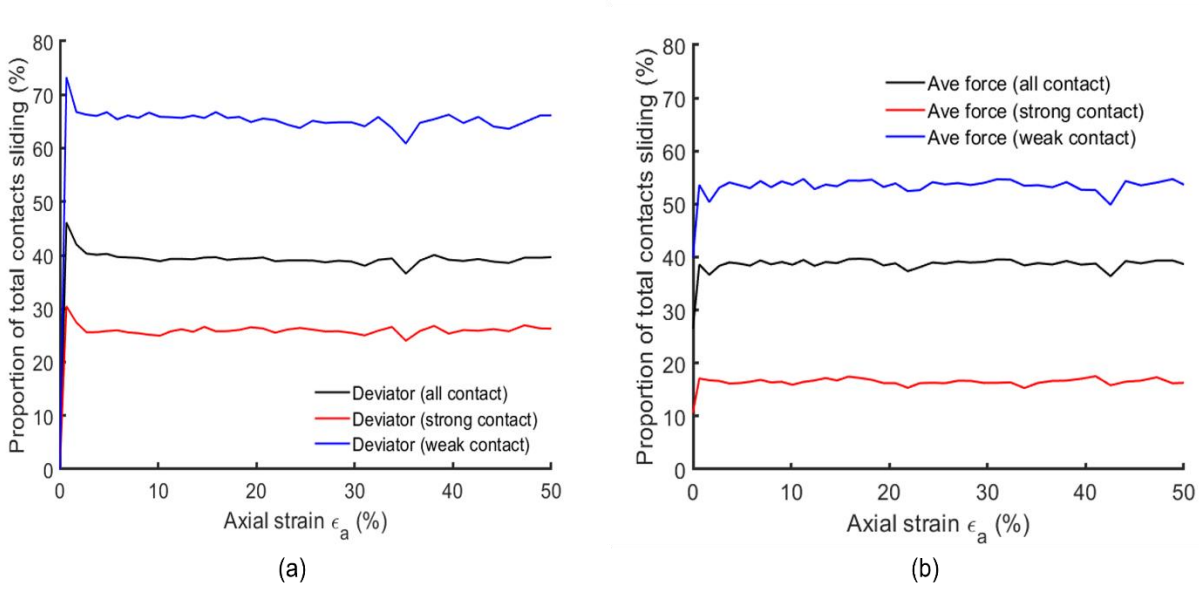

Figure A-22 Contribution weak and strong contact networks proportion of sliding contacts; a) when average force partitioning method is used; b) when deviator stress partitioning method is used. Dense sample sheared with 1000 kPa and constant p.

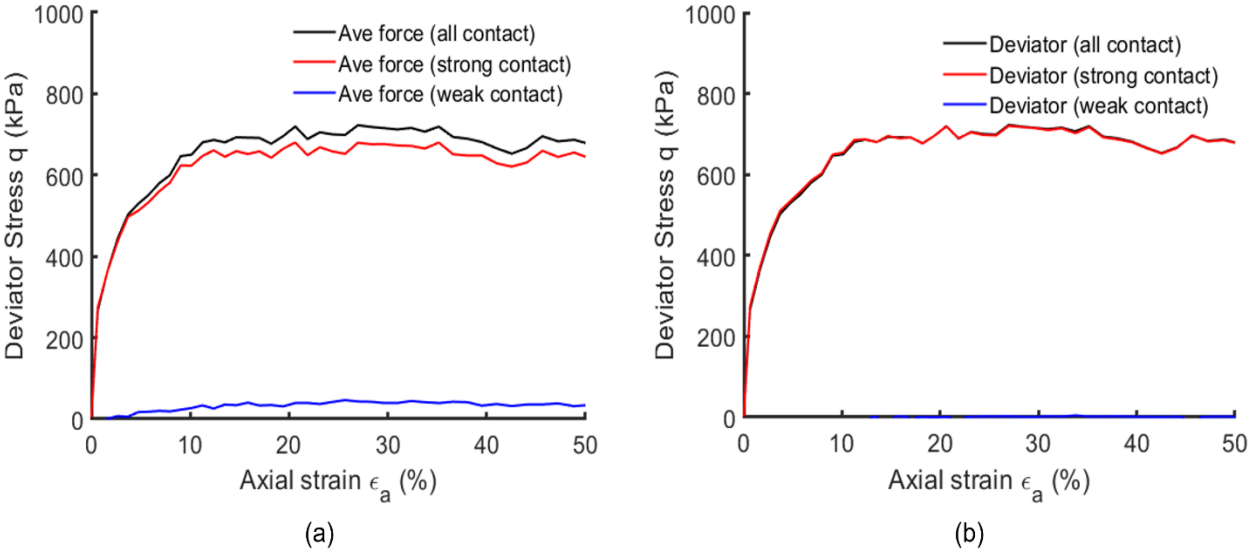

Figure A-23 Contribution weak and strong contact networks to the deviator stress; a) when average force partitioning method is used; b) when deviator stress partitioning method is used. Loose sample sheared with 1000 kPa and constant p.

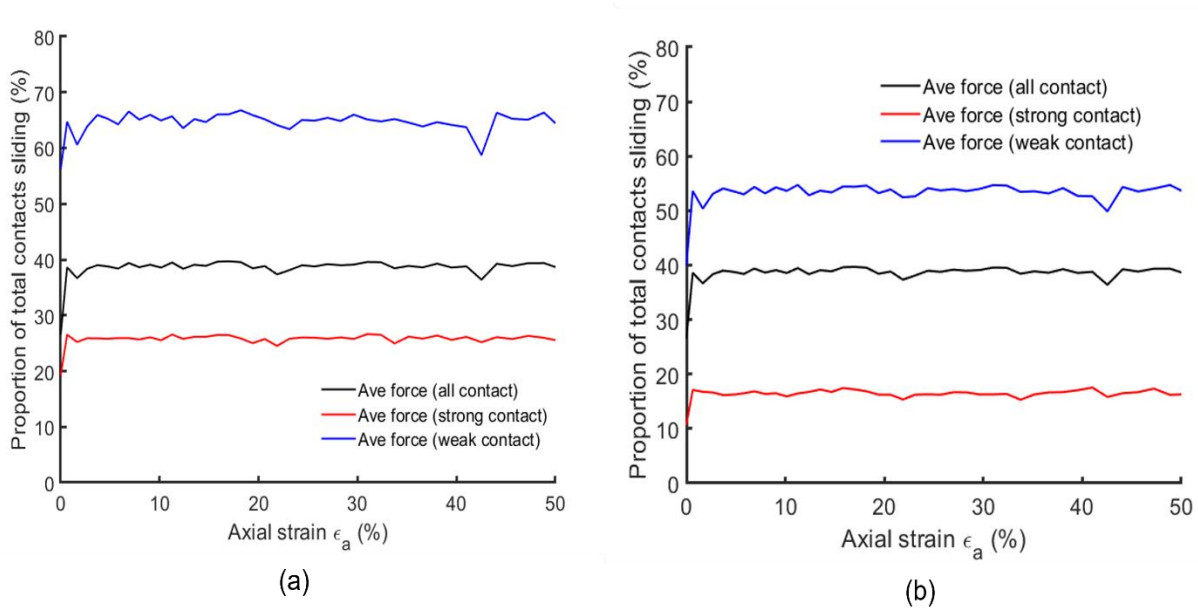

Figure A-24 Contribution weak and strong contact networks proportion of sliding contacts; a) when average force partitioning method is used; b) when deviator stress partitioning method is used. Loose sample sheared with 1000 kPa and constant p.

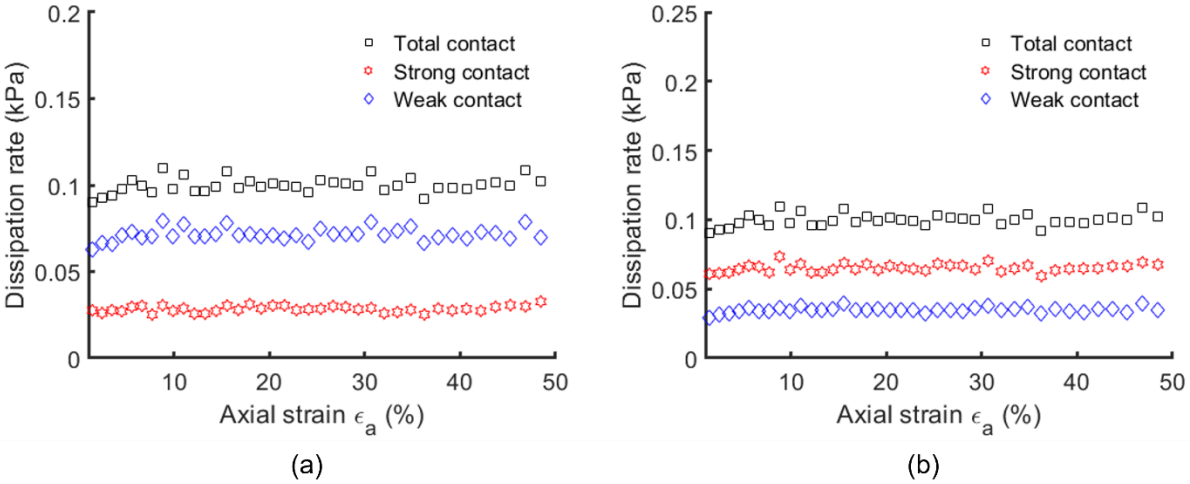

Figure A-25 Contribution of weak and strong networks to the energy dissipation from probe test for loose sample sheared with constant σ_r (σ_3 = 250 kPa); a) average force partition; b) deviator stress partition

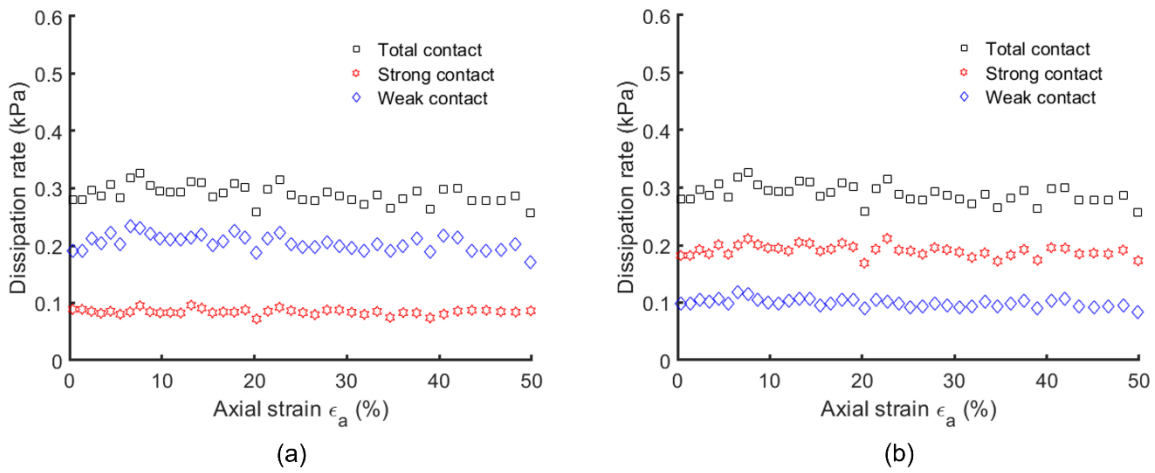

Figure A-26 Contribution of weak and strong networks to the energy dissipation from probe test for dense sample sheared with constant σ_r (σ_3 = 500 kPa); a) average force partition; b) deviator stress partition

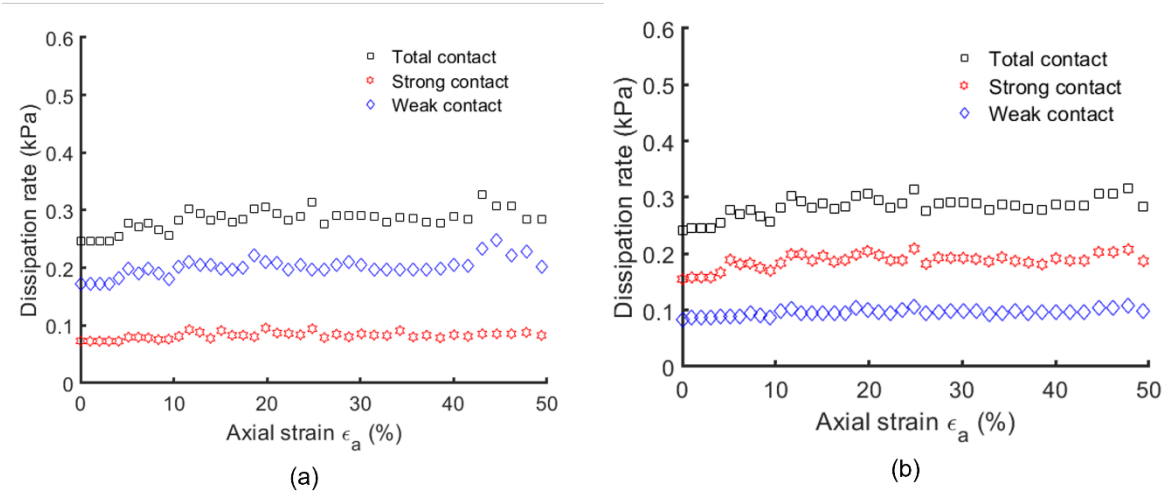

Figure A-27 Contribution of weak and strong networks to the energy dissipation from probe test for loose sample sheared with constant σ_r (σ_3 = 500 kPa); a) average force partition; b) deviator stress partition

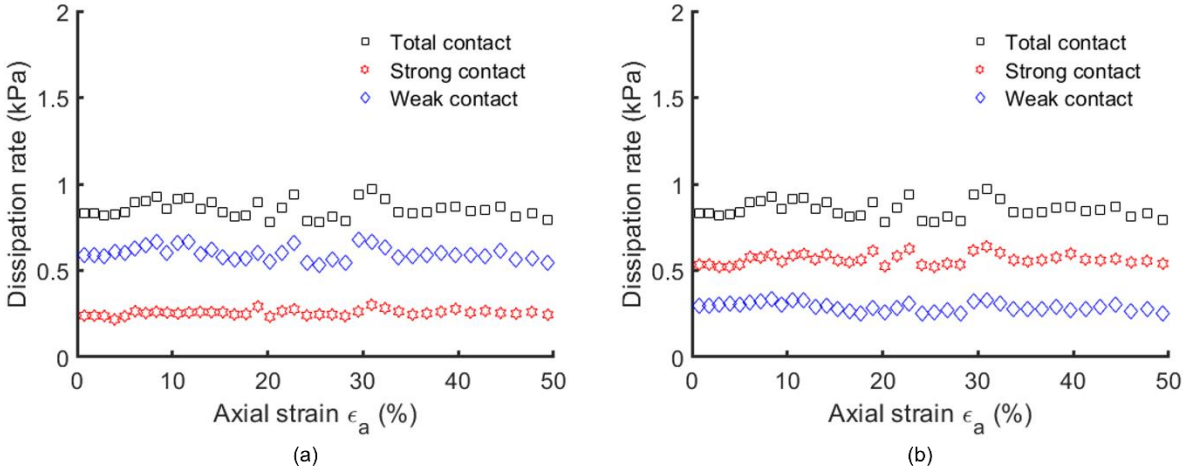

Figure A-28 Contribution of weak and strong networks to the energy dissipation from probe test for dense sample sheared with constant σ_r (σ_3 = 1000 kPa); a) average force partition; b) deviator stress partition

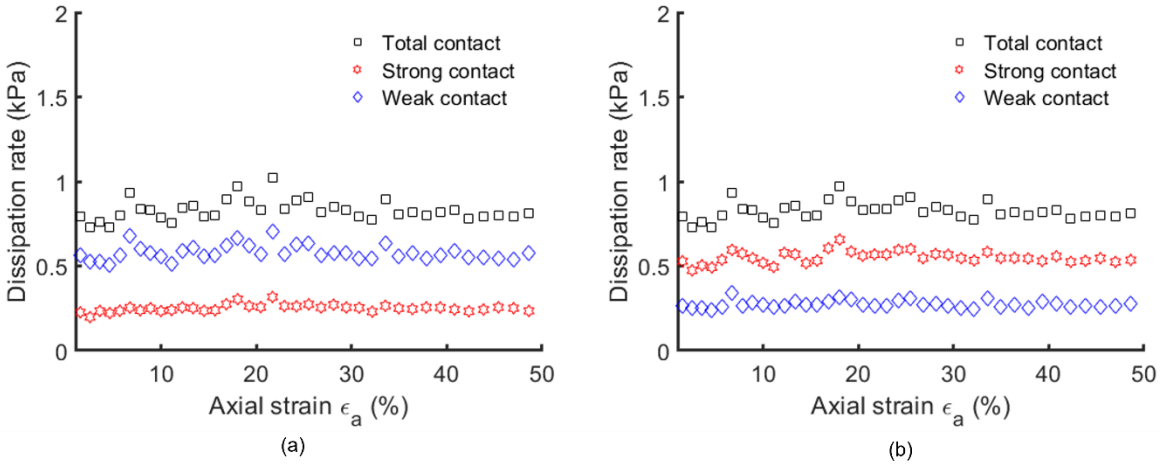

Figure A-29 Contribution of weak and strong networks to the energy dissipation from probe test for loose sample sheared with constant σ_r. (σ_3 = 1000 kPa); a) average force partition; b) deviator stress partition